KUNGL TEKNISKA HÖGSKOLAN

TRITA-MEK
Technical Report 2001:01
ISSN 0348-467X
ISRN KTH/MEK/TR--01/01--SE

Studies of turbulent boundary layer flow through direct numerical simulation

Martin Skote

Doctoral Thesis
Stockholm, 2001

Royal Institute of Technology
Department of Mechanics

Studies of turbulent boundary layer flow through direct numerical simulation

by

Martin Skote

Februari 2001
Technical reports from
Royal Institute of Technology
Department of Mechanics
SE-100 44 Stockholm, Sweden

Typsatt i $\mathcal{AMS}$-LaTeX.

Akademisk avhandling som med tillstånd av Kungliga Tekniska Högskolan i Stockholm framlägges till offentlig granskning för avläggande av teknologie doktorsexamen fredagen den 23:e februari 2001 kl 10.15 i Kollegiesalen, Administrationsbyggnaden, Kungliga Tekniska Högskolan, Valhallavägen 79, Stockholm.

Norstedts Tryckeri AB, Stockholm 2001

Studies of turbulent boundary layer flow through direct numerical simulation

Martin Skote
Department of Mechanics, Royal Institute of Technology
SE-100 44 Stockholm, Sweden

Abstract

The objective has been to study turbulent boundary layers under adverse pressure gradients (APG) through direct numerical simulation (DNS). The numerical code is based on a pseudo-spectral technique which is suitable for the simple geometry (flat plate) considered here. A large effort has been put into the optimization of the numerical code on various super computers. Five large simulations have been performed, ranging from a zero pressure gradient boundary layer to a separating flow. The simulations have revealed many features of APG turbulent boundary layers which are difficult to capture in experiments. Especially the near-wall behavior has been investigated thoroughly, both through the statistical and instantaneous flow.

Theoretical work based on the turbulent boundary layer equation has been conducted with the aim to develop near-wall laws suitable for turbulence models. The conditions for self-similarity and relations between mean flow parameters have been reviewed and applied in the DNS. The results from the simulations have confirmed the theoretical part of this work.

The turbulent flows have also been investigated using turbulence models. A boundary layer under strong APG is difficult to predict correctly, and the separating boundary layer is one of the most difficult flows in this respect. The near-wall damping was improved by comparing DNS data and model predictions. The asymptotic behavior of an APG boundary layer for large Reynolds numbers has been determined through asymptotic analysis and with the aid of turbulence models.

The DNS data have also been utilized for the investigation of instantaneous turbulence structures. The turbulent boundary layer was found to be populated by near-wall low-speed streaks and vortices shaped like a horseshoe, in agreement with earlier investigations. The instability mechanism behind the formation of these vortices is examined through a simulation of an artificial low-speed streak introduced in a laminar boundary layer.

The turbulence statistics from the simulations have also been compared with other simulations of turbulent boundary layers and Couette flow.

Descriptors: Turbulence, direct numerical simulation, boundary layer, separation, parallel computers, turbulence modelling.

Preface

This thesis considers direct numerical simulation of turbulent boundary layer flows. The introductory part is a summary of the work contained in the nine papers included, and thus is not a general review of the subject. The thesis is based on and contains the following papers.

Paper 1. Skote, M., Henningson, D.S. & Henkes, R.A.W.M. 1998 Direct numerical simulation of self-similar turbulent boundary layers in adverse pressure gradients. *Flow, Turbulence and Combustion*, **60**, 47–85.

Paper 2. Henkes, R.A.W.M., Skote, M. & Henningson, D.S. 1997 Application of turbulence models to equilibrium boundary layers under adverse pressure gradient. *Eleventh Symposium on Turbulent Shear Flows, Grenoble, France*, 33:13–33:18.

Paper 3. Skote, M. & Henningson, D.S. 1999 Analysis of the data base from a DNS of a separating turbulent boundary layer. *Center for Turbulence Research, Annual Research Briefs 1999*, 225–237.

Paper 4. Skote, M. & Henningson, D.S. 2000 Direct numerical simulation of separating turbulent boundary layers. Submitted to *Journal of Fluid Mechanics*.

Paper 5. Skote, M. & Wallin, S. 2000 Near-wall damping in model predictions of separated flows. FFA TN 2000-72.

Paper 6. Komminaho, J. & Skote, M. 2000 Reynolds stress budgets in Couette and boundary layer flows. Submitted to *Flow, Turbulence and Combustion*.

Paper 7. Skote, M., Haritonidis J.H. & Henningson, D.S. 2000 Instabilities in turbulent boundary layers. Submitted to *Physics of Fluids*.

Paper 8. Alvelius, K. & Skote, M. 1999 The performance of a spectral simulation code for turbulence on parallel computers with distributed memory. TRITA-MEK 2000:17.

Paper 9. Lundbladh, A., Berlin, S., Skote, M., Hildings, C., Choi, J., Kim, J. & Henningson, D.S. 1999 An efficient spectral method for simulation of incompressible flow over a flat plate. TRITA-MEK 1999:11.

The papers are re-set in the present thesis format. Some of them are based on publications in conference proceedings (Skote & Henningson 1997, 1998, 1999; Skote *et al.* 2000).

Division of work between authors

The DNS was performed with a numerical code already in use for mainly transition research. It is based on a pseudo-spectral technique and has been further developed by Skote (MS) for extracting flow quantities needed in turbulence research. The necessary changes of the code for the porting to computers with distributed memory have been completed.

The DNS in paper 1 was performed by MS. The turbulence model calculations were done by MS together with Henkes (RH). The theoretical work was performed by MS. The writing was done by MS with great help from Henningson (DH).

The DNS data in paper 2 are the same as in paper 1. The model predictions were conducted by RH. The paper was written mainly by RH.

The DNS data in paper 3 were taken from Na & Moin (1998). The evaluation of the data and the writing was done by MS with help from DH. The theoretical part of the work was done by MS.

The DNS in paper 4 was performed by MS. The theoretical work was done by MS. The writing was done by MS with help from DH.

In paper 5, the a priori tests were performed by MS, while the model predictions were performed by Wallin (SW). The theoretical work and writing was done by MS and SW together.

The Couette data were produced and evaluated by Komminaho (JK) in paper 6. The boundary layer data were produced and evaluated by MS. JK wrote the part about the Couette flow, while the part about the boundary layer was written by MS.

Haritonidis (JH) came up with the original idea for the work in paper 7. The simulations were performed by MS and JH together. The stability analysis was performed by MS with a lot of help from JH and DH. The paper was written by MS with help from JH and DH.

The work described in paper 8 was performed by Alvelius and MS together. It was also written together.

MS contribution in paper 9 was the pressure solver and to compile and organize the report.

Contents

"A dry maple leaf fell off and is dropping to the ground; its movement is exactly like the flight of a butterfly. Isn't it strange? The most mournful and dead—resembles the most gay and lively."

Ivan Turgenev

CHAPTER 1

Introduction

The phenomenon leading to such an exclaim of wonder as on the previous page is caused by the motion of air, which mysteries are investigated in the field of fluid mechanics.

Actually, there is no mystery at all. Newton's second law of motion and a constitutive relation regarding the viscous forces describe the motion in mathematical terms (equations). The equations are called Navier-Stokes (N-S) equations and form together with the continuity equation (conservation of mass) a system of four equations for the four variables: velocity vector (three components) and pressure. However, because the flow can be complicated enough to even resemble living things, it is difficult to solve the governing equations. In other words, the flow is represented by a simple equation (when put in a mathematical formulation), but the solution may not be simple. Only very special solutions to the N-S equations can be solved mathematically to a closed expression, i.e. the velocity vector given as a function of time and space. For more realistic situations, the solution has to be calculated with the aid of a computer. Alternatively, experiments have to be conducted to extract information about the flow.

Most of the flows in nature and in technical applications are turbulent, i.e. the velocity fluctuates rapidly in time and space. This is what makes the dry leaf come to life. Other examples include the flow over the wing of an aircraft and the flow of blood through our veins.

To numerically solve the N-S equations is called direct numerical simulation (DNS) and is an enormous challenge for the super computers in use today. The difficulties that arise when performing DNS are due to the wide range of scales in the turbulence that need to be resolved, making the simulations large and time consuming. By scales one means the lengths (both in time and space) that are important for the dynamics of the flow. The large scales are determined by the outer, geometrical constraints, and the smallest scales are determined by the viscosity (inner friction). The range of scales is measured by the Reynolds number.

Another example of the complexity of fluid motion, actually involving a butterfly, is that the flap of such tiny wings might be responsible for a full storm on the other side of the earth. This illustrates another difficulty in the prediction of fluid flows; the sensitivity to changes in boundary conditions

or initial conditions, which manifests itself in, among other things, the large uncertainty in weather forecasts.

The usual concept in research of physical phenomena is to translate the physics to mathematics, then solve the mathematical problem, and finally translate the answer back to physics. The construction of a mathematical model of the physical reality usually requires some assumption about the physics — a simplification, or at least an interpretation of nature. In the part of fluid mechanics dealt with here, the assumptions are

i the continuum hypothesis; the molecules are so small and many that they constitute a continuum. This is the basis of fluid mechanics, and will not be further discussed.

ii the incompressibility of fluid; the density of the fluid is constant. The work presented here concerns flow at relatively low speed, thus compressibility is of no concern.

iii Newtonian fluid; the relationship between the stresses and the rates of deformation is linear. The work presented here concerns air or water, which are Newtonian fluids.

A physical experiment is the natural method for extracting information about fluid flows. Why would one want to perform a numerical simulation? There is a number of advantages with DNS over experiments. The most obvious ones include the information of the flow close to the wall, which is crucial in many aspects. It is difficult to measure close to the surface, while the full information is available from numerical data. Furthermore, to have access to all flow variables at the same instant is important in turbulence research, and is only possible with numerical simulations.

However, because the limited performance of computers, DNS is constrained to simple geometries and low Reynolds numbers. Thus, DNS is only suitable for basic studies of turbulence.

From an engineering point of view, the information needed for the design consists of the average of the turbulent flow. Therefore, the full N-S equations describing every detail in time and space are not necessary, or even desirable, to solve. It is sufficient to solve the equations for the averaged flow, which are obtained by taking the time or ensemble average of the full N-S equations. The equations describing the mean flow have terms included that describe the influence of the fluctuating part of the velocity on the mean. These terms are unknown and must be modelled, i.e. they need to be expressed in the mean flow variables. A lot of research has been devoted to this so called turbulence modelling. All of the numerical calculations of turbulent flows of engineering interest are performed using turbulence models.

The flow around an object that moves in air or water is responsible for such phenomena as drag and lift. Close to a solid surface the flow forms a boundary layer, where the speed of the fluid relative the object rapidly decreases to zero. In this relatively thin layer many of the most interesting features of the aerodynamic property of the body are determined. Thus, the boundary layer is of engineering significance in most applications. Furthermore, the flow within

this boundary layer is often turbulent. This type of flow, called turbulent boundary layer flow, is the topic of this thesis.

In this thesis some features of the flow are compared with theoretical expressions, obtained from the averaged N-S equations (Reynolds equations), or more specifically, a simplified version (the turbulent boundary layer equation). The motivation for the theoretical work is to explain the behaviour of the mean flow of the turbulent boundary layer. Furthermore, relating the DNS data with theoretical results give an opportunity to advance turbulence models further than is possible if only comparisons between DNS data and model predictions are made.

References to papers 1 through 9 will be made in the following chapters. The papers are included in the thesis and the proper reference is stated in the preface.

CHAPTER 2

Direct numerical simulation

2.1. Numerical method

The direct numerical simulations presented in this thesis have all been performed with the spectral algorithm described in detail in paper 9. In a spectral method the solution is approximated by an expansion in smooth functions, e.g. trigonometric functions as in our case. The earliest applications to partial differential equations were developed by Kreiss & Oliger (1972) and Orszag (1972), who named the method pseudo-spectral. The term pseudo-spectral refers to the multiplications in the non-linear terms, which are calculated in physical space to avoid the evaluation of convolution sums. The transformation between physical and spectral space can be efficiently done by Fast Fourier Transform (FFT) algorithms that became generally known in the 1960's, see Cooley & Tukey (1965).

The high accuracy in spectral methods compared to finite-element or finite difference discretizations is a result of the fast convergence rate of spectral approximations of a function. Efficient implementations of pseudo-spectral methods can be made thanks to the low costs of performing FFTs. Moreover, the data structure makes the algorithms suitable for both vectorization and parallelization. However, the spectral approximation limits the applications to simple geometries.

Pseudo-spectral methods became widely used for a variety of flows during the 1980's. Early turbulent boundary layer results were presented by Spalart & Leonard (1987), who used a parallel approximation of the boundary layer. The first spatial (no parallel approximation) turbulent boundary layer computation was performed by Spalart & Watmuff (1993).

The algorithm used for the simulations in this thesis is similar to that for channel geometry of Kim *et al.* (1987), using Fourier series expansion in the wall parallel directions and Chebyshev series in the normal direction and pseudo-spectral treatment of the non-linear terms. The time advancement used is a four-step low storage third-order Runge-Kutta method for the non-linear terms and a second-order Crank-Nicolson method for the linear terms. Aliasing errors from the evaluation of the non-linear terms are removed by the $3/2-$rule when the horizontal FFTs are calculated.

The numerical code is written in FORTRAN and consists of two major parts; one linear part where the equations are solved in spectral space, and one non-linear part where the non-linear terms in the equations are computed in

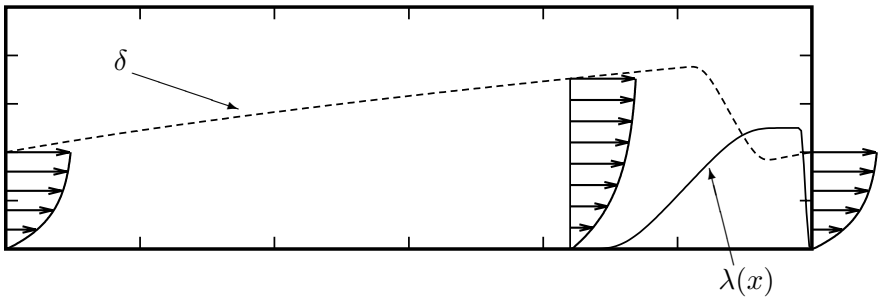

FIGURE 2.1. The boundary layer thickness δ (dashed) of a laminar mean flow that grows downstream in the physical domain and is reduced in the fringe region by the forcing. The flow profile is returned to the desired inflow profile in the fringe region, where the fringe function $\lambda(x)$ is non-zero.

physical space. The linear part needs data for one spanwise (z) position at a time since the equations are solved in the wall normal (y) direction. The non-linear part needs data for one y position at a time since the FFT is performed in the horizontal directions (spanwise and streamwise). The flow variables are stored at an intermediate level with spectral representation in the horizontal directions and physical representation in the y direction. All spatial derivatives are calculated with spectral accuracy. The main computational effort in these two parts is in the FFT.

Since the boundary layer is developing in the downstream direction, it is necessary to use non-periodic boundary conditions in the streamwise direction. This is possible while retaining the Fourier discretization if a fringe region, similar to that described by Bertolotti *et al.* (1992), is added downstream of the physical domain. In the fringe region the flow is forced from the outflow of the physical domain to the inflow. In this way the physical domain and the fringe region together satisfy periodic boundary conditions. The fringe region is implemented by the addition of a volume force F, to the Navier-Stokes equations:

$$\frac{\partial u_i}{\partial t} + u_j \frac{\partial u_i}{\partial x_j} = -\frac{1}{\rho}\frac{\partial p}{\partial x_i} + \nu \frac{\partial^2 u_i}{\partial {x_j}^2} + F_i. \tag{2.1}$$

The force

$$F_i = \lambda(x)(\tilde{u}_i - u_i) \tag{2.2}$$

is non-zero only in the fringe region; $\tilde{u}_i$ is the laminar inflow velocity profile the solution u_i is forced to and $\lambda(x)$ is the strength of the forcing. The form of $\lambda(x)$ is designed to minimize the upstream influence. See Nordström *et al.* (1999) for an investigation of the fringe region technique. Figure 2.1 illustrates

the variation of the boundary layer thickness and the mean flow profile in the computational box for a laminar case, as well as a typical fringe function $\lambda(x)$.

The code has been thoroughly checked and used in several investigations by a number of users on a variety of workstations and super computers.

2.2. Computer implementation

Many super computers of various types have been used for the simulations. All of the computers have been parallel, i.e. multiple processors are working together at the same time. The computers can be divided in two groups with respect to processor type, and two groups with respect to memory configuration.

A processor has either scalar or vector registers. A scalar processor performs operations on one element at a time with fast access to memory, whereas a vector processor performs operations on several elements at the same time.

The processors can have access to a large memory, common to all processors (shared memory), or have their own memory, unique for all processors (distributed memory).

All combinations of the different types have been used and the computers are listed in table 2.1.

	shared memory	distributed memory
scalar processor	SGI Origin 200	Cray T3E, IBM SP2
vector processor	Cray J90, C90, T90	Fujitsu VPP300, NWT

TABLE 2.1. The four categories of super computers

While the parallelization of the code on shared memory computers is straightforward, a lot of effort was needed for the parallelization and optimization of the code on computers with distributed memory, see paper 8. Communication between processors is necessary when the operations on the data set are to be performed in the two different parts of the code. The data set (velocity field) is divided between the different processors along the z direction. Thus, in the linear part, no communication is needed. When the non-linear terms are calculated, each processor needs data for a horizontal plane. The main storage is kept at its original position on the different processors. In the non-linear part each processor collects the two dimensional data from the other processors, on which it performs the computations, and then redistributes it back to the main storage.

The tuning of a code for optimal performance consists of two parts. One is the single processor tuning and the other is the parallel optimization. The tuning for one processor is dependent on the type of processor, whereas the parallelization is connected to the memory configuration. The two main issues for the single processor performance are the vectorized versus scalar FFT. For the parallelization the inherent structure of the code makes it suitable for shared

memory systems, and for distributed memory the MPI (Message-Passing Interface) is utilized.

An overview of the performance on the different computers used for the simulations presented in this thesis is shown in table 2.2. The peak performance in the table is the theoretical maximum speed you could obtain on a single processor. This number is more closely obtained in reality for vector processors. Note that the clock frequency usually quoted in connection with personal computers is somewhat misleading in this context. The clock frequency for e.g. the SP2 processor is only 160 MHz, but it is capable of four operation in each clock cycle, making the top performance 640 million floating point operations per second (640 Mflop/s).

The largest computer used for the simulations was the Numerical Wind Tunnel (NWT) at the National Aerospace Laboratory (NAL), Tokyo. It was built in the early 90's and consists of 166 vector processors from Fujitsu.

Computer	# processors	peak performance	code performance
Cray J90	1	220	100[1]
Cray J90	8		600
Cray C90	1	952	522[1]
Cray C90	4		1500
Cray T90	1	1700	710
Fujitsu VPP300	1	2200	525
Fujitsu NWT	1	1700	320[2]
Fujitsu NWT	64		20500
Cray T3E	1	600	30[2]
Cray T3E	64		1900
IBM SP2	1	640	55[2]
IBM SP2	64		3500
SGI Origin 200	1	450	53
SGI Origin 200	4		181

TABLE 2.2. The speed on various super computers in Mflop/s. [1] Measured with optimal vector length, same performance not possible on several processors. [2] Not measured, but calculated from performance on 64 processors for comparison.

2.3. Performed simulations

The adverse pressure gradient is implemented through the variation of the streamwise velocity at the freestream (U). In all of the simulations presented in this thesis the form of U has been,

$$U = U_0(1 - \frac{x}{x_0})^m. \tag{2.3}$$

Both the exponent m and the virtual origin x_0 are parameters defining the shape of U. The parameters used in the simulations are given in table 2.3.

The simulations start with a laminar boundary layer at the inflow which is triggered to transition by a random volume force near the wall. All the quantities are non-dimensionalized by the freestream velocity (U) and the displacement thickness (δ^*) at the starting position of the simulation ($x = 0$), where the flow is laminar. The Reynolds number is set by specifying $Re_{\delta^*} = U\delta^*/\nu$ at $x = 0$, and the values are given in table 2.3. The length (including the fringe), height and width of the computational box are listed in table 2.3 together with the number of modes used. Also included in table 2.3 are the total number of collocation points, denoted N_c.

Case	Re_{δ^*}	L_x	L_y	L_z	N_x	N_y	N_z	N_c	m	x_0
ZPG	450	600	30	34	640	201	128	$37 \cdot 10^6$	0	∞
A1	400	450	18	24	480	121	96	$13 \cdot 10^6$	-0.077	-60
A2	400	450	24	24	480	161	96	$17 \cdot 10^6$	-0.15	-60
A3	400	700	65	80	512	193	192	$43 \cdot 10^6$	-0.25	-62
SEP	400	700	65	80	720	217	256	$90 \cdot 10^6$	-0.35	-50

TABLE 2.3. Numerical parameters. L denotes the size of the computational box. N denotes the number of modes.

The five different simulations are presented in six of the nine papers included in this thesis, as well as in a number of conference proceedings not included. The simulations have different notations in the papers and are summarized in table 2.4.

Thesis	paper 1	paper 2	paper 4	paper 5	paper 6	paper 7
ZPG					ZPG	ZPG
A1	APG1	APG1				
A2	APG2	APG2			APG1	
A3			APG1	APG1	APG2	
SEP			SEP	SEP		

TABLE 2.4. The simulations are presented in different papers with a notation summarized here.

CHAPTER 3

Fundamental analysis of turbulent boundary layer flows

In most applications it is the mean flow that sets the limit on the performance and hence determines the design. The rapid turbulent fluctuations in time and space are not in themselves as interesting as their influence on the time-averaged flow. The equations to be solved to obtain the steady mean flow is the averaged Navier-Stokes equations (Reynolds equations),

$$\frac{\partial u_i}{\partial x_i} = 0, \tag{3.1}$$

$$u_j \frac{\partial u_i}{\partial x_j} = -\frac{1}{\rho}\frac{\partial P}{\partial x_i} + \nu \frac{\partial^2 u_i}{\partial {x_j}^2} - \frac{d}{dx_j}\langle u_i' u_j' \rangle, \tag{3.2}$$

where $\langle u_i' u_j' \rangle$ is the Reynolds stress tensor, which is the quantity that accounts for the influence of the turbulent fluctuations on the mean flow u_i. P is the mean pressure.

By solving equation (3.2), the mean flow u_i is obtained. However, $\langle u_i' u_j' \rangle$ is an unknown quantity that needs to be expressed in u_i and its derivatives in order to obtain a solvable equation. Thus, one objective for DNS is to obtain turbulence statistics from which the true coupling between mean flow and Reynolds stresses can be extracted. From the results it is possible to draw conclusions about the validity of current turbulence models and also to develop new models. Furthermore, the solution to equation (3.2) does not contain any information about the instantaneous flow. However, for the coupling between the mean flow and Reynolds stresses, the instantaneous structure of the flow could be of importance.

3.1. The boundary layer equations

In a steady two-dimensional boundary layer the mean flow equations (3.1) and (3.2) reduce to,

$$\frac{\partial u}{\partial x} + \frac{\partial v}{\partial y} = 0, \tag{3.3}$$

$$u\frac{\partial u}{\partial x} + v\frac{\partial u}{\partial y} = -\frac{1}{\rho}\frac{dP}{dx} + \nu\frac{\partial^2 u}{\partial y^2} - \frac{\partial}{\partial y}\langle u'v' \rangle - \frac{\partial}{\partial x}\left(\langle u'u' \rangle - \langle v'v' \rangle\right), \tag{3.4}$$

where u is the mean streamwise velocity, v the mean wall normal velocity, $\frac{dP}{dx}$ the pressure gradient, $\langle u'v' \rangle$, $\langle u'u' \rangle$, $\langle v'v' \rangle$ the Reynolds stresses, ρ the

density and ν the kinematic viscosity. Equation (3.4) is the turbulent analogy to the laminar second order boundary layer approximation, i.e. terms up to order $(\delta/L)^2$ are kept, where δ is a typical length in the normal direction and L is a typical length in the streamwise direction. The last term in equation (3.4) can be neglected in most situations, and the resulting equation is a first order boundary layer approximation. This simplified turbulent boundary layer equation will be denoted TBLE throughout this chapter. The TBLE can be further simplified by the distinction between an inner part and an outer part.

3.2. Scalings and self-similarity

One important concept in the analysis of equation (3.4) is self-similarity, which means that velocity profiles at different downstream positions collapse on a single curve. In order to achieve this, proper scaling has to be used.

The concept of scaling and self-similarity has been an important tool in physics for a long time. According to Barenblatt (1996), the first application was made by Fourier (1822), in the context of heat conduction.

By reducing a partial differential equation — with two or more independent variables, to an ordinary equation — with one independent variable, an enormous simplification of the problem has been made.

The velocities and Reynolds stresses in equation (3.4) are dependent on both x and y. However, under certain conditions the dependency can be reduced to only one *similarity* coordinate (which depends on x and y).

In turbulent boundary layer theory one usually distinguish between two regions of the flow with different characteristics. The individual terms in equation (3.4) are of different importance in the two regions of the boundary layer flow. The viscous term is only important in the inner region, while the advection terms are only significant in the outer part.

3.2.1. *The outer part*

In the outer part of a turbulent boundary layer, equation (3.4) can be reduced to,

$$u\frac{\partial u}{\partial x} + v\frac{\partial u}{\partial y} = -\frac{1}{\rho}\frac{dP}{dx} - \frac{\partial}{\partial y}\langle u'v'\rangle. \tag{3.5}$$

The partial differential equation (3.5) is converted to an ordinary differential equation through the rescaling,

$$\begin{aligned} (u-U)/u_\tau = F(\eta), \qquad & -\langle u'v'\rangle/{u_\tau}^2 = R(\eta), \\ \eta = y/\Delta(x), \qquad & \Delta = U\delta^*/u_\tau. \end{aligned} \tag{3.6}$$

U is the freestream velocity, u_τ is the friction velocity (defined in the next section) and δ^* is the displacement thickness. These scalings yields an equation of the form,

$$-(\beta-2\omega)F + \gamma F^2 - (\alpha-2\beta-2\omega)\eta\frac{dF}{d\eta} - \chi\frac{dF}{d\eta}\int_0^\eta F d\eta = \frac{dR}{d\eta}, \tag{3.7}$$

with

$$\alpha = \left(\frac{U}{u_\tau}\right)^2 \frac{d\delta^*}{dx},\ \beta = \frac{\delta^*}{\tau_w}\frac{dp}{dx}, \tag{3.8}$$

$$\omega = \frac{1}{2}\frac{\delta^*}{u_\tau}\left(\frac{U}{u_\tau}\right)^2 \frac{du_\tau}{dx},$$

$$\gamma = \frac{U}{u_\tau}\frac{\delta^*}{u_\tau}\frac{du_\tau}{dx},\ \chi = \frac{U}{u_\tau}\frac{d\delta^*}{dx} + \frac{\delta^*}{u_\tau}\frac{dU}{dx}.$$

If the scalings in (3.6) is to produce an ODE of equation (3.7), all the terms $\alpha, \beta, \gamma, \chi, \omega$ must be constants. The conditions under which constant parameters can occur are discussed next.

The classical treatment of the equations which involves outer and inner equations and a matching of the solutions, leads to the logarithmic friction law,

$$\frac{u_\tau}{U} = \frac{1}{C + \frac{1}{\kappa}\ln Re_{\delta^*}}, \tag{3.9}$$

where κ is the Kármán constant and $Re_{\delta^*} = U\delta^*/\nu$. Equation (3.9) shows that $u_\tau/U \to 0$ in the limit of very high Reynolds number. A series expansion of the terms (3.8) in the small parameter (u_τ/U) is performed in paper 2. Letting $u_\tau/U \to 0$, the asymptotic version of equation (3.7) is obtained,

$$-2\beta F - (1+2\beta)\eta\frac{dF}{d\eta} = \frac{dR}{d\eta}, \tag{3.10}$$

which is called the defect layer equation. The same asymptotic version was obtained by Tennekes & Lumley (1972). Also Wilcox (1993) performed an asymptotic analysis but made some mistakes as pointed out in paper 2 and by Henkes (1998).

A different approach to equation (3.4) is presented in paper 1, in which the asymptotic theory is substituted with an analysis permitting a finite ratio u_τ/U. Since the logarithmic function grows very slowly when the argument is large, a better assumption than $u_\tau/U \to 0$ for moderately high Reynolds numbers is that $u_\tau/U \approx$ constant. If u_τ/U is regarded as constant and an outer length scale varies linearly, the condition $\beta =$constant is fulfilled if the freestream variation is of the form $U \sim x^m$, which was shown by Townsend (1956) and Mellor & Gibson (1966). When specifying a profile in a power-law form it can be written,

$$U = U_0(1 - \frac{x}{x_0})^m. \tag{3.11}$$

Utilizing these constraints, the TBLE becomes,

$$-2\beta F + \frac{\beta}{m}(1+m)\eta\frac{dF}{d\eta}$$

$$+\frac{u_\tau}{U}\left\{-\beta F^2 + \frac{\beta}{m}(1+m)\frac{dF}{d\eta}\int_0^\eta F d\eta\right\} = \frac{dR}{d\eta} + \frac{1}{Re_{\delta^*}}\frac{d^2F}{d\eta^2}. \tag{3.12}$$

If now $u_\tau/U \to 0$, the asymptotic version becomes,

$$-2\beta F + \frac{\beta}{m}(1+m)\eta\frac{dF}{d\eta} = \frac{dR}{d\eta}. \tag{3.13}$$

The relation between the equations (3.10), (3.12) and (3.13), and what they can be used for is discussed in the next chapter.

3.2.2. *The inner part*

The analysis of the flow near the wall is important because many features of the flow of engineering significance is determined in the near-wall region. In the inner part of a zero pressure gradient boundary layer, equation (3.4) can be reduced to,

$$0 = \nu\frac{\partial^2 u}{\partial y^2} - \frac{\partial}{\partial y}\langle u'v'\rangle. \tag{3.14}$$

The right hand side is interpreted as the gradient of the shear stress τ (or actually the gradient of τ/ρ), and equation (3.14) can be integrated from the wall to give an expression for τ itself as a function of y and x,

$$\frac{\tau}{\rho} \equiv \nu\frac{\partial u}{\partial y} - \langle u'v'\rangle = \left(\nu\frac{\partial u}{\partial y} - \langle u'v'\rangle\right)\Bigg|_{y=0} \tag{3.15}$$

The Reynolds stress is zero at the wall and we define the friction velocity u_τ as,

$$u_\tau \equiv \sqrt{\nu\frac{\partial u}{\partial y}\Bigg|_{y=0}}. \tag{3.16}$$

If we use the viscous scaling (or plus units); $u^+ \equiv u/u_\tau$, $y^+ \equiv yu_\tau/\nu$ and $\tau^+ \equiv \tau/(\rho u_\tau^2)$, equation (3.15) can be written,

$$\tau^+ \equiv \frac{du^+}{dy^+} - \langle u'v'\rangle^+ = 1, \tag{3.17}$$

which implies that all the dependency on x is included in u_τ. The assumption that u^+ is a function of only y^+ was first made by Prandtl (1932). In the viscous sub-layer, where the Reynolds stress is negligible, equation (3.17) can be integrated to yield $u^+ = y^+$, i.e. the velocity profile is a function of only one variable, which in turn depends on both x and y.

Equation (3.17) with the pressure gradient term included can be written as,

$$\tau^+ = 1 + \left(\frac{u_p}{u_\tau}\right)^3 y^+, \tag{3.18}$$

with

$$u_p \equiv \left(\nu\frac{1}{\rho}\frac{dP}{dx}\right)^{1/3}. \tag{3.19}$$

The linear behavior of the total shear stress revealed in equation (3.18) was first observed by Stratford (1959*a*,*b*).

In the viscous sub-layer the Reynolds shear stress approaches zero and equation (3.18) can be integrated to give,

$$u^+ = y^+ + \frac{1}{2}\left(\frac{u_p}{u_\tau}\right)^3 (y^+)^2. \tag{3.20}$$

This equation was first derived by Patel (1973), and reduces to the usual linear profile in ZPG case, when $u_p \to 0$.

It can be shown that the pressure gradient term decreases with increasing Reynolds number. The term is thus important only for low Reynolds numbers. However, close to separation, where u_τ approaches zero, it is clear that the terms becomes infinite, even for large Reynolds numbers.

For the ZPG case, the scaling of the total shear stress with u_τ gives a self-similar profile ($\tau^+ = 1$). From equation (3.18) it is observed that the velocity scale u_τ does not results in a self-similar expression. However, equation (3.18) can be formulated as

$$\tau^* \equiv \frac{1}{u_*^2}\left(\nu\frac{\partial u}{\partial y} - \langle u'v'\rangle\right) = 1, \tag{3.21}$$

where u_* is a velocity scale that depends on y and can be expressed as

$$u_*^2 = u_\tau^2 + \frac{u_p^3}{u_\tau} y^+. \tag{3.22}$$

The only velocity scale in the inner part of the ZPG boundary layer is u_τ. By normalizing the velocity gradient with y and u_τ, and assume this scaling leads to a constant non-dimensional velocity gradient for large enough y^+, (see e.g. Bradshaw & Huang (1995)), we get the equation,

$$\frac{y}{u_\tau}\frac{\partial u}{\partial y} = \frac{1}{\kappa}. \tag{3.23}$$

When expressed in inner scales and integrated, equation (3.23) yields the logarithmic velocity profile.

In the APG boundary layer, the velocity scale is u_*, and using this velocity scale in the normalization of the velocity gradient yields,

$$\frac{y}{u_*}\frac{\partial u}{\partial y} = \frac{1}{\kappa}. \tag{3.24}$$

When expressed in inner scales and integrated, equation (3.24) yields,

$$u^+ = \frac{1}{\kappa}\left(\ln y^+ - 2\ln\frac{\sqrt{1+\lambda y^+}+1}{2} + 2(\sqrt{1+\lambda y^+}-1)\right) + B, \tag{3.25}$$

with

$$\lambda = \left(\frac{u_p}{u_\tau}\right)^3.$$

A more thorough derivation of equation (3.25) is given in paper 4. Townsend (1961), Mellor (1966) and Afzal (1996) have derived similar equations, albeit with different methods and assumptions. Equation (3.25) will be compared

with DNS data in the next chapter where also the corresponding equation for the separated boundary layer will be presented.

CHAPTER 4

Turbulent boundary layers under adverse pressure gradients

The turbulent boundary layer under an adverse pressure gradient (APG) is decelerated, which does not mean that the turbulence intensity decreases. On the contrary, the flow becomes even more unstable and the turbulence activity is enhanced. The boundary layer also grows (thickens) more rapidly under the influence of an APG. Since the momentum of the fluid is lower close to the wall than further up in the boundary layer, the flow near the wall is more severely affected by the pressure gradient. If the pressure gradient is strong enough, the flow close to the wall separates, i.e. reversed flow appears.

4.1. General features

In figure 4.1 the freestream velocity (U) for all five simulations included in this thesis are shown. These profiles constitute the boundary condition on the upper edge of the computational box and define the APG. The resulting skin friction ($C_f \equiv 2(u_\tau/U)^2$) of the four attached boundary layers are shown in figure 4.2. As the APG is increased the C_f is reduced. If the APG is strong enough it induces separation ($C_f < 0$), which occurs for the freestream distribution used in the case SEP. The C_f for SEP is shown in figure 4.3, where also the C_f distributions for previously completed simulations of a separated turbulent boundary layer are included. The two earlier simulations were performed by Na & Moin (1998) and Spalart & Coleman (1997). In figure 4.3 the x values have been recalculated in our simulation coordinates. However, the relative starting positions of the boundary layers cannot be calculated and are here matched by letting the starting points of all three simulations be located at $x = 0$. From figure 4.3 it is clear that the separation bubble is longer in the present simulation (case SEP) than in the other two. In figure 4.3 the C_f from our simulation has been calculated using the same technique as in Na & Moin (1998) and Spalart & Coleman (1997), i.e. with a value of unity for the freestream velocity. More results from the separated boundary layer simulation are presented in section 4.4.

The streamwise velocity profile at $x = 300$ is shown for the five cases in figure 4.4. The simulations were performed with different heights of the computational box, as seen in figure 4.4. The heights in A3 and SEP were actually 65 but the profiles are shown up to 45. The freestream velocity is unity

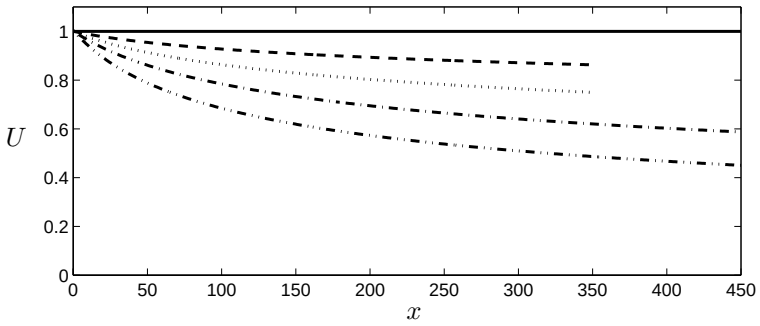

FIGURE 4.1. U. — ZPG; - - A1; $\cdots$ A2; $-\cdot-$ A3; $-\cdot\cdot-$ SEP.

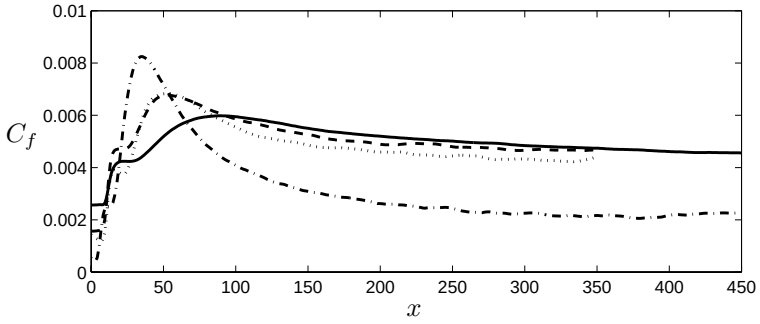

FIGURE 4.2. C_f. — ZPG; - - A1; $\cdots$ A2; $-\cdot-$ A3.

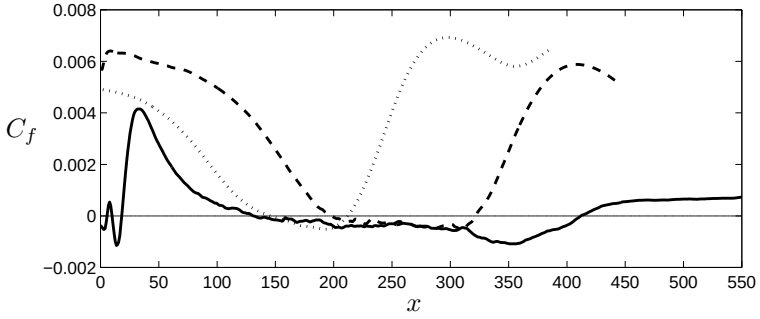

FIGURE 4.3. — C_f from SEP; - - C_f from Na & Moin (1998); $\cdots$ C_f from Spalart & Coleman (1997).

only for ZPG. The profile from SEP exhibits negative values of the velocity close to the wall, showing that separation has occurred.

The streamwise velocity fluctuations form elongated structures near the wall in a ZPG boundary layer. It is generally thought that the structures are weakened in an APG flow. This is illustrated in figure 4.5, where the streamwise

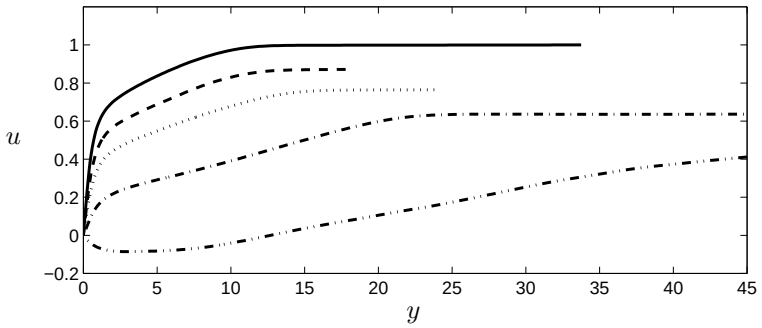

FIGURE 4.4. Streamwise velocity profiles at $x = 300$. — ZPG; - - A1; $\cdots$ A2; $- \cdot -$ A3; $- \cdot\cdot -$ SEP.

velocity fluctuations in a horizontal plane from ZPG, A3 and SEP are shown. The figure shows the whole computational boxes in the spanwise direction and excluding the transitional part and fringe region in the streamwise direction. The dark color represents the low-speed regions and light color represents the area containing high-speed fluid. The streaks formed in the ZPG case (figure 4.5a) are spaced 100 viscous units in the spanwise direction. The streaks in the A3 case are shown in figure 4.5b. The structures are weakened at the end of the domain as compared with those in the beginning, showing the damping effect of the APG on the structures. The spacing between the structures increases from 100 (the same as for a ZPG layer) at the beginning to about 130 at the end, based on the local u_τ.

The SEP case is shown in figure 4.5c. There are still some structures in the separated flow, though not at all as long and frequent as in the ZPG or A3. Before separation, which occurs at approximately $x = 142$, the streaks are visible, but are rapidly vanishing in the beginning of the separated region. There is notable increase in the streak formation around $x = 350$, where the friction coefficient is at its lowest values, c.f. figure 4.3. Thus, there are indications that streaks may reappear in a separated region if the back flow is severe enough. After the reattachment at $x = 412$ the streaks are not immediately appearing, but are clearly visible after $x = 450$.

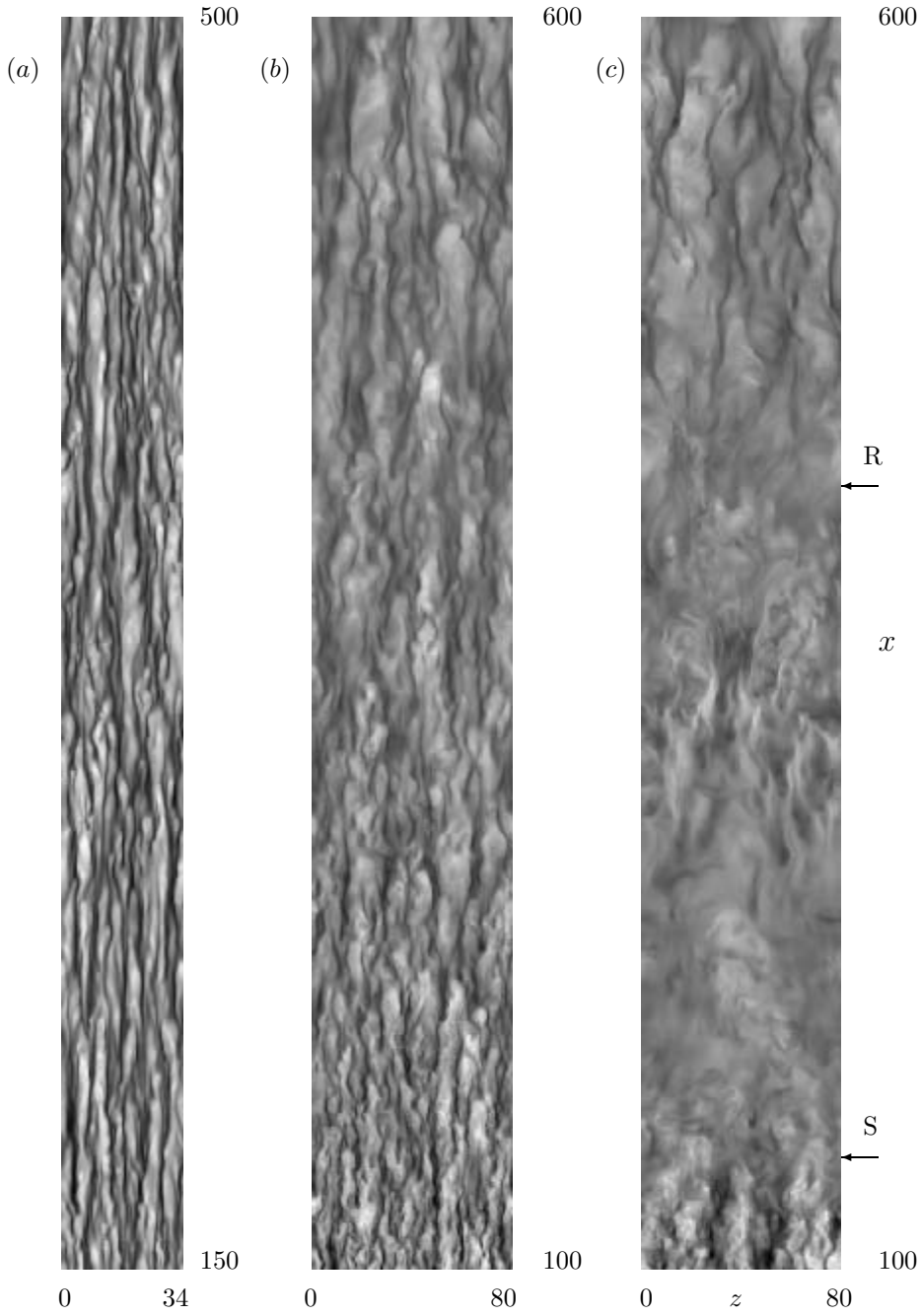

FIGURE 4.5. Streamwise velocity fluctuations in a horizontal plane at $y^+ = 10$. (a) ZPG. (b) A3. (c) SEP. The points denoted S and R represent the separation and reattachment respectively.

4.2. The outer region of the boundary layer

4.2.1. *Self-similarity*

The simulations presented in paper 1 showed constant β, see table 4.1. However, the functions $F(\eta)$ and $R(\eta)$ are not self-similar for low Reynolds numbers as shown with DNS in paper 1. For large Reynolds numbers, the functions $F(\eta)$ and $R(\eta)$ do become self-similar and converge to the asymptotic defect layer equation given be equation (3.10), as shown with turbulence models in paper 2 and by Henkes (1998).

The shapes of $F(\eta)$ from the simulations are shown in figure 4.6. The β parameter has a strong influence on the profile shape for A3, while the A1 and A2 profiles are closer to the ZPG profile.

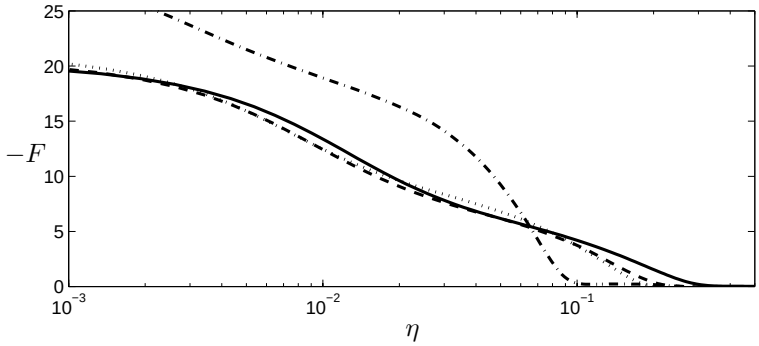

FIGURE 4.6. Velocity profiles at $x = 300$. — ZPG; - - A1; $\cdots$ A2; $- \cdot -$ A3.

4.2.2. *Mean flow parameters*

The equation describing the outer region can be integrated from the wall to the freestream, and thereby provide relations between mean flow parameters. If equation (3.13) is integrated, the relation

$$m = -\frac{\beta}{1+3\beta} \tag{4.1}$$

is obtained, and when put back in equation (3.13), equation (3.10) is recovered.

When integrating equation (3.10) it should be noted that the wall boundary condition is $R(0) = 1$ and not $R(0) = 0$. The reason for this is that the near-wall region is neglected when $u_\tau/U \to 0$.

The non-linear equation (3.12) can also be integrated and yields the relation,

$$m = -\frac{\beta}{H(1+\beta)+2\beta}, \tag{4.2}$$

where H is the shape factor. The limit $u_\tau/U \to 0$, can now be obtained by letting $H \to 1$, and the relation (4.1) is recovered from (4.2).

To compare the relations (4.1) and (4.2), a number of experiments and DNS are summarized in table 4.1. There is obviously a much better agreement with the non-linear theory, showing that even in high Reynolds number experiments, the asymptotic expressions are of limited value.

The more rapidly U is decreased, the lower C_f is obtained, as shown in figures 4.1 and 4.2. While the relative difference in U between the cases remains the same, a dramatic decrease in C_f occurs between A2 and A3. In other words, the closer to separation the boundary layer is, the more sensitive on the freestream velocity distribution it is. The relation between m and β should reveal this behavior. That so is the case is seen from figure 4.7, where equation (4.2) has been plotted for the two values of H, between which separation has been observed to occur. The limiting value of m increases with H but is confined between -0.22 and -0.25, which is consistent with the observed values in experiments and DNS. The rapid and strongly non-linear approach to separation ($\beta \to \infty$) is consistent with the strong decrease in C_f between A2 and A3 in figure 4.2.

Case	β	H	m	$m = -\frac{\beta}{H(1+\beta)+2\beta}$	$m = -\frac{\beta}{1+3\beta}$
A1	0.24	1.60	-0.077	-0.097	-0.14
A2	0.65	1.63	-0.15	-0.16	-0.22
A3	4.5	1.97	-0.23	-0.23	-0.31
Bradshaw 1	0.9	1.4	-0.15	-0.20	-0.24
Bradshaw 2	5.4	1.54	-0.255	-0.26	-0.31
Skåre & Krogstad	20.0	2.0	-0.22	-0.24	-0.33
Elsberry	25.0	2.45	-0.22	-0.22	-0.33
Stratford	∞	2.5	-0.23	-0.22	-0.33
Spalart & Leonard	1.8	1.65	-0.21	-0.22	-0.28
	8.0	1.92	-0.23	-0.24	-0.32
	∞	2.3	-0.22	-0.23	-0.33
	0.9	1.55	-0.18	-0.19	-0.24
	5.4	1.86	-0.24	-0.24	-0.31

TABLE 4.1. Comparison of m from the non-linear/linear theory. The data are taken from the following references (from top to bottom) Bradshaw (1967), Skåre & Krogstad (1994), Elsberry *et al.* (2000), Stratford (1959*a*), Spalart & Leonard (1987).

4.3. The inner part of the boundary layer

4.3.1. *The viscous sub-layer*

Profiles in the viscous scaling are compared for the different APG cases in figure 4.8. All of them matches closely the linear profile $u^+ = y^+$. Thus, even

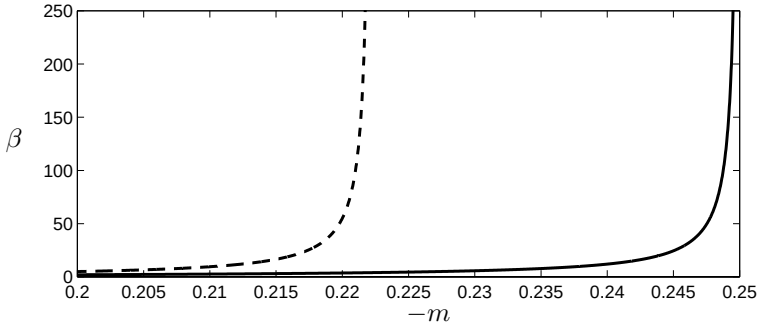

FIGURE 4.7. β as a function of m from equation (4.2) for — H=2.0 and - - H=2.5.

under strong APG the inclusion of the pressure gradient term does not seem to be of importance. However, close to separation or reattachment, when u_τ is small, the velocity profile is strongly influenced by the pressure gradient term. In figure 4.9, a velocity profile from the SEP case (in the attached region) illustrates the importance of the pressure gradient term.

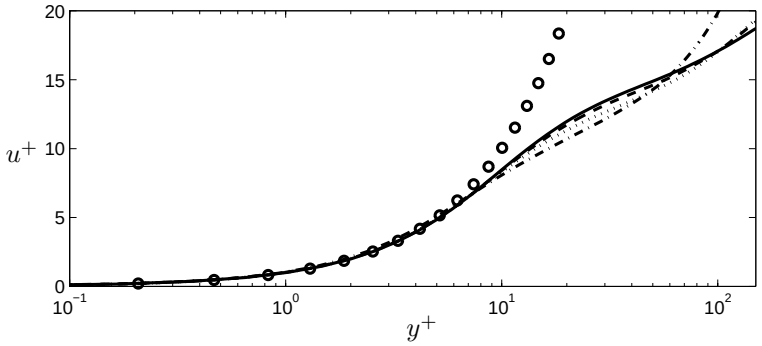

FIGURE 4.8. Velocity profiles at $x = 300$. — ZPG; - - A1; $\cdots$ A2; $-\cdot-$ A3; $\circ$ $u^+ = y^+$.

4.3.2. *The overlap region*

An example of comparison between DNS data and equation (3.25) is shown in figure 4.10. DNS data from the attached region (at $x = 450$) of the case SEP is shown as a solid line in figure 4.10. The dashed line is equation (3.25) and the dotted line is the logarithmic law for the ZPG boundary layer. The value of additive constant is $B = -2$, which is in agreement with the earlier investigation of the flow just upstream of separation in the simulation of Na & Moin (1998), see paper 3.

The value of the Kármán constant, κ, has been set to 0.41 throughout this thesis. Lately, Österlund *et al.* (2000) have shown that the value of the

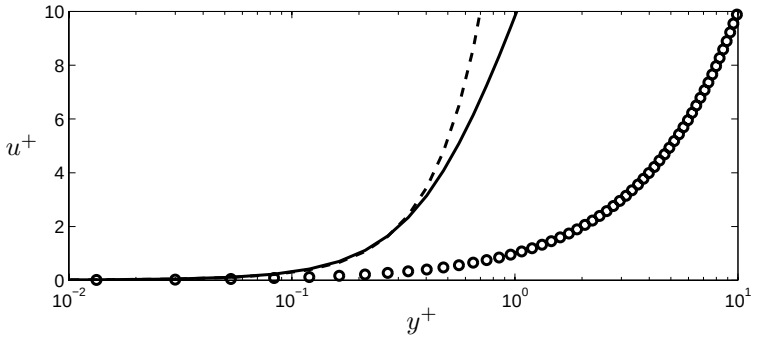

FIGURE 4.9. Velocity profile close to reattachment. — SEP; - - equation (3.20); ∘ $u^+ = y^+$.

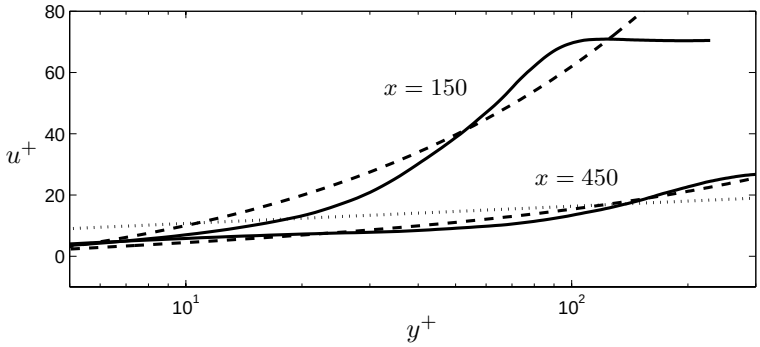

FIGURE 4.10. Velocity profiles from SEP: — DNS; - - equation (3.25) for $x = 450$ and equation (4.8) for $x = 150$; $\cdots$ $u^+ = \frac{1}{0.41}\ln y^+ + 5.1$.

Kármán constant actually is 0.38 for large enough Reynolds number. However, Spalart (1988) has shown that the old value of 0.41 gives good agreement for low Reynolds numbers. In a number of earlier investigations the influence of the Reynolds number on the Kármán constant has been debated, see e.g. Simpson (1970).

4.4. Separation

In paper 4, one of the boundary layers was separated for a large portion of the flow. The contours of mean streamwise velocity are shown in figure 4.11 with positive values shown as solid lines and negative as dashed.

At the point of separation the wall shear stress is zero, i.e. $u_\tau = 0$. Thus the scaling with u_τ encounters a singularity. When considering a strong APG or separation, the singularity can be avoided by using the velocity scale u_p instead of u_τ. This was noted by Stratford (1959*b*), Townsend (1961) and Tennekes & Lumley (1972). By rescaling equation (3.20) the following expression for the

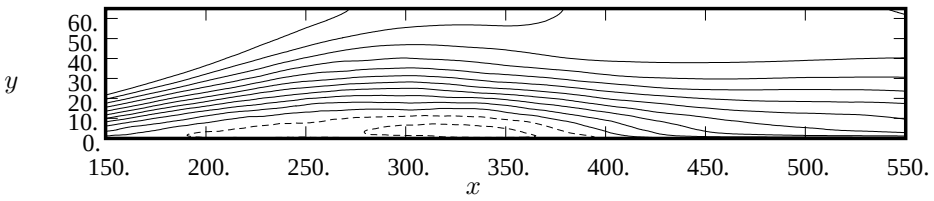

FIGURE 4.11. SEP: contours of mean velocity. Positive values shown as solid lines, negative as dashed.

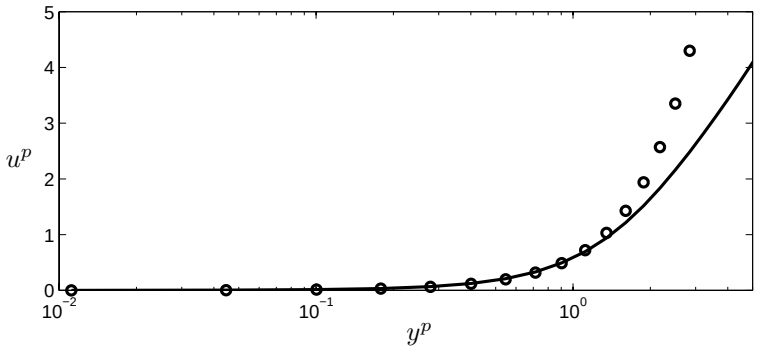

FIGURE 4.12. Velocity profile close to reattachment. — SEP; ∘ $u^p = \frac{1}{2}(y^p)^2$.

velocity profile in the viscous sub-layer is obtained,

$$u^p \equiv \frac{u}{u_p} = \frac{1}{2}(y^p)^2 + \left(\frac{u_\tau}{u_p}\right)^2 y^p, \tag{4.3}$$

where $y^p \equiv y u_p/\nu$. In the limit of separation, when $u_\tau \to 0$, equation (4.3) reduces to

$$u^p = \frac{1}{2}(y^p)^2. \tag{4.4}$$

Thus, in this rescaled form, the singularity is avoided. The profile from the SEP case at reattachment is shown in figure 4.12 together with the asymptotic expression (4.4). This is the same velocity profile as was shown in figure 4.9. Equation (3.25) can be rewritten in the pressure gradient scaling for the overlap region, and the resulting expression asymptotes to the square-root law when $u_\tau \to 0$,

$$u^p = \frac{1}{\kappa} 2\sqrt{y^p} + C, \tag{4.5}$$

which was first obtained by Stratford (1959*b*).

In the separated region the velocity gradient at the wall is negative, and the definition of u_τ needs to be changed to

$$u_\tau \equiv \sqrt{-\nu \frac{\partial u}{\partial y}\Big|_{y=0}}. \tag{4.6}$$

An integration from the wall was a crucial step in the derivation of the total shear stress. Both the velocity profile in the viscous sub-layer and in the overlap region depends on the expression for the total shear stress. In a separated boundary layer the wall boundary condition is different due to change of sign in the definition of u_τ, which leads to a velocity profile in the viscous sub-layer that reads,

$$u^+ = -y^+ + \frac{1}{2}\left(\frac{u_p}{u_\tau}\right)^3 {y^+}^2. \tag{4.7}$$

The velocity profile in the overlap region becomes, in the separated region,

$$u^+ = \frac{1}{\kappa}\left[2\sqrt{\lambda y^+ - 1} - 2\arctan\left(\sqrt{\lambda y^+ - 1}\right)\right] + B, \tag{4.8}$$

with

$$\lambda = \left(\frac{u_p}{u_\tau}\right)^3.$$

One of the profiles (at $x = 150$) from the separated region is shown in figure 4.10 together with the profile given by equation (4.8). The additive constant is $B = -7$ for the separated case. Observe that no part of the back-flow region is shown in figure 4.10. The reader is referred to paper 4 for velocity profiles in the back-flow region.

CHAPTER 5

Modelling of turbulence

The modelling of turbulence can be divided in three major groups. The one we will talk about most is the Reynolds average Navier-Stokes (RANS) modelling. With this expression it is meant that the Reynolds equations are closed by a model for the Reynolds stresses. The second group is large eddy simulation (LES) where the flow is resolved for the large scales while the small scales are modelled. This is completely left out in this work. The third group is the models based on the actual structure of turbulence. The models can e.g. be used for RANS modelling (Perry *et al.* 1994) or for turbulence control purposes.

5.1. RANS modelling

If the mean flow of a turbulent flow is to be calculated by solving the equations (3.1) and (3.2), a relation between the Reynolds stresses and the mean flow is required.

5.1.1. *Basic concepts*

Often the two-dimensional boundary layer is calculated using the equations (3.3) and (3.4) with the last term neglected. Hence, only the Reynolds shear stress needs to be related to the velocity. The simplest relation is the mixing length,

$$-\langle u'v'\rangle^+ = (l^+)^2 \left(\frac{du^+}{dy^+}\right)^2 \qquad \text{with} \qquad l^+ = \kappa y^+, \tag{5.1}$$

which was first developed by Prandtl (1925). This relation has received a lot of interest during the years and particularly the near-wall behavior of (5.1) is of great importance, even for more sophisticated models. The wall is not naturally accounted for in the relation (5.1), but a successful wall-damping function (f_1) was introduced by van Driest (1956),

$$f_1 = 1 - \exp(-y^+/A^+), \tag{5.2}$$

which is applied on the mixing length $l^+ = \kappa y^+ f_1$.

The mixing length is based on the concept of turbulent viscosity, first introduced by Boussinesq (1877). The Boussinesq hypothesis can be generalized to the form,

$$a_{ij} = -2\frac{\nu_T}{K} S_{ij}, \tag{5.3}$$

where ν_T is the turbulent viscosity. Here we have introduced the anisotropy tensor, $a_{ij} \equiv \langle u_i' u_j'\rangle/K - 2\delta_{ij}/3$, and rate of strain tensor, $S_{ij} \equiv 1/2(U_{i,j} + U_{j,i})$.

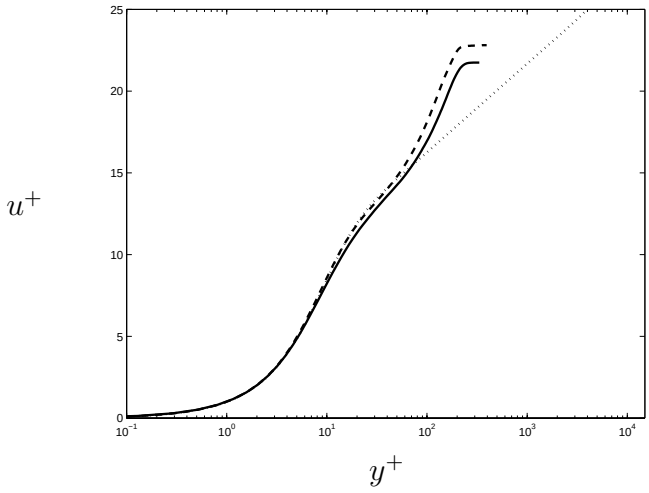

FIGURE 5.1. Velocity profiles from A2 in inner scaling. — DNS; - - DRSM; $\cdots$ Asymptotic DRSM.

There exists a number of methods to develop better models than the mixing length for ν_T. In e.g. the two-equation models ν_T is written in the form,

$$\nu_T = C_\mu \frac{K^2}{\varepsilon} \qquad \text{or} \qquad \nu_T = \frac{K}{\omega}, \tag{5.4}$$

and two transport equations for K and ε or ω have to be solved.

There are also many models not based on the Boussinesq hypothesis. In the differential Reynolds stress model (DRSM) the transport equations for the Reynolds stresses themselves are solved. This leads to a much greater computational effort than for the two-equation models. In addition, numerical issues become important. However, in some cases the DRSM is required to capture features of the flow that cannot be predicted by other models.

In the explicit algebraic Reynolds stress model (EARSM), the advection and viscous diffusion of the anisotropy are neglected in the transport equations, and an algebraic equation for the anisotropy is obtained. This kind of model is based on a two-equation model and can be written in a similar form as a generalized Boussinesq hypothesis.

In paper1 the DRSM of Hanjalić *et al.* (1995) was used to investigate the asymptotic behavior of the boundary layer for large Reynolds numbers. Furthermore, the model was used to predict the mean flow at the same low Reynolds number as the DNS. The model predictions showed that low Reynolds number effects are well captured by the DRSM. An example from the case A2 is shown in figure 5.1. The velocity profile from the low Reynolds number DNS (solid line) is well predicted by the DRSM (dashed line). The asymptotic profile calculated with the DRSM at high Reynolds number develops into a self-similar profile (dotted line).

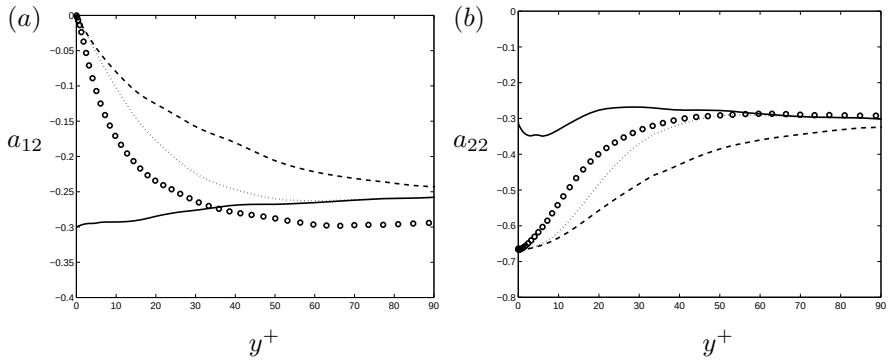

FIGURE 5.2. A3 at $x = 150$: $\circ$ DNS; — non-damped EARSM; Damped EARSM with the scaled coordinate in f_1 as - - y^+; $\cdots$ y^*. a) a_{12}. b) a_{22}.

In paper 2 a number of two-equations models were compared with DNS data and experimental data. The general conclusion from that investigation is that the $k-\omega$ model is reasonably accurate, while the $k-\epsilon$ model gives rather large deviations for strong adverse pressure gradients.

5.1.2. *Improvement of wall damping*

In paper 5 the EARSM model of Wallin & Johansson (2000) was used for the investigation of the near-wall behavior. By using DNS data in the model expressions for the Reynolds stresses close to the wall, the influence of the wall-damping functions can be examined. The wall-damping is based on the van Driest function, equation (5.2). However, in an APG boundary layer, equation (5.2) is not valid. Some of the work in the earlier mixing length models have been concentrated on finding a relation between the constant A^+ and the pressure gradient, see e.g. Granville (1989). A different method to improve the wall-damping is used in paper 5. The viscous scaling of y in equation (5.2) is replaced with the scalings related to the work in paper 4. The improved near-wall damping is illustrated in figure 5.2, where the expressions for the anisotropy are evaluated from DNS data. The DNS data is represented with circles and the non-damped (i.e. $f_1 = 1$) model evaluation is shown as the solid line. By damping with $f_1 = 1$ based on y^+ the dashed line is obtained. If y^+ is replaced with $y^* \equiv yu_*/\nu$, where u_* is defined from equation (3.22), the dotted profile is obtained. Thus, the wall-damping is much improved by changing from the viscous scaling to the relevant scaling in an APG flow.

DNS data from the case A3 was also used by Wallin & Johansson (2000) to evaluate the damping of the EARSM model.

5.2. Instantaneous flow structures

Turbulence does not consist of randomly fluctuating velocities. The experiments of Kline *et al.* (1967) showed that low-speed streaks populate the near-wall region. Since then many different types of structures and models for the dynamics of turbulence structures have been proposed, see the introduction of paper 7.

Most models trying to capture the essential mechanisms in turbulence are conceptual, not predictive, in the sense they do not relate Reynolds stresses to the mean flow, but try to explain the various steps in the production and regeneration of turbulence. For a general review of the subject, see Robinson (1991).

In paper 7 the instability mechanism of a turbulent low-speed streak is addressed. Simulations of an artificial streak in a laminar boundary layer were performed in order to examine the instability in a controlled environment. This laminar simulation was also used for reproducing and further investigate the results from an experimental investigation by Acarlar & Smith (1987).

The laminar streak breaks down due to an instability originating from an inflectional velocity profile. The instability calculations using the Orr-Sommerfeld equations gave qualitative agreement in the growth rate and streamwise wavenumber with the corresponding values extracted from the DNS velocity fields. The instability waves riding on the streak, roll up to form a horseshoe vortex. Some striking similarities between the vortices that appear in the laminar simulation and the ones found in a ZPG turbulent boundary layer were found. To illustrate the qualitative agreement, a small part of the turbulent boundary layer is shown in figure 5.3, while the laminar streak is shown in figure 5.4. The horseshoe vortices are visualized with regions of low pressure. The light grey structures represent the low-speed streaks and the darker ones represent regions with low pressure. The flow is directed upward in the figures.

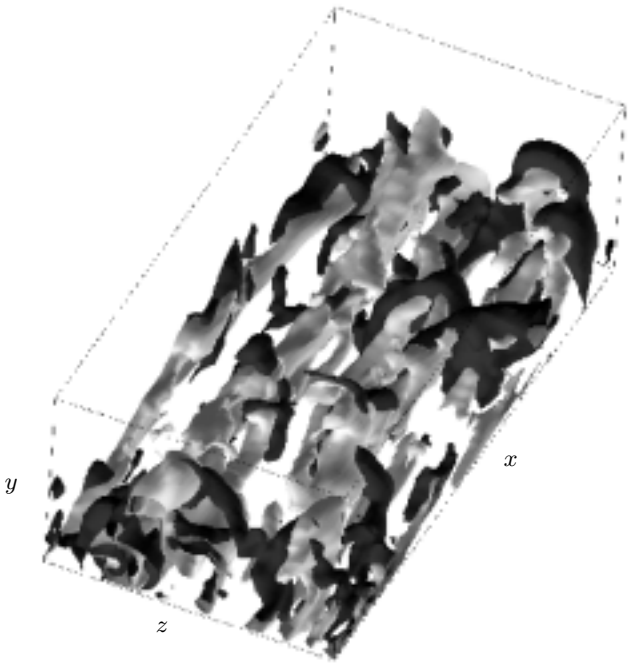

FIGURE 5.3. The turbulent boundary layer.

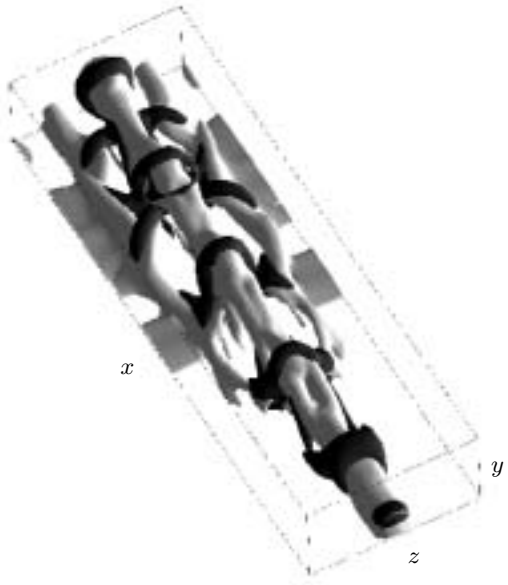

FIGURE 5.4. The laminar low-speed streak.

CHAPTER 6

Conclusions and outlook

The direct numerical simulations have been completed with a code which runs efficiently on all types of super computers in use today. Besides the obvious wishes for higher Reynolds number, larger computational box and higher resolution, there is a number of possible extensions for future DNS. A natural extension to this work is the turbulent boundary layer with a three-dimensional mean flow. Although some theoretical work has been presented for this type of flow, (e.g. Degani *et al.* 1993), DNS would be interesting for comparison. Wall roughness and wall curvature are also complications that are of engineering significance.

A consistent analysis of the turbulent boundary layer equations for the inner part in this work has given the theoretical expressions for the streamwise velocity profile in the viscous sub-layer and overlap region. The analysis could perhaps be extended to include complications of the kind mentioned above, see e.g. Townsend (1976).

The work on turbulence modelling leaves some unanswered questions. The damping of the non-linear terms in the EARSM model is one such issue. However, the near-wall laws for APG boundary layers developed here could be of great importance in turbulence model predictions of such flows. The laws are suitable as boundary conditions through wall functions if well defined freestream data are available. The work on coherent structures and their dynamics can be developed to obtain a more complete picture. Specially the instability mechanism of the low-speed streaks in a turbulent flow needs to be more thoroughly investigated. The concept of two instability mechanisms present in turbulence could lead to a more unified view on the self-sustained turbulence regeneration cycle. The knowledge about turbulence structures should be utilized in a predictive model, maybe in a similar manner as in the investigation of Perry *et al.* (1994).

For more specific conclusions, the reader is referred to papers 1 through 8.

Acknowledgments

First of all I wish to thank my advisor, Professor Dan Henningson, whose enthusiasm and energy never ceased to inspire me. His ability to always ask me the questions I needed for my thoughts to turn the right direction, astonished me every time.

Professor Ruud Henkes introduced me to turbulence modelling, and his numerical code was of great importance for my work. Our collaboration at TU Delft was the most productive month of my time as a Ph.d. student.

The many fruitful discussions with Professor Joseph Haritonidis during my stay at Ohio State University (OSU) in Columbus gave me insight in perhaps the most confusing part of turbulence research; coherent structures. I also wish to thank him for letting me stay in his cozy house, and introducing me to the finest cuisine of Ohio.

My stay at the Center for Turbulence Research (CTR) at Stanford University was a great opportunity to meet some of the most prominent researchers in turbulence. Professor Parviz Moin is acknowledged for letting me spend a month analyzing their DNS data base.

The financial support for my visits to OSU and CTR was partly covered with the aid of Knut och Alice Wallenbergs stiftelse and The Foundation BLANCEFLOR Boncompagni-Ludovisi, née Bildt.

The National Aerospace Laboratory (NAL) in Tokyo is acknowledged for letting me work there as an STA-fellow. This work was fully financed by the Japan Science and Technology Corporation (JST). Doctor Naoki Hirose was of invaluable help, both for work and for my life in Tokyo. I thank him also for letting me stay in his guest house in Tokyo. I also wish to thank Doctor Yuichi Matsuo for his help during my struggle with the Numerical Wind Tunnel. I will not forget those long debugging nights. My second visit to NAL was financed by The Scandinavia-Japan Sasakawa Foundation.

My colleagues at the department have provided a stimulating atmosphere. I thank you all for that and for the many interesting discussions about almost everything (and many times about nothing at all). Special thanks are sent to Doctor Krister Alvelius, whose brilliant ideas were of great help while working with the code. I also wish to thank Doctor Stefan Wallin who I had the pleasure to work with under a few but very productive brainstorming meetings.

This work was sponsored by the Swedish National Board for Industrial and Technical Development (NUTEK). The support was covered during the first year by the NUTEK 'strömningsprogram' through The Aeronautical Research Institute of Sweden (FFA). The program was terminated and financial support was instead found through the Parallel and Scientific Computing Institute (PSCI).

Computer time was provided by the Center for Parallel Computers (PDC) at the Royal Institute of Technology (KTH), the National Supercomputer Center in Sweden (NSC) at Linköping University, and the National Aerospace Laboratory (NAL) in Tokyo.

Bibliography

Acarlar, M. S. & Smith, C. R. 1987 A study of hairpin vortices in a laminar boundary layer. Part 2. Hairpin vortices generated by fluid injection. *J. Fluid Mech.* **175**, 43–48.

Afzal, N. 1996 Wake layer in a turbulent boundary layer with pressure gradient: a new approach. In *IUTAM Symposium on Asymptotic Methods for Turbulent Shear flows at High Reynolds Numbers* (ed. K. Gersten), pp. 95–118. Kluwer Academic Publishers.

Barenblatt, G. I. 1996 *Scaling, Self-Similarity, and Intermediate Asymptotics*. Cambridge University Press.

Bertolotti, F. P., Herbert, T. & Spalart, P. R. 1992 Linear and nonlinear stability of the Blasius boundary layer. *J. Fluid Mech.* **242**, 441–474.

Boussinesq, T. V. 1877 Essai sur la théorie des eaux courantes. *Mém. prés. Acad. Sci.* 3rd edn, Paris XXIII, p.46.

Bradshaw, P. 1967 The turbulent structure of equilibrium boundary layers. *J. Fluid Mech.* **29**, 625–645.

Bradshaw, P. & Huang, G. P. 1995 The law of the wall in turbulent flow. *Proc. Roy. Soc. Lond. Ser. A* **451**, 165–188.

Cooley, J. W. & Tukey, J. W. 1965 An algorithm for the machine calculation of complex Fourier series. *Math. Comput.* **19**, 297–301.

Degani, A. T., Smith, F. T. & Walker, J. D. A. 1993 The structure of a three-dimensional turbulent boundary layer. *J. Fluid Mech.* **250**, 43–68.

van Driest, E. R. 1956 On turbulent flow near a wall. *J. Aero. Sci.* **23**, 1007–1011.

Elsberry, K., Loeffler, J., Zhou, M. D. & Wygnanski, I. 2000 An experimental study of a boundary layer that is maintained on the verge of separation. *J. Fluid Mech.* **423**, 227–261.

Fourier, J. 1822 *Théorie analytique de la chaleur*. Firmin Didot, Paris.

Granville, P. S. 1989 A modified van driest formula for the mixing length of turbulent boundary layers in pressure gradients. *J. Fluids Eng.* **111**, 94–97.

Hanjalić, K., Jakirlić, S. & Hadžić, I. 1995 Computation of oscillating turbulent flows at transitional *Re*-numbers. In *Turbulent Shear Flows 9* (eds. F. Durst, N. Kasagi & B. E. Launder), pp. 323–342. Springer-Verlag.

Henkes, R. A. W. M. 1998 Scaling of equilibrium boundary layers under adverse pressure gradient using turbulence models. *AIAA J.* **36**, 320–326.

Kim, J., Moin, P. & Moser, R. 1987 Turbulence statistics in fully developed channel flow. *J. Fluid Mech.* **177**, 133–166.

Kline, S. J., Reynolds, W. C., Schraub, F. A. & Runstadler, P. W. 1967 The structure of turbulent boundary layers. *J. Fluid Mech.* **30**, 741.

Kreiss, H.-O. & Oliger, J. 1972 Comparison of accurate methods for the integration of hyperbolic equations. *Tellus* **XXIV**, 199–215.

Mellor, G. L. 1966 The effects of pressure gradients on turbulent flow near a smooth wall. *J. Fluid Mech.* **24**, 255–274.

Mellor, G. L. & Gibson, D. M. 1966 Equilibrium turbulent boundary layers. *J. Fluid Mech.* **24**, 225–253.

Na, Y. & Moin, P. 1998 Direct numerical simulation of a separated turbulent boundary layer. *J. Fluid Mech.* **374**, 379–405.

Nordström, J., Nordin, N. & Henningson, D. S. 1999 The fringe region technique and the fourier method used in the direct numerical simulation of spatially evolving viscous flows. *SIAM J. Sci. Comp.* **20** (4), 1365–1393.

Orszag, S. A. 1972 Comparison of pseudospectral ans spectral approximations. *Stud. Appl. Math.* **51**, 253–259.

Österlund, J. M., Johansson, A. V., Nagib, H. M. & Hites, M. H. 2000 A note on the overlap region in turbulent boundary layers. *Phys. Fluids* **12**, 1–4.

Patel, V. C. 1973 A unified view of the law of the wall using mixing-length theory. *Aeronaut. Q.* **24**, 55–70.

Perry, A. E., Marušić, I. & Li, J. D. 1994 Wall turbulence closure based on classical similarity laws and the attached eddy hypothesis. *Phys. Fluids* **6** (2), 1024–1035.

Prandtl, L. 1925 Bericht über Untersuchungen zur ausgebildeten Turbulenz. *Zeitschrift für Angewandte Mathematik und Mechanik* **5**, 136.

Prandtl, L. 1932 Zur turbulenten Strömung in Rohren und längs Platten. *Ergebn. Aerodyn. Versuchsanst. Göttingen* **4**, 18–29.

Robinson, S. K. 1991 Coherent motions in the turbulent boundary layer. *Ann. Rev. Fluid Mech.* **23**, 601–639.

Simpson, R. L. 1970 Characteristics of turbulent boundary layers at low Reynolds numbers with and without transpiration. *J. Fluid Mech.* **42**, 769–802.

Skåre, P. E. & Krogstad, P.-Å. 1994 A turbulent equilibrium boundary layer near separation. *J. Fluid Mech.* **272**, 319–348.

Skote, M. & Henningson, D. 1997 Direct numerical simulation of turbulent boundary layers with adverse pressure gradients. In *Advances in DNS/LES* (eds. C. Liu & Z. Liu), pp. 215–222. Greyden Press.

Skote, M. & Henningson, D. 1998 Direct numerical simulation of adverse pressure gradient turbulent boundary layers. In *Advances in Turbulence VII* (ed. U. Frisch), pp. 171–174. Kluwer Academic Publishers.

Skote, M. & Henningson, D. 1999 Dns of a turbulent boundary layers under a strong adverse pressure gradient. In *Recent Advances in DNS and LES* (eds. D. Knight & L. Sakell), pp. 373–384. Kluwer Academic Publishers.

Skote, M., Henningson, D., Hirose, N., Matsuo, Y. & Nakamura, T. 2000 Parallel dns of a separating turbulent boundary layer. In *Proceedings of Parallel CFD 2000, Trondheim*.

Spalart, P. R. 1988 Direct simulation of a turbulent boundary layer up to $Re_\theta = 1410$. *J. Fluid Mech.* **187**, 61–98.

Spalart, P. R. & Coleman, G. N. 1997 Numerical study of a separation bubble with heat transfer. *European J. Mechanics B/Fluids* **16**, 169.

Spalart, P. R. & Leonard, A. 1987 Direct numerical simulation of equilibrium turbulent boundary layers. In *Turbulent Shear Flows 5* (eds. F. Durst, B. E. Launder, J. L. Lumley, F. W. Schmitd & J. H. Whitelaw), pp. 234–252. Springer-Verlag.

Spalart, P. R. & Watmuff, J. H. 1993 Experimental and numerical study of a turbulent boundary layer with pressure gradients. *J. Fluid Mech.* **249**, 337–371.

Stratford, B. S. 1959*a* An experimental flow with zero skin friction throughout its region of pressure rise. *J. Fluid Mech.* **5**, 17–35.

Stratford, B. S. 1959*b* The prediction of separation of the turbulent boundary layer. *J. Fluid Mech.* **5**, 1–16.

Tennekes, H. & Lumley, J. L. 1972 *A First Course in Turbulence*. The MIT Press.

Townsend, A. A. 1956 *The structure of turbulent shear flow*. Cambridge University Press.

Townsend, A. A. 1961 Equilibrium layers and wall turbulence. *J. Fluid Mech.* **11**, 97–120.

Townsend, A. A. 1976 *The Structure of Turbulent Shear Flow*. Cambridge University Press.

Wallin, S. & Johansson, A. V. 2000 An explicit algebraic Reynolds stress model for incompressible and compressible turbulent flows. *J. Fluid Mech.* **403**, 89–132.

Wilcox, D. C. 1993 *Turbulence Modeling for CFD*. DCW Industries, Inc.

P1

Paper 1

Direct numerical simulation of self-similar turbulent boundary layers in adverse pressure gradients

By Martin Skote*, Dan S. Henningson*† and Ruud A. W. M. Henkes‡

Direct numerical simulations of the Navier-Stokes equations have been carried out with the objective of studying turbulent boundary layers in adverse pressure gradients. The boundary layer flows concerned are of the equilibrium type which makes the analysis simpler and the results can be compared with earlier experiments and simulations. This type of turbulent boundary layers also permits an analysis of the equation of motion to predict separation. The linear analysis based on the assumption of asymptotically high Reynolds number gives results that are not applicable to finite Reynolds number flows. A different non-linear approach is presented to obtain a useful relation between the freestream variation and other mean flow parameters. Comparison of turbulent statistics from the zero pressure gradient case and two adverse pressure gradient cases shows the development of an outer peak in the turbulent energy in agreement with experiment. The turbulent flows have also been investigated using a differential Reynolds stress model. Profiles for velocity and turbulence quantities obtained from the direct numerical simulations were used as initial data. The initial transients in the model predictions vanished rapidly. The model predictions are compared with the direct simulations and low Reynolds number effects are investigated.

1. Introduction

The analysis of adverse pressure gradient (APG) turbulent boundary layers has been going on for a long time. Disagreement in the approach of analysis as well as contradiction in results from experiments are found in the literature. Only in recent years have direct numerical simulations (DNS) of these flows become possible, albeit for low Reynolds numbers.

The conditions needed for self-similarity as well as for the onset of separation have been the subject of several investigations. Clauser (1954) performed

*Department of Mechanics, Royal Institute of Technology (KTH), SE-100 44 Stockholm, Sweden
†Aeronautical Research Institute of Sweden (FFA), Box 11021, SE-161 11 Bromma, Sweden
‡Shell Research and Technology Centre Amsterdam, P.O. Box 3003, 1003 AA Amsterdam, The Netherlands

experiments where he adjusted the pressure gradient such that a self-similar turbulent boundary layer was obtained. A constant non-dimensional pressure gradient,

$$\beta = \frac{\delta^*}{\tau_w}\frac{dP}{dx},$$

was shown to be a condition for self-similarity. Here δ^* is the displacement thickness, τ_w is the wall shear stress and dP/dx is the pressure gradient. Townsend (1976) and Mellor & Gibson (1966) showed that self-similarity is obtained if the freestream variation has the form of a power law in the downstream direction, $U \sim x^m$, where U is the freestream velocity and x is the streamwise coordinate. Townsend used non-specified length and velocity scales and analyzed the equation describing the outer part of the turbulent boundary layer. His analysis showed that in addition to the condition $U \sim x^m$ the length scale must vary linearly with the downstream coordinate. Mellor & Gibson analyzed the integrated momentum equation with the length and velocity scales $\Delta = (U/u_\tau)\delta^*$ and u_τ, where u_τ is the friction velocity. Under certain approximations they obtain that for flows with $\beta = \text{const.}$ the freestream variation is $U \sim x^m$ and $\Delta \sim x$. Tennekes & Lumley (1972) analyzed the integrated momentum equation with an assumption of sufficiently high Reynolds number, so that the velocity defect law could be linearized, and they obtained a relation between the exponent and Clauser's non-dimensional pressure gradient β which reads

$$m = -\frac{\beta}{1+3\beta}.$$

Following Clauser, a number of measurements have been carried out in self-similar adverse pressure gradient turbulent boundary layers near separation. Bradshaw (1967) measured three self-similar turbulent boundary layers with $m = 0, -0.15, -0.255$. In the last case the turbulence intensities showed peak values in the outer part of the layer and the boundary layer was near separation. Skåre & Krogstad (1994) experiments near separation showed that the shape factor approaches 2 and $m = -0.22$. In their experiments $\beta = 20$ and the shape factor as well as the ratio u_τ/U was found to be constant. They also obtained self-similar velocity profiles. Stratford (1959*a*) performed measurements on a turbulent boundary layer near separation as well as an analysis of the inner and outer equations (Stratford 1959*b*). He concluded that the asymptotic form of the separation profile near the wall is proportional to $y^{1/2}$, which was also theoretically verified by Durbin & Belcher (1992).

The value of m near separation has also been investigated theoretically. Head (1976) used an integral method to calculate the turbulent boundary layer for $m = -0.15, -0.255, -0.35$ and concluded that the solution is unique in the first case whereas multiple solutions exist in the second. No solution was obtained in the third case. Schofield (1981) analyzed the self-similar boundary layers based on the Schofield-Perry law. He concluded that there is no solution for $m < -0.3$ and only one solution exists for $m > -0.23$.

In recent years direct numerical simulations of turbulent boundary layers have become an important complement to experiments. Spalart (1988) carried out DNS of a zero pressure gradient turbulent boundary layer. Spalart & Leonard (1987) performed DNS of self-similar APG turbulent boundary layer using a similarity coordinate system. In these simulations the shape factor approaches 2.3 and $m = -0.22$ near separation. Spalart & Watmuff (1993) compared experiments and DNS of an APG turbulent boundary layer in a varying pressure gradient and they found good agreement. Recent simulations have also been made past the point of separation. Coleman & Spalart (1993) and Spalart & Coleman (1997) performed DNS of a separation bubble with heat transfer. Na & Moin (1996) have performed DNS of a separation bubble and they presented the Reynolds stresses and turbulent energy budgets.

Regarding self-similar adverse pressure gradient turbulent boundary layer, both theoretical work and experiments support the idea that a power law freestream velocity is a requirement for self-similarity. The assumption of infinite Reynolds number and the use of specific velocity and length scales have given a relation between m and β. The consensus from the experiments and DNS performed for turbulent boundary layers near separations seems to be that separation occurs for about $-0.25 < m < -0.20$ with a shape factor of about 2.

The work presented here starts in section 2 with an introduction to the concept of self-similarity of turbulent boundary layers subjected to adverse pressure gradients. A relation between the non-dimensional pressure gradient and m is also derived. The numerical code for the turbulence model prediction and the code for the DNS is described in section 3. Section 4 is devoted to results from the DNS as well as comparison with turbulence model predictions. In section 5 we sum up and draw conclusions.

2. Analysis of the turbulent boundary layer equations

The first part of this section consists of a review of the asymptotic behavior of adverse pressure gradient boundary layer flows. In the second part the analysis is extended and the restriction to asymptotically high Reynolds number is relaxed, and in the last part the relation to earlier work is discussed.

2.1. *Linearized analysis*

The equations for an incompressible two-dimensional turbulent boundary layer are

$$\frac{\partial u}{\partial x} + \frac{\partial v}{\partial y} = 0 \tag{1}$$

$$u\frac{\partial u}{\partial x} + v\frac{\partial u}{\partial y} = -\frac{1}{\rho}\frac{dP}{dx} + \nu\frac{\partial^2 u}{\partial y^2} - \frac{\partial}{\partial y}\langle u'v'\rangle \tag{2}$$

where u is the mean streamwise velocity, v the mean wall normal velocity, dP/dx the pressure gradient, $\langle u'v'\rangle$ the Reynolds stress, ρ the density and ν

the kinematic viscosity. If the pressure gradient is not too large, the scalings in the inner part of the boundary layer remain the same as in the zero pressure gradient case. For the outer part however, the analysis must take into account even a weak pressure gradient. The equation describing the outer part of an incompressible turbulent boundary layer is given by

$$u\frac{\partial u}{\partial x} + v\frac{\partial u}{\partial y} = -\frac{1}{\rho}\frac{dP}{dx} - \frac{\partial}{\partial y}\langle u'v'\rangle. \tag{3}$$

A self-similar solution has no explicit dependence on x. Thus we seek solutions of the form

$$(u-U)/u_\tau = F(\eta), \qquad -\langle u'v'\rangle/{u_\tau}^2 = R(\eta), \tag{4}$$

where

$$\eta = y/\Delta(x), \qquad \Delta = U\delta^*/u_\tau. \tag{5}$$

Substituting these expressions into equation (3) we obtain

$$-2\beta F - (1+2\beta)\eta\frac{dF}{d\eta} = \frac{dR}{d\eta}, \tag{6}$$

when $u_\tau/U \to 0$. The classical treatment of the equations which involves outer and inner equations and a matching of the solutions, leads to the logarithmic friction law,

$$\frac{u_\tau}{U} = \frac{1}{C + \frac{1}{\kappa} ln Re_{\delta^*}}, \tag{7}$$

where κ is the Kármán constant and $Re_{\delta^*} = U\delta^*/\nu$. Equation (7) shows that $u_\tau/U \to 0$ in the limit of very high Reynolds number, which is utilized in the derivation of equation (6). This derivation is given in different ways by Tennekes & Lumley (1972), Mellor & Gibson (1966) and Henkes (1998).

From equation (6) one obtains a condition for self-similarity as a parameter β that should be constant

$$\beta = \frac{\delta^*}{\tau_w}\frac{dP}{dx}. \tag{8}$$

That β should be constant follows from a balance of the skin friction force and the pressure gradient force, as argued by Clauser (1954).

Assuming a self-similar boundary layer, we proceed to give the Tennekes & Lumley (1972) analysis resulting in a relationship between β and m. We start with the integrated momentum equation,

$$\left(\frac{U}{u_\tau}\right)^2 \frac{d}{dx}\Theta - \frac{2\beta}{H} = 1 + \beta, \tag{9}$$

which is equation (2) integrated from the wall to the freestream. We rewrite the velocity defect term as

$$u(U-u) = U(U-u) - (U-u)^2. \tag{10}$$

If the velocity defect is assumed to be of order u_τ, the last term is an order u_τ/U smaller than the others and can be neglected, giving

$$\frac{u}{U}\left(1-\frac{u}{U}\right) \to \left(1-\frac{u}{U}\right) \tag{11}$$

if $u_\tau/U \to 0$. From this equation it is clear that the linearization is equivalent to the assumption of a shape factor equal to unity since $\Theta = \delta^*$. The linearized version of equation (9) thus becomes

$$\frac{U}{{u_\tau}^2}\frac{d}{dx}(\Delta u_\tau) = 1 + 2\beta. \tag{12}$$

By keeping the ratio u_τ/U approximately constant in equation (12) Tennekes & Lumley obtain a relation between m and β which reads

$$m = -\frac{\beta}{1+3\beta} \tag{13}$$

with

$$U \sim x^m. \tag{14}$$

2.2. *Non-linear analysis*

A shape factor equal to unity is an unrealistic approximation in most practical cases, see Fernholz & Finley (1996) for an assessment of data from experiments on zero pressure gradient turbulent boundary layers. Since we are interested in using a relation such as (13) for separation prediction it would be useful to obtain results that are not restricted to asymptotically high Reynolds numbers. We will now derive a relation between β and m without this restriction.

The full integrated momentum equation (9) can be written as

$$\frac{U'\delta^*}{U\delta^{*\prime}} = -\frac{\beta}{H(1+\beta)+2\beta+(H-1)\beta(1-\frac{{u_\tau}'U}{u_\tau U'})}, \tag{15}$$

where the $'$ denotes x-derivative. We have used the relation

$$H = \frac{1}{1-\frac{u_\tau}{U}G} \tag{16}$$

with

$$G = \int_0^\infty F^2 d\eta. \tag{17}$$

G must be constant if the boundary layer is to be self-similar, i.e. F does not change its shape. From equation (16) the limit $H \to 1$ as $u_\tau/U \to 0$ is consistent with the linearization (11) described above. The use of the limit value $u_\tau/U \to 0$ as $Re \to \infty$ is motivated by equation (7). Since the logarithmic function grows very slowly when the argument is large, a better assumption than $u_\tau/U \to 0$ for moderately high Reynolds numbers is that $u_\tau/U \approx$ constant, which is consistent with many of the numerical investigations and experiments described in the introduction. If u_τ/U is kept constant, which implies that

$$\frac{u_\tau' U}{u_\tau U'} = 1, \tag{18}$$

equation (15) can be written as

$$\frac{U'\delta^*}{U\delta^{*\prime}} = -\frac{\beta}{H(1+\beta)+2\beta} = m. \tag{19}$$

Equation (19) can be integrated to give

$$\frac{U}{U_0} = \left(\frac{\delta^*}{\delta_0^*}\right)^m, \tag{20}$$

where the subscript 0 refers to the initial values at $x = 0$ The definition of β, equation (8), can be written as

$$\beta = -\frac{\delta^*}{u_\tau^2} U \frac{dU}{dx}. \tag{21}$$

Combining equations (20) and (21) and integrating gives

$$\frac{U}{U_0} = \left[1 - \frac{\beta}{m\delta_0^*}\left(\frac{u_\tau}{U}\right)^2 x\right]^m \tag{22}$$

and

$$\frac{\delta^*}{\delta_0^*} = 1 - \frac{\beta}{m\delta_0^*}\left(\frac{u_\tau}{U}\right)^2 x. \tag{23}$$

Introducing x_0 as a virtual leading edge where $\delta^* = 0$ we derive from equation (23) that

$$\delta_0^* = \frac{\beta}{m}\left(\frac{u_\tau}{U}\right)^2 x_0. \tag{24}$$

Using equation (24), the equations (22) and (23) can be written as

$$\frac{U}{U_0} = \left(1 - \frac{x}{x_0}\right)^m, \qquad \frac{\delta^*}{\delta_0^*} = 1 - \frac{x}{x_0}. \tag{25}$$

The result is that

$$U \sim x^m, \qquad \delta^* \sim x, \tag{26}$$

with

$$m = -\frac{\beta}{H(1+\beta)+2\beta}. \tag{27}$$

Equation (13) is recovered from equation (27) by setting $H = 1$.

In section 4.2.2 a comparison between the relations (13) and (27) will show that the linearization, which might be correct for asymptotically high Reynolds number, is insufficient for low and moderate Reynolds number flows.

2.3. *Relation to previous work*

Equation (15) can be integrated if the right hand side is assumed to be constant. This was done by Mellor & Gibson (1966) who found that

$$U \sim \tilde{x}^m \tag{28}$$

with

$$\tilde{x} = \int_0^x \frac{u_\tau U_0}{u_{\tau 0} U} dx, \tag{29}$$

where m in their case is equal to the right hand side of equation (15). With $u_\tau/U = \text{const.}$ the variable $\tilde{x}$ in equation (28) becomes x and the results in equations (26) and (27) are recovered. Due to the slow increase of $\ln(Re)$ with Re, H and u_τ/U are far from their asymptotic values of 1 and 0 respectively in many experiments and DNS. They are on the other hand fairly constant in a large range of Reynolds numbers for the same reason. Thus it seems as equations (28) and (29) do not add substantially new information to the non-linear theory with a constant u_τ/U as an approximation.

The relation (27) was obtained by Rotta (1962), although expressed in G and u_τ/U. This work was apparently unnoticed by Townsend (1976) and Mellor & Gibson (1966), whose work is closely related to Rotta's.

An alternative to the procedure of letting $u_\tau/U \to 0$ for high Reynolds numbers to obtain self-similar equations, is to scale the velocity defect with U instead of u_τ to obtain full similarity of equation (3). This is done by George & Castillo (1993). One of the consequences is that the logarithmic region in the velocity profile is substituted by a power law region. The same scaling was used by Townsend (1960) for the near separation case, where he also used the half-power law, $u \sim y^{1/2}$, of Stratford (1959*b*). He develops a theory to predict the experiment by Stratford (1959*a*) with the assumption of constant eddy viscosity. To predict the velocity profile Townsend had to change the values of measured constants in his calculations, e.g. the exponent m is 0.234 instead of the measured 0.25.

Using the constraint $u_\tau/U = \text{const.}$ together with $U \sim x^m$ in equation (3) gives instead of equation (6) the following equation

$$2mF - (1+m)\eta\frac{dF}{d\eta} - \frac{u_\tau}{U}(1+m)\frac{dF}{d\eta}\int_0^\eta F d\eta + \frac{u_\tau}{U}mF^2 = -\frac{dR}{d\eta}\frac{m}{\beta}. \quad (30)$$

Integrating this equation gives $m = -1/(H+2)$ which is the same as relation (27) for $\beta \to \infty$. In equation (30) the viscous term is neglected, which means that $\nu(\partial u/\partial y)(y=0) = 0$, i.e. we implicitly obtain the case at separation. Adding the viscous term, which reads

$$\nu\frac{d^2F}{d\eta^2}\frac{1}{\Delta u_\tau}\frac{m}{\beta}, \quad (31)$$

to the right hand side of equation (30) and integrating gives the relation

$$m = -\frac{\beta}{H(1+\beta)+2\beta},$$

which is the same as (27). In the integrations above the following relations have been used,

$$-\int_0^\infty F d\eta = \int_0^\infty \eta\frac{dF}{d\eta}d\eta = 1, \quad (32)$$

$$\int_0^\infty F^2 d\eta = -\int_0^\infty \left(\frac{dF}{d\eta}\int_0^\eta F d\eta\right)d\eta = \frac{H-1}{H\frac{u_\tau}{U}}. \quad (33)$$

3. Computational tools and parameters

3.1. *The DNS Code*

The code used for the direct numerical simulations (DNS) is developed at KTH and FFA (Lundbladh *et al.* 1992, 1994). The numerical approximation consists of spectral methods with Fourier discretization in the horizontal directions and Chebyshev discretization in the normal direction. Since the boundary layer is developing in the downstream direction, it is necessary to use non-periodic boundary conditions in the streamwise direction. This is possible while retaining the Fourier discretization if a fringe region is added downstream of the physical domain. In the fringe region the flow is forced from the outflow of the physical domain to the inflow. In this way the physical domain and the fringe region together satisfy periodic boundary conditions. The fringe region is implemented by the addition of a volume force F, to the Navier-Stokes equations:

$$\frac{\partial u_i}{\partial t} + u_j \frac{\partial u_i}{\partial x_j} = -\frac{1}{\rho}\frac{\partial p}{\partial x_i} + \nu \frac{\partial^2 u_i}{\partial {x_j}^2} + F_i. \tag{34}$$

The force

$$F_i = \lambda(x)(\tilde{u}_i - u_i) \tag{35}$$

is non-zero only in the fringe region; $\tilde{u}_i$ is the laminar inflow velocity profile the solution u_i is forced to and $\lambda(x)$ is the strength of the forcing with a maximum of about 1. The form of $\lambda(x)$ is designed to minimize the upstream influence and is sketched in Figure 1. The figure shows the whole computational box with the fringe region at the end. The dotted line shows how the boundary layer grows downstream and is forced back to its inflow value in the fringe region. The forcing at the beginning of the fringe region is towards the boundary layer as it would continue downstream. This is done to damp the disturbances before the actual forcing towards the inflow profile starts. See Nordström *et al.* (1999) for an investigation of the fringe region technique.

Time integration is performed using a third order Runge-Kutta method for the advective and forcing terms and Crank-Nicolson for the viscous terms. A 2/3-dealizing rule is used in the streamwise and spanwise direction.

3.2. *Numerical parameters*

Results from two direct numerical simulations of APG turbulent boundary layers as well as one zero pressure gradient case (ZPG) are presented. In the first APG case (APG1) the pressure gradient is close to that for which the corresponding laminar boundary layer would separate and in the second case (APG2) the pressure gradient is the same as in Bradshaw's first experimental APG case (Bradshaw 1967). The pressure gradient is applied through the variation of the freestream velocity, which is described by a power law, $U \sim x^m$. For APG1 $m = -0.077$ and for APG2 $m = -0.15$, which corresponds to $\beta \approx 0.24$ and $\beta \approx 0.65$ respectively. The results from the ZPG are taken from a simulation by Henningson & Lundbladh (1995). This simulation was done

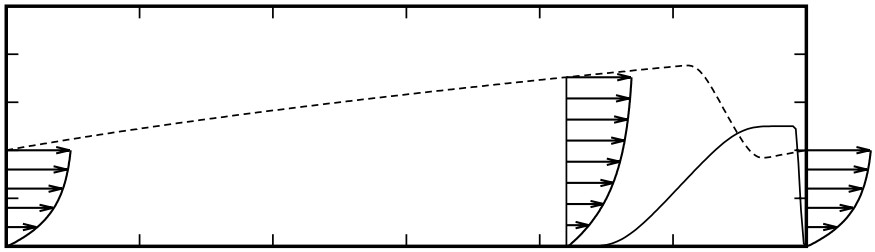

FIGURE 1. Computational box with the fringe region — $\lambda(x)$, the fringe function. - - the boundary layer thickness.

with a different set of parameters, see Table 1, and is not as highly resolved as the other two. The results are included only as a comparison to the two APG simulations. The simulations start with a laminar boundary layer at the inflow which is triggered to transition by a random volume force near the wall. All the quantities are non-dimensionalized by the freestream velocity (U) and the displacement thickness (δ^*) at the starting position of the simulation ($x = 0$) where the flow is laminar. At that position $Re_{\delta^*} = 400$. The length (including the fringe), height and width of the computation box were $450 \times 24 \times 24$ in these units for the largest case, APG2. The number of modes in this simulation was $480 \times 161 \times 96$, which gives a total of 7.5 million modes or 17 million collocation points. For comparison with the other cases, see Table 1. In all simulations the fringe region has a length of 50 and the trip is located at $x = 10$. The useful region starts at $x = 150$, which corresponds to different values of Re_Θ as also found in Table 1.

The simulations were run for a total of 4500 time units (δ^*/U), and the sampling for the turbulent statistics was performed during the 2000 last time units. It was verified that the accuracy of the DNS and its statistics was sufficient by repeating the computation of the APG1 case on a coarser resolution ($320 \times 101 \times 64$ modes) and with a shorter averaging time (1000 time units), see Henkes *et al.* (1997). The differences between the two resolutions are shown in Figures 2a and 2b, where the mean velocity and Reynolds stresses are shown. The difference between the coarser grid case (APG1a) and the full resolution case (APG1) is small even though the number of points is reduced by a factor of almost 2/3 in all directions. The resolutions of the cases APG1 and APG2 were thus considered to be sufficient.

Case	L_x	L_y	L_z	NX	NY	NZ	ΔX^+	ΔZ^+	Useful region, Re_Θ
ZPG	500	12	25	320	81	64	31	7.8	$350 - 525$
APG1a	450	18	24	320	101	64	24	6.5	$390 - 620$
APG1	450	18	24	480	121	96	16	4.3	$390 - 620$
APG2	450	24	24	480	161	96	13	3.6	$430 - 690$

TABLE 1. Numerical parameters.

3.3. *The turbulent boundary layer code*

To be able to investigate the relevance of the asymptotic analysis described above the use of turbulence models is the only option. Direct numerical simulation is possible only for low Reynolds number flows and experiments are performed at higher, but not high enough Reynolds number for the full asymptotic behavior to appear. We will also use model predictions at low Reynolds number for comparison with DNS. It is possible to draw conclusions about the low Reynolds number effects in the DNS data by comparing model predictions at low and high Reynolds numbers.

The equations solved are (1) and (2) together with a closure for the Reynolds shear tress $\langle u'v' \rangle$. In the calculations described here the Differential Reynolds Stress Model of Hanjalić *et al.* (1995) is used. The model contains transport equations for the Reynolds stresses, the turbulent kinetic energy and the dissipation rate, see Appendix A. The ϵ equation contains a source term

$$S_{\epsilon 4} = C_{\epsilon 4} \frac{\epsilon}{k} \left(\langle v'^2 \rangle - \langle u'^2 \rangle \right) \frac{\partial u}{\partial x}, \tag{36}$$

where ϵ is the dissipation rate, k the turbulent kinetic energy, $\langle u'^2 \rangle$ and $\langle v'^2 \rangle$ the streamwise and normal Reynolds stresses and $C_{\epsilon 4}$ a constant. The term (36) is a simplified version of the original term and introduced by Hanjalić & Launder (1980). They also showed that (36) gives a significant contribution to the ϵ equation in boundary layer flows with streamwise pressure gradient. For a complete description of the model, see Henkes (1997). The calculations were made with a parabolic boundary layer code. The discretization is based on the finite volume method with a second-order upwind scheme in the downstream direction. In the normal direction is either a central scheme or a first-order upwind scheme used, depending on the ratio between the convection and diffusion term. The grid is uniform in the downstream direction but stretched in the normal direction. To account for the growth of the boundary layer in the downstream direction, at several x positions the outer edge was increased and the y grid points were redistributed. All the calculations presented in this paper have been checked to be grid independent. This was done by doubling the number of points in the x and y directions.

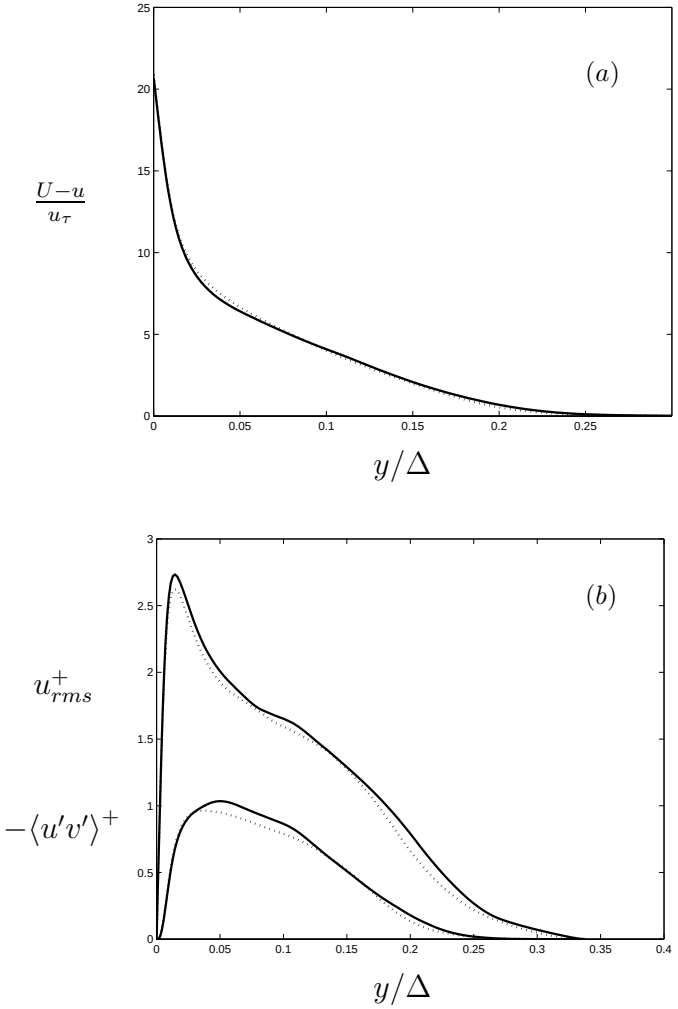

FIGURE 2. (a) Velocity defect. (b) u^+_{rms} and Reynolds stress for — $480 \times 121 \times 96$; $\cdots$ $320 \times 101 \times 64$.

4. DNS Results

In this section the results from the direct numerical simulations are presented. Section 4.1 deals with the flow structures. The downstream behavior of the mean flow quantities is described in section 4.2. The results are compared with the results obtained from the analysis of the integrated momentum equation from section 2.2. Comparison with other DNS and experiments is also made. In section 4.3, turbulent statistics are presented and results obtained from the equations describing the inner part of the turbulent boundary layer are compared with the statistics from the DNS. In the last section 4.4, results using

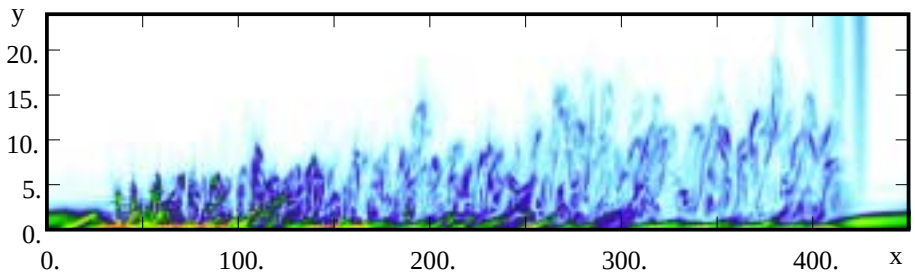

FIGURE 3. APG2: Contours of vorticity.

the differential Reynolds stress model are compared with the low Reynolds number DNS data. The model predictions are also extended to high Reynolds numbers to determine the asymptotic behavior.

4.1. *Flow structures*

Figure 3 shows an instantaneous vorticity flow field from the APG2 case. At $x = 0$ the boundary layer is laminar and at $x = 10$ the stochastic volume force triggers transition. The transition to turbulence is rapid and at approximately $x = 150$ the turbulent flow has become fully developed. In the turbulent region, shear layers inclined in the downstream direction can be seen as red and yellow contours. They indicate the presence of turbulent 'bursts' in the near wall region. In the outer part of the boundary layer larger scale vortical structures can be seen. Note the 'fringe region' at the end of the computational box, starting at $x = 400$.

The streamwise velocity fluctuations close to the wall in Figure 4 show the dominance of streamwise aligned streaks. The speed of the low speed streaks is about 0.16 and 0.29 for the high speed streaks at the position of $y^+ = 10$. The spacing of the low speed streaks is about 100 plus-units. These values are about the same as those found in zero pressure gradient turbulent boundary layers, see Figure 5 for comparison. If the whole field in the normal direction is shown at a value of $x = 280$ as in Figure 6, a second layer of 'streaks' is found at $y = 3.5 - 8$.

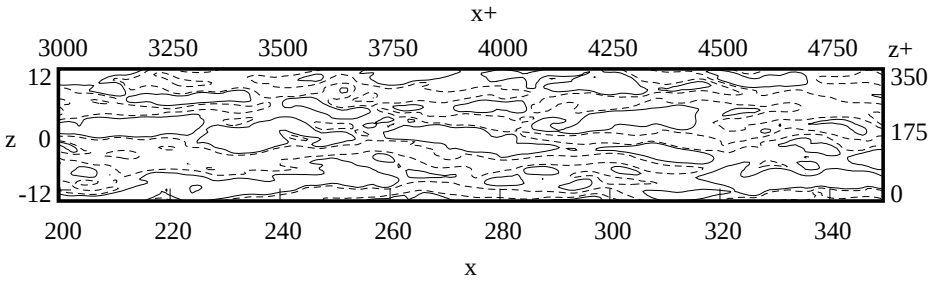

FIGURE 4. APG2: Streamwise velocity fluctuation in a plane $y = 0.7$ or $y^+ = 10$, contours at -0.05 (dashed) and 0.05.

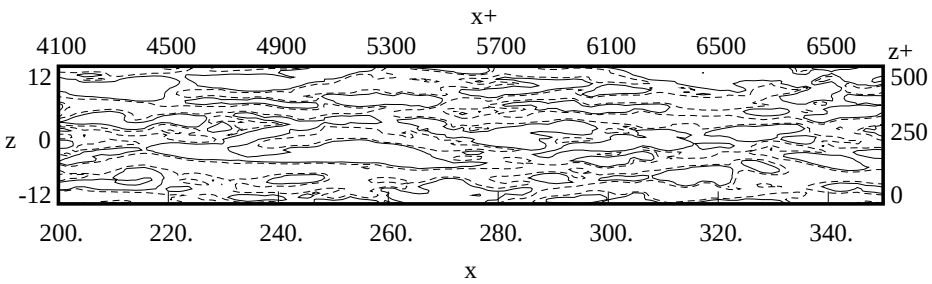

FIGURE 5. ZPG: Streamwise velocity fluctuation in a plane $y = 0.5$ or $y^+ = 10$, contours at -0.05 (dashed) and 0.05.

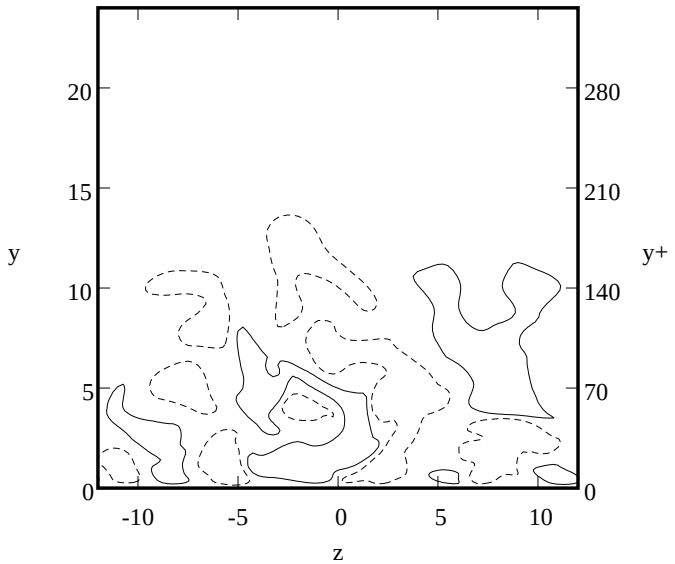

FIGURE 6. APG2: Streamwise velocity fluctuation in a plane $x = 280$, contours at -0.05 (dashed) and 0.05.

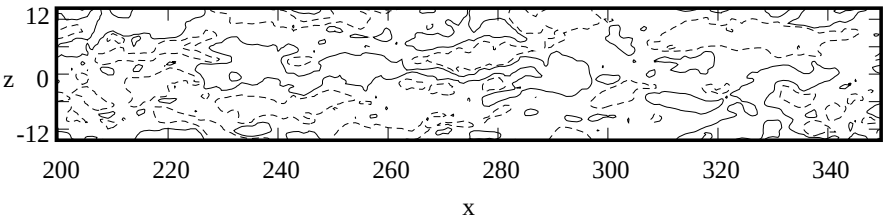

FIGURE 7. APG2: Streamwise velocity fluctuation in a plane $y = 4$ or $\eta = 0.6$, contours at -0.05 (dashed) and 0.05.

If plotted in a plane at $y = 4$ (Figure 7) it can be seen that the streaky structures in the outer part of the boundary layer are shorter and wider compared to the ones closer to the wall. The upper streaks are also present in the zero pressure gradient case and are not a consequence of the adverse pressure gradient, but they are intensified by the pressure gradient and can be related to the outer maximum observed in the turbulent kinetic energy and turbulent production. This observation is further discussed in section 4.3.2. Comparing Figures 4 and 5 the streaks close to the wall also become shorter for stronger adverse pressure gradients. In the DNS of Spalart & Leonard (1987) for a turbulent boundary layer near separation the streaks have become so thick and short that they are instead aligned in the spanwise direction. A part of the computational box is shown in Figure 8 for the APG2 case. The color bar indicates the streamwise disturbance velocity. The contour plots are at the blue level of -0.08. Notice the long streaks close to the wall and the shorter streaks located in the upper part of the boundary layer.

4.2. *Mean flow characteristics*

4.2.1. *Self-similarity*

The β-parameter is shown for the two APG cases in Figure 9a, and H as a function of Re_Θ for all three cases in Figure 9b. The β-parameter is close to constant and the shape factor varies slowly, particularly for the higher adverse pressure gradient. As seen in Figure 10 the Clauser parameter, G (equation 17), is about 7.6 for APG1 and varies between 8.0 and 8.3 for APG2 (further discussed in section 4.4.1). Thus we can conclude that the simulations fulfill the requirements for self-similarity reasonably well. In Figure 11 the skin friction, C_f, is shown together with the freestream velocity. C_f is lower for higher pressure gradients and would become zero at separation. Note that the figures showing β and C_f include the small laminar state and the transitional region.

The velocity profiles from the two present simulations are compared with Spalart's ZPG case (Spalart 1988) at almost the same Reynolds number $Re_\Theta = 670$ in Figure 12. There is a small shift downward of the logarithmic part, but

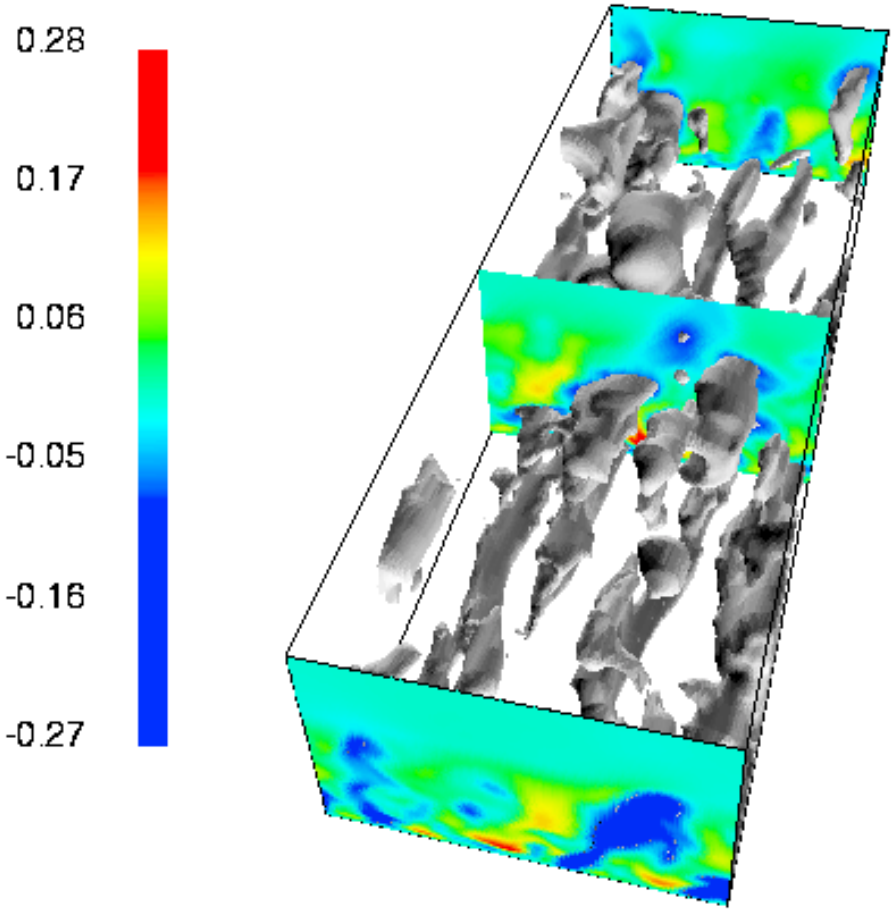

FIGURE 8. APG2: Streamwise velocity fluctuations. The color bar indicates the streamwise disturbance velocity. The level of the contour plot is -0.08. The streamwise direction is upward in the figure. The extension of the box is x=246—319, y=0—15, z=-12—12.

the log-region is too small to draw any conclusions about the effect of the adverse pressure gradient on the log-law.

As the β-parameter is constant we might expect a self-similar boundary layer. From the velocity profiles in the outer scaling at positions downstream (Figure 13b), it is difficult to draw any conclusions about self-similarity in the outer part of the boundary layer since the Reynolds number variation is small. In the inner scaling, the self-similarity is very clear since the velocity profiles collapse in the inner part as seen in Figure 13a.

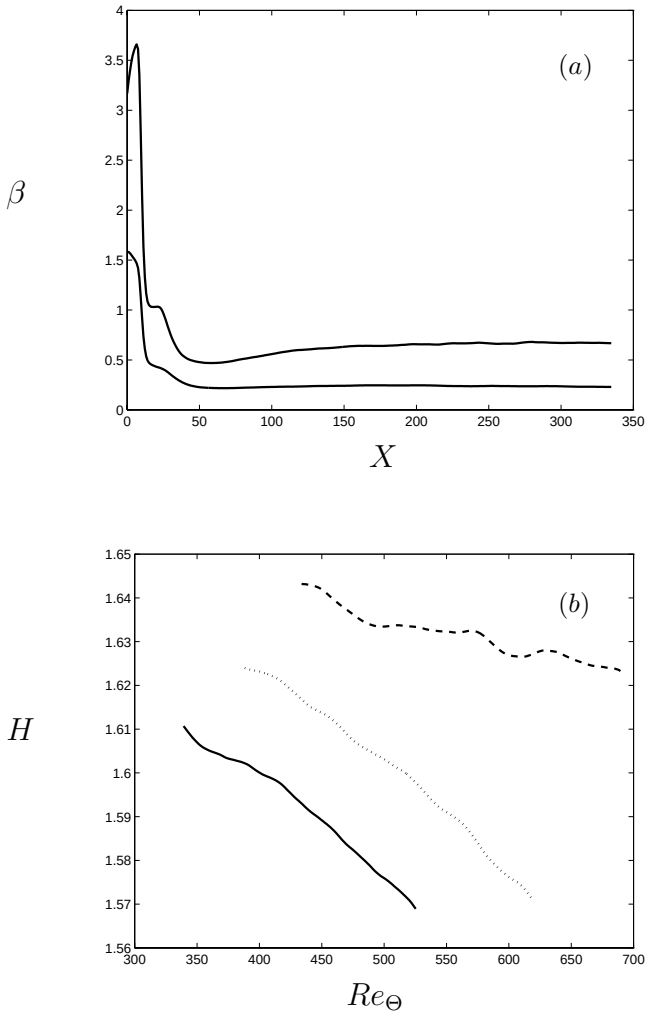

FIGURE 9. (a) β for the two APG cases. (b) H. — ZPG; $\cdots$ APG1; - - APG2.

4.2.2. *Separation prediction*

In Table 2 we have compiled data from the present simulations, together with data from existing experiments and numerical simulations. The relationship between β and m obtained from the linear, equation (13), and non-linear, equation (27), theories are evaluated. The overall conclusion from the table is that the relation from the non-linear analysis is in much better agreement with the measured and simulated cases than the linearized relation. It should be noted that the considered cases have widely different Reynolds numbers.

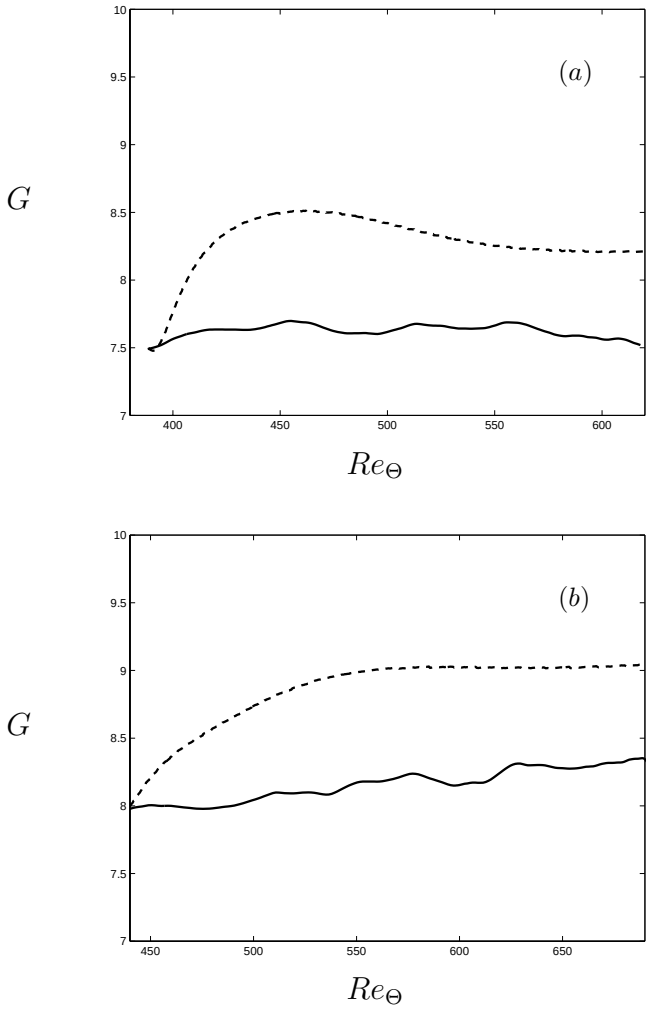

FIGURE 10. (a) G for APG1. (b) G for APG2. — DNS; - - DRSM.

The first two cases are the simulations presented here. The non-linear relation is in better agreement for the stronger pressure gradient (APG2). This might be explained from Figure 9b where the shape factor is closer to a constant in APG2 than APG1. Bradshaw's two measurements (Bradshaw 1967) are shown next, where a better agreement is obtained for the stronger pressure gradient. Skåre & Krogstad (1994) performed experiments on turbulent boundary layers near separation. The agreement with the non-linear relation is excellent while the linear counterpart does not agree. We also see that the shape factor is about two and not one as the linear analysis requires. The data from the measurements by Stratford (1959*a*) of a turbulent boundary layer near

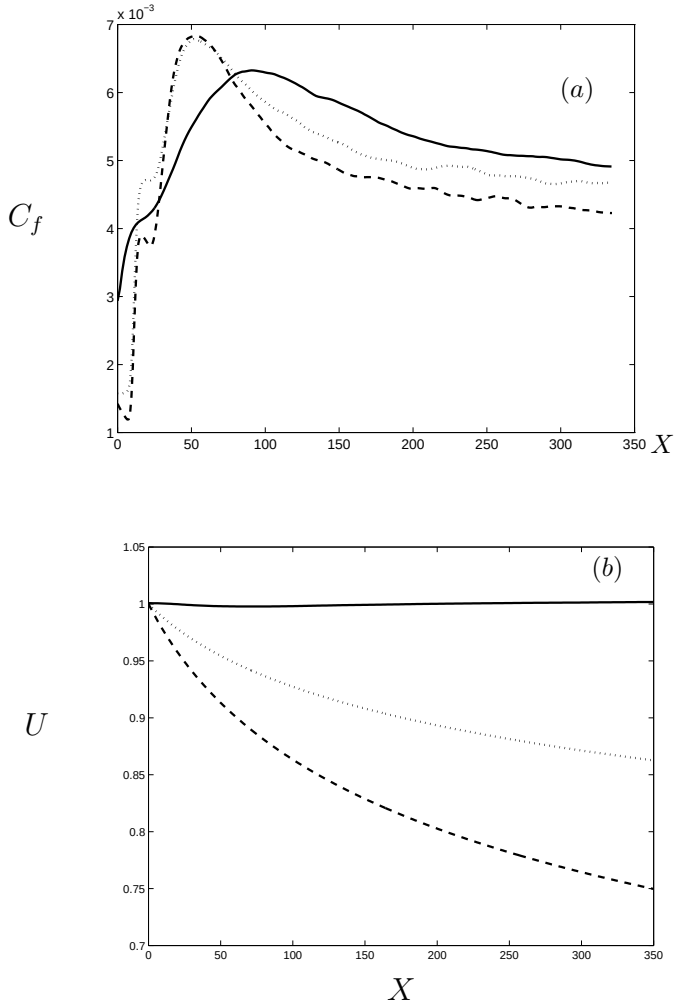

FIGURE 11. (a) C_f. (b) U. — ZPG; $\cdots$ APG1; - - APG2.

separation lead to the same conclusions as the previous case. The last five cases are from the DNS of Spalart & Leonard (1987). The agreement is good for all these cases, the first two are equivalent to the measurements by Clauser (1954), and the third one is near separation. These simulations were performed using a similarity coordinate system which permitted temporal simulations of spatially developing boundary layer. They also performed simulations of Bradshaw's two cases by using the same value of β. The first case corresponds closely to our APG2. The Reynolds number based on the displacement thickness is the same in their simulation as at the end of our spatial simulation. Their value of the shape factor is lower than ours, and m is more negative.

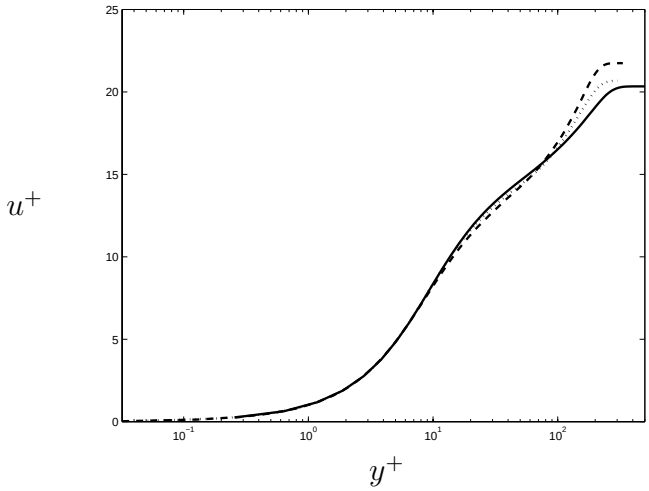

FIGURE 12. Velocity profiles in the inner scaling for — Spalart; $\cdots$ APG1; - - APG2.

Case	β	H	m	$m = -\frac{\beta}{H(1+\beta)+2\beta}$	$m = -\frac{\beta}{1+3\beta}$
APG1	0.24	1.60	-0.077	-0.097	-0.14
APG2	0.65	1.63	-0.15	-0.16	-0.22
Bradshaw 1	0.9	1.4	-0.15	-0.20	-0.24
Bradshaw 2	5.4	1.54	-0.255	-0.26	-0.31
Skåre & Krogstad	20.0	2.0	-0.22	-0.24	-0.33
Stratford	∞	2.5	-0.23	-0.22	-0.33
Spalart & Leonard	1.8	1.65	-0.21	-0.22	-0.28
	8.0	1.92	-0.23	-0.24	-0.32
	∞	2.3	-0.22	-0.23	-0.33
	0.9	1.55	-0.18	-0.19	-0.24
	5.4	1.86	-0.24	-0.24	-0.31

TABLE 2. Comparison of m from the non-linear/linear theory.

Using the linearized relation (13) gives a value of the parameter $m = -0.33$ for all three investigations of near separation in Table 2. The non-linear relation (27) reduces to $m = -1/(H + 2)$, which gives much more realistic values of m since the shape factor in the experiments is far from its asymptotic value of one in the near separation cases.

The conclusion from this comparison is that the approximation $u_\tau/U =$ const. can be used successfully if one is interested in obtaining relations between mean flow parameters at low and moderate Reynolds numbers. Even though the Reynolds number in experiments is high enough to get self-similarity, the

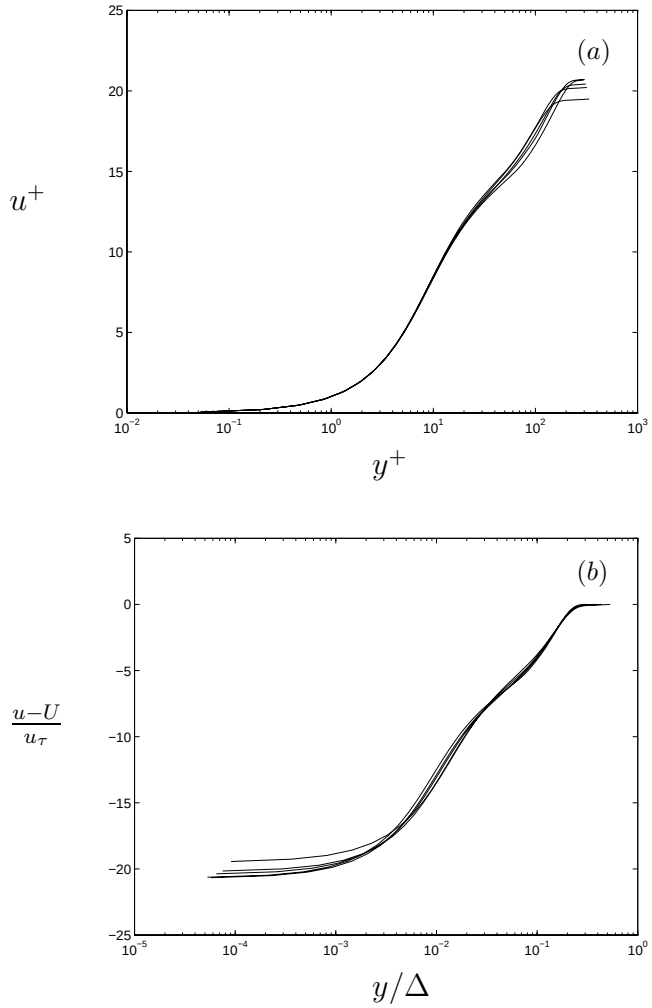

FIGURE 13. APG1: Velocity profiles for five positions downstream, starting at $x = 150$ with an increment of 50, ending at $x = 350$. (a) Inner scaling. (b) Outer scaling.

slow variation of H and thus u_τ/U makes the approximation $u_\tau/U \to 0$ unsuitable as a starting point for the analysis of the equations. This slow variation is also evident in the calculations with turbulence models, which will be described later.

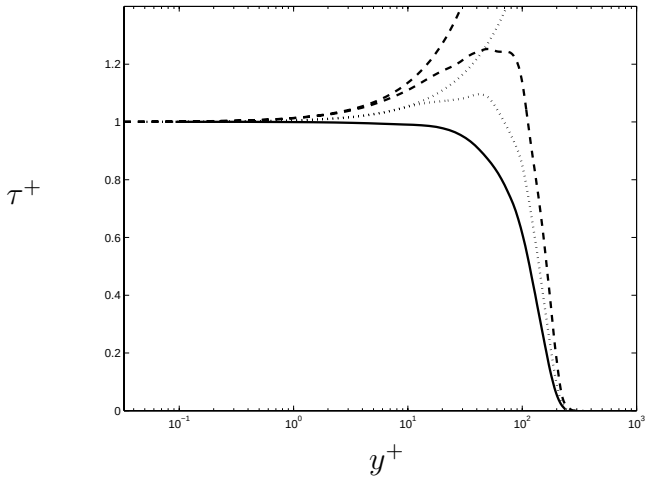

FIGURE 14. Shear stress. — ZPG; ··· APG1; - - APG2. Shear stress evaluated from equation (40) diverges, whereas the total shear stress from DNS approaches zero for large y^+.

4.3. *Higher order statistics*

4.3.1. *Scalings in the inner part of the boundary layer*

The equations governing the inner part of an adverse pressure gradient boundary layer are the continuity equation (1) and the momentum equation (2) with the non-linear, advective terms neglected, i.e.

$$0 = -\frac{1}{\rho}\frac{dP}{dx} + \nu\frac{\partial^2 u}{\partial y^2} - \frac{\partial}{\partial y}\langle u'v'\rangle. \tag{37}$$

When using the inner length and velocity scales ν/u_τ and u_τ respectively, equation (37) can be written as

$$0 = -\frac{\beta}{Re_*} + \frac{\partial^2 u^+}{\partial y^{+^2}} - \frac{\partial}{\partial y^+}\langle u'v'\rangle^+, \tag{38}$$

where $Re_* = (u_\tau\delta^*)/\nu$. If the ratio β/Re_* is smaller than the other terms, the equation reduces to the same one that governs the inner part of a ZPG boundary layer. However, for APG cases at low Reynolds numbers or close to separation this term cannot be neglected. Equation (38) can be written as

$$\frac{\partial}{\partial y^+}\left(\frac{\partial u^+}{\partial y^+} - \langle u'v'\rangle^+\right) = \frac{\beta}{Re_*} = \frac{\nu}{u_\tau^3}\frac{1}{\rho}\frac{dP}{dx} \tag{39}$$

and after integration, one finds the following expression for the total shear stress

$$\tau^+ \equiv \frac{\partial u^+}{\partial y^+} - \langle u'v'\rangle^+ = 1 + \frac{\nu}{u_\tau^3}\frac{1}{\rho}\frac{dP}{dx}y^+. \tag{40}$$

The total shear stress, τ^+, from the DNS and the curves $\tau^+(y^+)$ represented by equation (40) are shown in Figure 14. The term

$$\frac{\beta}{Re_*} = \frac{\nu}{u_\tau^3}\frac{1}{\rho}\frac{dP}{dx} \tag{41}$$

is evidently important for the shear stress distribution in the inner part of the boundary layer at low Reynolds numbers. If we define a new velocity scale,

$$u_p = \left(\nu\frac{1}{\rho}\frac{dP}{dx}\right)^{1/3}, \tag{42}$$

the term (41) can be written as

$$\frac{\beta}{Re_*} = \left(\frac{u_p}{u_\tau}\right)^3. \tag{43}$$

One might expect that it is the magnitude of the ratio between the two velocity scales u_p and u_τ that determines which one to use in the scaling of equation (37). If u_p and ν/u_p are used as the velocity and length scales respectively, the integrated version of equation (37) becomes

$$\frac{\partial u^p}{\partial y^p} - \langle u'v'\rangle^p = y^p + \left(\frac{u_\tau}{u_p}\right)^2. \tag{44}$$

If $u_\tau \ll u_p$, i.e. the boundary layer is close to separation, the scalings based on u_p should be used, but for the APG cases considered here, u_τ is the proper scaling, which is evident from Figure 13a, where the velocity profiles for downstream positions are shown. The profiles collapse on the curve $u^+ = y^+$ in the viscous sub-layer, which is consistent with equation (40), which reduces to

$$\frac{\partial u^+}{\partial y^+} = 1 \tag{45}$$

when $y^+ \to 0$.

When multiplying equation (40) by $\partial u^+/\partial y^+$ we get the mean energy budget.

$$\left(\frac{\partial u^+}{\partial y^+}\right)^2 - \langle u'v'\rangle^+\frac{\partial u^+}{\partial y^+} = \frac{\partial u^+}{\partial y^+} + \frac{\beta}{Re_*}y^+\frac{\partial u^+}{\partial y^+}. \tag{46}$$

The same equation is obtained if equation (38) is multiplied by u^+. The terms are noted from left to right: direct dissipation, production, transport and pressure gradient term. The mean budget for the APG2 case in the inner region is shown in Figure 15a. The largest contribution in the near wall region comes from the direct dissipation which is balanced by the transport term. At $y^+ = 5$ the pressure gradient term has reached its maximum and then stays constant. The production of turbulent energy has its maximum at $y^+ = 9$ where the production and direct dissipation are equal in magnitude. All the terms balance each other, though the total sum deviates from zero at large values of y^+. If the advective terms also are included in the total budget, the sum becomes zero but these terms are small compared to the others.

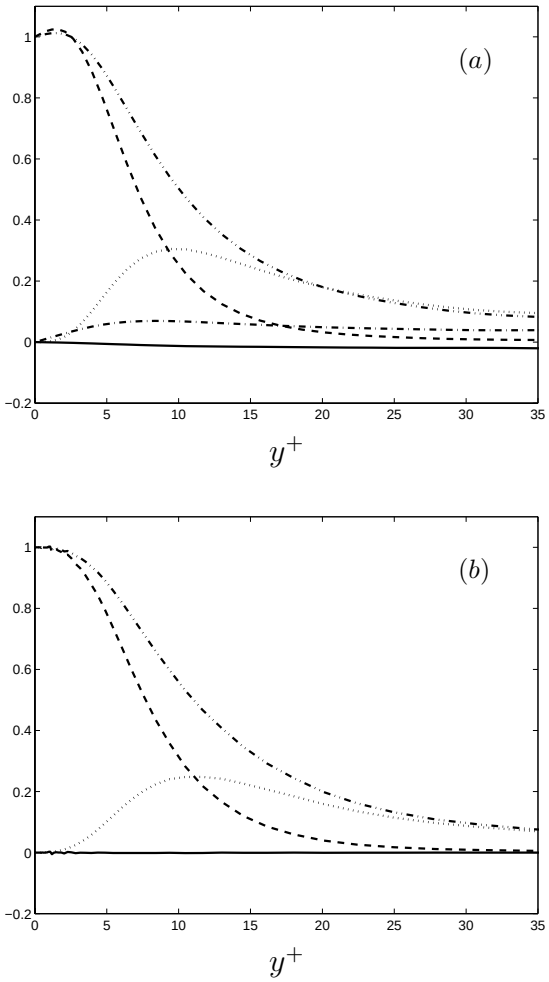

FIGURE 15. Energy budget for DNS: - - Dissipation; ⋯ Production; - ⋯ - Transport; - ⋯ - Pressure gradient term; — Total. (a) DNS. (b) DRSM, asymptotic.

The same energy budget but for the DRSM prediction is almost identical. More interesting is to look at the budget for the high Reynolds number case, which is shown in Figure 15b. Here the pressure gradient term has vanished from the budget. This is due to the term $1/Re_*$ in the pressure gradient term in equation (46). The sum of the terms is zero which implies that the advective terms no longer has any influence on the inner layer.

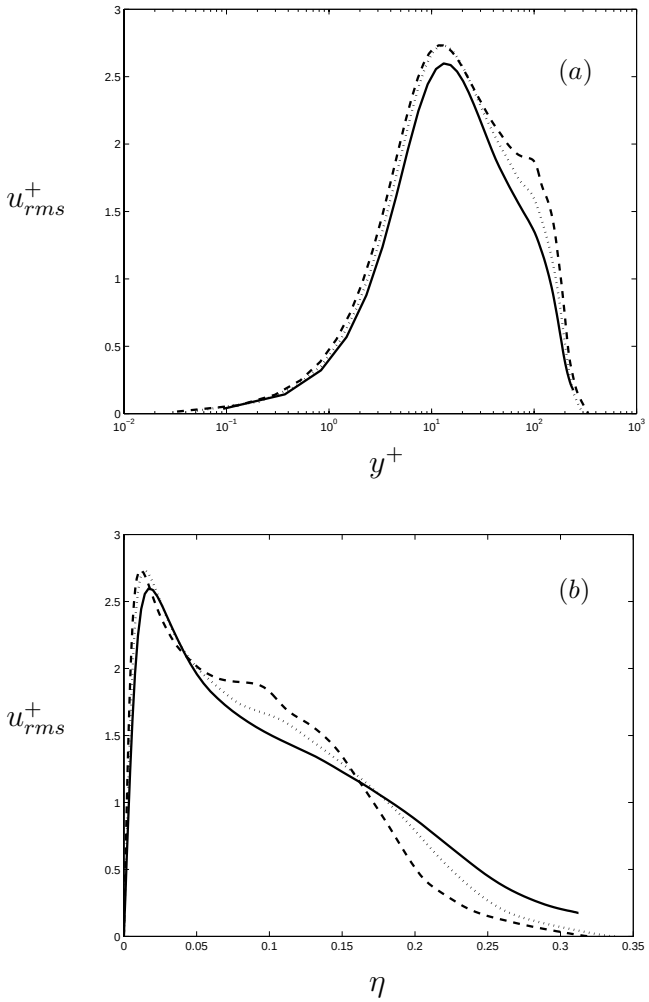

FIGURE 16. u^+_{rms} at $x = 300$. — ZPG; $\cdots$ APG1; - - APG2. (a) Inner scaling. (b) Outer scaling.

4.3.2. *The Reynolds stresses and turbulent production*

In Figure 16 u_{rms} for the ZPG/APG cases are shown in inner and outer scaling for the same streamwise station. There is only a slight difference between the cases in the inner region but in the outer region the tendency towards a second peak in the u_{rms} profile for the highest pressure gradient marks a clear difference. This outer maximum has been observed in a number of experimental studies, such as Bradshaw (1967), Samuel & Joubert (1974), Nagano *et al.* (1992) and Skåre & Krogstad (1994). The production term in the turbulent energy budget also has an outer peak for the higher pressure gradient case, as

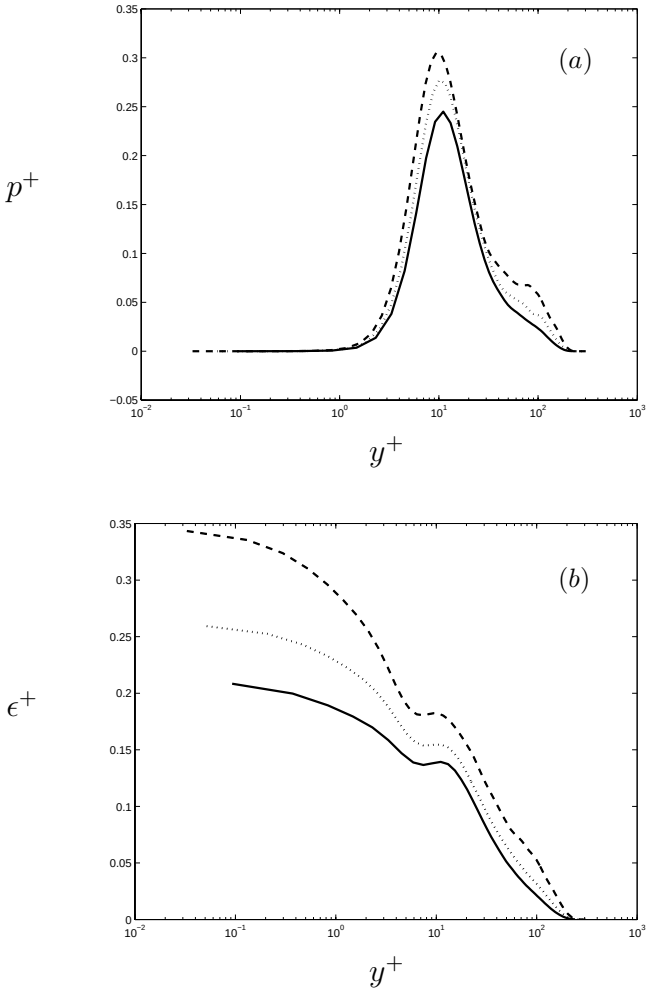

FIGURE 17. (a) Production at $x = 300$. (b) Dissipation at $x = 300$. — ZPG; $\cdots$ APG1; - - APG2.

seen in Figure 17a. These outer peaks in the turbulent energy and production might be related to the enhanced streak formation in the outer part of the boundary described in section 4.1. There are no outer peaks in the v_{rms} and w_{rms} profiles.

The location of the inner maximum of the production can be motivated by the form of the near-wall limit of the turbulent boundary layer equations. The integrated inner equation for the ZPG case can be written as

$$-\langle u'v'\rangle^+ = 1 - \frac{\partial u^+}{\partial y^+}. \tag{47}$$

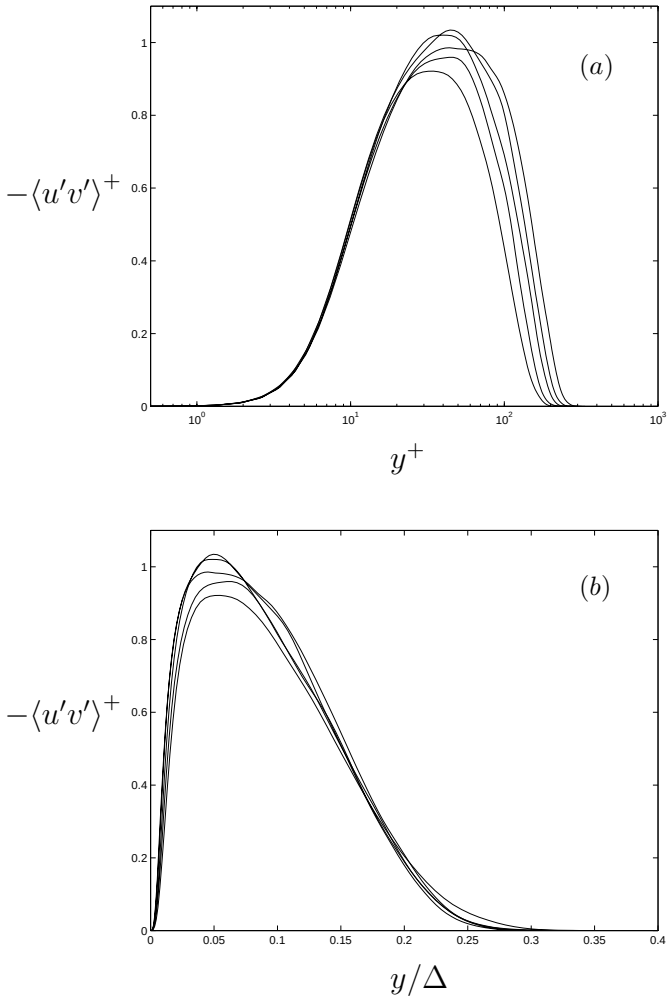

FIGURE 18. APG1: Reynolds shear stress profiles for five positions downstream, starting at $x = 150$ with an increment of 50, ending at $x = 350$. (a) Inner scaling. (b) Outer scaling.

When used in the expression for the turbulent production

$$p^+ = -\langle u'v'\rangle^+ \frac{\partial u^+}{\partial y^+}, \tag{48}$$

this yields

$$p^+ = \left(1 - \frac{\partial u^+}{\partial y^+}\right) \frac{\partial u^+}{\partial y^+}. \tag{49}$$

p^+ has a maximum of 0.25 at the position where $\partial u^+/\partial y^+ = 0.5$. The inner maximum is increased due to the pressure gradient but the position is not changed as can be seen in Figure 17a.

The dissipation is shown in Figure 17b, where an increased dissipation for higher pressure gradients is observed near the wall.

The profiles for the Reynolds stress in the outer scaling (Figure 18b) show that self-similarity is not yet obtained since the maximum grows downstream. In the inner scaling the profiles collapse as seen in Figure 18a. This non-similarity in the outer part is due to low Reynolds number, as will be more clearly understood when a comparison with model predictions is made in the next section, where also the higher order statistics from the DNS will be considered.

4.4. *Comparison with turbulence model predictions*

Henkes (1998) has tested some turbulence models for high Reynolds number self-similar APG turbulent boundary layers at high Reynolds number. All the tested models, $k-\epsilon$, $k-\omega$ and differential Reynolds stress models, give results that approach the same asymptotic scalings for the velocity and the Reynolds shear stress. However, differences occur in the scaled similarity profiles, as well as in parameters like H, G and C_f. When comparing with available experiments at moderate Reynolds numbers, the differential Reynolds stress model turns out to be superior to the others. Here we will use the Differential Reynolds Stress Model (DRSM) of Hanjalić *et al.* (1995) described in section 3.3 for both the high and low Reynolds number predictions.

4.4.1. *Low Reynolds number*

In this section calculations with the DRSM performed at low Reynolds numbers for comparison with data from our DNS (Henkes *et al.* 1997) are presented. Mean turbulent profiles for the velocities, Reynolds stresses and the dissipation from the DNS at $x = 150$ were used as initial data. Comparison was made at $x = 350$ for APG1 and $x = 335$ for APG2. At these positions the Re_Θ is approximately 620 for APG1 and 690 for APG2. The DRSM calculations show that transients are dominating in the beginning of the calculations but at the point of comparison with the DNS-data the solution is not sensitive to small changes in initial data. It was also checked that changes in the length and velocity scales of the initial data did not affect the solution at the point of comparison. Thus the comparison is meaningful since the difference between the model predictions at low and high Reynolds number are due to the dependence on the Reynolds number and not to the influence of the initial conditions.

The shape factor is shown in Figures 19a and 19b for APG1 and APG2. After the decay of the initial transients the Reynolds number dependence of the shape factor is captured by the model, although there is a slight offset in the numerical values. The comparison of the Clauser parameter G for the DNS and DRSM is shown in Figures 10a and 10b. As in the case of the shape

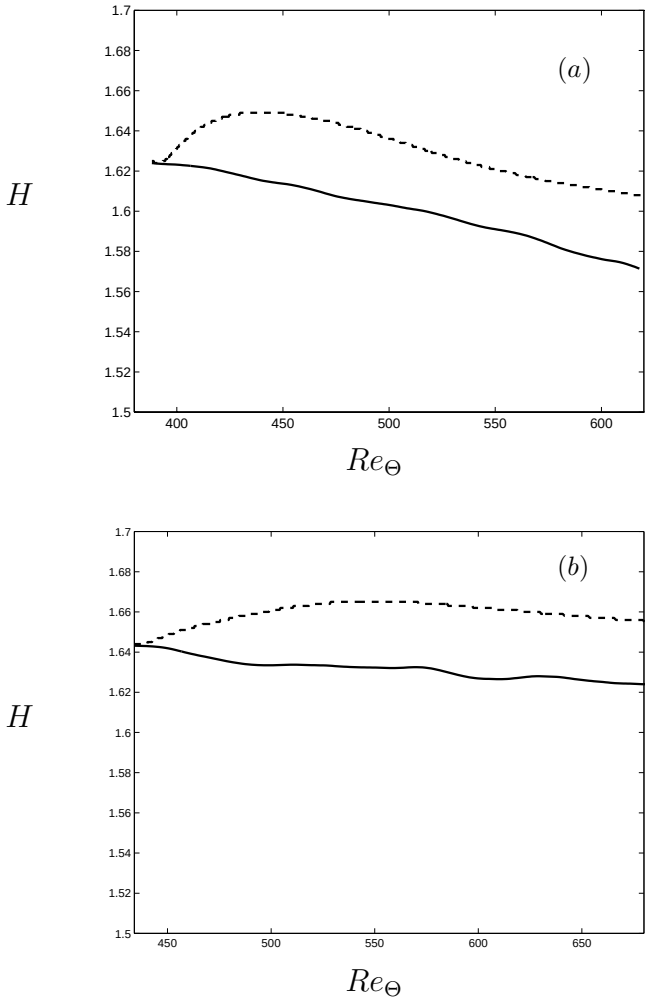

FIGURE 19. (a) H for APG1. (b) H for APG2. — DNS; - - DRSM.

factor, the Reynolds number dependence is captured after the decay of the initial transients. The profiles for the mean velocity, the Reynolds stress and u_{rms} from the model predictions are compared with the DNS data in Figures 20 to 22. Only the APG2 case is shown since here the differences between DNS and DRSM are larger than for the APG1 case. The self-similar high Reynolds number profiles according to the DRSM are also shown in these figures for comparison, but will be discussed more thoroughly in the next section.

In Figures 20a and 20b the mean velocity profiles from the DNS and DRSM are shown together with the self-similar high Reynolds number profile. At the point of comparison, only a small logarithmic part in the inner layer is found as

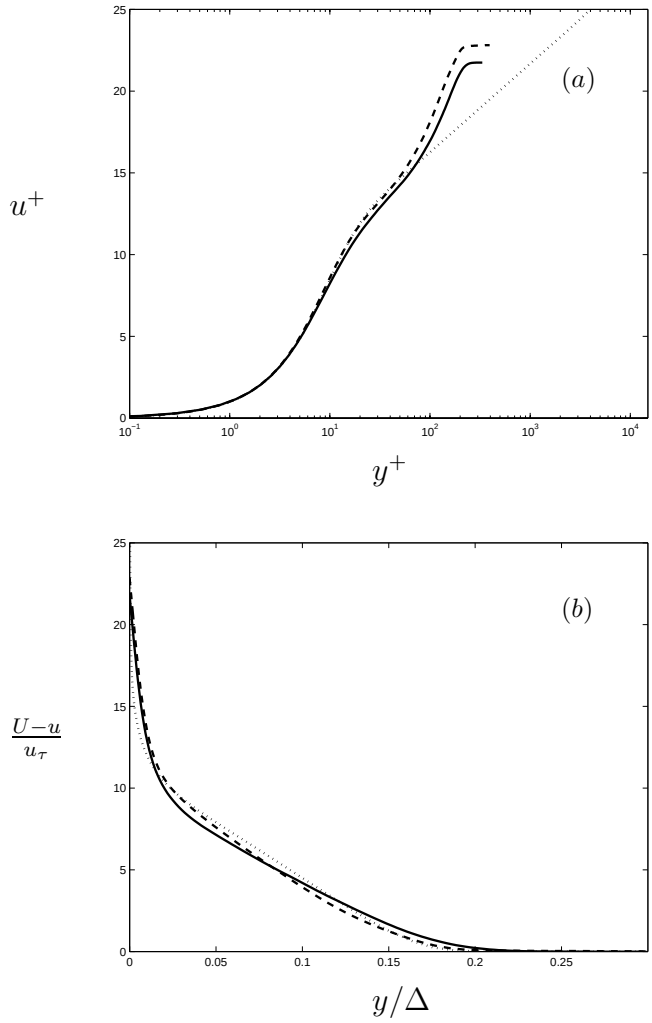

FIGURE 20. Velocity profiles for APG2. — DNS; - - DRSM; ··· Asymptotic. (a) Inner scaling. (b) Outer scaling.

seen in Figure 20a. The agreement between the DRSM and DNS in the inner part is excellent. The velocity profiles in the outer scaling do not show very large differences between the DNS, DRSM and the asymptotic DRSM profile as seen in Figure 20b. The Reynolds stress profiles in the inner and outer scalings are shown in Figures 21a and 21b. In the near wall region, the DRSM profile is in close agreement with DNS and the deviation from the asymptotic profile is well captured by the model. The plateau value of 1 seen in the asymptotic profile has not yet been developed. The peak in the profiles belongs to the outer part of the boundary layer as seen in Figure 21b and is larger in the asymptotic

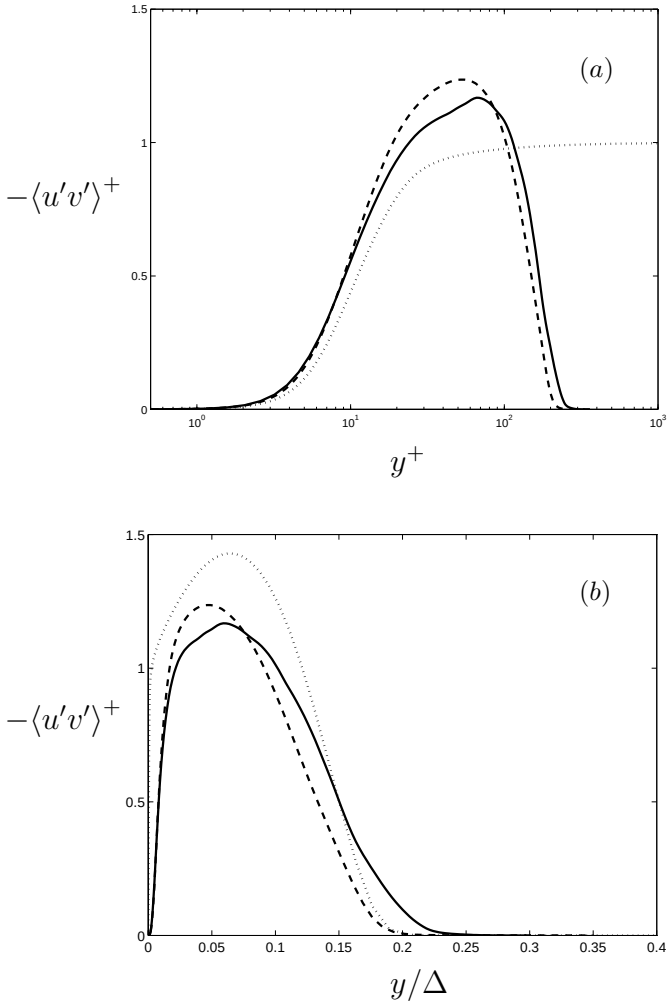

FIGURE 21. Reynolds stress for APG2.— DNS; - - DRSM; ··· Asymptotic. a) Inner scaling. b) Outer scaling.

profile. Figure 21b also reveals that the DRSM gives a profile below the DNS in the outer part of the boundary layer. The u_{rms} profiles in the inner and outer scalings are shown in Figures 22a and 22b. In the near wall region region, the profile from the DRSM is closer to the asymptotic profile than the DNS profile. The inner peak value in the asymptotic profile is lower than the peaks in the low-Re profiles. In the outer scaling, shown in Figure 22b, the DRSM profile is below the DNS profile in the same way as for the Reynolds stress profiles. The outer peak seen in the low-Re profiles is still relatively far from its value in the asymptotic DRSM profile. By comparing the inner and outer peaks in

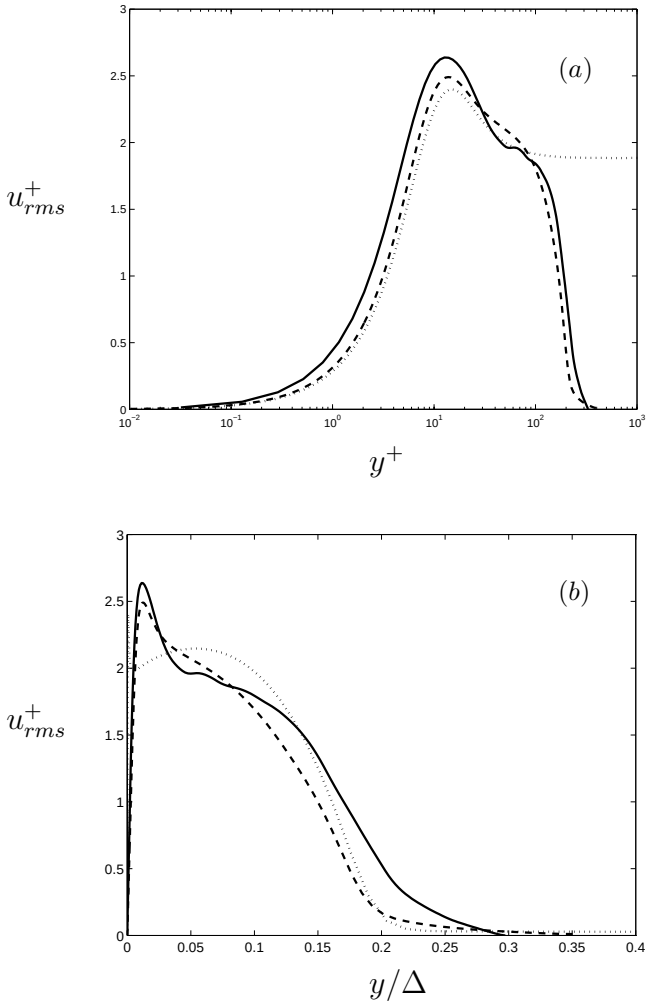

FIGURE 22. u^+_{rms} for APG2. — DNS; - - DRSM; $\cdots$ Asymptotic. a) Inner scaling. b) Outer scaling.

the u_{rms} profiles, we may conclude that turbulent energy is transfered from the inner part to the outer part of the boundary layer when the self-similar state is approached.

These results show that although differences between the DRSM solution at $Re_\theta = 690$ and the similarity solution are significant, the results with the DRSM closely agree with the DNS at $Re_\Theta = 690$. This suggests that the DRSM reproduces the physics of adverse pressure gradient boundary layers at relatively low Reynolds numbers.

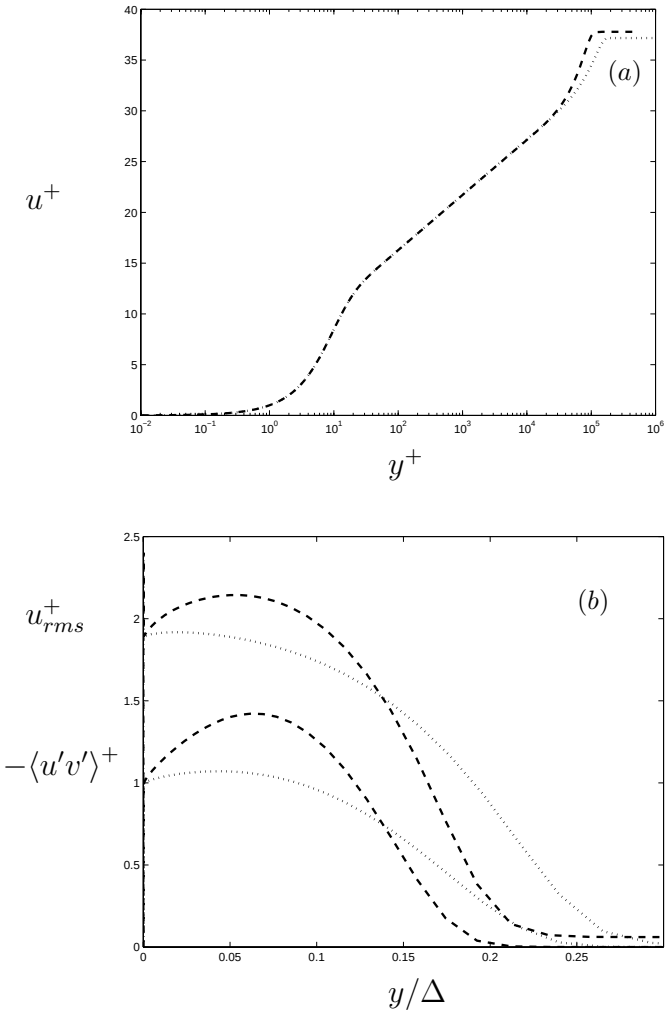

FIGURE 23. High Reynolds number profiles: a) Velocity defect. b) u^+_{rms} and $-\langle u'v' \rangle^+$. $\cdots$ APG1; - - APG2.

4.4.2. *High Reynolds number*

DRSM predictions of the two adverse pressure gradients cases, APG1 and APG2, were started at the same Reynolds number at which the DNS was performed and then continued up to very high Reynolds number. Above Re_Θ of about 10^4 the velocity and Reynolds stress profiles in the outer scaling are self-similar.

The self-similar velocity profiles in the inner scaling, (Figure 23a), show that the slope of the asymptotic profile, i.e. the Kármán constant, does not

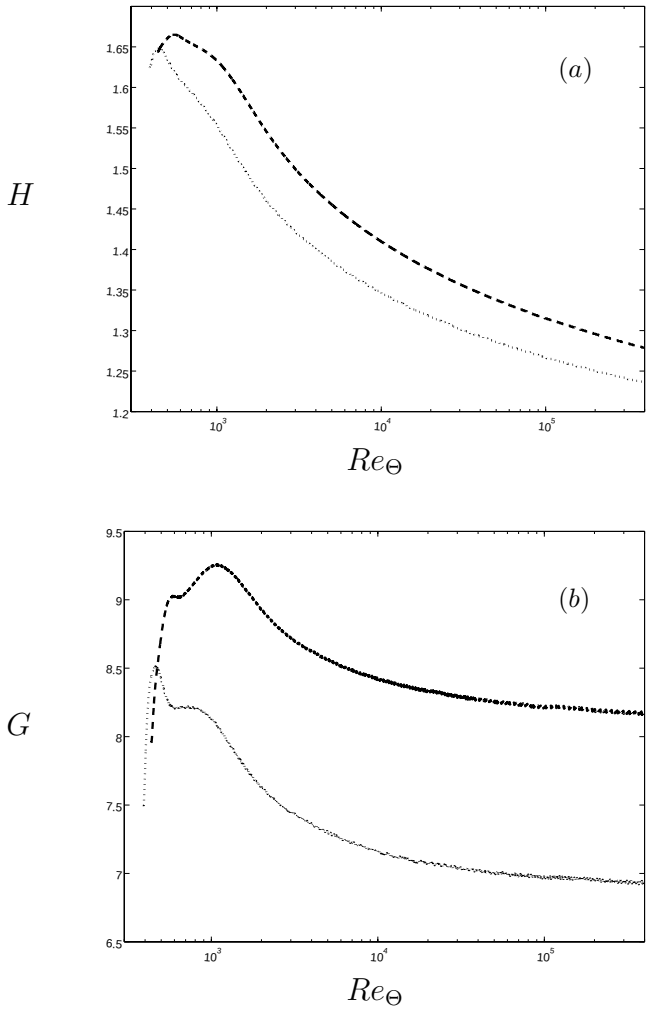

FIGURE 24. a) H. b) G. $\cdots$ APG1; - - APG2.

change with the pressure gradient. In Figure 23b the self-similar Reynolds stress and u_{rms} profiles are shown in the outer scaling. The peaks in the profiles are the outer ones. The inner peak of the u_{rms} and the plateau value of 1 for the Reynolds shear stress are not visible in the outer scaling. Compare with the Figures 21 and 22 where the asymptotic profiles are shown in both the inner and outer scalings. It is only for the APG2 case that the outer peak in the u_{rms} profile appears. Apparently the adverse pressure gradient in APG1 is too weak for an outer peak to develop. The asymptotic behavior of H and G are shown in Figures 24a and 24b. H should approach 1 and G a constant value at infinite Re. The figures show that the asymptotic values and therefore complete

self-similarity are far from being reached although the Reynolds number is very large. The values are further from the asymptotic values for APG2 than for APG1.

From the mean velocity and Reynolds stress profiles one might conclude that self-similarity is obtained, but the downstream variation of H and G show that the asymptotic state of the flow is very slowly approached. In the experiments by Skåre & Krogstad (1994) the results were interpreted as self-similarity although the constant shape factor was far from the asymptotic value. These experiments were performed at Re_Θ between 10^4 and 10^5, and the results can be explained by the high Reynolds number behavior of the velocity profile and the shape factor which appear to be constant if the Reynolds number is not varied enough. The slow variation of mean flow parameters was also utilized to derive the mean flow relations in section 2.2.

5. Summary and Conclusions

DNS of the Navier-Stokes equations has been carried out with the objective of studying APG turbulent boundary layers. The pressure gradient parameter is found to be constant when the freestream velocity varies according to a power law, which has also been shown to follow from the turbulent boundary layer equations. To relate the exponent in the power law to the pressure gradient parameter, an analysis based on the assumption of asymptotically high Reynolds number was first reviewed. The assumption implies that the ratio of the friction velocity to the freestream velocity is zero. This is obtained from the logarithmic friction law and the matching of inner and outer solution of the mean turbulent boundary layer equations. Another consequence of the assumption is that the shape factor becomes one, which is equivalent to a linearization of the velocity defect. The mean turbulent flow was investigated with a differential Reynolds stress model for high Reynolds numbers. These investigations showed that even at very high Reynolds number the asymptotic value for the shape factor is still far from being obtained although a self-similar state of the velocity and Reynolds shear stress profiles has been reached. This is also evident from a number of experiments and can also be related to the fact that the logarithmic function increases slowly when the argument is large. These observations motivated a different approach to the analysis of the mean turbulent boundary layer equations.

A non-linear analysis of the equations describing the mean flow based on the approximation of a constant ratio of the freestream velocity to the friction velocity was presented. The analysis leads to a relation for the power law, in which both the pressure gradient parameter and the shape factor appear. This relation gives better agreement with available numerical and physical experiments than the linearized analysis. It was shown that the agreement is better over a range of different Reynolds numbers, particularly regarding the parameters for which separation occurs. The relation from the linearized, asymptotic

analysis is recovered from the new relation obtained from the less restricted analysis by letting the shape factor become one.

Comparison of turbulent statistics from the ZPG and the two APG cases shows the development of a second peak in the turbulent energy in agreement with experiment. The analysis of the inner equations and investigation of the behavior of the total shear stress showed that the pressure gradient parameter is also important in the inner layer at the low Reynolds number flows performed with DNS. The Reynolds shear stress profiles showed no self-similar state although the pressure gradient parameter was constant. This is due to low Reynolds number effects and motivated the use of model predictions to first try to reproduce the low Reynolds number effects and then increase the Reynolds number as to obtain the self-similar state.

The differential Reynolds stress model was used to predict the mean flow at the same low Reynolds number as the DNS. Initial data for the model predictions were taken from the DNS at the lowest Reynolds number where fully developed turbulence was obtained. After the decay of some small initial transients the Reynolds number dependence of mean flow parameters such as the shape factor and Clauser parameter, was captured by the model. Comparison with data from DNS at the highest Reynolds number obtained, showed that low Reynolds number effects are well captured by the model. The model predictions could be continued up to high Reynolds numbers to obtain self-similarity. By comparing the profiles at low and high Reynolds numbers, the lack of self-similarity in the Reynolds stress profiles in the DNS could thus be attributed to effects of low Reynolds number.

Acknowledgments

This work was sponsored by the Swedish National Board for Industrial and Technical Development (NUTEK).

Appendix A.

The two-dimensional boundary layer equations for the Differential Reynolds Stress Model of Hanjalić *et al.* (1995) are:

Conservation of mass:

$$\frac{\partial u}{\partial x} + \frac{\partial v}{\partial y} = 0. \tag{50}$$

Conservation of momentum:

$$u\frac{\partial u}{\partial x} + v\frac{\partial u}{\partial y} = -\frac{1}{\rho}\frac{dP}{dx} + \nu\frac{\partial^2 u}{\partial y^2} - \frac{\partial}{\partial y}\langle u'v'\rangle. \tag{51}$$

Equation for the Reynolds shear stress:

$$u\frac{\partial\langle u'v'\rangle}{\partial x}+v\frac{\partial\langle u'v'\rangle}{\partial y}=\frac{\partial}{\partial y}\left[\left(\nu+C_s\frac{k}{\epsilon}\langle v'^2\rangle\right)\frac{\partial\langle u'v'\rangle}{\partial y}\right]+P_{12}+\Phi_{12}-\epsilon_{12}, \quad (52)$$

with

$$P_{12}=-\langle v'^2\rangle\frac{\partial u}{\partial y},$$

$$\Phi_{12}=-\left(C_1+\frac{3}{2}C_1^w f_w\right)\frac{\epsilon}{k}\langle u'v'\rangle+\left(1-\frac{3}{2}C_2^w f_w\right)C_2\langle v'^2\rangle\frac{\partial u}{\partial y},$$

$$\epsilon_{12}=\epsilon f_s\frac{\langle u'v'\rangle}{k}\frac{1+f_d}{1+\frac{3}{2}\frac{\langle v'^2\rangle}{k}f_d}.$$

Equations for the Reynolds normal stresses:

$$u\frac{\partial\langle u'^2\rangle}{\partial x}+v\frac{\partial\langle u'^2\rangle}{\partial y}=\frac{\partial}{\partial y}\left[\left(\nu+C_s\frac{k}{\epsilon}\langle v'^2\rangle\right)\frac{\partial\langle u'^2\rangle}{\partial y}\right]+P_{11}+\Phi_{11}-\epsilon_{11}, \quad (53)$$

$$u\frac{\partial\langle v'^2\rangle}{\partial x}+v\frac{\partial\langle v'^2\rangle}{\partial y}=\frac{\partial}{\partial y}\left[\left(\nu+C_s\frac{k}{\epsilon}\langle v'^2\rangle\right)\frac{\partial\langle v'^2\rangle}{\partial y}\right]+P_{22}+\Phi_{22}-\epsilon_{22}, \quad (54)$$

$$u\frac{\partial\langle w'^2\rangle}{\partial x}+v\frac{\partial\langle w'^2\rangle}{\partial y}=\frac{\partial}{\partial y}\left[\left(\nu+C_s\frac{k}{\epsilon}\langle v'^2\rangle\right)\frac{\partial\langle w'^2\rangle}{\partial y}\right]+P_{33}+\Phi_{33}-\epsilon_{33}, \quad (55)$$

with

$$P_{11}=2P_k, \qquad P_{22}=0, \qquad P_{33}=0, \qquad P_k=-\langle u'v'\rangle\frac{\partial u}{\partial y},$$

$$\Phi_{11}=-C_1\epsilon\left(\frac{\langle u'^2\rangle}{k}-\frac{2}{3}\right)+C_1^w f_w\frac{\epsilon}{k}\langle v'^2\rangle-\frac{2}{3}C_2P_k(2-C_2^w f_w),$$

$$\Phi_{22}=-C_1\epsilon\left(\frac{\langle v'^2\rangle}{k}-\frac{2}{3}\right)-2C_1^w f_w\frac{\epsilon}{k}\langle v'^2\rangle+\frac{2}{3}C_2P_k(1-2C_2^w f_w),$$

$$\Phi_{33}=-C_1\epsilon\left(\frac{\langle w'^2\rangle}{k}-\frac{2}{3}\right)+C_1^w f_w\frac{\epsilon}{k}\langle v'^2\rangle+\frac{2}{3}C_2P_k(1+C_2^w f_w),$$

$$\epsilon_{11}=\epsilon\left[\frac{2}{3}(1-f_s)+f_s\frac{\langle u'^2\rangle}{k}\frac{1}{1+\frac{3}{2}\frac{\langle v'^2\rangle}{k}f_d}\right],$$

$$\epsilon_{22} = \epsilon \left[\frac{2}{3}(1-f_s) + f_s \frac{\langle v'^2 \rangle}{k} \frac{1+3f_d}{1+\frac{3}{2}\frac{\langle v'^2 \rangle}{k} f_d} \right],$$

$$\epsilon_{33} = \epsilon \left[\frac{2}{3}(1-f_s) + f_s \frac{\langle w'^2 \rangle}{k} \frac{1}{1+\frac{3}{2}\frac{\langle v'^2 \rangle}{k} f_d} \right].$$

Equation for the turbulent kinetic energy:

$$u\frac{\partial k}{\partial x} + v\frac{\partial k}{\partial y} = \frac{\partial}{\partial y}\left[\left(\nu + C_s \frac{k}{\epsilon}\langle v'^2 \rangle \right) \frac{\partial k}{\partial y} \right] + P_k - \epsilon. \tag{56}$$

Equation for the dissipation rate of turbulent energy:

$$u\frac{\partial \epsilon}{\partial x} + v\frac{\partial \epsilon}{\partial y} = \frac{\partial}{\partial y}\left[\left(\nu + C_\epsilon \frac{k}{\epsilon}\langle v'^2 \rangle \right) \frac{\partial \epsilon}{\partial y} \right] + C_{\epsilon 1} f_{\epsilon 1} \frac{\epsilon}{k} P_k - C_{\epsilon 2} f_{\epsilon 2} \frac{\epsilon \tilde{\epsilon}}{k} +$$
$$+ C_{\epsilon 3} f_\mu \langle v'^2 \rangle \left(\frac{\partial^2 u}{\partial y^2} \right)^2 + S_{\epsilon 4} + S_l, \tag{57}$$

with

$$\tilde{\epsilon} = \epsilon - 2\nu \left(\frac{\partial \sqrt{k}}{\partial y} \right)^2,$$

$$S_l = \max\left\{ \left[\left(\frac{1}{C_l}\frac{\partial l}{\partial y} \right)^2 - 1 \right] \left(\frac{1}{C_l}\frac{\partial l}{\partial y} \right)^2 ; 0 \right\} \frac{\epsilon \tilde{\epsilon}}{k} A,$$

$$l = \frac{k^{3/2}}{\epsilon},$$

$$S_{\epsilon 4} = C_{\epsilon 4} \frac{\epsilon}{k} \left(\langle v'^2 \rangle - \langle u'^2 \rangle \right) \frac{\partial u}{\partial x}.$$

C_1, C_2, C_1^w, C_2^w are functions which depend on the local turbulence-based Reynolds number, $Re_t = k^2/(\nu\epsilon)$, the invariant parameter of the stress anisotropy tensor, A, and the invariant parameter of the dissipation anisotropy tensor, E.

A is defined as

$$A = 1 - \frac{9}{8}(A_2 - A_3),$$

with $A_2 = a_{ij}a_{ji}, A_3 = a_{ij}a_{jk}a_{ki}$ and $a_{ij} = \langle u_i' u_j' \rangle / k - (2/3)\delta_{ij}$.

E is defined as

$$E = 1 - \frac{9}{8}(E_2 - E_3),$$

with $E_2 = e_{ij}e_{ji}, E_3 = e_{ij}e_{jk}e_{ki}$ and $e_{ij} = \epsilon_{ij}/\epsilon - (2/3)\delta_{ij}$.

The functions in the pressure-strain correlation in the equations for the turbulent stresses are taken as

$$C_1 = C + \sqrt{A}E^2, \qquad C_2 = 0.8\sqrt{A},$$

$$C_1^w = \max\{1 - 0.7C; 0.3\}, \qquad C_2^w = \min\{A; 0.3\},$$

with

$$C = 2.5AF^{1/4}f, \qquad F = \min\{0.6; A_2\}, \qquad f = \min\left\{\left(\frac{Re_t}{150}\right)^{3/2}; 1\right\}.$$

The functions and constants in the equation for the dissipation rate are taken as

$$f_s = 1 - \sqrt{A}E^2, \qquad f_d = \frac{1}{1 + 0.1Re_t},$$
$$C_\epsilon = 0.18, \qquad C_{\epsilon 1} = 1.44, \qquad C_{\epsilon 2} = 1.92, \qquad C_{\epsilon 3} = 0.25, \qquad C_{\epsilon 4} = 2.6,$$
$$f_\mu = 1, \qquad f_{\epsilon 1} = 1, \qquad f_{\epsilon 2} = 1 - \frac{C_{\epsilon 2} - 1.4}{C_{\epsilon 2}} exp\left[-\left(\frac{Re_t}{6}\right)^2\right].$$

Finally, $C_s = 0.22$, $C_l = 2.5$ and

$$f_w = \min\left\{\frac{k^{3/2}}{C_w \epsilon y}; 1.4\right\}$$

with $C_w = 2.5$.

For further details about the various terms included in the equations above, see references Henkes (1997) and Hanjalić *et al.* (1995).

References

Bradshaw, P. 1967 The turbulent structure of equilibrium boundary layers. *J. Fluid Mech.* **29**, 625–645.

Clauser, F. H. 1954 Turbulent boundary layers in adverse pressure gradients. *J. Aero. Sci.* **21**, 91–108.

Coleman, G. N. & Spalart, P. R. 1993 Direct numerical simulation of a small separation bubble. In *Near-Wall Turbulent Flows* (eds. R. So, C. Speziale & B. Launder), pp. 227–286. Elsevier.

Durbin, P. A. & Belcher, S. E. 1992 Scaling of adverse-pressure-gradient turbulent boundary layers. *J. Fluid Mech.* **238**, 699–722.

Fernholz, H. H. & Finley, P. J. 1996 The incompressible zero-pressure-gradient turbulent boundary layer: An assessment of the data. *Prog. Aerospace Sci.* **32**, 245–311.

George, W. K. & Castillo, L. 1993 Boundary layers with pressure gradient: another look at the equilibrium boundary layer. In *Near-Wall Turbulent Flows* (eds. R. M. C. So, C. G. Speziale & B. E. Launder), pp. 901–910. Elsevier.

Hanjalić, K., Jakirlić, S. & Hadžić, I. 1995 Computation of oscillating turbulent flows at transitional *Re*-numbers. In *Turbulent Shear Flows 9* (eds. F. Durst, N. Kasagi & B. E. Launder), pp. 323–342. Springer-Verlag.

Hanjalić, K. & Launder, B. E. 1980 Sensitizing the dissipation equation to irrotational strains. *J. Fluids Eng.* **102**, 34–40.

Head, M. R. 1976 Equilibrium and near-equilibrium turbulent boundary layers. *J. Fluid Mech.* **73**, 1–8.

Henkes, R. A. W. M. 1997 Comparison of turbulence models for attached boundary layers relevant to aeronautics. *Appl. Sci. Res.* **57**, 43–65.

Henkes, R. A. W. M. 1998 Scaling of equilibrium boundary layers under adverse pressure gradient using turbulence models. *AIAA J.* **36**, 320–326.

Henkes, R. A. W. M., Skote, M. & Henningson, D. S. 1997 Application of turbulence models to equilibrium boundary layers under adverse pressure gradient. Eleventh Symposium on Turbulent Shear Flows, Grenoble, France.

Henningson, D. S. & Lundbladh, A. 1995 Evaluation of turbulence models from direct numerical simulations of turbulent boundary layers. FFA-TN 1995-09, Aeronautical Research Institute of Sweden, Bromma.

Lundbladh, A., Henningson, D. S. & Johansson, A. V. 1992 An efficient spectral integration method for the solution of the Navier-Stokes equations. FFA-TN 1992-28, Aeronautical Research Institute of Sweden, Bromma.

Lundbladh, A., Schmid, P. J., Berlin, S. & Henningson, D. S. 1994 Simulation of bypass transition in spatially evolving flows. Proceedings of the AGARD Symposium on Application of Direct and Large Eddy Simulation to Transition and Turbulence, AGARD-CP-551.

Mellor, G. L. & Gibson, D. M. 1966 Equilibrium turbulent boundary layers. *J. Fluid Mech.* **24**, 225–253.

Na, Y. & Moin, P. 1996 Direct numerical simulation of studies of turbulent boundary layers with adverse pressure gradient and separation. *Tech. Rep.* TF-68. Thermosciences Division, Department of Mechanical Engineering, Stanford University.

Nagano, Y., Tagawa, M. & Tsuji, T. 1992 Effects of adverse pressure gradients on mean flows and turbulence statistics in a boundary layer. In *Turbulent Shear Flows 8* (eds. F. Durst, R. Friedrich, B. E. Launder, F. W. Schmitd, U. Schumann & J. H. Whitelaw), pp. 7–21. Springer-Verlag.

Nordström, J., Nordin, N. & Henningson, D. S. 1999 The fringe region technique and the fourier method used in the direct numerical simulation of spatially evolving viscous flows. *SIAM J. Sci. Comp.* **20** (4), 1365–1393.

Rotta, J. C. 1962 Turbulent boundary layers in incompressible flow. *Prog. Aerospace Sci.* **2**, 3–219.

Samuel, A. E. & Joubert, P. N. 1974 A boundary layer developing in an increasingly adverse pressure gradient. *J. Fluid Mech.* **66**, 481–505.

Schofield, W. H. 1981 Equilibrium boundary layers in moderate to strong adverse pressure gradients. *J. Fluid Mech.* **113**, 91–122.

Skåre, P. E. & Krogstad, P.-Å. 1994 A turbulent equilibrium boundary layer near separation. *J. Fluid Mech.* **272**, 319–348.

Spalart, P. R. 1988 Direct simulation of a turbulent boundary layer up to $Re_\theta = 1410$. *J. Fluid Mech.* **187**, 61–98.

Spalart, P. R. & Coleman, G. N. 1997 Numerical study of a separation bubble with heat transfer. *European J. Mechanics B/Fluids* **16**, 169.

Spalart, P. R. & Leonard, A. 1987 Direct numerical simulation of equilibrium turbulent boundary layers. In *Turbulent Shear Flows 5* (eds. F. Durst, B. E. Launder, J. L. Lumley, F. W. Schmitd & J. H. Whitelaw), pp. 234–252. Springer-Verlag.

Spalart, P. R. & Watmuff, J. H. 1993 Experimental and numerical study of a turbulent boundary layer with pressure gradients. *J. Fluid Mech.* **249**, 337–371.

Stratford, B. S. 1959*a* An experimental flow with zero skin friction throughout its region of pressure rise. *J. Fluid Mech.* **5**, 17–35.

Stratford, B. S. 1959*b* The prediction of separation of the turbulent boundary layer. *J. Fluid Mech.* **5**, 1–16.

Tennekes, H. & Lumley, J. L. 1972 *A First Course in Turbulence*. The MIT Press.

Townsend, A. A. 1960 The development of turbulent boundary layers with negligible wall stress. *J. Fluid Mech.* **8**, 143–155.

Townsend, A. A. 1976 *The Structure of Turbulent Shear Flow*. Cambridge University Press.

P2

Paper 2

Application of turbulence models to equilibrium boundary layers under adverse pressure gradient

By Ruud A. W. M. Henkes [*], Martin Skote[†] and Dan S. Henningson[†‡]

Four classes of turbulence models (algebraic, $k-\epsilon$, $k-\omega$ and a differential Reynolds-stress model) are applied to boundary layers under adverse pressure gradient with a constant equilibrium parameter $\beta = \frac{\delta^*}{\tau_w}\frac{dp}{dx}$. Numerical solutions up to $Re_\theta = 10^8$ give the classical scalings in the inner and outer layer for all models. Comparison is made with experiments of Clauser at $\beta \approx 2$ and 8 and with recent experiments by Skåre and Krogstad at $\beta = 20$. We have also performed new direct numerical simulations at $\beta \approx 0.25$ and 0.65 up to $Re_\theta = 700$. The differential Reynolds-stress model shows the best agreement with the experiments and the DNS.

1. Introduction

The present study considers the scalings according to four commonly used turbulence models for equilibrium boundary layers under an adverse pressure gradient. According to Clauser (1954), the boundary layer is in equilibrium if the parameter $\beta = \frac{\delta^*}{\tau_w}\frac{dp}{dx}$ is independent of the streamwise position. The scalings are derived from the turbulence models without making any additional a priori assumptions, which means that the scalings follow from the straightforward numerical solution of the boundary-layer equations. Computations are made up to the very large Reynolds number of $Re_\theta \approx 10^8$, which is sufficient for the similarity scalings to appear. A strong grid refinement was applied close to the wall. By doubling the number of grid points, the solutions were verified to be numerically accurate.

The classical theory, which is mainly due to Clauser (1954) and Coles (1956), finds that the boundary layer can be split up in an inner layer (wall

[*]Faculty of Aerospace Engineering, Delft University of Technology, Kluyverweg 1, 2629 HS Delft, The Netherlands. Present address: Shell Research and Technology Centre Amsterdam, P.O. Box 3003, 1003 AA Amsterdam, The Netherlands

[†]Department of Mechanics, Royal Institute of Technology (KTH), SE-100 44 Stockholm, Sweden

[‡]Aeronautical Research Institute of Sweden (FFA), Box 11021, SE-161 11 Bromma, Sweden

function), with length scale ν/u_τ and velocity scale u_τ, and an outer layer (defect layer), with the velocity scale u_τ and the length scale $\Delta = \delta^* U/u_\tau$ (where U denotes the local free-stream velocity).

The results for the turbulence models are compared with experiments at moderate Reynolds numbers ($Re_\theta = 10^4$ to 10^5) for $\beta \approx 2$ and 8, obtained by Clauser (1954), and with more recent experiments at $\beta = 20$, being close to separation, due to Skåre (1994) and Skåre & Krogstad (1994). Furthermore, the results with the turbulence models are also compared with new direct numerical simulations for $\beta \approx 0.25$ and 0.65 up to $Re_\theta \approx 700$, which we performed with a spectral code.

2. Scaling analysis

To derive the scalings of the boundary layer under an adverse pressure gradient one can start from the turbulent boundary-layer equations for an incompressible flow, which read

$$\frac{\partial u}{\partial x} + \frac{\partial v}{\partial y} = 0, \tag{1}$$

$$u\frac{\partial u}{\partial x} + v\frac{\partial u}{\partial y} = -\frac{1}{\rho}\frac{dp}{dx} + \nu\frac{\partial^2 u}{\partial y^2} - \frac{\partial}{\partial y}\overline{u'v'}. \tag{2}$$

Here x and y are the coordinates along and normal to the wall, respectively; u and v are the corresponding velocity components; p is the pressure; ρ is the density; ν is the kinematic viscosity; and $-\overline{u'v'}$ is the Reynolds shear stress.

According to the classical theory, the velocity scale in both the inner and outer layer is the same, namely u_τ, which is the wall-shear stress velocity $(\tau_w/\rho)^{1/2}$, with τ_w being the wall-shear stress $\mu(\partial u/\partial y)_w$. The length scale differs, and is ν/u_τ for the inner layer and $\Delta = \delta^* U/u_\tau$ for the outer layer; δ^* is the displacement thickness, and U is the local outer-edge velocity. Tennekes & Lumley (1972) and Wilcox (1993) have derived a so-called defect-layer equation, which is the equation that describes the similarity solution in the outer layer. There is, however, a striking difference between the derivations of Tennekes & Lumley and Wilcox. We have reconsidered the analysis (for more details see Henkes, 1998) and find agreement with the results by Tennekes & Lumley.

When it is assumed that molecular diffusion can be neglected in the outer layer, the boundary-layer equations (1)-(2) can be transformed into

$$(\beta - 2\omega)f + \gamma f^2 + (\alpha - 2\beta - 2\omega)\eta f' - \chi f' \int_0^\eta f\,d\eta = r', \tag{3}$$

with

$$\alpha = \left(\frac{U}{u_\tau}\right)^2 \frac{d\delta^*}{dx},\ \beta = \frac{\delta^*}{\tau_w}\frac{dp}{dx}, \tag{4}$$

$$\omega = \frac{1}{2}\frac{\delta^*}{u_\tau}\left(\frac{U}{u_\tau}\right)^2 \frac{du_\tau}{dx},$$

$$\gamma = \frac{U}{u_\tau}\frac{\delta^*}{u_\tau}\frac{du_\tau}{dx},\ \chi = \frac{U}{u_\tau}\frac{d\delta^*}{dx} + \frac{\delta^*}{u_\tau}\frac{dU}{dx}.$$

Here $\eta = y/\Delta$, $f(\eta) = \dfrac{U-u}{u_\tau}$, and $r(\eta) = -\dfrac{\overline{u'v'}}{u_\tau^2}$. A prime denotes differentiation to η.

The coefficients can be developed in a series with respect to the small quantity u_τ/U (see Henkes, 1998), which gives

$$\alpha = 1 + 3\beta + (1+\beta)C^* \frac{u_\tau}{U} + ..., \tag{5}$$

$$\omega = -\frac{1}{2}\beta - \frac{1}{2\kappa}(1+2\beta)\frac{u_\tau}{U} + ...,$$

$$\gamma = -\beta\frac{u_\tau}{U} - \frac{1}{\kappa}(1+2\beta)\left(\frac{u_\tau}{U}\right)^2 + ...,$$

$$\chi = (1+2\beta)\frac{u_\tau}{U} + ...,$$

with $C^* = \int_0^\infty f^2 d\eta$, and κ is the Von Kármán constant. To leading order eq. (5) gives

$$\alpha = 1 + 3\beta,\ \omega = -\frac{1}{2}\beta,\ \gamma = \chi = 0. \tag{6}$$

Therefore, for increasing Re_θ (giving $u_\tau/U \to 0$) equation (3) converges to the following defect-layer equation for the outer layer

$$2\beta f + (1+2\beta)\eta f' = r', \tag{7}$$

with boundary conditions

$$f \to -\frac{1}{\kappa}\ln\eta + C' \text{ for } \eta \to 0, \tag{8}$$

$$f \to 0 \text{ for } \eta \to \infty,$$

and the integral restriction

$$\int_0^\infty f d\eta = 1. \tag{9}$$

The boundary condition for $\eta \to 0$ follows from matching with the logarithmic wall function, and the integral restriction follows from the conservation of momentum. Equation (7) was also obtained by Tennekes & Lumley, but Wilcox took $\omega = 0$ (instead of $\omega = -\frac{1}{2}\beta$) and thus arrived at a different equation.

3. Turbulence models

To solve the boundary-layer equations (1) and (2) or the defect-layer equation (7), a turbulence model is needed to represent the Reynolds shear stress. The following models are considered:

- Algebraic model of Cebeci & Smith (1974)
- Two-equation low-Reynolds-number $k-\epsilon$ model of Launder & Sharma (1974)
- Two-equation low-Reynolds-number $k-\omega$ model of Wilcox (1993)
- Differential Reynolds-Stress Model (DRSM) of Hanjalić *et al.* (1995)

The algebraic model uses an algebraic relation to approximate the turbulent viscosity which appears in $-\overline{u'v'} = \nu_t \dfrac{\partial u}{\partial y}$. The $k-\epsilon$ model solves differential equations for the turbulent kinetic energy and the turbulent dissipation rate ϵ to model the turbulent viscosity, whereas the $k-\omega$ model solves a differential equation for ω instead of ϵ (where ω is proportional to ϵ/k). The DRSM is the most complete model, as it solves differential equations for all Reynolds shear and normal stresses, as well as for ϵ. More details of the models are given in the cited references, and in Henkes (1997).

The boundary-layer equations are solved with a marching numerical procedure, after discretization with a second-order finite-difference scheme. A Cartesian grid is used with a very strong grid refinement in the lower part of the inner layer. To account for the growth of the boundary layer in streamwise direction, at several x positions the outer edge was increased and the y grid points were redistributed. All results presented in this paper are guaranteed to be grid independent. This was checked by doubling the number of points in x and y direction. A typical y grid consists of 200 or 400 points.

The defect-layer equation (7) only depends on the single coordinate η. This ordinary differential equation was numerically discretized with a second-order difference scheme, applying 200 or 400 points. An iteration process was used to satisfy the boundary conditions and the integral restriction.

4. Direct numerical simulations

DNS were carried out for the pressure gradients $\beta \approx 0.25$ and $\beta \approx 0.65$ with a code developed at KTH and FFA by Lundbladh *et al.* (1992, 1994). The spectral method applies Fourier modes in the horizontal directions and Chebyshev modes in the wall-normal direction. Since the boundary layer is developing in the downstream direction, the physical boundary conditions in that direction are non-periodic. To capture these with periodic Fourier modes, a fringe region is added downstream of the physical domain, where the flow is forced from the outflow of the physical domain to the inflow. In this way the physical domain and the fringe region together satisfy periodic boundary conditions. The fringe region is implemented by the addition of a volume force having a form designed to minimize the upstream influence. Time integration is performed using a third-order Runge-Kutta method for the advective and forcing terms and Crank-Nicolson for the viscous terms.

The simulations start with a laminar boundary layer at the inflow which is tripped by a random volume force near the wall. All the quantities are nondimensionalized by the free-stream velocity and the displacement thickness at the starting position of the simulation ($x = 0$) where the flow is laminar. At that position $Re_{\delta^*} = 400$. The length (including the fringe), height and width of the computational domain were $450 \times 24 \times 24$ δ^* units.

The number of modes was $480 \times 161 \times 96$, which gives a resolution in plus units of $\Delta x^+ = 16$ and $\Delta z^+ = 4.3$. The useful region was confined to

$x^* = x/\delta^* = 150 - 350$ which corresponds to Re_{δ^*} from 550 to 1200 or Re_θ from 330 to 700. The simulations were run for a total of 4500 time units (δ^*/U), and the sampling for the turbulent statistics was performed during the 2000 last time units. The good accuracy of the DNS and its statistics was verified by repeating the computation on a coarser resolution ($320 \times 101 \times 64$ modes), and with a shorter averaging time (1000 time units).

5. Large-Re behaviour

The boundary-layer equations were solved for the four turbulence models with different β values. The calculations were started at $Re_\theta = 300$, where the results from DNS by Spalart (1988) for a zero-pressure gradient were used as starting profiles. At each downstream position the outer-edge velocity was iteratively updated until the chosen β was obtained. The calculations were extended up to about $Re_\theta = 10^8$.

For all considered models the classical scalings turn out to appear for increasing Reynolds number. An example is given in Fig. 1, which shows the velocity and Reynolds-shear stress in the inner and outer layer, as obtained with the DRSM for $\beta = 1$. In the inertial sublayer, being the outer part of the inner layer, the velocity (Fig. 1a) converges to the logarithmic law-of-the-wall; the generally accepted best fit to experiments (having $\kappa = 0.41$ and $C = 5$) is shown as a long-dashed line. The velocity in the outer layer (Fig. 1b), when scaled with u_τ and Δ, converges to a single similarity profile, the so-called defect law. Only the solution for $Re_\theta = 10^3$ shows some deviation from the similarity state, but up to at least graphical accuracy no changes are found from $Re_\theta = 10^4$ on. The Reynolds shear stress in the outer part of the inner layer (Fig. 1c) approaches the wall function $-\overline{u'v'}^+ = 1$. The Reynolds shear stress in the outer layer (Fig. 1d) converges to a similarity shape, which shows a local maximum. The appearance of a maximum for the Reynolds shear stress in the outer layer (with $-\overline{u'v'}/u_\tau^2 > 1$), and also for the turbulent kinetic energy, is characteristic for adverse pressure gradient boundary layers ($\beta > 0$); such a maximum is not found for the zero pressure gradient boundary layer ($\beta = 0$). We checked that the similarity profiles for the different quantities in the inner layer are independent of β, which is in agreement with the classical theory, showing that the same wall function holds independent of the pressure gradient.

We verified that the boundary-layer solution in the outer layer converges to the similarity solution described by the defect-layer equation (7). However, the convergence rate for increasing Re_θ towards the similarity state becomes slower for increasing β. For example, for all β values the shape factor converges to $H = 1$ at $Re_\theta \to \infty$, but the shape factor at $Re_\theta = 10^8$ for $\beta = 0$, 8 and 20 still is 14%, 47%, and 71%, respectively, above its asymptotic value.

An interesting practical question is how the outer-edge velocity should be chosen to realize an equilibrium turbulent boundary layer, as represented by a certain constant β value. Bradshaw (1967) has suggested that a practically

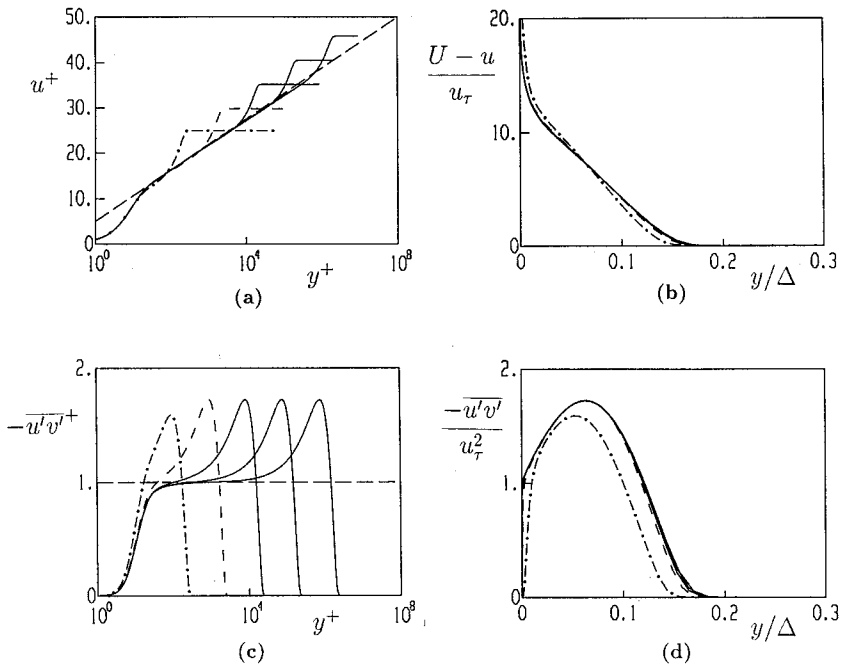

FIGURE 1. Appearance of the law-of-the-wall and the defect law for increasing Reynolds number according to the DRSM with $\beta = 1$; $Re_\theta = 10^3$ $(- \cdot -)$, 10^4 $(- -)$, 10^5, 10^6, and 10^7 (solid lines); Velocity in (a) the inner layer and (b) the outer layer; Reynolds shear stress in (c) the inner layer and (d) the outer layer. (long dash in (a) denotes the experimental wall function for the velocity, and in (c) the theoretical wall function for the Reynolds shear stress).

constant β results if the outer-edge velocity is chosen as $U \propto (x - x_o)^m$ (where x_0 is a virtual origin, and m is a constant power). To verify this we prescribed m and computed β for increasing Re_θ, but β turns out to be very sensitive to m when m comes closer to -0.25 (that is where turbulent separation is about to occur). This problem was overcome by prescribing β instead of m. Fig. 2 shows the results for the DRSM. Here the local m value is defined as $\frac{x}{U}\frac{dU}{dx}$. The turbulence model does not give a Reynolds-number independent m power for equilibrium layers; instead the power becomes slightly more negative for increasing Reynolds number.

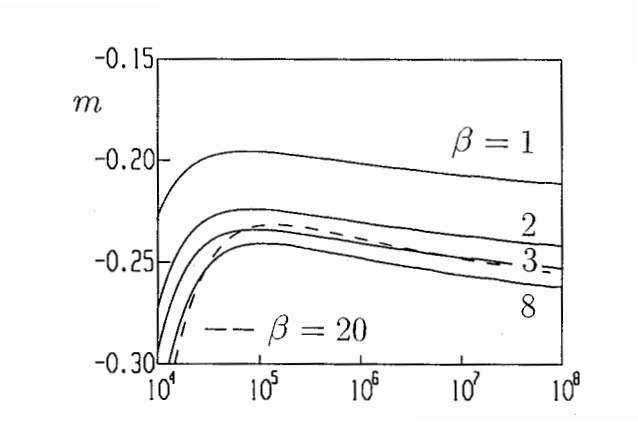

FIGURE 2. Reynolds-number dependence of the m power in the outer-edge velocity according to the DRSM.

Some authors, including Clauser (1954) (who measured $\beta \approx 2$ and 8), have reported difficulties to establish a stable flow in the windtunnel when the adverse pressure gradient becomes stronger. On the grounds of this experience, Clauser has suggested that the same outer-edge velocity (represented by the same m value) can correspond with two equilibrium boundary layers (i.e. two β values). This means that an established experimental equilibrium boundary layer can suddenly lose stability and jump to the other flow type. This is indeed what is found with the DRSM in Fig. 2. For a given Re_θ (above 10^6) the m-power decreases for β values up to about 8, above which the power increases again. For example, the m value for $\beta = 3$ is almost the same as for $\beta = 20$ (for which experiments were performed by Skåre & Krogstad, 1994). A similar nonuniqueness is found with the other turbulence models.

6. Comparison with experiments

The solution in the outer layer, as computed from the boundary-layer equations with different turbulence models, is compared with experiments in Fig. 3 for the streamwise velocity and in Fig. 4 for different turbulence quantities. The computational curves correspond to $Re_\theta = 10^6$ for $\beta = 2$ and 8, and to $Re_\theta = 5 \times 10^4$ for $\beta = 20$. All models, except for the $k - \epsilon$ model, closely predict the experimental streamwise velocity (Fig. 3); the $k - \epsilon$ model overpredicts the experimental wall-shear stress coefficient for $\beta = 20$ at $Re_\theta = 5 \times 10^4$ by 145%. The DRSM is superior, as it gives a value which is only 7% too large, whereas the algebraic model and the $k - \omega$ model give a slightly larger deviation of -15% and $+17\%$, respectively.

All models also closely reproduce the experimental Reynolds-shear stress (Fig. 4a), but the $k - \epsilon$ model somewhat overpredicts the boundary-layer thickness. The DRSM predicts the structure parameter ($= -\overline{u'v'}/k$) best (Fig. 4b), and is in fact very close to the experiments for $\beta = 20$. The DRSM also gives a quite good prediction of the Reynolds normal stresses (Fig. 4c).

With respect to the structure parameter, the experiments in Fig. 4b show that its value is almost constant, and equal to about 0.3, across most of the outer-layer thickness. This implies that the Reynolds shear stress is proportional to the turbulent kinetic energy, as was also discussed by Bradshaw (1967) on the grounds of his own experiments for a weaker adverse pressure gradient. Most turbulence models (including the $k - \epsilon$ model, the $k - \omega$ model, and the DRSM) have chosen the model constants such that the proportionality with the structure parameter 0.3 is reproduced for flows in which the production of turbulence energy P_k ($= -\overline{u'v'}\partial u/\partial y$) equals the turbulent dissipation rate ϵ. For example the $k - \epsilon$ model has $-\overline{u'v'} = \nu_t \partial u/\partial y$, with $\nu_t = c_\mu k^2/\epsilon$. As the constant c_μ is set to 0.09 this gives $-\overline{u'v'}/k = 0.3$ when $P_k = \epsilon$.

7. Comparison with DNS

The DNS were performed for the outer edge velocity $U \propto (x - x_0)^m$, with $m = -0.077$ and $m = -0.15$. At the relatively low Re_θ up to which the DNS were feasible, the corresponding equilibrium parameter β is found to be about 0.25 and 0.65, and the shape factor H is about 1.60 and 1.63, respectively.

The calculations with the DRSM at low Reynolds numbers are compared with the new DNS. Profiles for the velocity and turbulence obtained from the DNS at $x^* = 150$ were used as initial data for the model calculations. We varied the initial turbulence and dissipation rate in the model computations, and found that the initial transients already had decayed at $x^* = 335$, where the comparison with the DNS was made. Thus the comparison is meaningful since the difference between the model predictions at low and high Reynolds number (see Fig. 5) are due to the dependence on the Reynolds number and not to the influence of the initial conditions.

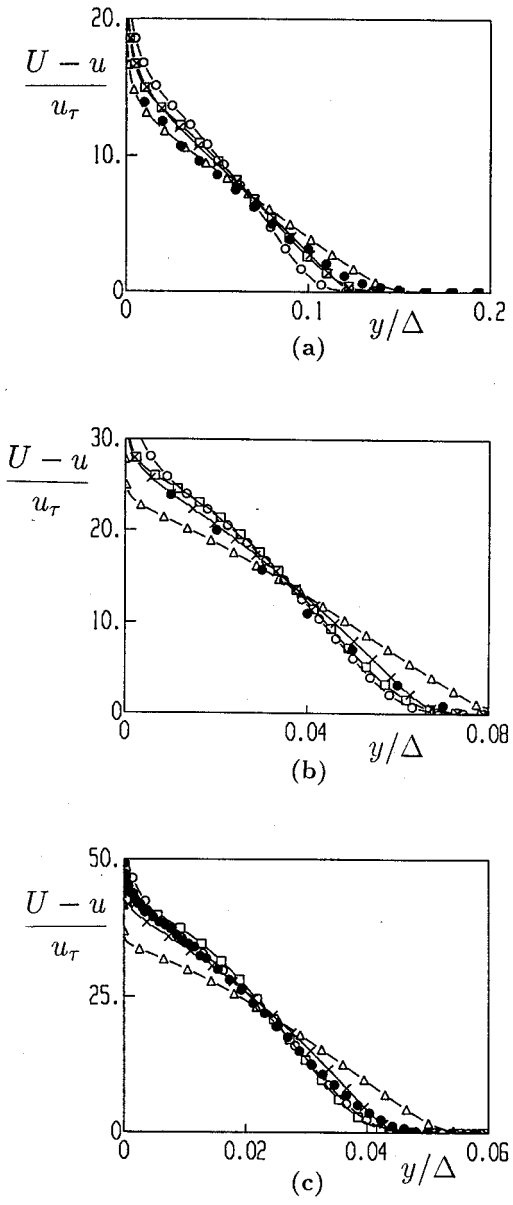

FIGURE 3. Comparison between turbulence models and experiments for the streamwise velocity under different equilibrium conditions; (a) $\beta = 2$ (• experiments by Clauser), (b) $\beta = 8$ (• experiments by Clauser), (c) $\beta = 20$ (• experiments by Skåre and Krogstad), models: O−O algebraic; $\triangle - \triangle$ $k-\epsilon$; $\times - \times$ $k-\omega$; $\square - \square$ DRSM

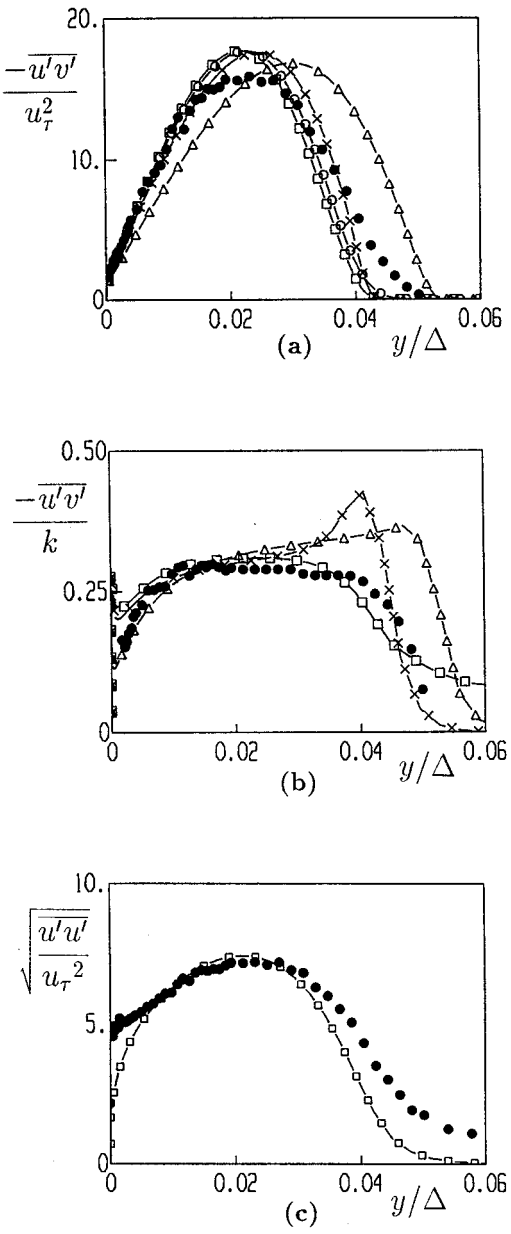

FIGURE 4. Comparison between turbulence models and experiments for the turbulence in an equilibrium boundary layer with $\beta = 20$; (a) Reynolds shear stress, (b) structure parameter, (c) Reynolds normal stress along the wall. models: O−O algebraic; $\triangle - \triangle$ $k-\epsilon$; $\times - \times$ $k-\omega$; $\square - \square$ DRSM

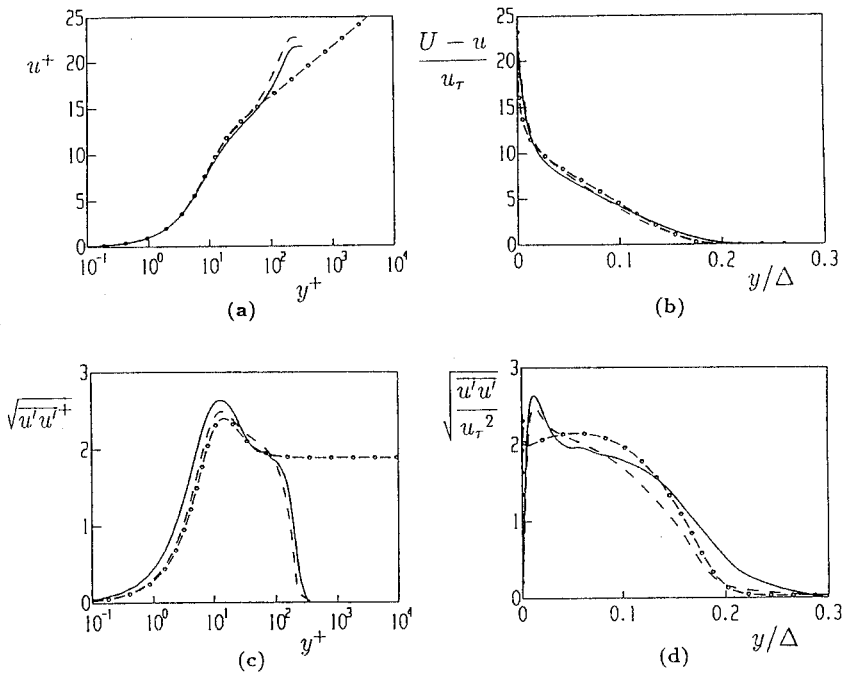

FIGURE 5. Comparison for $\beta \approx 0.65$; — DNS at $Re_\theta = 670$; - - DRSM at $Re_\theta = 670$; -o- similarity solution for the DRSM. Streamwise velocity in (a) inner-layer scalings, and (b) outer-layer scalings. Streamwise normal stress in (c) inner-layer scalings and (d) outer-layer scalings.

Figs 5a,b show close agreement for the velocity profile in inner-layer and outer-layer scalings at $Re_\theta = 670$ and $\beta \approx 0.65$, as computed with the DNS and DRSM. The figure also shows the large-Re similarity state for the DRSM. In fact $Re_\theta = 670$ is still so low that only a small logarithmic part in the inner layer is found. The streamwise Reynolds normal stress for $\beta \approx 0.65$ is compared in Figs 5c,d. The results are shown in both inner and outer layer scalings, and the similarity solution for the DRSM is included as well. Differences between the solution at $Re_\theta = 670$ and the similarity solution are significant. The results with the DRSM closely agree with the DNS at $Re_\theta = 670$, showing that the DRSM reproduces the physics of adverse pressure-gradient boundary layers at relatively low Reynolds numbers. The peak in the Reynolds normal stress in the DNS and DRSM at $Re_\theta = 670$ is part of the inner layer, but there already is a tendency to develop a second peak in the outer layer, which indeed has been established in the similarity solution with the DRSM. New DNS at larger

β, which will show an even stronger peak in the outer layer for the turbulent kinetic energy, are underway.

8. Conclusions

The numerical solution of the boundary-layer equations up to $Re_\theta = 10^8$ shows that four classes of turbulence models converge to the same classical scalings in the inner and outer layer for turbulent equilibrium boundary layers under an adverse pressure gradient. The solution in the outer layer converges to the defect law described by the defect-layer equation of Tennekes & Lumley, and not to the defect-layer equation of Wilcox (only for $\beta = 0$, both formulations are equal). Convergence to the similarity solution becomes slower for increasing β value. There is a nonunique relation between the m power in the outer-edge velocity and the equilibrium parameter β for all four turbulence models, which is in agreement with the experimental findings of Clauser.

Comparison with experiments, particularly the recent experiments by Skåre and Krogstad at $\beta = 20$, shows that among the tested turbulence models, the Differential Reynolds Stress Model is superior. But also the algebraic model and the $k-\omega$ model are reasonably accurate. The $k-\epsilon$ model gives rather large deviations for strong adverse pressure gradients, where it considerably overpredicts the wall-shear stress. The DRSM was also compared with our new DNS for $\beta \approx 0.25$ and 0.65 at the relatively low Reynolds number $Re_\theta = 670$. It turns out that the DRSM correctly predicts the low-Reynolds-number effects for the evolution of the boundary layer to its high-Re similarity solution.

References

Bradshaw, P. 1967 The turbulent structure of equilibrium boundary layers. *J. Fluid Mech.* **29**, 625–645.

Cebeci, T. & Smith, A. M. O. 1974 *Analysis of Turbulent Boundary Layers*. Academic Press.

Clauser, F. H. 1954 Turbulent boundary layers in adverse pressure gradients. *J. Aero. Sci.* **21**, 91–108.

Coles, D. 1956 The law of the wake in the turbulent boundary layer. *J. Fluid Mech.* **1**, 191–226.

Hanjalić, K., Jakirlić, S. & Hadžić, I. 1995 Computation of oscillating turbulent flows at transitional *Re*-numbers. In *Turbulent Shear Flows 9* (eds. F. Durst, N. Kasagi & B. E. Launder), pp. 323–342. Springer-Verlag.

Henkes, R. A. W. M. 1997 Comparison of turbulence models for attached boundary layers relevant to aeronautics. *Appl. Sci. Res.* **57**, 43–65.

Henkes, R. A. W. M. 1998 Scaling of equilibrium boundary layers under adverse pressure gradient using turbulence models. *AIAA J.* **36**, 320–326.

Launder, B. E. & Sharma, B. I. 1974 Application of the energy-dissipation model of turbulence to the calculation of flow near a spinning disk. *Let. Heat Mass Transfer* **1**, 131 – 138.

Lundbladh, A., Henningson, D. S. & Johansson, A. V. 1992 An efficient spectral integration method for the solution of the Navier-Stokes equations. FFA-TN 1992-28, Aeronautical Research Institute of Sweden, Bromma.

Lundbladh, A., Schmid, P. J., Berlin, S. & Henningson, D. S. 1994 Simulation of bypass transition in spatially evolving flows. Proceedings of the AGARD Symposium on Application of Direct and Large Eddy Simulation to Transition and Turbulence, AGARD-CP-551.

Skåre, P. E. 1994 Experimental investigation of an equilibrium boundary layer in strong adverse pressure gradient. University of Trondheim, PhD Thesis, Report NTH 1994:179 (D).

Skåre, P. E. & Krogstad, P.-Å. 1994 A turbulent equilibrium boundary layer near separation. *J. Fluid Mech.* **272**, 319–348.

Spalart, P. R. 1988 Direct simulation of a turbulent boundary layer up to $Re_\theta = 1410$. *J. Fluid Mech.* **187**, 61–98.

Tennekes, H. & Lumley, J. L. 1972 *A First Course in Turbulence*. The MIT Press.

Wilcox, D. C. 1993 *Turbulence Modeling for CFD*. DCW Industries, Inc.

Paper 3

P3

Analysis of the data base from a DNS of a separating turbulent boundary layer

By Martin Skote[*] and Dan S. Henningson[*†]

1. Motivation and objectives

This work was performed at CTR during a month-long visit in May 1999. The data base analyzed comes from a simulation performed by Na & Moin (1998*a*).

Although the data from the simulations have been used in the study of the structure of the wall pressure (Na & Moin 1998*b*), an analysis of the mean flow had not been conducted to a great extent. The aim of this work is to investigate the near wall scalings of the turbulent mean flow close to separation.

The scalings are very important for the correct behavior of wall damping functions used in turbulence models. For a zero pressure gradient (ZPG) boundary layer, the damping functions and boundary conditions in the logarithmic layer are based on a theory where the friction velocity,

$$u_\tau \equiv \sqrt{\nu \left.\frac{\partial u}{\partial y}\right|_{y=0}}, \tag{1}$$

is used as a velocity scale. However, in the case of a boundary layer under an adverse pressure gradient (APG), u_τ is not the correct velocity scale, especially not for a strong APG and low Reynolds number. In the case of separation this is clear since u_τ becomes zero. In a number of studies the case of separation has been investigated. The various theories will be presented in the section where the analysis is presented.

Also, for moderate pressure gradients, the near wall region is influenced if the Reynolds number is low enough. The combination of a pressure gradient and low Reynolds number give a flow that deviates from the classical near wall laws. The equations governing the inner part of the boundary layer can be analyzed, and the theory is applicable to the results from the direct numerical simulations investigated here.

In section 2 the numerical method and flow geometry is briefly described. The results from the investigation of the mean flow are presented in four parts in section 3. The first part (3.1) is devoted to the total shear stress. Here

[*]Department of Mechanics, Royal Institute of Technology (KTH), SE-100 44 Stockholm, Sweden
[†]Aeronautical Research Institute of Sweden (FFA), Box 11021, SE-161 11 Bromma, Sweden

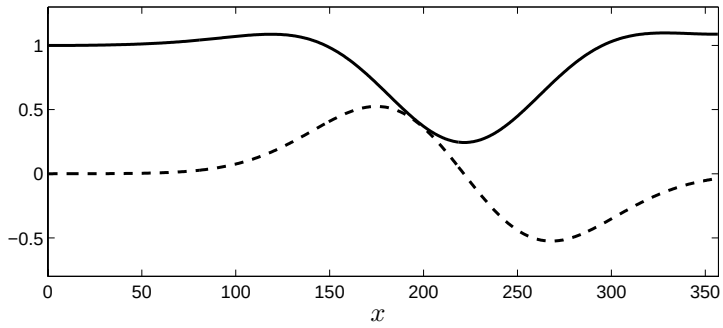

FIGURE 1. Freestream velocity. — : U; - - : V.

the alternative velocity scale based on the pressure gradient is introduced, and the effect of the APG on the inner part of the boundary layer is discussed. Continued investigation of the total shear stress in the second part (3.2) leads to the logarithmic law of the velocity profile. The law is extended to the APG case and is shown to be in fair agreement with DNS data. To further investigate the different velocity scales, the viscous sub-layer is investigated in the third part (3.3). And finally, in the fourth part (3.4), some earlier theories regarding the APG flow and separation are briefly presented.

2. Numerical method and flow characteristics

The simulation evaluated here was performed by Na & Moin (1998*a*), using a second-order finite difference method. The computational box was $350\times64\times50$ based on the δ^* at the turbulent inflow. The number of modes was $513\times193\times129$. The inflow condition was taken from Spalart's ZPG simulation. It consists of a mean turbulent velocity profile with superimposed turbulence with randomized amplitude factors while the phase was unchanged. The boundary conditions applied on the upper boundary are the prescribed wall normal velocity and zero spanwise vorticity,

$$v(x, L_y, z) = V(x) \qquad \left.\frac{\partial u}{\partial y}\right|_{x,L_y,z} = \frac{dV(x)}{dx}. \tag{2}$$

In Fig. 1 the two components of the freestream velocity are shown as a function of the downstream coordinate x. The two components are denoted U and V in the streamwise and wall normal directions respectively. Elsewhere in the flow the two components of the mean velocity are denoted u and v. There is no third direction in the mean flow.

The wall normal velocity (V) is prescribed in order to create a separation bubble. The point of separation is at $x = 158$, and the reattachment occurs at $x = 257$.

V varies in the downstream direction and thus induces a gradient in the u component at the freestream boundary, due to the zero vorticity condition.

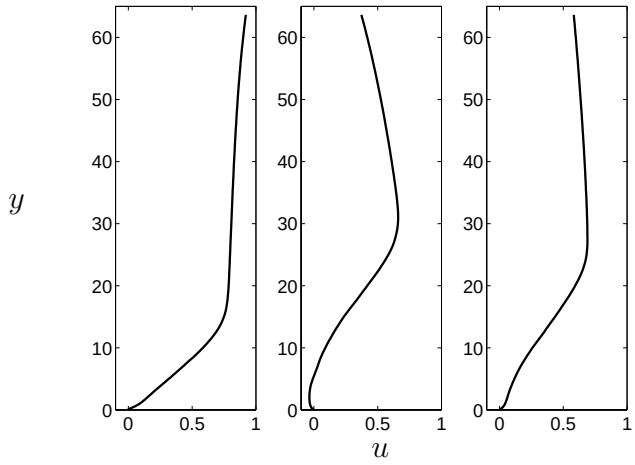

FIGURE 2. Velocity profiles at $x = 157$, 200, and 260.

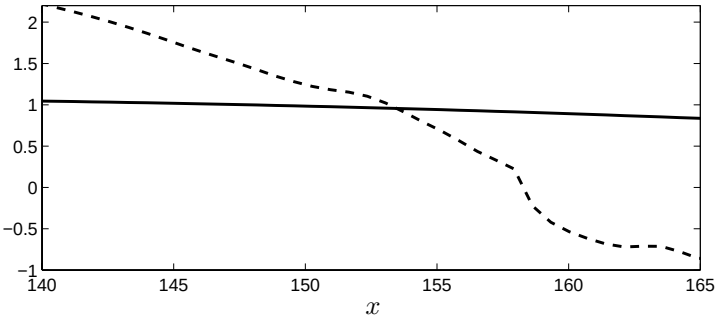

FIGURE 3. In the vicinity of the separation. — : U; - - : $u_\tau \times 100$.

In Fig. 2 three velocity profiles are shown from different downstream positions before, inside, and after the separation bubble. The gradients at the freestream boundary due to the boundary conditions are clearly visible. Since the boundary conditions applied in the simulation do not allow the $y-$derivative of the velocity profile to be zero at the upper boundary, all quantities involving δ^* or other integral quantities become ambiguous. The near wall behavior is not influenced by this gradient, and the analysis of the boundary layer equations can be compared with the DNS data.

The quantities shown in Fig. 3 as a function of the downstream direction in the vicinity of the separation are U and u_τ. There is a strong variation of u_τ at the point of separation as seen in Fig. 3.

3. Mean flow profiles

In this section the existing theoretical theories will be presented together with results from the DNS. Much of the theory is based on the two distinct regions

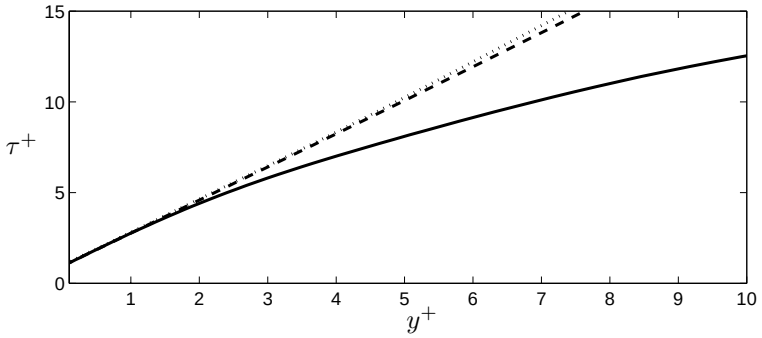

FIGURE 4. Total shear stress at $x = 150$. — : DNS; - - : Eq. (4); $\cdots$: Eq. (5).

of the flow, the inner and outer part respectively. Since only the inner part of the boundary layer will be considered here, the theory concerning the outer part is omitted.

3.1. *The total shear stress*

When neglecting the non-linear, advective terms in the equations describing the mean flow, the equation governing the inner part of the boundary layer is obtained. This equation can, when using the inner length and velocity scales ν/u_τ and u_τ be written,

$$0 = -\frac{\nu}{u_\tau^3}\frac{1}{\rho}\frac{dP}{dx} + \frac{d^2u^+}{dy^{+2}} - \frac{d}{dy^+}\langle u'v'\rangle^+, \tag{3}$$

where $\langle u'v'\rangle$ is the Reynolds shear stress. If the term involving the pressure gradient is smaller than the other terms, the equation reduces to the equation governing the inner part of a ZPG boundary layer. However, for the APG case considered here, this term cannot be neglected. Equation (3) can be integrated to give an expression for the total shear stress,

$$\tau^+ \equiv \frac{du^+}{dy^+} - \langle u'v'\rangle^+ = 1 + \frac{\nu}{u_\tau^3}\frac{1}{\rho}\frac{dP}{dx}y^+ \tag{4}$$

The total shear stress, τ^+, from the DNS and the curve $\tau^+(y^+)$ represented by Eq. (4) are shown in Fig. 4 at the position $x = 150$. The third and dotted line is obtained when considering that the pressure gradient is slightly dependent on the wall normal coordinate, in which case the integration of Eq. (3) yields,

$$\tau^+ = 1 + \int_0^{y^+} \frac{\nu}{u_\tau^3}\frac{1}{\rho}\frac{dP}{dx}(y^+)dy^+. \tag{5}$$

As seen in Fig. 4, the two expressions (4) and (5) are nearly identical. For a zero pressure gradient case, Eq. (4) predicts a constant shear stress of unity.

The pressure gradient term in Eq. (4) is evidently important for the shear stress distribution in the inner part of the boundary layer. This was observed in,

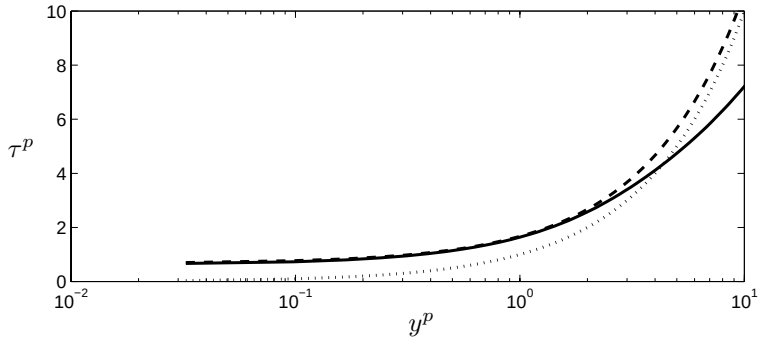

FIGURE 5. Total shear stress at $x = 150$. — : DNS; - - : Eq. (8); $\cdots$: asymptotic profile $\tau^p = y^p$.

among others, the experiments by Bradshaw (1967), Samuel & Joubert (1974) and Skåre & Krogstad (1994). It can be shown that the pressure gradient term decreases with increasing Reynolds number. The term is thus important only for low Reynolds numbers. However, close to separation, where u_τ approaches zero, it is clear that the terms becomes infinite even for large Reynolds numbers.

When considering separation the singularity mentioned above can be avoided by introducing the velocity scale,

$$u_p \equiv \left(\nu \frac{1}{\rho} \frac{dP}{dx}\right)^{1/3}. \tag{6}$$

First Eq. (4) is formulated as

$$\tau^+ = 1 + (\frac{u_p}{u_\tau})^3 y^+. \tag{7}$$

The velocity scale u_p has to be used instead of u_τ if the last term in Eq. (7) becomes very large, which happens if $u_\tau \ll u_p$, i.e. the boundary layer is close to separation. This was noted by Stratford (1959), Townsend (1961) and Tennekes & Lumley (1972). By multiplying Eq. (7) by $(u_p/u_\tau)^2$, the following expression for $\tau^p \equiv \tau/u_p^2$ is obtained,

$$\tau^p = y^p + (\frac{u_\tau}{u_p})^2, \tag{8}$$

with the asymptotic form $\tau^p = y^p$ when separation is approached, where $y^p \equiv yu_p/\nu$. Thus, in this rescaled form, the singularity is avoided.

In Figs. 5 and 6 the shear stress scaled with u_p is shown at $x = 150$ and $x = 158$. Both the linear expression (8) and its asymptotic form are shown. At $x = 150$ the separation has not been reached, thus the asymptotic version deviates while the profile from Eq. (8) coincides with the DNS data. At $x = 158$ the asymptotic expression agrees with the profile from DNS since $u_\tau = 0$ at that position.

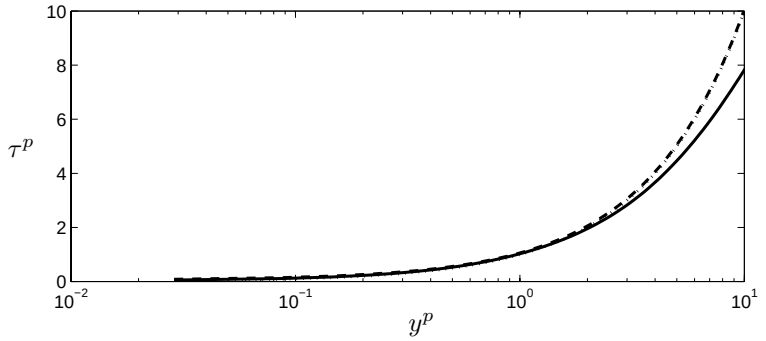

FIGURE 6. Total shear stress at $x = 158$. — : DNS; - - : Eq. (8); $\cdots$: asymptotic profile $\tau^p = y^p$.

3.2. *The logarithmic region*

Now, when the velocity scale u_p has been introduced, it is possible to investigate how other theoretical results for a ZPG turbulent boundary layer can be modified by the presence of an APG.

The Eq. (3) and the equation for the outer part of the boundary layer constitute a problem with inner and outer solutions. This problem has been treated with the method of matched asymptotic expansions by, among others, Mellor (1972) and Afzal (1996). The aim is to obtain higher order terms in the matching of the inner and outer solutions. The small parameter that is used in the expansions is u_τ/U, which is related to the Reynolds number through the logarithmic friction law.

The presentation here will be very brief and only the inner part is discussed. For the ZPG case, the scaling of the total shear stress with u_τ gives a self-similar profile ($\tau^+ = 1$). From Eqs. (7) and (8) it is observed that neither u_τ nor u_p as velocity scale results in a self-similar expression. However, Eq. (4) can be formulated as

$$\tau^* \equiv \frac{1}{u_*^2}\left(\nu\frac{\partial u}{\partial y} - \langle u'v'\rangle\right) = 1, \tag{9}$$

where u_* is a velocity scale that depends on y and can be expressed in either plus or pressure gradient units,

$$u_*^2 = u_\tau^2 + \frac{u_p^3}{u_\tau}y^+ = u_\tau^2 + u_p^2 y^p. \tag{10}$$

Thus, by scaling the total shear stress with u_*, a self-similar expression is obtained ($\tau^* = 1$).

For the ZPG case, the matching of the inner and outer equations results in the equation,

$$y^+\frac{du^+}{dy^+} = \frac{1}{\kappa}. \tag{11}$$

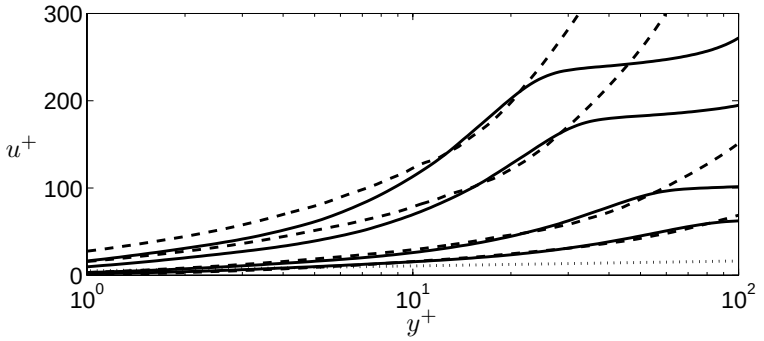

FIGURE 7. Velocity profiles. — : DNS; - - : Eq. (15) with $\kappa = 0.41$ and $B = -2$; $\cdots$: $u^+ = \frac{1}{0.41} \ln y^+ + 5.1$.

If now u_* is used as the velocity scale, the velocity gradient can be formulated as,

$$\nu \frac{\partial u}{\partial y} \frac{1}{u_*^2} = \left(\frac{\partial u}{\partial y} \right)^* . \tag{12}$$

The matching between the inner and outer equations as described by Afzal (1996) results in

$$y^* \left(\frac{\partial u}{\partial y} \right)^* = \frac{1}{\kappa}, \tag{13}$$

where

$$y^* \equiv y u_* / \nu = \sqrt{(y^+)^2 + (y^p)^3}. \tag{14}$$

In the same way as Eq. (11) can be integrated to give the logarithmic law for the ZPG case, Eq. (13) above can be integrated. However, Eq. (13) must be formulated with either u_τ or u_p as velocity scale before being integrated. If u_τ is chosen as velocity scale, the integration of Eq. (13) yields,

$$u^+ = \frac{1}{\kappa} \left(\ln y^+ - 2 \ln \frac{\sqrt{1 + \lambda y^+} + 1}{2} + 2(\sqrt{1 + \lambda y^+} - 1) \right) + B, \tag{15}$$

with

$$\lambda = \left(\frac{u_p}{u_\tau} \right)^3 . \tag{16}$$

The expression (15) is not self-similar due to the term λ, which is Reynolds number dependent.

Equation (15) is the same expression as Afzal (1996) arrived at. It is also similar to the equation which Townsend (1961) derived from mixing length arguments. The velocity profiles from the DNS of Na and Moin close to the point of separation are shown together with the standard log-law and the extended log-law (15) in Fig. 7. The separation occurs at $x = 158$ and the four velocity profiles are shown at $x = 150, 155, 157, 158$.

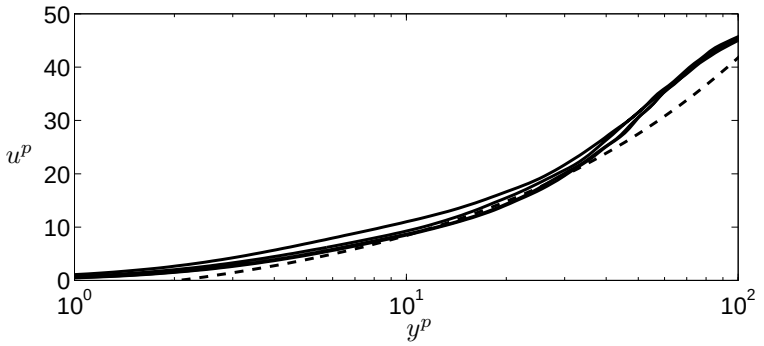

FIGURE 8. Velocity profiles. — : DNS; - - : Eq. (18) with $\kappa = 0.41$ and $C = -7$.

From Fig. 7 it is clear that the logarithmic law, valid for ZPG flows, is a poor instrument for obtaining boundary conditions in the log-layer for turbulence models. The extended log-layer, which involves the pressure gradient, seems to capture the deviation from the logarithmic profile surprisingly well. The parameters κ and B have not been adjusted to fit the DNS data; rather, the standard values have been used. In addition, the region where Eq. (15) is valid can be discussed.

When $u_p \to 0$, Eq. (13) reduces to the equivalent equation for the ZPG case (11), and the usual log-law is recovered. If $u_\tau \to 0$, Eq. (13) reduces to,

$$\sqrt{y^p}\frac{\partial u^p}{\partial y^p} = \frac{1}{\kappa}, \tag{17}$$

and the half-power law is obtained,

$$u^p \equiv \frac{u}{u_p} = \frac{1}{\kappa} 2\sqrt{y^p} + C, \tag{18}$$

which was first obtained by Stratford (1959).

Since it is shown that the scaling based on u_p is preferred over u_τ close to separation, the profiles in Fig. 7 should collapse better when scaled with u_p. The same velocity profiles as in Fig. 7 are plotted together with the half-power law (18) in Fig. 8.

An interesting observation is that Eq. (18) leads to a shape factor of two with a small correction due to the constant C. The correction vanishes for large Reynolds numbers when $u_p/U \to 0$. In both DNS at low Reynolds numbers (Spalart & Leonard 1987) and experiments at large Reynolds numbers (Skåre & Krogstad 1994) of flows near separation, a shape factor close to two was observed. The shape factor is 1.8 at separation for the flow of Na and Moin. But, as discussed earlier, the gradient of the velocity profile at the upper boundary give a value of the shape factor that cannot be considered a proper one.

By expressing Eq. (13) in pressure gradient units and integrating, the following expression for u^p is obtained,

$$u^p = \frac{1}{\kappa}\left(2\sqrt{\gamma^2 + y^p} + \gamma \ln y^p - 2\gamma \ln(\sqrt{\gamma^2 + y^p} + \gamma)\right) + C, \tag{19}$$

where

$$\gamma = \frac{u_\tau}{u_p}.$$

In the limit of $u_\tau \to 0$, Eq. (18) is recovered. The velocity profiles collapse much better in the pressure gradient scaling as can be seen from Fig. 8 where the asymptotic profile (18) is also shown. The profiles obtained from Eq. (19) do not vary much for different downstream positions, hence only the asymptotic profile is shown.

The two expressions (15) and (19) are equivalent; only the choice of scaling when integrating Eq. (13) differs. They are both dependent on the Reynolds number through the terms λ and γ respectively. Equation (13) cannot be integrated directly to yield $u^*(y^*)$ independent on the Reynolds number. This is due to the term

$$\left(\frac{\partial u}{\partial y}\right)^*,$$

which cannot be expressed in only $u^* \equiv u/u_*$ and y^*. However, these arguments regarding the lack of self-similarity of the velocity profile will be clearer if the viscous sub-layer, where the Reynolds stress can be neglected, is considered.

3.3. *The viscous sub-layer*

In the viscous sub-layer the Reynolds shear stress approaches zero and Eq. (8) can be integrated to give,

$$u^p = \frac{1}{2}y^{p2} + \left(\frac{u_\tau}{u_p}\right)^2 y^p \tag{20}$$

In plus units this equation becomes,

$$u^+ = y^+ + \frac{1}{2}\left(\frac{u_p}{u_\tau}\right)^3 y^{+2}. \tag{21}$$

This equation reduces to the usual linear profile in ZPG case.

Figure 9 shows velocity profiles near the wall for $x = 150$ and $x = 158$ in plus units. The higher profile is located at $x = 158$. The solid lines are DNS data and the dashed ones are the profiles from Eq. (21). The dotted line is the profile valid for the ZPG case ($u_p = 0$). As seen from Fig. 9, the linear approximation works reasonably well at $x = 150$, upstream of separation. But at $x = 158$, the effect from the pressure gradient is too large. The profiles diverge as separation is approached since the second term in Eq. (21) becomes infinite.

Figure 10 shows velocity profiles near the wall for $x = 150$ and $x = 158$ in pressure gradient units. The higher profile is located at $x = 150$. In this

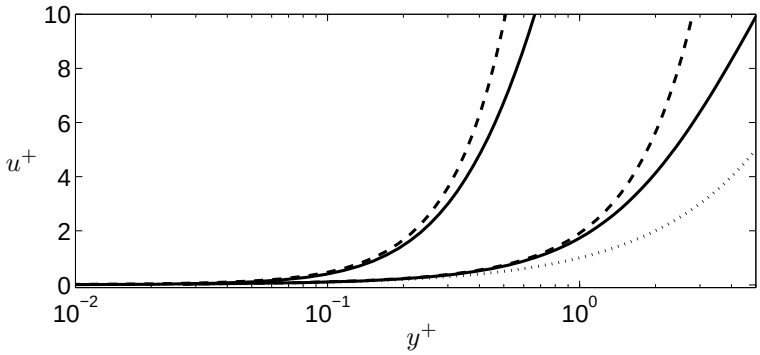

FIGURE 9. Velocity profiles at $x = 150$ and $x = 158$. — : DNS; - - : $y^+ + \frac{1}{2}\left(\frac{u_p}{u_\tau}\right)^3 y^{+2}$; $\cdots$: y^+.

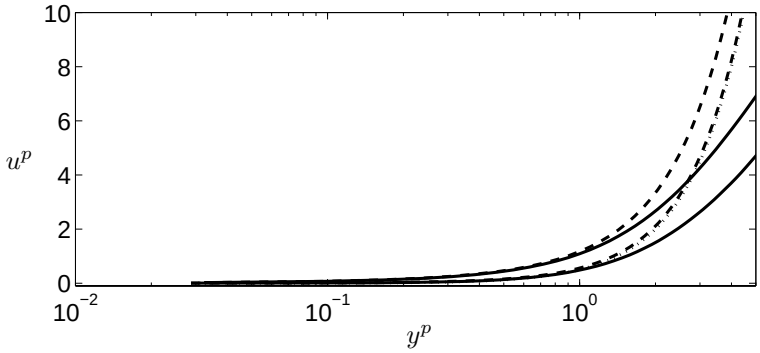

FIGURE 10. Velocity profiles at $x = 150$ and $x = 158$. — : DNS; - - : $\frac{1}{2}y^{p2} + (\frac{u_\tau}{u_p})^2 y^p$; $\cdots$: $\frac{1}{2}y^{p2}$.

case the asymptotic profile (dotted) is valid at separation. The solid lines are DNS data and the dashed are the profiles given by Eq. (20). From Fig. 10 one can draw the conclusion that the pressure gradient scaling is preferred since the profiles approach an asymptotic profile instead of diverging infinitely as u_τ approaches zero.

In both the viscous and logarithmic region, the velocity has been scaled with two different velocities, u_τ and u_p. Both of these scalings give in an asymptotic state a Reynolds number independent expression. The representations in plus units, Eqs. (15) and (21), return to the ZPG formulation when u_p approaches zero. The representation in pressure gradient units, Eqs. (19) and (20), become the square-root and square profiles when separation is approached.

In both these scalings the velocity profile is dependent of the ratio between u_τ and u_p as seen in the four equations mentioned above. However, the total

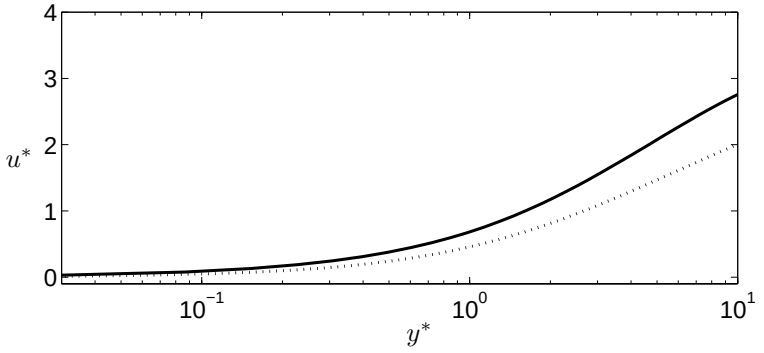

FIGURE 11. Velocity profiles at $x = 150$ and $x = 158$. — : DNS at $x = 150$; $\cdots$: DNS at $x = 158$.

shear stress could be made independent of this ratio by scaling with u_*, Eq. (9). Thus the profiles are self-similar with respect to Reynolds number and pressure gradient. In order to obtain an expression for the velocity scaled with u_* in the viscous sub-layer, Eq. (9) with the Reynolds stress equal to zero must be solved. Thus, it is

$$\nu \frac{\partial u}{\partial y} \frac{1}{u_*^2} = 1. \tag{22}$$

that needs to be solved. The solution $u^*(y^*)$ should be independent of the ratio between u_τ and u_p. Equation (22) formulated in star units gives

$$\frac{\partial u^*}{\partial y^*} + \frac{1}{2} \left(\frac{y^p}{y^*} \right)^3 \left(y^* \frac{\partial u^*}{\partial y^*} + u^* \right) = 1, \tag{23}$$

where the relation between y^* and y^p is given by Eq. (14), which can be written

$$y^{*2} = \left(\frac{u_\tau}{u_p} \right)^2 (y^p)^2 + (y^p)^3. \tag{24}$$

The ratio between u_τ and u_p is still present in Eq. (24), thus no independent solution can be found. This is also evident from DNS data where the profiles are scattered for different downstream positions as shown in Fig. 11.

3.4. *Comparison with other theories for the logarithmic region*

According to Tennekes & Lumley (1972), the scaling with pressure gradient velocity u_p should lead to the same form of matching as in the zero pressure gradient case. From this assumption a logarithmic law is obtained in the same manner as the usual procedure of matching the outer and inner solutions. The log-law becomes,

$$u^p = \frac{1}{\kappa} \ln(y^p) + B. \tag{25}$$

Equation (25) is shown in Fig. 12 together with DNS data from the positions $x = 150$ and $x = 158$.

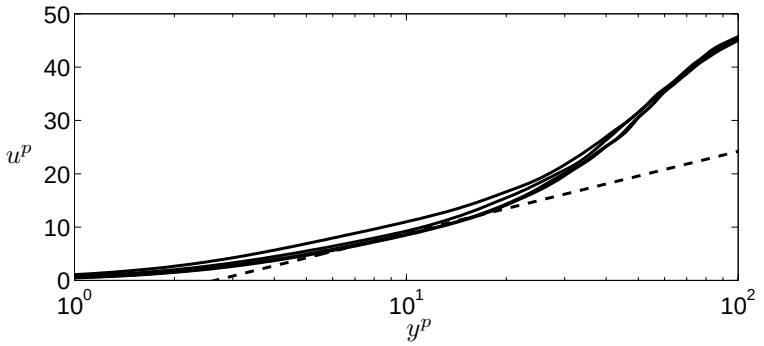

FIGURE 12. Velocity profiles. — : DNS; - - : Eq. (25) with $\kappa = 0.15$, $B = -6.5$.

According to Stratford (1959), the velocity profile should be a half-power law close to separation. Also Yaglom (1979) showed that a dimensional analysis gives the following expression for the velocity profile close to separation,

$$u^+ = K^+\sqrt{\lambda y^+} + K_1^+, \tag{26}$$

which can be expressed in pressure gradient scaling,

$$u^p = K\sqrt{y^p} + K_1. \tag{27}$$

Yaglom (1979) also proposed a fairly complicated dependence of K and K_1 on u_p and u_τ. This dependency was introduced to extend the theory valid at separation to the region upstream of detachment. It cannot be regarded as a sound procedure to incorporate a functional behavior in constants of an expression valid only in an asymptotic state. It seems to be a better approach to the equations to introduce the mixed velocity scale u_* and do the analysis leading to Eq. (19).

4. Conclusion

The scalings in the near wall region of a turbulent boundary layer close to separation have been analyzed. Two different velocity scales appears naturally in the governing equation: the friction velocity and the pressure gradient velocity. With the aid of the momentum equation governing the inner part, it is possible to derive a mixed velocity scale. By using this velocity scale and matching the inner and outer solutions, an extended logarithmic law is obtained. When approaching the zero pressure gradient case, the familiar log-law and plus scales are recovered. In the limit of separation, the half-power law in pressure gradient scaling is obtained. In the vicinity of separation, the extended logarithmic law in plus scaling give profiles in agreement with DNS data. The profiles are widely scattered when using the friction velocity as a velocity scale due to the large variation of the friction velocity in the vicinity of separation. When using pressure gradient scalings, the profiles are much less scattered, and the

extended logarithmic law in its asymptotic form (half-power law) agrees with the DNS data.

The mixed velocity scale, which depends on y, was shown to give self-similar profiles for the total shear stress. For the velocity however, no such profiles can be derived. Thus, for practical purposes such as boundary conditions for RANS-modeling and wall-damping functions, the extended logarithmic law should give more reasonable results than the corresponding zero pressure gradient laws. When the friction velocity varies rapidly or approaches zero, the scaling with pressure gradient velocity is preferred since the singularity at separation is avoided.

Even in the viscous sub-layer, the pressure gradient influences the velocity profile if the Reynolds number is low enough. The two velocity scales based on the friction velocity and pressure gradient velocity give profiles that are independent on Reynolds number only in the limit of zero pressure gradient and separation respectively. The comparison with data in the viscous sub-layer from direct numerical simulation shows that the velocity scale based on the pressure gradient can indeed be used in this region of the flow close to separation. In fact, such scaling shows that the velocity profiles approach an asymptotic, self-similar profile at separation. If the friction velocity scaling is used, the profiles diverge as separation is approached. This scaling gives an asymptotic self-similar profile (the linear profile) in the limit of zero pressure gradient.

References

Afzal, N. 1996 Wake layer in a turbulent boundary layer with pressure gradient: a new approach. In *IUTAM Symposium on Asymptotic Methods for Turbulent Shear flows at High Reynolds Numbers* (ed. K. Gersten), pp. 95–118. Kluwer Academic Publishers.

Bradshaw, P. 1967 The turbulent structure of equilibrium boundary layers. *J. Fluid Mech.* **29**, 625–645.

Mellor, G. L. 1972 The large reynolds number, asymptotic theory of turbulent boundary layers. *Intl J. Engng Sci.* **10**, 851–873.

Na, Y. & Moin, P. 1998*a* Direct numerical simulation of a separated turbulent boundary layer. *J. Fluid Mech.* **374**, 379–405.

Na, Y. & Moin, P. 1998*b* The structure of wall-pressure fluctuations in turbulent boundary layers with adverse pressure gradient and separation. *J. Fluid Mech.* **377**, 347–373.

Samuel, A. E. & Joubert, P. N. 1974 A boundary layer developing in an increasingly adverse pressure gradient. *J. Fluid Mech.* **66**, 481–505.

Skåre, P. E. & Krogstad, P.-Å. 1994 A turbulent equilibrium boundary layer near separation. *J. Fluid Mech.* **272**, 319–348.

Spalart, P. R. & Leonard, A. 1987 Direct numerical simulation of equilibrium turbulent boundary layers. In *Turbulent Shear Flows 5* (eds. F. Durst, B. E.

Launder, J. L. Lumley, F. W. Schmitd & J. H. Whitelaw), pp. 234–252. Springer-Verlag.

Stratford, B. S. 1959 The prediction of separation of the turbulent boundary layer. *J. Fluid Mech.* **5**, 1–16.

Tennekes, H. & Lumley, J. L. 1972 *A First Course in Turbulence*. The MIT Press.

Townsend, A. A. 1961 Equilibrium layers and wall turbulence. *J. Fluid Mech.* **11**, 97–120.

Yaglom, A. M. 1979 Similarity laws for constant-pressure and pressure-gradient turbulent wall flows. *Ann. Rev. Fluid Mech.* **11**, 505–40.

Paper 4

P4

Direct numerical simulation of separating turbulent boundary layers

By Martin Skote and Dan S. Henningson

Dept. of Mechanics, KTH, SE-100 44, Stockholm, Sweden

Direct numerical simulation of two turbulent boundary layer flows has been performed. The boundary layers are both subject to a strong adverse pressure gradient. In one case a separation bubble is created while in the other the boundary layer is everywhere attached. The data from the simulations are used to investigate scaling laws near the wall, a crucial concept in turbulence models. Theoretical work concerning the inner region in a boundary layer under an adverse pressure gradient is reviewed and extended to the case of separation. Excellent agreement between theory and data from the direct numerical simulation is found in the viscous sub-layer, while a qualitative agreement is obtained for the overlap region.

1. Introduction

The separation of boundary layer flow is of crucial importance in many applications, including airfoils, rear windows on cars, and turbine blades. Separation is difficult to predict with current turbulence models, and the design of devices that either loose their functionality or have their optimum performance close to the onset of separation is an engineering difficulty.

A vast number of theoretical and/or experimental work has been presented throughout the last decades, and lately direct numerical simulations (DNS) have become an important tool for further investigation of this type of flows. Although laboratory experimental techniques have improved and the reliability of results from experiments has increased, there is still need for DNS for improving the results in the near-wall region. Also, turbulent structures and the instantaneous flow fields are better analyzed using DNS results.

1.1. *Theoretical investigations*

In most theoretical investigations of boundary layers it is of crucial importance to determine the relevant velocity scale. For a zero pressure gradient (ZPG) boundary layer such a velocity scale is naturally chosen as the friction velocity,

$$u_\tau \equiv \sqrt{\nu \left.\frac{\partial u}{\partial y}\right|_{y=0}}. \tag{1}$$

However, in the case of a boundary layer under an adverse pressure gradient (APG), u_τ is not the relevant velocity scale. This is true especially for strong APGs and low Reynolds numbers. For a separating boundary layer this is clear since u_τ becomes zero in this case. In a number of studies the case of a strong APG and separation has been investigated theoretically. In many such studies a velocity scale based on the pressure gradient is defined,

$$u_p \equiv \left(\nu \frac{1}{\rho} \frac{dP}{dx} \right)^{1/3}. \tag{2}$$

In an analysis based on u_p, Stratford (1959) obtained a square-root law for the velocity profile from the assumption of zero wall stress and mixing length theory. Townsend (1961) refined the theory based on mixing length to the case of non-zero (but positive) wall shear stress and obtained a law with both square-root and logarithmic parts based on u_τ as a velocity scale. Kader & Yaglom (1978) extended the Stratford velocity profile to the case of positive wall stress. However, they kept the square-root law based on u_p, and let the influence of a non-zero wall shear stress be accounted for by varying the constants. Mellor (1966) arrived at a similar expression as Townsend. The work of Townsend was later reviewed by McDonald (1969) who included non-linear inertia effects in the expression for the velocity profile.

Afzal (1996) obtained similar expressions for the velocity profile as Townsend by using asymptotic matching. Durbin & Belcher (1992) also used asymptotic theory for the analysis of velocity profiles. They obtained a three layer structure of the turbulent boundary layer under an APG. Melnik (1989) also obtained a three layer structure by extending the asymptotic analysis of Yajnik (1970) and Mellor (1972) with an algebraic turbulence model. Skote & Henningson (1999) simplified the formulation of Townsend and showed that the analysis could be valuable for turbulence modelling purposes.

Instead of using u_τ or u_p as the velocity scale and letting the velocity profile depend on the pressure gradient and Reynolds number, some investigators have tried to make the profiles collapse on a single curve in an outer scaling. This seems to be possible only if a velocity scale is determined a posteriori, with the objective to make the profiles collapse. Coles (1956) proposed a wake function to account for the variation of the velocity profile in the outer (or wake) region of the boundary layer. The form of the wake function has later been modified in a number of ways, see e.g. Musker (1979) for further references. Perry & Schofield (1973) and Schofield (1981) used a scaling for the outer part of the velocity profile designed to match the profiles to a half-power law close to the wall. They claimed that the velocity scale is related to the maximum shear stress.

Thus, there are two fundamentally different theoretical approaches to the velocity profile in a turbulent boundary layer under a strong APG. One is focusing on the local pressure gradient as the important parameter determining the shape of the velocity profile, the other is focusing on a velocity scale, defined

through a fitting procedure, that will make the velocity profiles collapse onto a single curve. In this work we will develop further the analysis where the local pressure gradient is the key factor.

1.2. *Experiments*

Many experiments have been performed on separated flows, albeit most of them consider separation caused by a sharp edge, or an obstacle, see e.g. the review of Simpson (1996) for a collection of references, and the work of Hancock (2000) for references to the latest experiments.

The experiments on separation of a flat plate turbulent boundary layer include the works of Perry & Fairlie (1975), Simpson *et al.* (1977, 1981*a*,*b*), Dengel & Fernholz (1990), Driver (1991) and Alving & Fernholz (1996, 1995). Some of these investigations have also tried to develop different scalings of the velocity profile in both outer and inner variables.

Simpson *et al.* (1977) showed that the Perry-Schofield scaling is supported upstream of separation, however with the the streamwise derivative of the longitudal and normal Reynolds stresses included in the estimation of the maximum shear stress. They concluded that the shear stress gradient is less than the streamwise pressure gradient due to the Reynolds stresses and the convective terms in the momentum equation.

Simpson *et al.* (1981*a*,*b*) developed a scaling based on the maximum back-flow velocity and its distance from the wall for the back-flow profile, which was shown to consist of three layers: the layer closest to the wall which is governed by viscous forces, a relatively flat intermediate layer and the outer back-flow which is dominated by the large-scale outer region flow. No universal 'back-flow function' could be found. Upstream of separation the logarithmic law was valid, as well as the Perry-Schofield scaling for the outer part. As separation is approached the scalings are not fulfilled. Furthermore, they concluded that the velocity profile in the outer part is not described by a universal wake function. The normal and streamwise Reynolds stresses contribute to the turbulence energy production at separation, and the enhanced turbulence energy production in the outer region supply turbulence energy to the back-flow region by turbulent diffusion.

Dengel & Fernholz (1990) performed measurements in an axisymmetric turbulent boundary layer. Three cases were investigated with skin friction zero, slightly negative, and slightly positive. They concluded that the logarithmic law is not valid when the first reverse-flow events occur. Furthermore, the velocity profile does not confirm the Perry-Schofield scaling. Instead they let a seventh order polynomial represent an asymptotic velocity profile close to separation. However, Dengel & Fernholz did not base the velocity scale on the maximum stress. Instead, they obtained the velocity scale by fitting the velocity profiles to a half-power law, as suggested by Schofield (1981). Reynolds stresses increased downstream in all three cases and the turbulence production had its maximum far out in the boundary layer.

Driver (1991) performed measurements on two boundary layers on an axisymmetric body with similar pressure distributions but very different flows. One is attached and the other is separated. He concluded that above a certain value of the pressure gradient (in viscous scaling) the mean flow profile does not obey the law of the wall. The attached boundary layer was found to be in equilibrium and the Clauser parameter was nearly constant.

Alving & Fernholz (1996) performed an experiment on an axisymmetric body with a turbulent boundary layer that separates in a short region. They reported decreased Reynolds stresses in the inner region and large peaks away from the wall. After reattachment, the inner region is slower in its recovery than the outer part and the recovery does not start at the wall. Hence, the large scale structures are intact over the separation bubble and then interact with near-wall flow after reattachment. Alving & Fernholz (1995) investigated the scaling of the velocity profiles from their experiment. They compared the Durbin-Belcher and Perry-Schofield scalings, with the conclusion that the latter works better than the former. However, they did not actually use the velocity scale proposed by Perry & Schofield (1973), but rather determined their velocity scale so that the velocity profiles close to separation collapse with the profile given by Dengel & Fernholz (1990).

The consensus from the experiments mentioned above is that the turbulence is intensified above a separated region while it is decreased in the back-flow itself. Velocity profiles at streamwise positions close to the separation point can only be made to collapse in the outer part by a fitting procedure of the velocity scale. Upstream of separation the experiments give no evidence on how the velocity profiles should be scaled. No universal profile for the back-flow seems to exist and the proper scaling is still an open question.

1.3. *Direct numerical simulations*

A few direct numerical simulations (DNS) of separated turbulent boundary layer flows have been performed earlier.

Na & Moin (1998*a*,*b*), hereafter abbreviated as NM, used a second-order finite difference method to simulate a turbulent separation bubble. The computational box was $350 \times 64 \times 50$ based on the δ^* at the turbulent inflow. The number of points was $513 \times 193 \times 129$. The inflow condition was taken from Spalart's temporal ZPG simulation. The velocity profiles were neither linear in the viscous sub-layer nor logarithmic further from the wall at all streamwise positions. The location of maximum turbulence intensity occurred above the separation bubble.

The near-wall flow from the simulation by NM has previously been investigated by Skote & Henningson (1999). Good agreement between theory regarding the viscous sub-layer (recapitulated here in section 2.1.1) and DNS data was found in the region just upstream of separation.

Spalart & Coleman (1997), hereafter abbreviated as SC, performed DNS of a separation bubble with heat transfer. They used a spectral code with

$640 \times 200 \times 256$ modes. Their inflow-outflow boundary condition was based on the fringe region technique with a turbulent inflow. Their results showed that separation has large effects on the boundary layer, and that many assumptions which are valid for an attached layer cannot be applied to the separated boundary layer. The Reynolds shear stress increased dramatically over the separation bubble as did the turbulent kinetic energy. This is explained by a lift-up of turbulent fluid from the wall region that weakens the blocking effect of the wall. The increased turbulent energy can also be explained by a contribution from the normal and streamwise Reynolds stresses as argued by SC. Negative production of turbulent kinetic energy was observed in the later part of the separation bubble. This was not further explained by SC but was probably due to a positive Reynolds shear stress in that part of the flow. However, SC recognized that the effect of the rapid distortion on the boundary layer might lead to results which are not valid for turbulent separation bubbles in general.

In both of these simulations the boundary condition on the upper boundary was set by imposing a normal velocity that varies downstream and thus controls the separation bubble. Many results are hence similar for both simulations. The streamwise velocity profiles have a gradient at the upper boundary due to the boundary condition, thus the velocity profiles constitute a boundary layer with no freestream edge, where the streamwise velocity gradient and the normal velocity are small.

Both NM and SC noted that the streaks near the wall are eliminated by an APG. In NM they concluded that the vortical structures are lifted above the bubble and impinge on the wall in the reattachment region.

The simulations performed here are different from the ones by NM and SC in some important aspects. First, the boundary condition used in the present simulations gives a boundary layer with a well defined freestream edge, thus permitting an investigation of integral parameters which was not possible in NM and SC. Second, the separated region is longer than in NM and SC, hence the local distortion of the boundary layer is less severe. The strength of the back-flow is also stronger, which reveals new phenomena.

In this work we start with a review and extension of the theory concerning velocity profiles in an attached and separated turbulent boundary layer in section 2. The results from the simulations are presented in section 3. A presentation of the numerical methodology, including a resolution check, is given in section 3.1. This is followed by a general description of the flow, including both instantaneous structures and turbulence statistics, in section 3.2. The theoretical results from section 2 are compared with DNS data in section 3.3. The results are further discussed in section 4, and comparison with NM and SC will be made, as well as with some experimental data.

In the present work we focus on the near-wall flow since few results from the near-wall region in a separated flow have previously been reported. The flow close to the wall is scrutinized by comparing results from theoretical considerations with data obtained from the DNS

2. The turbulent boundary layer equations

In the past, much effort has been spent to obtain numerically solvable ordinary differential equations for the parameters quantifying the turbulent boundary layer. See e.g. Schlichting (1979), Rotta (1962) and Cebeci & Smith (1974) for references. Using such methods, separation and reattachment can be predicted in some cases. However, no general formula to predict separation has been offered. The emphasis today is shifted towards more general closures of the Navier-Stokes equations, based on turbulence models. Therefore, no attempts to analyze or improve the methods based on simplified versions of the turbulent boundary layer equation (TBLE) are conducted here. The TBLE is used to extend and improve the theoretical understanding of the streamwise velocity profile in the inner region of the turbulent boundary layer.

The near-wall behavior of a turbulent boundary layer close to separation, or fully separated, is difficult to analyze with the TBLE, since a separated flow does not permit the simplifications of the Navier-Stokes equations leading to the TBLE. However, even if the TBLE is not valid when the downstream development of a separating boundary layer is to be calculated, it can still be used to understand what happens locally in the boundary layer.

Results from a straightforward analysis of the TBLE is of importance for the development and calibration of turbulence models. The near-wall laws derived for ZPG boundary layers have been used extensively for obtaining boundary conditions in calculations of boundary layer flow with turbulence models. Thus, better near-wall laws for turbulent boundary layers would improve the predictions made of APG flows using turbulence models. The near-wall laws presented here can be used for such purposes.

In section 2.1 the analysis of the TBLE will be presented for two reasons. First we wish to strengthen the arguments and results from some of the previous authors. The analysis reported here clarifies how and under what circumstances previous results are applicable. Second, the modified analysis can be repeated for the separated case. This analysis is presented in section 2.2. The theoretical results for the separated case are derived from the same arguments as for the attached case. It is only the changed boundary condition at the wall that make the resulting expressions for the velocity profile different from the ones describing an attached boundary layer.

2.1. *The attached boundary layer*

The analysis of the TBLE will be divided into three parts. The first and second parts deal with the total shear stress in the inner region of the boundary layer, where the advective terms in the TBLE are neglected. The analysis in the first part will lead to a velocity profile in the viscous sub-layer, where also the Reynolds stress can be neglected. The overlap region is investigated in the second part.

The third part is devoted to the outer part of the boundary layer, where the viscous term in the TBLE is neglected. Together with the analysis of the

outer part, an integration of the TBLE with all terms included, gives some relations between mean flow parameters, such as shape factor and skin friction.

2.1.1. *The inner region*

The analysis of the inner region (near-wall flow) will be performed in more detail than the analysis of the outer part, since the low Reynolds number together with an adverse pressure gradient give a flow that differs substantially from the ZPG flow. Also, the results for the separated flow will be based on the analysis of the APG flow.

When neglecting the non-linear, advective terms in the equations describing the mean flow, the equation governing the inner part of the boundary layer is obtained. Using the inner length and velocity scales ν/u_τ and u_τ, the equation can be written,

$$0 = -\frac{\nu}{u_\tau^3}\frac{1}{\rho}\frac{dP}{dx} + \frac{d^2u^+}{dy^{+^2}} - \frac{d}{dy^+}\langle u'v'\rangle^+, \tag{3}$$

where $\langle u'v'\rangle$ is the Reynolds shear stress. If the term involving the pressure gradient is negligible small compared to the other terms, the equation reduces to the equation governing the inner part of a ZPG boundary layer. However, for strong APG cases at finite Reynolds numbers, this term cannot be neglected. Equation (3) can be integrated to give an expression for the total shear stress,

$$\tau^+ \equiv \frac{du^+}{dy^+} - \langle u'v'\rangle^+ = 1 + \frac{\nu}{u_\tau^3}\frac{1}{\rho}\frac{dP}{dx}y^+ \tag{4}$$

For a ZPG case, equation (4) predicts a constant shear stress of unity in the inner region.

The pressure gradient term in equation (4) is evidently important for the shear stress distribution in the inner part of the boundary layer. This was observed in, among others, the experiments by Bradshaw (1967), Samuel & Joubert (1974) and Skåre & Krogstad (1994), and the DNS by Spalart & Watmuff (1993) and Skote *et al.* (1998). It can be shown that the pressure gradient term decreases with increasing Reynolds number, and thus is important only for low Reynolds numbers. However, close to separation, where u_τ approaches zero, it is clear that the pressure gradient term becomes infinite, even for large Reynolds numbers.

When considering a strong APG or separation, the singularity mentioned above can be avoided by introducing the velocity scale u_p, defined in equation (2). To see this, we first formulate equation (4) as

$$\tau^+ = 1 + \left(\frac{u_p}{u_\tau}\right)^3 y^+. \tag{5}$$

The velocity scale u_p has to be used instead of u_τ if the last term in equation (5) becomes very large which happens if $u_\tau \ll u_p$, i.e. the boundary layer is close to separation. This was noted by Stratford (1959), Townsend (1961)

and Tennekes & Lumley (1972). By multiplying equation (5) by $(u_p/u_\tau)^2$, the following expression for $\tau^p \equiv \tau/(\rho u_p^2)$ as a function of $y^p \equiv y u_p/\nu$ is obtained,

$$\tau^p = y^p + \left(\frac{u_\tau}{u_p}\right)^2. \tag{6}$$

Equation (6) has the asymptotic form $\tau^p = y^p$ when separation is approached. Thus, in this rescaled form, the singularity is avoided.

There are three possible complications in the above analysis. First, the pressure gradient may depend on the normal coordinate. This was proved to be important when the analysis was compared with the data from the simulation of NM, see Skote & Henningson (1999). However, due to the straightforward boundary conditions used in the present simulation, no such dependence exists in the data presented here. The second complication is that the TBLE contains the streamwise derivative of longitudal and normal Reynolds stresses. These terms may be important in a strong APG flow as was noted by Rotta (1962). A third complication is the non-linear inertia terms, which can influence the total shear stress as argued by McDonald (1969). However, in the present simulations these two terms are not important and will be disregarded in the following.

Now, in the viscous sub-layer the Reynolds shear stress approaches zero and equation (6) can be integrated to give,

$$u^p \equiv \frac{u}{u_p} = \frac{1}{2}(y^p)^2 + \left(\frac{u_\tau}{u_p}\right)^2 y^p. \tag{7}$$

In the limit of separation, when $u_\tau/u_p \to 0$, equation (7) reduces to

$$u^p = \frac{1}{2}(y^p)^2. \tag{8}$$

In viscous units, equation (7) becomes,

$$u^+ = y^+ + \frac{1}{2}\left(\frac{u_p}{u_\tau}\right)^3 (y^+)^2. \tag{9}$$

This equation reduces to the usual linear profile in ZPG case, when $u_p/u_\tau \to 0$.

The two expressions (5) and (6) are equivalent. It is in the limits of $u_\tau/u_p \to 0$ and $u_p/u_\tau \to 0$ respectively that the formulation becomes crucial. The same observation is true for the expressions (7) and (9). However, when plotting data from the rapidly varying separation bubble of NM, the scaling based on u_p gives a much better collapse of the profiles. In the scaling based on u_τ, the profiles are scattered, due to the strong variation of u_τ. In the simulations presented here, the pressure gradient is varying less violently.

2.1.2. *The overlap region*

The velocity profiles derived in this section will have asymptotic forms that are consistent with the profiles in the viscous sub-layer derived in the previous section. That is, the two velocity scales (u_τ and u_p), yield two different velocity

profiles, valid in the limits of ZPG ($u_p/u_\tau = 0$) and separation ($u_\tau/u_p = 0$) respectively. In flows between these asymptotic states (APG flows), the two scalings are equivalent and both give a velocity profile that depends on the Reynolds number and the pressure gradient through the ratio between u_τ and u_p.

We now proceed with the analysis by first considering the total shear stress. For the ZPG case, the scaling of the total shear stress with u_τ gives a self-similar profile ($\tau^+ = 1$). From equations (5) and (6) it is observed that neither u_τ nor u_p as velocity scale results in a self-similar expression. However, equation (4) can be formulated as

$$\tau^* \equiv \frac{1}{u_*^2}\left(\nu\frac{\partial u}{\partial y} - \langle u'v'\rangle\right) = 1, \tag{10}$$

where u_* is a velocity scale that depends on y and can be expressed in either viscous or pressure gradient units,

$$u_*^2 = u_\tau^2 + \frac{u_p^3}{u_\tau}y^+ = u_\tau^2 + u_p^2 y^p. \tag{11}$$

Thus, by scaling the total shear stress with u_*, a self-similar expression is obtained ($\tau^* = 1$). The velocity scale u_* reduces to u_τ if u_p becomes zero, i.e. for a ZPG boundary layer. If instead u_τ becomes zero, i.e. for a boundary layer at separation, the velocity scale becomes $u_* = u_p\sqrt{y^p}$. However, when $u_* = u_p\sqrt{y^p}$ is inserted in equation (10) we can write the equation as $\tau^p = y^p$, i.e. we use u_p as the velocity scale. Note that for the special case with $u_\tau = 0$, the velocity scale u_* is zero at the wall. This is natural since the velocity gradient is zero at the wall.

The logarithmic behavior of the turbulent boundary layer is obtained from the matching of the velocity gradient, or equivalently, the shear stress, in the inner and outer regions of the boundary layer. The matching also requires a consistency condition that results in the logarithmic friction law.

For the matching of the inner and outer equations, it is enough to observe that the total shear stress can be written in the form (10) in the inner part. In the outer part it is assumed that the velocity gradient can be written,

$$\frac{\partial u}{\partial y} = F' u_*/\Delta, \tag{12}$$

where F' is a function of a similarity variable (y/Δ) and Δ is the outer length scale. Equation (12) should be considered as the scaled formulation of the velocity gradient for the outer part, corresponding to the scaled velocity gradient for the inner part, which can be written as

$$\frac{\partial u}{\partial y} = f' u_*^2/\nu, \tag{13}$$

where f' is a function of a similarity variable (yu_*/ν).

If the total shear stress is scaled with u_* in the outer and inner parts, and assumptions (12) and (13) are valid, then the matching of the total shear stress gives the equation,

$$y^* \left(\frac{\partial u}{\partial y}\right)^* = \frac{1}{\kappa}, \tag{14}$$

where a short notation is used for the scaled velocity derivative,

$$\left(\frac{\partial u}{\partial y}\right)^* \equiv \nu \frac{\partial u}{\partial y} \frac{1}{u_*^2}. \tag{15}$$

The scaled normal coordinate is

$$y^* \equiv y u_* / \nu = \sqrt{(y^+)^2 + (y^p)^3}. \tag{16}$$

For the ZPG case, for which $u_p = 0$, equation (14) is reduced to,

$$y^+ \frac{du^+}{dy^+} = \frac{1}{\kappa}. \tag{17}$$

When integrated, equation (17) gives the logarithmic velocity profile.

In the same way as equation (17) can be integrated to give the logarithmic law for the ZPG case, equation (14) above can be integrated to give a velocity profile in either viscous scaling ($u^+ \equiv u/u_\tau = f(y^+)$) or pressure scaling ($u^p \equiv u/u_p = g(y^p)$). Both of these expressions will depend on the ratio between u_τ and u_p, and are thus not self-similar. A self-similar profile of the form $u^* \equiv u/u_* = h(y^*)$ is not consistent with equation (10). This is further discussed at the end of this section.

If u_τ is chosen as velocity scale, the integration of equation (14) yields,

$$u^+ = \frac{1}{\kappa}\left(\ln y^+ - 2\ln\frac{\sqrt{1+\lambda y^+}+1}{2} + 2(\sqrt{1+\lambda y^+}-1)\right) + B, \tag{18}$$

with

$$\lambda = \left(\frac{u_p}{u_\tau}\right)^3.$$

The expression (18) is not self-similar due to the term λ which is Reynolds number dependent. Equation (18) is the same expression as Afzal (1996) arrived at. It is also similar to the equation which Townsend (1961) derived from mixing length arguments.

If u_p is chosen as velocity scale, then (18) can be written,

$$u^p = \frac{1}{\kappa}\left(2\sqrt{\gamma^2 + y^p} + \gamma \ln y^p - 2\gamma \ln(\sqrt{\gamma^2 + y^p} + \gamma)\right) + C \tag{19}$$

where

$$\gamma = \frac{u_\tau}{u_p}.$$

For a ZPG boundary layer, for which $\lambda = 0$, equation (18) reduces to the logarithmic profile. In the other limit, at separation, when γ is zero, equation

(19) reduces to the half-power law,

$$u^p = \frac{1}{\kappa} 2\sqrt{y^p} + C, \tag{20}$$

which was first derived by Stratford (1959). Note that equation (20) can be rewritten in such a manner it is independent on the viscosity, as in the formulation by Stratford.

As mentioned earlier, it is not possible to solve equation (14) directly to obtain an expression for u^* as a function of only y^*. This is due to the scaled (with u_*) velocity gradient, which cannot be formulated independently of u_τ and u_p. The velocity gradient scaled with a constant velocity scale u_τ or u_p is, on the other hand, straightforward to express independently of the Reynolds number,

$$\nu \frac{\partial u}{\partial y} \frac{1}{u_\tau^2} = \left(\frac{\partial u}{\partial y} \right)^+ = \frac{du^+}{dy^+}. \tag{21}$$

Thus, in the ZPG case the equation permits a self-similar velocity profile (the logarithmic function). The same is true for the zero wall stress case (the half-power law). In all flows between these two asymptotic states, the velocity profile depends on the Reynolds number through the ratio between u_τ and u_p.

In other words, for all APG boundary layers, including the asymptotic states ZPG and separation, the total shear stress can be made self-similar by using the velocity scale u_*. For the ZPG and separating boundary layers, u_* reduces to a constant (y independent) velocity scale (u_τ and u_p respectively). This leads to that the velocity profile becomes self-similar for those two cases (due to equation (21) above). For all APG cases in between, the velocity scale u_* is not constant, and hence the velocity profile is not self-similar.

2.1.3. *The outer part*

The analysis of the integrated TBLE, together with the analysis of the outer part, where the viscous terms are neglected, was conducted thoroughly by Skote *et al.* (1998). Only the resulting equations, linking the mean flow parameters with each other, will be recapitulated.

The aim here is to simplify the equations under the assumption of self-similarity. The conditions for self-similarity and the resulting relations between mean flow parameters are presented. The reason for interest in self-similar flows originates from at least three arguments. First, the equation of motion are simpler to analyze. Second, turbulence models can be calibrated using a single profile, or investigated from an asymptotic approach. Third, calibration and determination of parameters such as friction velocity can be done in experiments.

If the viscous term is neglected in the equations describing the mean flow of a two-dimensional, incompressible, turbulent boundary layer, the equation governing the outer part of the layer is obtained. From this equation it is possible to deduce that a necessary condition for self-similarity is that a pressure

gradient parameter (denoted β) is constant,

$$\beta \equiv \frac{\delta^*}{\tau_w}\frac{dP}{dx} = \text{constant}. \tag{22}$$

Furthermore, if u_τ/U is regarded as constant and an outer length scale varies linearly, the condition β =constant is fulfilled if the freestream variation is of the form $U \sim x^m$, which when specifying a profile becomes,

$$U = U_0(1 - \frac{x}{x_0})^m. \tag{23}$$

If this form of the freestream is inserted in the TBLE together with the assumption that the velocity defect and Reynolds shear stress, when scaled with the friction velocity, are functions of an outer variable η,

$$\begin{aligned} (u-U)/u_\tau = F(\eta), \qquad & -\langle u'v'\rangle/{u_\tau}^2 = R(\eta), \\ \eta = y/\Delta(x), \qquad & \Delta = U\delta^*/u_\tau, \end{aligned} \tag{24}$$

the TBLE becomes,

$$\begin{aligned} -2\beta F + \frac{\beta}{m}(1+m)\eta\frac{dF}{d\eta} \\ +\frac{u_\tau}{U}\left\{-\beta F^2 + \frac{\beta}{m}(1+m)\frac{dF}{d\eta}\int_0^\eta F d\eta\right\} = \frac{dR}{d\eta} + \frac{1}{Re_{\delta^*}}\frac{d^2F}{d\eta^2}. \end{aligned} \tag{25}$$

The equation governing the outer part is obtained if the last term in equation (25) is neglected.

If F is of order unity, the terms within the bracket after u_τ/U can be neglected, which results in a linearization of the equation. This simplification is only valid in the limit of infinite Reynolds number, when $u_\tau/U \to 0$. However, closer to the wall, and for finite Reynolds number, F is of order U/u_τ and all terms in the equation are of the same order. Thus, when integrating from the wall to the freestream, the non-linear terms must be kept. The viscous term is also important since it is zero only for a boundary layer at the point of separation.

Thus, retaining all terms and integrating equation (25), the relationship,

$$m = -\frac{\beta}{H(1+\beta)+2\beta}, \tag{26}$$

is obtained. H is the shape factor. The asymptotic result for infinite Reynolds number, when $u_\tau/U \to 0$, is obtained by setting H equal to unity.

In the present APG simulation the Reynolds stress profiles at different positions are not self-similar, due to the small variation of u_τ/U. For large Reynolds numbers, the profiles tend to a self-similar state. This can be seen from e.g. the experiments with a strong pressure gradient of Skåre & Krogstad (1994), or from calculations with turbulence models as in Henkes (1998) or Skote *et al.* (1998).

From the definition of β, equation (22), and the freestream profile used, equation (23), it follows that if m and the ratio u_τ/U are constants, then,

$$\Delta = (1 - \frac{x}{x_0})\Delta_0. \tag{27}$$

All of these conditions and the resulting relations are investigated in the DNS data presented in section 3.2.1. Now the effect of a different velocity scale is investigated.

In the previous studies by Skote *et al.* (1998), the APG was not so strong that rescaling was required, neither in the inner nor in the outer region. For a strong APG or separated case, the scaling of the velocity defect with u_τ has to be reconsidered, following the arguments from the preceding sections.

As for the inner part, the rescaling merely means a change of the velocity scale from u_τ to u_p. When using u_p instead of u_τ as velocity scale, the parameter occurring in the TBLE is changed from β to β_p,

$$\beta_p \equiv -\frac{\delta^*}{u_p^2} U \frac{dU}{dx} = \beta \left(\frac{u_\tau}{u_p}\right)^2 = \frac{\delta^*}{\nu} u_p. \tag{28}$$

The TBLE scaled with u_p is equation (25) multiplied by $(u_p/u_\tau)^3$, and integrated it gives the relation,

$$m = -\frac{\beta_p}{H\left((\frac{u_\tau}{u_p})^2 + \beta_p\right) + 2\beta_p}, \tag{29}$$

which is identical to relation (26). If $u_\tau \to 0$, the relation (29) reduces to,

$$m = -\frac{1}{H+2}, \tag{30}$$

which is also what (26) reduces to when $u_\tau \to 0$, i.e. when $\beta \to \infty$.

In the analysis of the TBLE with u_p instead of u_τ, the self-similar expressions (24) are replaced with the following expressions,

$$\begin{aligned} (u-U)/u_p = F_p(\eta_p), \qquad & -\langle u'v'\rangle/{u_p}^2 = R_p(\eta_p), \\ \eta_p = y/\Delta_p(x), \qquad & \Delta_p = U\delta^*/u_p. \end{aligned} \tag{31}$$

The scaling of the velocity defect with u_p cannot give self-similar profiles since β_p is not constant according to the definition (2) of u_p. The ratio u_p/U is not constant either. Thus, a theoretical expression for the outer part in a boundary layer close to separation must be based on another kind of scaling.

There have been many attempts to properly describe the velocity profile in the outer part of the boundary layer, both for ZPG and APG flows. Coles (1956) proposed a wake function for the description of the velocity profile. Since then a number of changes and refinements have been presented. Musker (1979), among others, proposed a velocity profile that is valid from the wall to the freestream, consisting of a logarithmic function and a wake function of the polynomial form. Dengel & Fernholz (1990) disregarded the form of the

original wake function, and propose a polynomial fit to the velocity profile. A different approach was chosen by Perry & Schofield (1973), who found their velocity scale by a fitting procedure similar to the Clauser plot in the ZPG case. They also related the velocity scale to the maximum shear stress, but no experimental data have confirmed this relation. Durbin & Belcher (1992) derived a three-layered structure of the turbulent boundary layer under a strong adverse pressure gradient. No experimental data have verified their scalings.

With this abundance of theories and proposed functions for the description of the velocity profile in the outer part, it is difficult to extract the 'best' theory, especially with those containing a large number of constants to be adjusted to obtain the best fit with DNS data. Therefore, in the present work, the velocity profile in the outer part will not be investigated with respect to the vast number of suggested profiles described above. We are content with a comparison between the velocity scales u_τ and u_p.

The difficulties in finding an appropriate description of the velocity profile in the outer part of the boundary layer in strong APG flows with or without separation, may be attributed to 'historical effects', i.e. the flow is not determined by local parameters (except for equilibrium layers), but is influenced by downstream and upstream conditions. This is consistent with the arguments of Perry (1966), who divided the boundary layer into a wall region, where the flow is determined by local parameters, and a 'historical region' where this local or 'regional similarity' does not apply.

2.2. *The separated boundary layer*

The TBLE cannot be used as a tool if a calculation of the downstream behavior of a separated boundary layer from given boundary condition is to be performed, Rotta (1962), Perry & Fairlie (1975). However, the TBLE can still be used for the analysis of local velocity profiles.

In this section the case of separation will be discussed. The limit of zero shear stress ($u_\tau/u_p \to 0$) was approached in the analysis above, and the asymptotic version of the expression for the velocity in the viscous sub-layer was equation (8), and in the logarithmic region it was equation (20). These two expressions were obtained by setting $u_\tau = 0$ in equation (7) and (19) respectively. Now, if a separated flow is considered, the definition of u_τ has to be reconsidered. In the separated region, $\frac{\partial u}{\partial y}$ is negative. Thus, the definition of u_τ in equation (1) involves a square root of a negative number. Instead, the definition will be changed so that the square root will be taken of a positive number. Thus, to proceed with the analysis of the equations, the definition of the friction velocity will have to be changed to

$$u_\tau \equiv \sqrt{-\nu \left.\frac{\partial u}{\partial y}\right|_{y=0}}. \tag{32}$$

This change will affect the analysis outlined in the previous section. It is the boundary condition at the wall used when integrating the TBLE that will

be different from the attached case. In this section the analysis will start with the inner part, continue with the overlap region, and end with the outer part.

The equation for the inner part (3) will not be changed since the scaling is not affected by the change of definition of u_τ. However, in the integration leading to equation (4), the boundary condition at the wall is used and will now, with the definition (32), change sign. Thus, the analysis is the same as in section 2.1. It is only the boundary condition that change the expression from equation (6) to

$$\tau^p = y^p - \left(\frac{u_\tau}{u_p}\right)^2. \tag{33}$$

For the velocity in the viscous sub-layer the expression becomes,

$$u^p = \frac{1}{2}(y^p)^2 - \left(\frac{u_\tau}{u_p}\right)^2 y^p, \tag{34}$$

instead of equation (7). Due to the changed boundary condition, the corresponding equation in viscous scaling, equation (9), will read as,

$$u^+ = -y^+ + \frac{1}{2}\left(\frac{u_p}{u_\tau}\right)^3 (y^+)^2. \tag{35}$$

Note that the equations (7) (attached boundary layer) and (34) (separated boundary layer) take the same form,

$$u^p = \frac{1}{2}(y^p)^2, \tag{36}$$

when $u_\tau/u_p \to 0$. This asymptotic form is equal for the two cases since the asymptotic state is the onset of separation. On the other hand, the corresponding equations in the viscous scaling, equations (9) and (35), have the asymptotic forms $u^+ = y^+$ and $u^+ = -y^+$ respectively. Thus, the assumption that viscous forces are stronger than the pressure gradient give different profiles in the attached and separated region.

From equations (7) or (35) it is possible to extract the maximum negative velocity and the position where it occurs. In pressure gradient scaling the maximum back-flow is $-\frac{1}{2}(\frac{u_\tau}{u_p})^4$ at $y^p = (\frac{u_\tau}{u_p})^2$. These results are valid if the back-flow maximum is located in the viscous sub-layer.

Now the logarithmic part of the boundary layer will be discussed. According to equation (33), the velocity scale that produce a self-similar shear stress ($\tau^* = 1$) is,

$$u_*^2 = -u_\tau^2 + \frac{u_p^3}{u_\tau} y^+ = -u_\tau^2 + u_p^2 y^p. \tag{37}$$

By inserting either form of u_* into equation (14), two different expressions for the velocity profile are obtained. Using the viscous scaling yields,

$$u^+ = \frac{1}{\kappa}\left[2\sqrt{\lambda y^+ - 1} - 2\arctan\left(\sqrt{\lambda y^+ - 1}\right)\right] + B, \tag{38}$$

with

$$\lambda = \left(\frac{u_p}{u_\tau}\right)^3.$$

By using the pressure gradient scaling we obtain,

$$u^p = \frac{1}{\kappa}\left[2\sqrt{y^p - \gamma^2} - 2\gamma \arctan\left(\sqrt{\frac{y^p}{\gamma^2} - 1}\right)\right] + C, \tag{39}$$

where

$$\gamma = \frac{u_\tau}{u_p}.$$

The logarithmic dependence has been replaced by the arctan function. However, the asymptotic function (20) is recovered from equation (39) when $u_\tau/u_p \to 0$.

The equation (38) was actually derived by McDonald (1969) from Townsend's extended log law, however with the velocity scale u_p replaced with the shear stress gradient. McDonald argues that the shear stress gradient is different from the streamwise pressure gradient, and that the deviation originates from inertia effects.

After the analysis of the inner and logarithmic parts, we now proceed with the outer part. Since the separation (at least the weak one considered here) is a phenomenon confined to the inner part of the boundary layer, the outer part is not affected. However, the integration of the TBLE, presented in section 2.1.3, are affected since the boundary condition will change for a separated boundary layer compared to the attached one.

When integrating equation (25) in pressure gradient scaling, the changed boundary condition results in the relation,

$$m = -\frac{\beta_p}{H\left(-(\frac{u_\tau}{u_p})^2 + \beta_p\right) + 2\beta_p}, \tag{40}$$

This relation is almost identical with the relation (29), and the only difference is the sign in front of ${u_\tau}^2$, which enters through the boundary condition at the wall. The asymptotic version for vanishing wall shear stress is the same, equation (30).

3. Direct numerical simulations

The numerical code and a discussion about the resolution required are presented is section 3.1. The results from the simulations will be presented in two sections. The general description of the flow is presented in section 3.2. In section 3.3 the mean flow will be presented and compared to the theoretical results from section 2.

3.1. *Numerical considerations*

The code used for simulation is only a tool to provide the data wanted. However, the complexity of numerical issues makes it interesting to present the basic ideas behind the numerical solution procedure. Especially in combination with the use of super computers, the computational algorithm can itself lead to research in its own right.

3.1.1. *Numerical method and parallelization*

The code used for the direct numerical simulations (DNS) was developed at KTH and FFA, Lundbladh *et al.* (1999). The numerical approximation consists of spectral methods with Fourier discretization in the horizontal directions and Chebyshev discretization in the normal direction. Since the boundary layer is developing in the downstream direction, it is necessary to use non-periodic boundary conditions in the streamwise direction. This is possible while retaining the Fourier discretization if a fringe region is added downstream of the physical domain. In the fringe region the flow is forced from the outflow of the physical domain to the inflow. In this way the physical domain and the fringe region together satisfy periodic boundary conditions. The fringe region is implemented by the addition of a volume force F, to the Navier-Stokes equations:

$$\frac{\partial u_i}{\partial t} + u_j \frac{\partial u_i}{\partial x_j} = -\frac{1}{\rho}\frac{\partial p}{\partial x_i} + \nu \frac{\partial^2 u_i}{\partial {x_j}^2} + F_i. \tag{41}$$

The force

$$F_i = \lambda(x)(\tilde{u}_i - u_i) \tag{42}$$

is non-zero only in the fringe region; $\tilde{u}_i$ is the laminar inflow velocity profile which the solution u_i is forced to and $\lambda(x)$ is the strength of the forcing. The form of $\lambda(x)$ is designed to minimize the upstream influence. For an analysis of the fringe region technique, the reader is referred to Nordström *et al.* (1999).

Time integration is performed using a third order Runge-Kutta method for the advective and forcing terms and a Crank-Nicolson method for the viscous terms. A 2/3-dealizing rule is used in the streamwise and spanwise direction.

The numerical code is written in FORTRAN and consists of two major parts, one linear part where the equations are solved in spectral space, and one non-linear part where the non-linear terms in the equations are computed in physical space. The linear part needs data for one spanwise (z) position at a time since the equations are solved in the wall normal (y) direction. The non-linear part needs data for one y position at a time since the FFT is performed in the horizontal directions (spanwise and streamwise). The flow variables are stored at an intermediate level with spectral representation in the horizontal directions and physical representation in the y direction. All spatial derivatives are calculated with spectral accuracy. The main computational effort in these two parts is in the FFT.

The simulations were performed to a large extent on computers with distributed memory. The parallelization and optimization of the code for these type of computers were performed by Alvelius & Skote (2000). Communication between processors is necessary when the different operations on the data set are to be performed in the two different parts of the code. The data set (velocity field) is divided between the different processors along the z direction. Thus, in the linear part, no communication is needed. When the non-linear terms are calculated, each processor needs data for a horizontal plane. The main storage is kept at its original position on the different processors. In the non-linear part each processor collects the two-dimensional data from the other processors, on which it performs the computations and then redistributes it back to the main storage.

The boundary conditions are no-slip at the wall and at the freestream the normal derivative of the streamwise and spanwise velocity components are set to zero, while for the normal component the prescribed value of the APG is used,

$$\frac{\partial v}{\partial y} = \frac{\partial V_{APG}}{\partial y} = -\frac{\partial U_{APG}}{\partial x}. \tag{43}$$

These boundary conditions ensures that the prescribed APG is obtained.

3.1.2. *Numerical parameters*

The simulations were performed on various computers. The tuning of the pressure gradient for the desired flow situation was performed on a Cray T3E at NSC in Linköping, using 32 processors. After the design of the pressure gradient, a simulation with 20 million modes was performed on an IBM SP2 at PDC, KTH in Stockholm, using 32 processors. The results presented here are mainly from a second simulation with 40 million modes performed at the National Aerospace Laboratory (NAL), Tokyo. The same (with some differences due to the different types of processors) code was used on all three computers, using MPI (Message-Passing Interface) for the communication between the processors. The numerical method and the simulation performed at NAL was presented at the Parallel CFD 2000 conference in Trondheim.

The computer used at NAL was the Numerical Wind Tunnel (NWT), a parallel computer that consists of 166 vector processors from Fujitsu. The maximum performance on each processor is 1.7 Gflop/s. The main difference from the other two computers (CRAY T3E and IBM SP2) is the type of processor. While the other two consist of super-scalar processors, the NWT utilizes vector processors. These processors give a higher performance for each of the processing elements. The fast Fourier transforms (FFT), for which most of the time is spent during the simulation, have different structure for the scalar and vector processors.

The simulations start with a laminar boundary layer at the inflow which is triggered to transition by a random volume force near the wall. All the

quantities are non-dimensionalized by the freestream velocity (U) and the displacement thickness (δ^*) at the starting position of the simulation ($x = 0$), where the flow is laminar. At that position $Re_{\delta^*} = U\delta^*/\nu = 400$. The length (including the fringe), height and width of the computation box were $700 \times 65 \times 80$ in these units. The fringe region has a length of 100 and the trip is located at $x = 10$.

Results from two simulations are presented. One, which is called APG1, is a boundary layer subject to a strong APG. The flow in APG1 is everywhere attached. The second, which is called SEP, is a boundary layer under even stronger APG, and the flow is separated for a large portion.

Two different resolutions were used for the simulations. For APG1 the number of modes was $512 \times 193 \times 192$. After a simulation of SEP with the same resolution, a larger simulation was performed using the NWT. The number of modes in this simulation was $720 \times 217 \times 256$, which gives a total of 40 million modes or 90 million collocation points.

The simulations were run for a total of 7500 time units (δ^*/U), and the sampling for the turbulent statistics was performed during the last 2500 time units. The statistics were collected during the simulations and averaged in the spanwise direction. No filtering of the statistics has been used.

3.1.3. *Resolution check*

The simulation of a separated boundary layer was performed with two different resolutions and could be compared with each other. The turbulent statistics for both resolutions were computed from the same amount of simulation time. The general behavior in the streamwise direction is the same for the two resolution, i.e. there are no large differences in parameters such as friction velocity, shape factor etc. There were some differences in the region where the back-flow has its largest magnitude, which is now further investigated. Velocity profiles from two downstream positions are shown in figure 1, one at $x = 350$ where the back-flow is strongest, and one at $x = 500$, where the boundary layer is attached. A large part of the profile from the less resolved simulation at the point of maximum back-flow ($x = 350$) is below the profile from the well resolved simulation. However, close to the wall they collapse. In the attached region, the two profiles are essentially similar. Thus, the region where strong back-flow occurs is sensitive to the resolution, which means that caution is needed when simulating this type of flow. Also in the Reynolds shear stress some differences could be detected, most notably in the outer region, near the freestream. In the attached region there were no differences between the two resolutions for the Reynolds stresses. It should be noted that even though the history effects can influence the boundary layer downstream of reattachment, (see e.g. the investigations of Alving & Fernholz (1996)), the differences upstream of reattachment in the the two resolutions do not influence the boundary layer in the attached region.

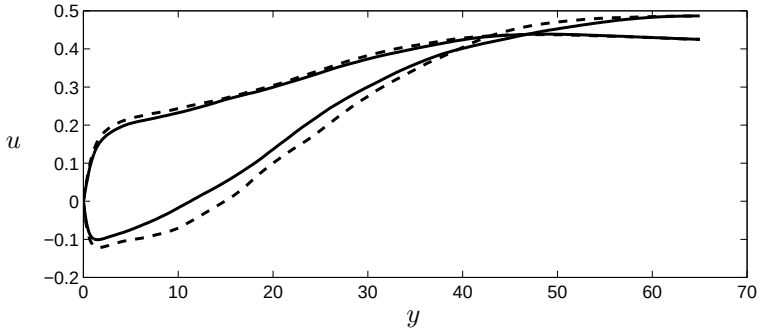

FIGURE 1. SEP: Velocity profile in the separated region at $x = 350$ and in the attached region at $x = 500$. — 720 × 217 × 256 modes; - - 512 × 193 × 192 modes.

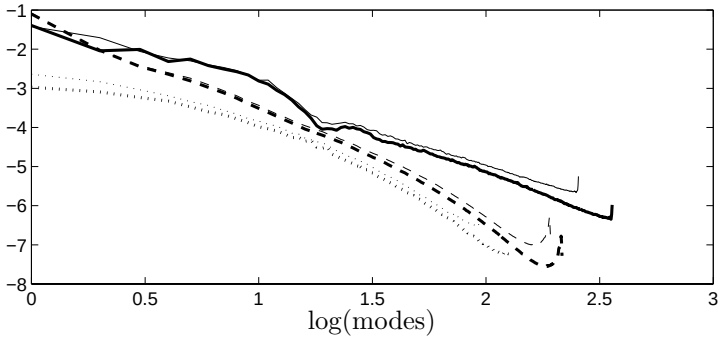

FIGURE 2. SEP: Energy contained in modes in — x; - - y; $\cdots$ z. Thick lines: 720 × 217 × 256; Thin lines: 512 × 193 × 192.

This investigation shows that the lower resolution is sufficient for the attached region, while in the separated region, the high resolution is crucial for capturing the correct behavior.

Comparison with the resolution in the simulations by NM and SC is possible by rescaling the size of the box of their simulations in the coordinates of the present simulation and divide with number of collocation points. The result is shown in table 1. The resolution is better for the present simulation than in NM in all three directions, even though their method has second order accuracy while our method, as in SC, is spectral.

To further confirm the resolution we show the energy in the flow as function of the spectral modes for the two resolutions in figure 2. The thick lines are from the well resolved case. Note that the two velocity fields are from different times, thus the curves from the two cases do not collapse. The energy decays consistently in the three directions when the resolution is refined. The small

	present	NM	SC
Δx	0.65	0.85	0.57
Δy	0.30	0.41	0.27
Δz	0.21	0.48	0.21

TABLE 1. Comparison of resolution between the present simulation and the simulations by SC and NM.

contamination in the highest modes moves to higher wavenumbers as resolution is increased.

3.2. *General description of the flow*

The general behavior of the mean flow parameters is described and discussed in section 3.2.1. The instantaneous velocity field will be presented in section 3.2.2, where a qualitative description of the structures appearing in the flow will be afforded. In section 3.2.3 a general description of some turbulence statistics are presented.

3.2.1. *Mean flow parameters*

In earlier simulations of APG turbulent boundary layers by the authors of the present work, Skote *et al.* (1998), the freestream velocity varied according to a power law in the downstream coordinate, $U \sim x^m$. The motivation for this was that a self-similar profile in the outer part could be developed. In the simulations presented here, the aim was to get a boundary layer as close to a separated state as possible. The tuning of the pressure gradient is extremely time consuming since the boundary layer has a slow response to any change in the pressure distribution.

The pressure gradient is determined through the freestream velocity, which is of the same functional form as in Skote *et al.* (1998),

$$U = \left(1 - \frac{x}{x_0}\right)^m. \tag{44}$$

The two parameters that can be changed are x_0 and m, and they are summarized in table 2.

The freestream velocity (U) for the two simulations, APG1 and SEP, are shown in figure 3, together with the skin friction (C_f). As seen from the figure, a small change in the freestream velocity has a great impact on the skin friction. A number of simulations were performed to obtain a boundary layer with a wall shear stress as close to zero as possible. These two simulations are the ones where we obtained u_τ closest to zero, and were therefore continued for a long time to get good statistics. The resolution was discussed in section 3.1, and the conclusion was that both simulations can be considered well resolved.

Even if the boundary condition (U) is almost the same for the two simulations, the resulting boundary layers contain very different flows. In APG1

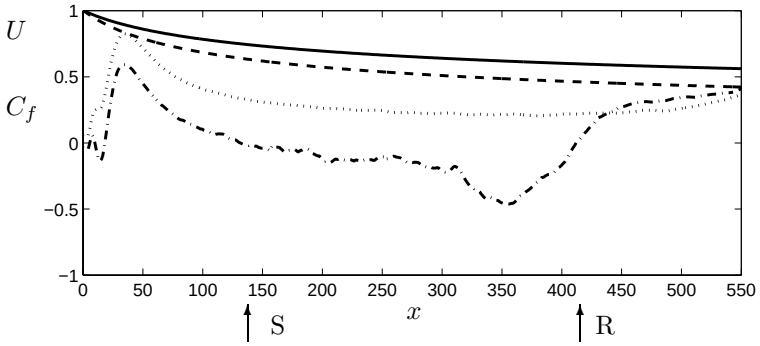

FIGURE 3. APG1: — U; $\cdots$ $C_f \times 100$. SEP: - - U; $-\cdot-$ $C_f \times 100$. S and R denotes point of separation and reattachment respectively for SEP.

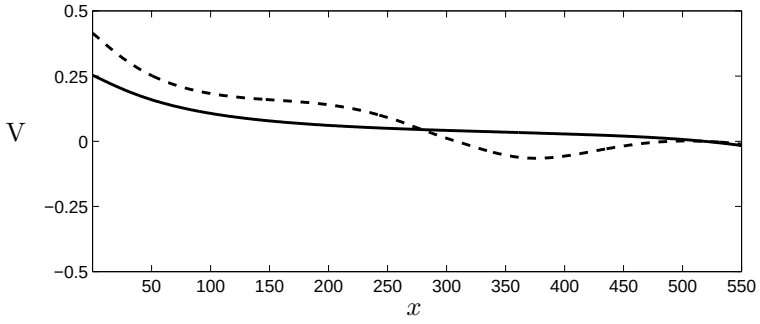

FIGURE 4. APG1: — V. SEP: - - V.

the boundary layer is subject to a strong APG, but is everywhere attached. In SEP the boundary layer is separated for a large portion of the computational domain. The resulting normal velocity at the freestream boundary (V) is shown for the two cases in figure 4.

The parameter β for APG1 is shown in figure 5, and is approximately constant. The shape factor from APG1 is almost exactly constant over the whole domain $x = 150 - 550$. The corresponding parameter β_p from SEP is also shown in figure 5 together with the shape factor. The boundary layer with separation is evidently not near equilibrium since β_p is not constant. The shape factor also varies strongly downstream as a consequence of the non-equilibrium as seen in figure 5.

Since β is constant in the APG1 case, it is possible to check the relation given by equation (26). Using β and H from APG1 (shown in figure 5), equation (26) yields an m close to -0.23, shown as the solid line in figure 6. However, the value of m was set to -0.25 in the simulation. The difference in the value of m is explained by the non-uniqueness of the two parameters in the freestream

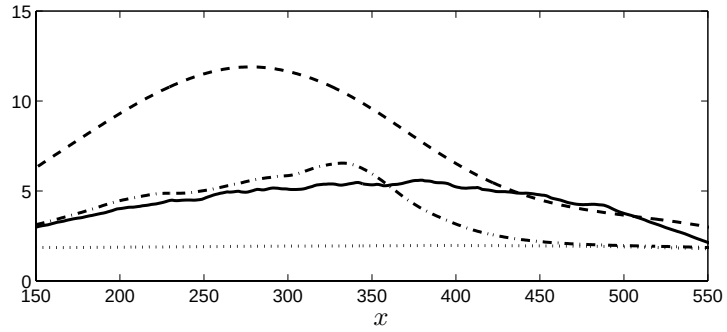

FIGURE 5. APG1: — β; $\cdots$ H. SEP: - - $\beta_p/10$; $-\cdot-$ H.

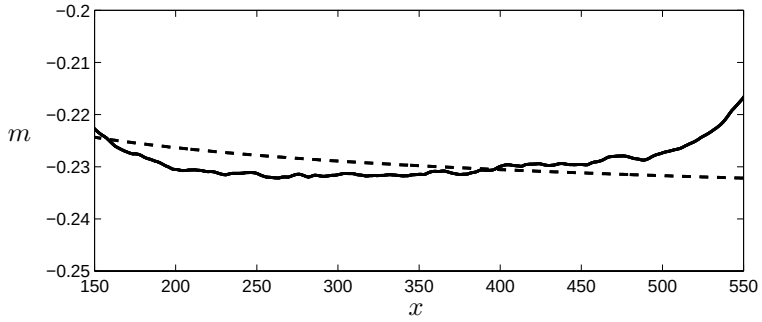

FIGURE 6. APG1: — m from equation (26); - - m from equation (44) with $x_0 = -50$.

velocity distribution. A specific distribution of U can be closely represented by different values of m and x_0. Thus, the imposed distribution of U can be obtained by applying a different set of the parameters m and x_0 than used in the definition of the distribution. However, the value of x_0 in the simulation can be determined by looking at the resulting outer length scale, Δ, shown in figure 7. The dashed line is equation (27) with $x_0 = -50$, thus a different value than the one used in the profile for U, which is $x_0 = -62$. By using the value of $x_0 = -50$, the exponent m can be calculated from the expression (44). The resulting m is shown as the dashed line in figure 6, matching approximately the m from equation (26). Thus, even if the freestream velocity is defined with the parameters $x_0 = -62$ and $m = -0.25$, the same freestream distribution is represented by $x_0 = -50$ (taken from the distribution of Δ) and $m \approx -0.23$ (the exact value of m is the dashed line in figure 6). These latter values of m and x_0 are the apparent parameters actually felt by the boundary layer and are called m^a and x_0^a in table 2.

The ratio between the two velocity scales (u_τ/u_p) is shown in figure 8 for the two cases. The ratio is fairly constant for APG1, and even in the case of separation the variation is not violent. This is in strong contrast to the rapid

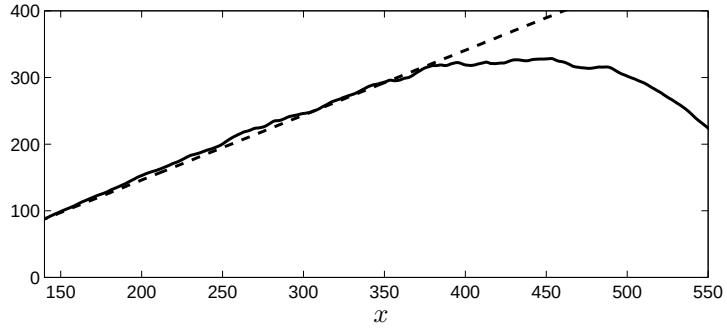

FIGURE 7. APG1: — Δ; - - equation (27) with $x_0 = -50$.

Case	m	x_0	m^a	x_0^a
APG1	-0.25	-62	-0.23	50
SEP	-0.35	-50		

TABLE 2. Freestream parameters. m and x_0 are the values in the simulation specifying the freestream velocity through equation (44). x_0^a and m^a are the actual values corresponding to equilibrium theory.

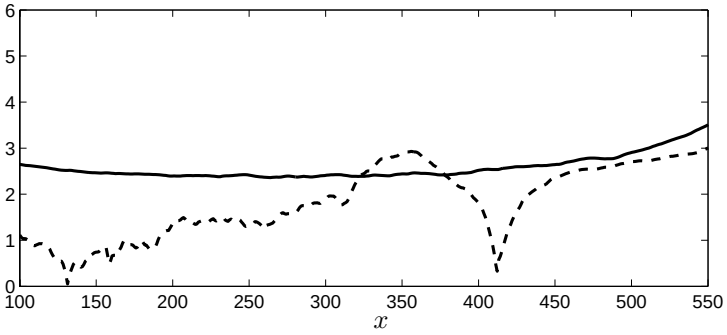

FIGURE 8. u_τ/u_p. APG1: — ; SEP: - -.

separation and attachment simulated by SC and NM. The constant ratio will have some consequences for the scaling of the velocity profiles shown in section 3.3.

The strong decrease in the skin friction before the reattachment cannot be explained by the mean momentum equation alone. The point of reattachment cannot be predicted either, but can be detected from the behavior of the normal velocity at the freestream boundary (figure 4). In the beginning of the computational domain the flow out of the box is generated by the strong decrease in the streamwise velocity. Later, the flow is inward, due to the fringe

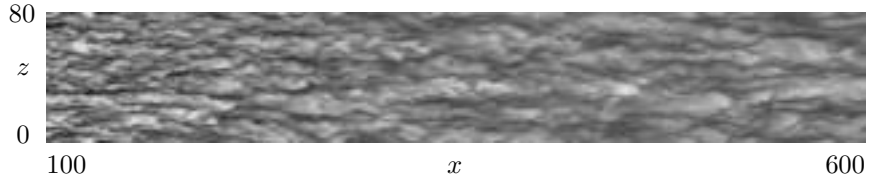

FIGURE 9. APG1: Streamwise velocity fluctuation in a plane at $y^+ = 10$. The dark area represents low-speed fluid

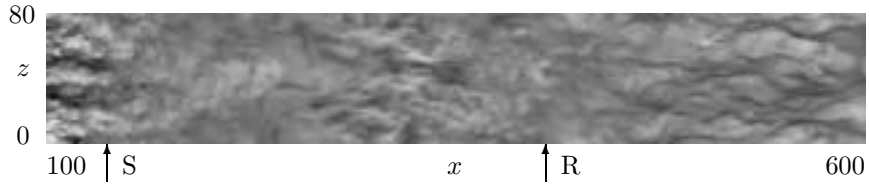

FIGURE 10. SEP: Streamwise velocity fluctuation in a plane at $y^+ = 10$. The dark area represents low-speed fluid

region, where the original, laminar boundary layer is restored. With a longer computational box, the point of reattachment would move downstream. The influence of the fringe is however not unphysical, since it only determines the boundary condition at the outflow. The boundary layer has to end somewhere, and this scenario is just one example. If a ZPG or APG layer is studied, where the exact form of the pressure gradient is important, the upstream influence of the fringe is important, since the equilibrium conditions are changed.

3.2.2. *Structures in the flow*

The streamwise velocity fluctuations form elongated structures near the wall in a ZPG boundary layer. It is generally thought that the structures are weakened in an APG flow. This is illustrated in figure 9, where shades of positive and negative fluctuations are shown for the APG1 case. The figure shows the whole computational box in the spanwise direction but the transitional part and fringe region are excluded in the streamwise direction. The normal position is $y^+ = 11.8$ in the beginning and $y^+ = 9.2$ at the end. The length in the streamwise direction is about 3400 in viscous units based on u_τ at $x = 350$. The structures are weakened at the end of the domain as compared with those in the beginning, showing the damping effect of the APG on the structures. The spacing between the structures increases from 100 (the same as for a ZPG layer) at the beginning to about 130 at the end, based on the local u_τ.

The SEP case is shown in figure 10. The normal position is also in this case around $y^+ = 10$ and the length of the region shown is about 2400. There are still some structures in the separated flow, though not at all as long and frequent as in APG1. Before separation, which occurs at approximately $x = 140$, the streaks are visible, but are rapidly vanishing in the beginning of the separated

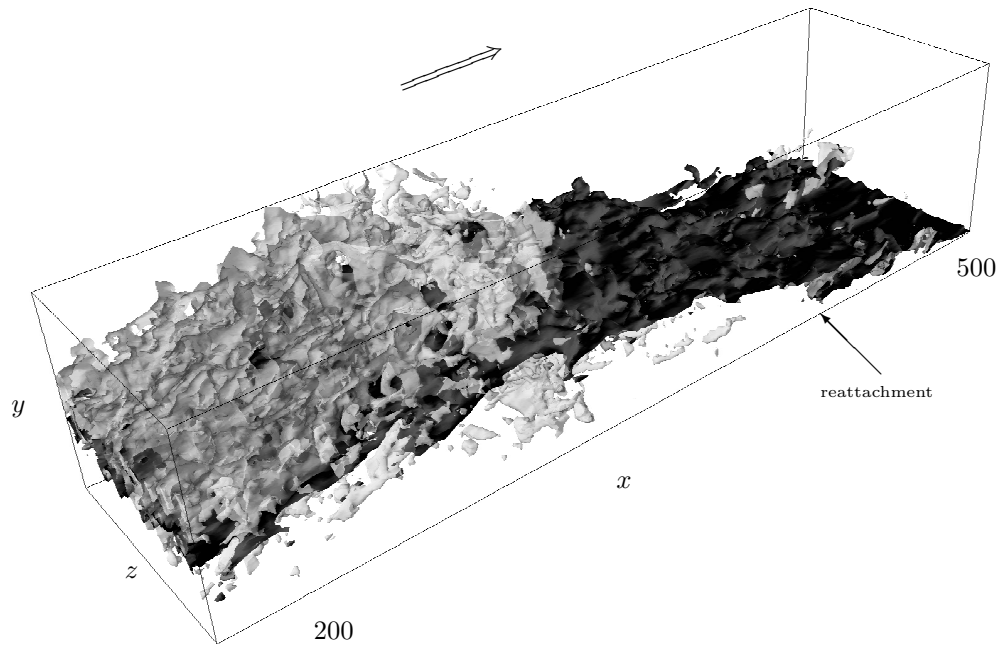

FIGURE 11. The separated boundary layer. Only a part of the computational box is shown. The light grey structures represent positive normal velocity and the darker ones represent positive streamwise velocity.

region. There is notable increase in the streak formation around $x = 350$, where the friction coefficient is at its lowest values, c.f. figure 3. Thus, there are indications that streaks may reappear in a separated region if the backflow is strong enough. After the reattachment at $x = 412$ the streaks are not immediately appearing, but are clearly visible after $x = 450$.

To illustrate some more features of the instantaneous flow structures in the separated case, contour plots of constant streamwise and normal velocity are plotted in a part of the computational box. In figures 11 and 12, the streamwise velocity, plotted in dark grey color, show a less ordered structure than in a ZPG boundary layer. However, the constant streamwise velocity show the same features above the separation bubble as after the reattachment point. The sheet formed by the constant value is bent upward over the recirculation region and comes down again when approaching reattachment. This is in agreement with various experimental observations, see the introduction. In figure 11, a positive constant value of the normal velocity is shown in light grey color. The

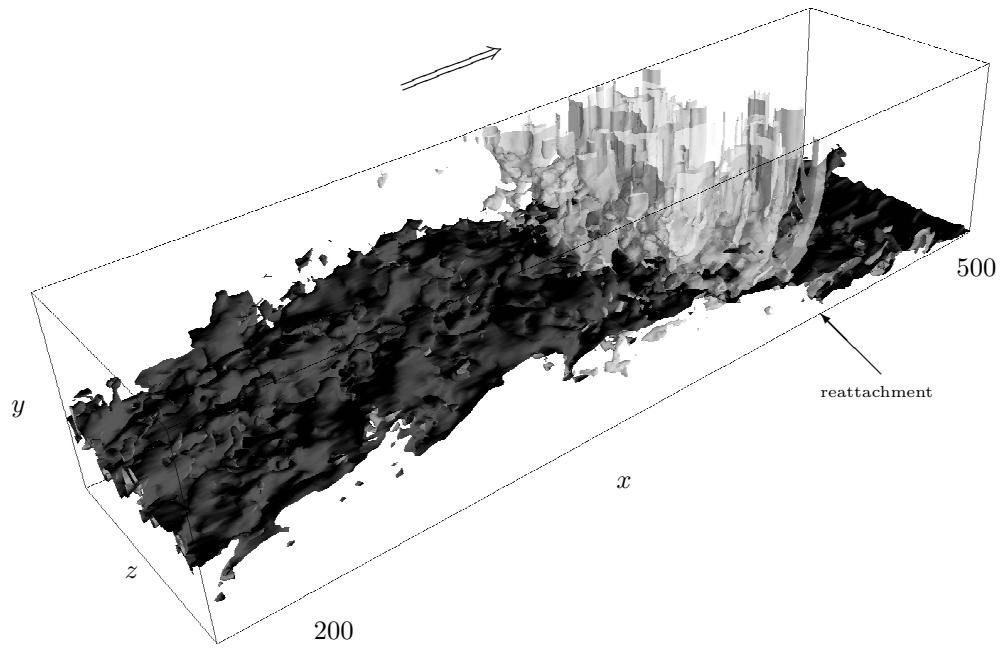

FIGURE 12. The separated boundary layer. Only a part of the computational box is shown. The light grey structures represent negative normal velocity and the darker ones represent positive streamwise velocity.

normal velocity is of the same disorganized form as the streamwise velocity. An opposite effect is revealed in figure 12, where a negative value of the normal velocity is shown. Here the structure is more ordered and forms tube-like structures where the fluid rushes from the freestream down towards the wall.

3.2.3. *Turbulence statistics*

A general description of the turbulent kinetic energy and its production is presented here. In this section the scaling of the turbulent statistics is based on the local freestream velocity. For the APG1 case the development of the turbulent kinetic energy is typical for an APG turbulent boundary layer. In figure 13 contours of constant levels of turbulent kinetic energy from 0.0005 to 0.006 are shown. The peak value is at all streamwise positions around 0.006. It is slightly larger in the beginning and decreases slowly downstream, while the position for the peak is shifted outward from $y = 4$ at $x = 150$ to $y = 18$ at $x = 550$. The turbulent kinetic energy development in SEP is more complicated

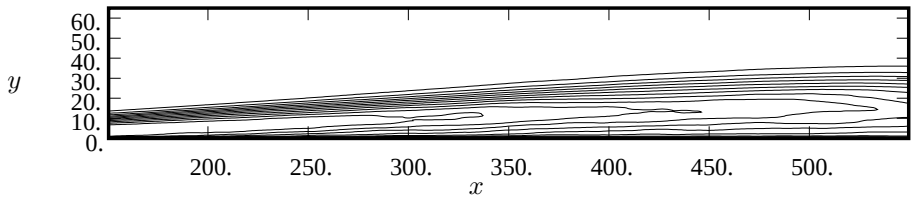

FIGURE 13. APG1: contours of turbulent kinetic energy.

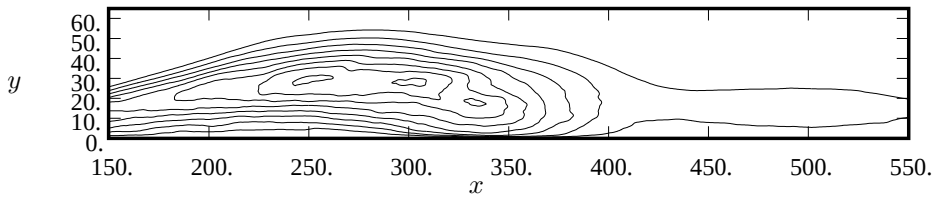

FIGURE 14. SEP: contours of turbulent kinetic energy.

and the discussion will be made with the aid of figure 14. In figure 14 contours of constant levels of turbulent kinetic energy from 0.005 to 0.025 are shown. At $x = 150$ the boundary layer has barely separated and the energy has one maximum of 0.0016 located far out in the boundary layer (approximately at $y = 18$). Further downstream, at position $x = 250$, the energy maximum has shifted outward to $y = 30$ with the larger value 0.025. The profile then stays approximately the same until the maximum starts to decrease and is moving towards the wall after $x = 330$. When comparing with the mean streamwise velocity in figure 15, it is noted that the peak in turbulent kinetic energy is located outside the recirculation zone. This was also noted by SC and Alving & Fernholz (1996) among others, (see the introduction in the present work). At $x = 350$ the profile of the energy is almost identical with the one at $x = 150$, but the maximum continues to decrease downstream, even though the location ($y = 18$) of the maximum is constant. The boundary layer is still subjected to an adverse pressure gradient, and the peak located far out in the boundary layer is a consequence of this. Nothing spectacular happens at the point of reattachment ($x = 412$). The peak value is stabilized after $x = 450$ at a value of 0.006, which is the same value as observed in the APG1 case.

The shear stress contribution to the production is shown in figure 16 for SEP. Approximately the same behavior as for the energy itself is observed up to $x = 330$. The maximum occurs closer to the wall, but still above the recirculation region. The streamwise Reynolds stresses do contribute to the production (not shown in the figure), but their contribution is fluctuating rapidly over the boundary layer and is much smaller than the production originating from

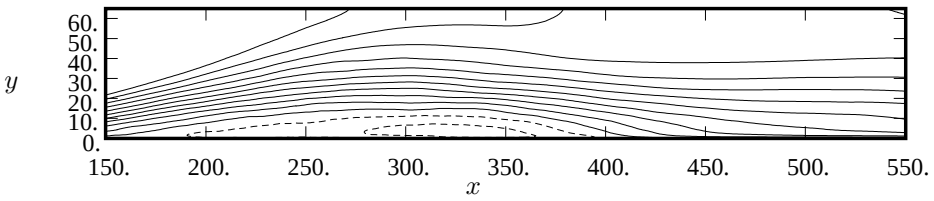

FIGURE 15. SEP: contours of mean velocity. Positive values shown as solid lines, negative as dashed.

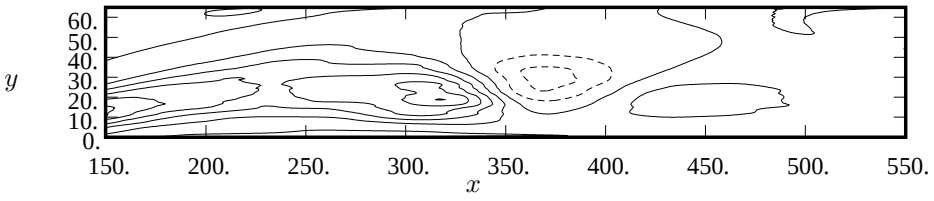

FIGURE 16. SEP: contours of production of turbulent kinetic energy. Positive values shown as solid lines, negative as dashed.

the shear stress, except close to the wall at some streamwise positions. From figure 16 it is also observed that there is a negative production (destruction) of turbulence kinetic energy in an area away from the wall, upstream of reattachment. This was also observed in the DNS of SC. The destruction is not a contribution from the streamwise production, but originates from positive values of the Reynolds shear stress in that region. In the DNS of NM no negative total production in the middle of the layer occurred, even if the production of Reynolds shear stress showed negative values both close to the wall and in the middle of the boundary layer. The destruction, and hence the positive values of the Reynolds shear stress, occur in the same region of the flow where the tube-like structures in the downward normal velocity are visible, c.f. figure 12.

3.3. *Comparison with analysis*

To compare the DNS data with the results from section 2, the mean flow profiles will be presented in different scalings and from different parts of the boundary layer. From figure 1 it is observed that the back-flow is very weak compared to the freestream velocity. The portion of the boundary layer where back-flow exists is small compared to the portion of positive streamwise velocity. But, the flow close to the wall is of course important, because it determines many of the features of the flow that are crucial from an engineering aspect.

From APG1 the data is compared with the results from the analysis of the TBLE for an attached boundary layer (section 2.1). From SEP the data

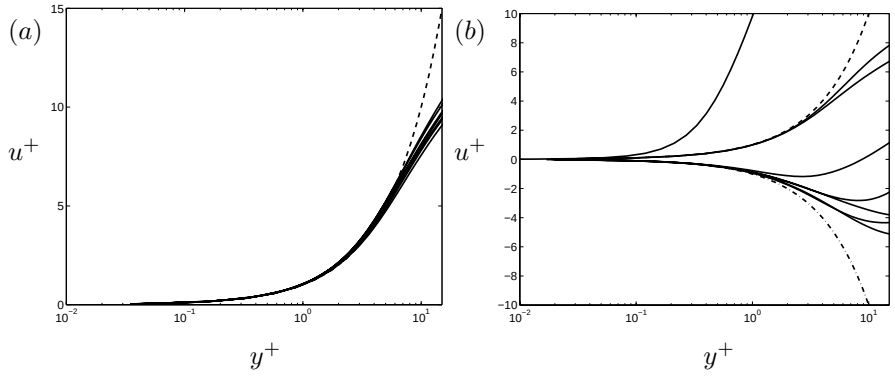

FIGURE 17. Velocity profiles at $x = 150$ to $x = 500$. a) APG1: — DNS; - - $u^+ = y^+$. b) SEP: — DNS; - - $u^+ = y^+$; -·- $u^+ = -y^+$.

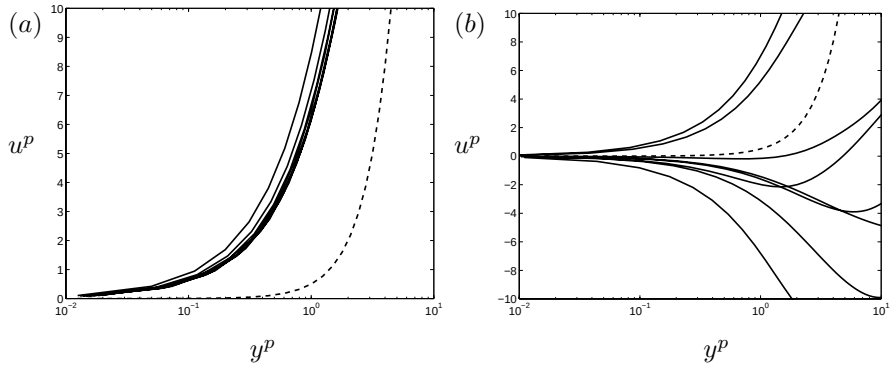

FIGURE 18. Velocity profiles at $x = 150$ to $x = 500$. a) APG1: — DNS; - - $u^p = \frac{1}{2}(y^p)^2$. b) SEP: — DNS; - - $u^p = \frac{1}{2}(y^p)^2$.

is compared with the results from the analysis of the TBLE for a separated boundary layer (section 2.2).

3.3.1. *The viscous sub-layer*

The near-wall profiles are plotted in the viscous scaling in figure 17 and are compared with the profiles given by the asymptotic versions of equations (9) and (35). For APG1 the collapse is good as seen in figure 17a. For the case SEP, shown in figure 17b, the profiles close to the $u^+ = y^+$ profile are the two in the attached region at positions $x = 450$ and $x = 500$. The profiles furthest from both asymptotes is from the positions closest to separation and reattachment, while the lowest (closest to $u^+ = -y^+$) is from the position with strongest back-flow.

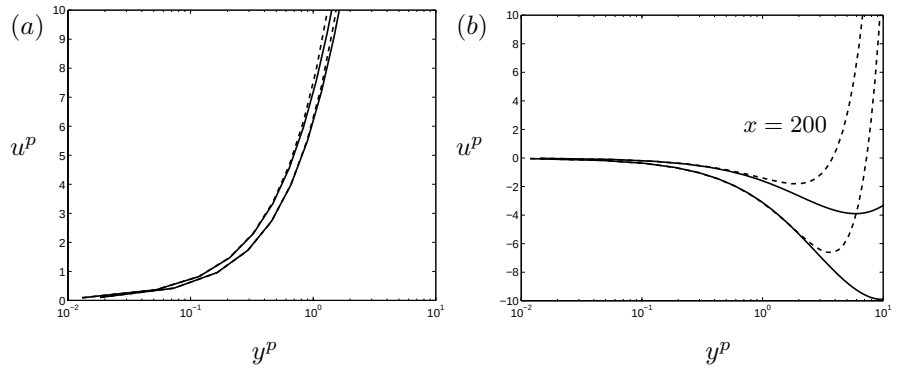

FIGURE 19. Velocity profiles in pressure gradient scaling. a) APG1: — DNS; - - $\frac{1}{2}(y^p)^2 + (\frac{u_\tau}{u_p})^2 y^p$. b) SEP: — DNS; - - $\frac{1}{2}(y^p)^2 - (\frac{u_\tau}{u_p})^2 y^p$.

In figure 18 the same profiles are shown in pressure gradient scaling and are compared with the profiles given by the asymptotic expression (36), which is the same for the attached and separated case. The spreading is the same as in the viscous scaling. That the profiles spread equally in the viscous scaling as in the pressure gradient scaling is due to the fact that the ratio u_τ/u_p is nearly constant, see figure 8. This is in strong contrast to the simulation of NM, where the variation in u_τ was enhanced by the rapidly growing pressure gradient. In their simulation, the velocity profiles collapsed much better when scaled with u_p than u_τ, (see Skote & Henningson (1999)). Figure 18 shows that the profiles are further from the asymptotic state (separation), than in the viscous scaling (figure 17), where the profiles showed some similarity with the asymptotic (ZPG) profile.

Velocity profiles in the pressure gradient scaling at two downstream positions are shown in figure 19, together with the theoretical expressions for the velocity profile in the viscous sub-layer. For APG1 (figure 19a) the positions are $x = 200$ and $x = 450$, and for SEP (figure 19b) they are $x = 200$ and $x = 300$. Here the asymptotic curve is not shown, but the pressure gradient dependent curves from equation (34) are shown. The DNS profiles and the corresponding curves given by equation (34) follow each other and show that even if the profiles are far from the asymptotic state (as shown in figure 18), the inclusion of the pressure gradient term gives a good agreement.

In summary, figure 17 shows that the scaling with u_τ works for APG1 but not for SEP. Figure 18 shows that the scaling with u_p does not work for APG1, nor for SEP, while figure 19 shows that with the inclusion of the pressure gradient term, the scaling with u_p works well in both cases.

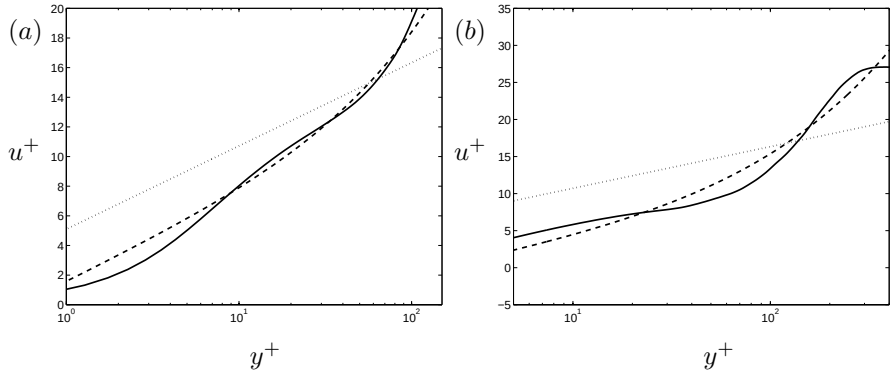

FIGURE 20. a) APG1: Velocity profile at $x = 350$. — DNS; - - equation (18) with $\kappa = 0.41$ and $B = 1.5$; $\cdots$ $u^+ = \frac{1}{0.41}\ln y^+ + 5.1$. b) SEP: Velocity profile at $x = 450$. — DNS; - - equation (18) with $\kappa = 0.41$ and $B = -2$; $\cdots$ $u^+ = \frac{1}{0.41}\ln y^+ + 5.1$.

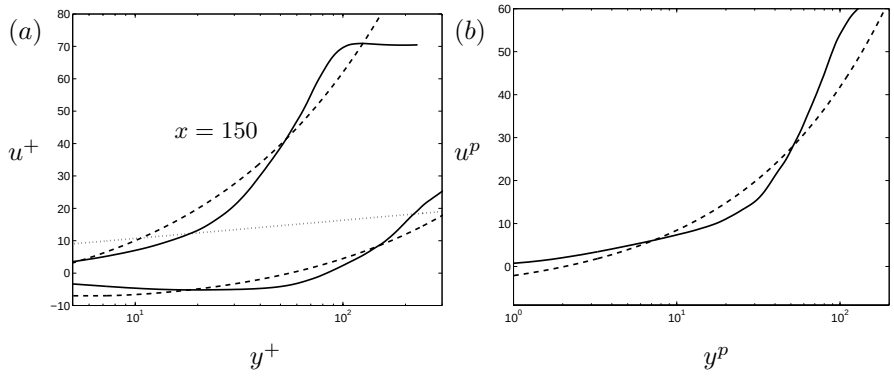

FIGURE 21. a) SEP: Velocity profiles at $x = 150$ and $x = 300$. — DNS; - - equation (38) with $\kappa = 0.41$ and $B = -7$; $\cdots$ $u^+ = \frac{1}{0.41}\ln y^+ + 5.1$. b) SEP: Velocity profile at reattachment $x = 412$. — DNS; - - $u^p = \frac{1}{0.41}2\sqrt{y^p} - 7$.

3.3.2. *The overlap region*

The laws presented in section 2.1.2 are compared with data from the simulations in figure 20. And the results from section 2.2 regarding the logarithmic region are presented in figure 21.

For APG1 the extended logarithmic law (18) gives profiles that are more in agreement than the usual ZPG logarithmic law, see figure 20a. However, the value of the additive constant B in equation (18), which has a value of -2 close to separation in both DNS and experiments, had to be set to $+1.5$ to fit the

DNS data in APG1. This is true for all streamwise positions, and hence the value of the additive constant seems to depend on the pressure gradient, and not the Reynolds number. In the attached region of separating boundary layer, the profile from equation (18) with $B = -2$ gives the best approximation, shown in figure 20b. This is in agreement with the earlier investigation of the flow just upstream of separation in the simulation of NM, see Skote & Henningson (1999).

The profiles in the separated region, figure 21a, are compared with the arctan law derived in section 2.2. The profile given by equation (38) is in much better agreement with DNS than the corresponding ZPG law, also shown in the figure. The additive constant is -7 for the separated case. It should also be noted that the extended logarithmic law derived for an attached layer under a strong APG, equation (18), gives a poor agreement with DNS data in the separated region (not shown in the figure). At the point of reattachment ($x = 412$) the profile is given in pressure gradient scaling in figure 21b. The asymptotic version of equation (39) is in good agreement with DNS data since u_τ is close to zero.

Thus, the conclusion is that the equations describing the overlap region derived in section 2 are in qualitative agreement with DNS data, and are far more consistent with DNS data than the corresponding ZPG laws.

However, due to the low Reynolds numbers, it is not possible to draw any definite conclusions regarding the overlap region. To properly clarify these matters, high Reynolds number data are required, and the experiments of Alving & Fernholz (1996) are therefore analyzed in section 4.

3.3.3. *The outer part*

As discussed earlier in section 2.1.3, there are many theories for describing the profiles in the outer part. All of these are at some point dependent on either experimental evidence or curve-fitting. An overall comparison and criticism of each of these theories is beyond the scope of the present investigation. In figure 22 the velocity profiles are plotted against the outer variable η for both cases but in different scalings. For APG1 the profiles collapse in the ZPG scaling despite the strong APG as seen in figure 22a. For the separated case in figure 22b, the profiles are shown in the pressure gradient scaling. The profiles are spread and do not collapse at all. However, the profiles collapse if plotted in the separated region and in the attached region separately, which is indicated with solid and dashed profiles. Thus, the profiles fall on a single curve if the distinction between the separated and attached region is made. However, since the viscous and pressure gradient velocity scales are almost constant throughout the boundary layer, the advantage with u_p over u_τ is confined to the point around separation or in a case where u_τ fluctuate more than u_p.

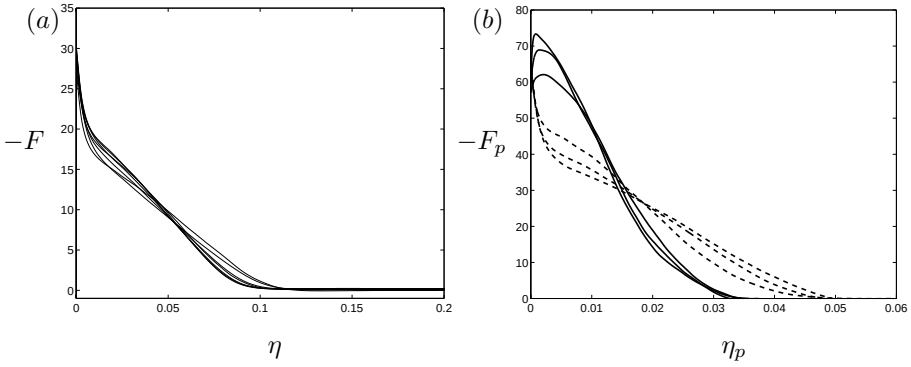

FIGURE 22. Velocity defect profiles at $x = 200$ — 500. a) APG1. b) SEP — $x = 250$, $x = 300$ and $x = 350$. - - $x = 450$, $x = 500$ and $x = 540$.

4. Discussion

In this section a comprehensive discussion about the relation between our results and others is presented.

4.1. *Comparison with earlier DNS*

The separated turbulent boundary layer simulated by DNS presented here has different characteristics compared to earlier DNS of a separation bubble. Efforts have earlier been made to create a bubble that starts and ends with a ZPG turbulent boundary layer. In the simulation presented here, the boundary layer is everywhere subject to an APG. To obtain a bubble with such a small extension in the streamwise direction as in the simulations of NM and SC, requires a strongly varying pressure gradient in order to force the boundary layer to separate and then reattach. The pressure gradient in those simulations was imposed by a strongly varying normal velocity at the freestream edge. This, in turn, creates a large normal gradient in the mean flow at the upper boundary. Here, the streamwise pressure gradient does not vary as rapidly as in the earlier DNS. However, the boundary layer reattaches upstream of the fringe region even if no favorable pressure gradient is applied. The variation of the normal velocity is much weaker than in NM, see figure 23. The freestream V varies approximately in the same way in SC as in NM.

The integrated quantities, such as the shape factor and momentum thickness, cannot be compared with data from earlier DNS of separated flow by SC and NM. This is due to the behavior of the velocity profiles at the freestream in those simulations. At some streamwise position the maximum value of u is located in the middle of the boundary layer, and the value at the upper boundary is three times lower. Figure 24 shows velocity profiles at the position of maximum back-flow from the three different simulations. The profiles from NM and SC show a considerable velocity gradient at the upper boundary, and

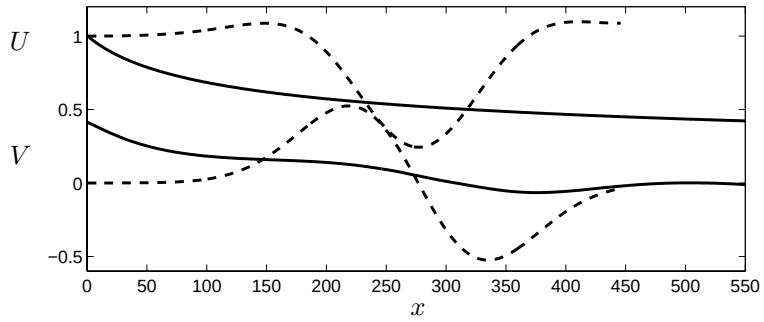

FIGURE 23. — V and U from SEP; - - V and U from NM. The profiles starting from unity is U.

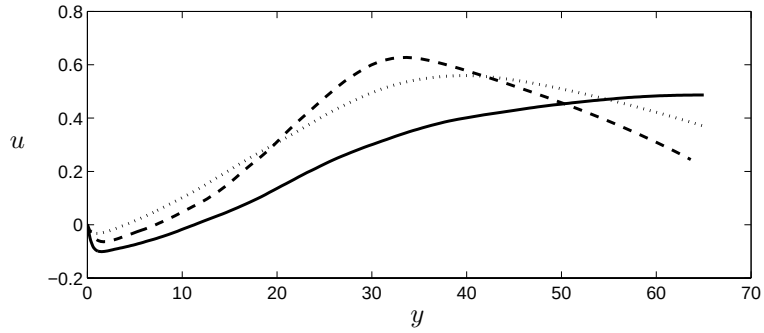

FIGURE 24. Velocity profiles. — from SEP; - - from NM; $\cdots$ from SC.

the value at the upper boundary of U varies strongly in NM, as seen from figure 23. Here the x values have been recalculated in our simulation coordinates. However, the relative starting positions of the boundary layers cannot be calculated and is here matched by letting the starting points of all three simulations be located at $x = 0$. Furthermore, from figure 24 it is clear that the back-flow is stronger in the present simulation than in NM and SC.

The strong gradient at the freestream makes it difficult to define a boundary layer edge. In the simulation presented here, no such ambiguity about the boundary layer edge and thickness exists. Since there was no real freestream in SC and NM, the friction coefficient, C_f, was calculated with the value of unity for the freestream velocity U at all streamwise positions. Comparison of the C_f from NM and SC with our simulation is made in figure 25. It is clear from figure 25 that our separation bubble is longer than the other two. In figure 25 the C_f from our simulation has been calculated using the same technique as in NM and SC, i.e. with a value of unity for the freestream velocity.

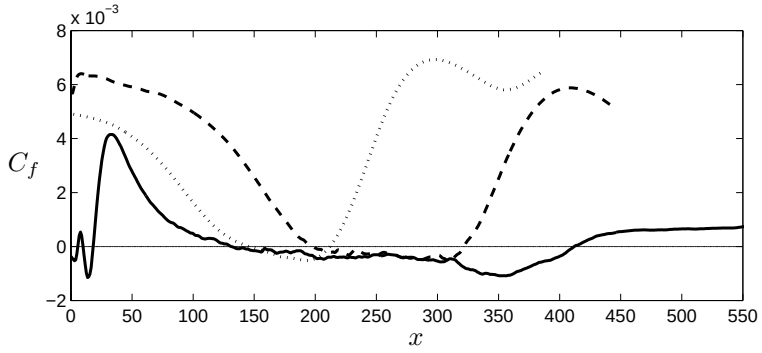

FIGURE 25. — C_f from SEP; - - C_f from NM; $\cdots$ C_f from SC.

4.2. *The overlap region in experiments*

To further investigate the theoretical expressions from section 2.1.2, but at a larger Reynolds number than is possible to reach with DNS, the experimental data from Alving & Fernholz (1996, 1995) are investigated.

In the work of Alving & Fernholz (1995) the velocity profiles showed considerable departure from the law of the wall valid for ZPG flow. By using the Perry-Schofield coordinates, modified by Dengel & Fernholz (1990), the curves were forced to collapse. However, the procedure of determining the velocity scale a posteriori, from the collapsed velocity profiles, make the analysis less valuable. The measured profiles are here examined from the other standpoint, the extended law of the wall. In figure 26 the profiles before separation and in the separated region are shown. Upstream of separation the extended logarithmic law (18) with the standard value of -2 for the additive constant predicts the profiles well. In the separated region (only one profile available) the profile given by equation (38) gives a better prediction than equation (18). However, a change in the additive constant in equation (18) can make the agreement with the experimental profile equally good.

Thus, the experimental data of Alving & Fernholz confirm and strengthen the conclusion drawn from our DNS data in section 3.3.2.

4.3. *Comparison with other theories for the overlap region*

A number of investigators have, with different methods, tried to obtain the theoretical velocity profile in APG flows, corresponding to the logarithmic profile in a ZPG flow.

According to Tennekes & Lumley (1972), the scaling with the pressure gradient velocity u_p (with $u_\tau = 0$) should lead to the same form of matching as in the zero pressure gradient case. From this assumption a logarithmic law is obtained in the same manner as the usual procedure of matching the outer

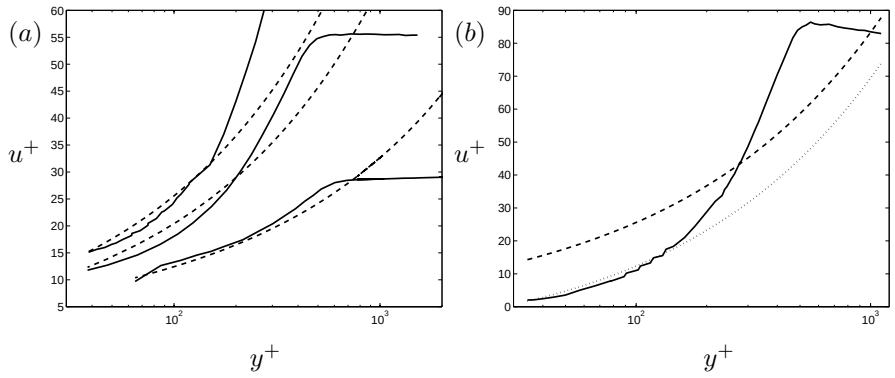

FIGURE 26. Experimental data from Alving & Fernholz (1995). a): Velocity profiles upstream of separation. - - equation (18) with $\kappa = 0.41$ and $B = -2$. b): Velocity profiles in the separated region. - - equation (18) with $\kappa = 0.41$ and $B = -2$. $\cdots$ equation (38) with $\kappa = 0.41$ and $B = -7$.

and inner solutions. The log law becomes,

$$u^p = \frac{1}{\kappa}\ln(y^p) + B. \tag{45}$$

This is clearly wrong, since the scaling with u_p leads to the the half-power law, equation (20).

According to Stratford (1959), the velocity profile should be a half-power law close to separation. Also Yaglom (1979) showed that a dimensional analysis gives the following expression for the velocity profile close to separation,

$$u^+ = K^+\sqrt{\lambda y^+} + K_1^+, \tag{46}$$

which can be expressed in pressure gradient scaling,

$$u^p = K\sqrt{y^p} + K_1. \tag{47}$$

Yaglom (1979) also proposed a fairly complicated dependence of K and K_1 on u_p and u_τ. This dependency was introduced to extend the theory valid at separation to the region upstream of detachment. It may not be regarded as a sound procedure to incorporate a functional behavior in constants of an expression valid only in an asymptotic state.

4.4. *Alternative scaling of the back-flow*

As suggested by Simpson (1983), the back-flow mean profiles may be scaled by the maximum mean back-flow velocity (u_N), together with the normal coordinate scaled with the distance from the wall to the maximum (N). The profiles scaled in this way are plotted in figure 27. Simpson (1983) also gives a logarithmic profile to be valid for $0.02 < y/N < 1.0$ with a constant A involved.

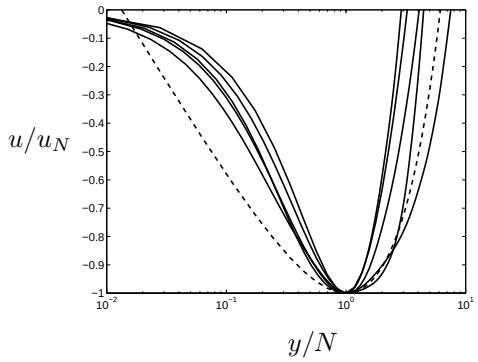

FIGURE 27. SEP: Velocity profiles at $x = 200$, $x = 250$, $x = 300$, $x = 350$ and $x = 400$. u_N and N are the maximum mean back-flow velocity and its distance from the wall. - - profile from equation (48)

$$\frac{u}{u_N} = A\left[\frac{y}{N} - \ln\left(\frac{y}{N}\right) - 1\right] - 1. \tag{48}$$

The constant A has been given a number of different values in numerous experimental investigations by, e.g. Dianat & Castro (1989) and Devenport & Sutton (1991). Thus, the law seems to be of limited value. For comparison, the profile given by equation (48) is also shown in figure 27 with $A = 0.3$ as suggested by Simpson (1983). The collapse of the profiles is poor, and the agreement with equation (48) is as bad as in the DNS of a backward-facing step by Le *et al.* (1997).

5. Conclusion

Direct numerical simulations of two turbulent boundary layers have been performed. The flows are subject to slightly different adverse pressure gradients, resulting in two very different flows. One is everywhere attached while the other is separated. The case with separation still forms a boundary layer with a clearly defined freestream edge, distinguishing it from earlier attempts to simulate a separation bubble.

The near-wall flow was shown to be predicted by a straightforward analysis of the turbulent boundary layer equations. The theory is based on two different velocity scales easily extracted from the parameters of the flow. Thus, the theory is applicable to turbulence modelling. Furthermore, it was possible to extend the theory to the case of separation.

The velocity profile in the viscous sub-layer was shown to obey a law dependent on the pressure gradient, in both the attached and separated cases. A velocity profile for the overlap region was derived and showed better consistency with DNS data than the corresponding law of the wall for a zero pressure gradient boundary layer. In the attached boundary layer the overlap profile consists

of square-root and logarithmic parts, while in the separated region it consists of square-root and arc-tangents functions.

The near-wall streaks are weakened by the adverse pressure gradient, and the spacing in viscous units is reduced. In the separated case streaks reappeared in the region with strong back-flow. The turbulent structures convecting from the region upstream of separation are lifted above the separation bubble, and are weakened before reaching reattachment. The normal velocity towards the wall in the vicinity of reattachment show a tube-like structure, where also positive Reynolds shear stress results in destruction of turbulence energy.

Comparison with earlier DNS of separated turbulent boundary layers shows that the present simulation is well resolved and has a stronger and larger recirculation region.

Acknowledgments

Computer time was provided by the Center for Parallel Computers (PDC) at the Royal Institute of Technology (KTH), the National Supercomputer Center in Sweden (NSC) at Linköping University, and the National Aerospace Laboratory (NAL) in Tokyo.

In addition we thank Doctor Naoki Hirose and coworkers for the help with implementing the code on the Numerical Wind Tunnel.

We would also like to thank Doctor Erik Lindborg and Professor Arne Johansson for fruitful discussions and for their valuable comments on the manuscript.

References

Afzal, N. 1996 Wake layer in a turbulent boundary layer with pressure gradient: a new approach. In *IUTAM Symposium on Asymptotic Methods for Turbulent Shear flows at High Reynolds Numbers* (ed. K. Gersten), pp. 95–118. Kluwer Academic Publishers.

Alvelius, K. & Skote, M. 2000 The performance of a spectral simulation code for turbulence on parallel computers with distributed memory. *Tech. Rep.* TRITA-MEK 2000:17. Royal Institute of Technology, Stockholm.

Alving, A. E. & Fernholz, H. H. 1995 Mean-velocity scaling in and around a mild, turbulent separation bubble. *Phys. Fluids* **7**, 1956–1969.

Alving, A. E. & Fernholz, H. H. 1996 Turbulence measurements around a mild separation bubble and downstream of reattachment. *J. Fluid Mech.* **322**, 297–328.

Bradshaw, P. 1967 The turbulent structure of equilibrium boundary layers. *J. Fluid Mech.* **29**, 625–645.

Cebeci, T. & Smith, A. M. O. 1974 *Analysis of Turbulent Boundary Layers*. Academic Press.

Coles, D. 1956 The law of the wake in the turbulent boundary layer. *J. Fluid Mech.* **1**, 191–226.

Dengel, P. & Fernholz, H. H. 1990 An experimental investigation of an incompressible turbulent boundary layer in the vicinity of separation. *J. Fluid Mech.* **212**, 615–636.

Devenport, W. J. & Sutton, E. P. 1991 Near-wall behavior of separated and reattaching flows. *AIAA J.* **29** (1), 25–31.

Dianat, M. & Castro, I. P. 1989 Measurements in separating boundary layers. *AIAA J.* **27** (6), 719–724.

Driver, D. M. 1991 Reynolds shear stress measurements in a separated boundary layer flow. AIAA Paper 91-1787.

Durbin, P. A. & Belcher, S. E. 1992 Scaling of adverse-pressure-gradient turbulent boundary layers. *J. Fluid Mech.* **238**, 699–722.

Hancock, P. E. 2000 Low reynolds number two-dimensional separated and reattaching turbulent shear flow. *J. Fluid Mech.* **410**, 101–122.

Henkes, R. A. W. M. 1998 Scaling of equilibrium boundary layers under adverse pressure gradient using turbulence models. *AIAA J.* **36**, 320–326.

Kader, B. A. & Yaglom, A. M. 1978 Similarity treatment of moving-equilibrium turbulent boundary layers in adverse pressure gradients. *J. Fluid Mech.* **89**, 305–342.

Le, H., Moin, P. & Kim, J. 1997 Direct numerical simulation of turbulent flow over a backward-facing step. *J. Fluid Mech.* **330**, 349–374.

Lundbladh, A., Berlin, S., Skote, M., Hildings, C., Choi, J., Kim, J. & Henningson, D. S. 1999 An efficient spectral method for simulation of incompressible flow over a flat plate. *Tech. Rep.* TRITA-MEK 1999:11. Royal Institute of Technology, Stockholm.

McDonald, H. 1969 The effect of pressure gradient on the law of the wall in turbulent flow. *J. Fluid Mech.* **35**, 311–336.

Mellor, G. L. 1966 The effects of pressure gradients on turbulent flow near a smooth wall. *J. Fluid Mech.* **24**, 255–274.

Mellor, G. L. 1972 The large reynolds number, asymptotic theory of turbulent boundary layers. *Intl J. Engng Sci.* **10**, 851–873.

Melnik, R. E. 1989 An asymptotic theory of turbulent separation. *Computers & Fluids* **17**, 165–184.

Musker, A. J. 1979 Explicit expression for the smooth wall velocity distribution in a turbulent boundary layer. *AIAA J.* **17**, 655–657.

Na, Y. & Moin, P. 1998*a* Direct numerical simulation of a separated turbulent boundary layer. *J. Fluid Mech.* **374**, 379–405.

Na, Y. & Moin, P. 1998*b* The structure of wall-pressure fluctuations in turbulent boundary layers with adverse pressure gradient and separation. *J. Fluid Mech.* **377**, 347–373.

Nordström, J., Nordin, N. & Henningson, D. S. 1999 The fringe region technique and the fourier method used in the direct numerical simulation of spatially evolving viscous flows. *SIAM J. Sci. Comp.* **20** (4), 1365–1393.

Perry, A. E. 1966 Turbulent boundary layers in decreasing adverse pressure gradients. *J. Fluid Mech.* **26**, 481–506.

Perry, A. E. & Fairlie, B. D. 1975 A study of turbulent boundary-layer separation and reattachment. *J. Fluid Mech.* **69**, 657–672.

Perry, A. E. & Schofield, W. H. 1973 Mean velocity and shear stress distributions in turbulent boundary layers. *Phys. Fluids* **16** (12), 2068–2074.

Rotta, J. C. 1962 Turbulent boundary layers in incompressible flow. *Prog. Aerospace Sci.* **2**, 3–219.

Samuel, A. E. & Joubert, P. N. 1974 A boundary layer developing in an increasingly adverse pressure gradient. *J. Fluid Mech.* **66**, 481–505.

Schlichting, H. 1979 *Boundary layer theory*. McGraw-Hill.

Schofield, W. H. 1981 Equilibrium boundary layers in moderate to strong adverse pressure gradients. *J. Fluid Mech.* **113**, 91–122.

Simpson, R. L. 1983 A model for the backflow mean velocity profile. *AIAA J.* **21** (1), 142–143.

Simpson, R. L. 1996 Aspects of turbulent boundary-layer separation. *Prog. Aerospace Sci.* **32**, 457–521.

Simpson, R. L., Chew, Y.-T. & Shivaprasad, B. G. 1981*a* The structure of a separating turbulent boundary layer. part 1. mean flow and reynolds stresses. *J. Fluid Mech.* **113**, 23–51.

Simpson, R. L., Chew, Y.-T. & Shivaprasad, B. G. 1981*b* The structure of a separating turbulent boundary layer. part 2. higher-order turbulence results. *J. Fluid Mech.* **113**, 53–73.

Simpson, R. L., Strickland, J. H. & Barr, P. W. 1977 Features of a separating turbulent boundary layer in the vicinity of separation. *J. Fluid Mech.* **79**, 553–594.

Skåre, P. E. & Krogstad, P.-Å. 1994 A turbulent equilibrium boundary layer near separation. *J. Fluid Mech.* **272**, 319–348.

Skote, M., Henkes, R. A. W. M. & Henningson, D. S. 1998 Direct numerical simulation of self-similar turbulent boundary layers in adverse pressure gradients. *Flow, Turbulence and Combustion* **60**, 47–85.

Skote, M. & Henningson, D. 1999 Analysis of the data base from a dns of a separating turbulent boundary layer. Center for Turbulence Research, Annual Research Briefs 1999, 225–237.

Spalart, P. R. & Coleman, G. N. 1997 Numerical study of a separation bubble with heat transfer. *European J. Mechanics B/Fluids* **16**, 169.

Spalart, P. R. & Watmuff, J. H. 1993 Experimental and numerical study of a turbulent boundary layer with pressure gradients. *J. Fluid Mech.* **249**, 337–371.

Stratford, B. S. 1959 The prediction of separation of the turbulent boundary layer. *J. Fluid Mech.* **5**, 1–16.

Tennekes, H. & Lumley, J. L. 1972 *A First Course in Turbulence*. The MIT Press.

Townsend, A. A. 1961 Equilibrium layers and wall turbulence. *J. Fluid Mech.* **11**, 97–120.

Yaglom, A. M. 1979 Similarity laws for constant-pressure and pressure-gradient turbulent wall flows. *Ann. Rev. Fluid Mech.* **11**, 505–40.

Yajnik, K. S. 1970 Asymptotic theory of turbulent shear flows. *J. Fluid Mech.* **42**, 411–427.

Paper 5

P5

Near-wall damping in model predictions of separated flows

By Martin Skote[*] and Stefan Wallin[†]

Data from the near-wall region of an attached and a separated turbulent boundary layer are used for the development of near-wall damping functions utilized in turbulence modelling. The model considered is an explicit algebraic Reynolds stress model. The data are taken from two direct numerical simulations. The turbulent boundary layer equation is analyzed in order to extend the validity of existing wall damping functions to turbulent boundary layers under severe adverse pressure gradients.

1. Introduction

Two turbulent boundary layers subject to adverse pressure gradients (APG) were investigated through direct numerical simulation (DNS) by Skote & Henningson (2000). The two APG distributions are quite similar, but the influence of the APG on the flow is strong, creating two very different boundary layer flows. One is everywhere attached (APG1), and the other is separated for a long streamwise section (SEP).

The data are here used for assessing the near-wall scaling of wall damping functions used in turbulence modelling. The particular model studied is the fully self-consistent explicit algebraic Reynolds stress model (EARSM) developed by Wallin & Johansson (2000), which can, in contrast to standard eddy-viscosity two-equation models, be successfully damped in the vicinity of a wall in zero pressure-gradient boundary layers by employing the standard van Driest damping function.

A relevant velocity scale is crucial for the correct behaviour of wall damping functions used in turbulence models. For a zero pressure gradient (ZPG) boundary layer, the damping functions and boundary conditions in the logarithmic layer are based on a theory in which the friction velocity,

$$u_\tau \equiv \sqrt{\nu \left.\frac{\partial u}{\partial y}\right|_{y=0}}, \tag{1}$$

is used as a velocity scale. However, in the case of a boundary layer under an APG, u_τ is not the relevant velocity scale, especially not for a strong APG

[*]Department of Mechanics, KTH, SE-100 44 Stockholm, Sweden
[†]Aeronautical Research Institute of Sweden,Box 11021, SE-161 11 Bromma, Sweden

and low Reynolds number. In the case of separation this is clear since u_τ becomes zero. Wall damping functions based on $y^+ \equiv yu_\tau/\nu$ are, thus, not appropriate. Other possibilities than y^+ that are used in near-wall damping functions are $Re_y \equiv \sqrt{K}y/\nu$ or the turbulent Reynolds number $Re_t \equiv K^2/\nu\varepsilon$ (see e.g. Wilcox (1993)). These alternatives do not have the singularity caused by that u_τ becomes zero.

The scaling laws developed in many previous studies have been in a form not suitable for turbulence models. Instead, the aim for the scaling of the velocity profile has often been to create a tool for different prediction methods based on the simplified turbulent boundary-layer equations (TBLE). The motivation for the thorough scaling analysis performed here is that the turbulence modelling can be improved if the correct scaling is used. However, the scalings are entirely motivated by the TBLE itself, i.e. turbulence modelling is disregarded when performing the scaling analysis of the TBLE.

Many of the earlier theoretical analyses were not performed with the same objectives as we have today. Hence, the results, though interesting in many aspects, perhaps lack a natural potential for direct application to the final goal — to calculate and predict a turbulent boundary layer flow.

Some basic ideas concerning the velocity scale in the inner part of the turbulent boundary layer under an APG are presented in section 2. It is shown that the total shear stress varies linearly in a turbulent boundary layer under an APG, if the Reynolds number is not large compared with the APG. The linear behaviour leads to a velocity scale dependent on the normal coordinate, replacing the friction velocity as a velocity scale.

The new velocity scale is used in the wall damping of the EARSM model in section 3. Comparison with the damping based on Re_y proposed by Wallin & Johansson (2000) is made, and an example of the performance of EARSM with the improved damping is given.

2. Scalings in the near-wall region

When neglecting the non-linear, advective terms in the equations describing the mean flow, the equation governing the inner part of the boundary layer is obtained. This equation can, when using the inner length and velocity scales ν/u_τ and u_τ be written,

$$0 = -\frac{\nu}{u_\tau^3}\frac{1}{\rho}\frac{dP}{dx} + \frac{d^2u^+}{dy^{+2}} - \frac{d}{dy^+}\langle u'v'\rangle^+, \tag{2}$$

where $\langle u'v'\rangle$ is the Reynolds shear stress. If the term involving the pressure gradient is smaller than the other terms, the equation reduces to the equation governing the inner part of a ZPG boundary layer. However, for strong APG cases at finite Reynolds numbers, this term cannot be neglected. Equation (2) can be integrated to give an expression for the total shear stress,

$$\tau^+ \equiv \frac{du^+}{dy^+} - \langle u'v'\rangle^+ = 1 + \frac{\nu}{u_\tau^3}\frac{1}{\rho}\frac{dP}{dx}y^+. \tag{3}$$

For a zero pressure gradient case, equation (3) predicts a constant shear stress of unity. For an APG case with a freestream distribution of the form $U \sim x^m$, the last term in equation (3) can be shown (Skote *et al.* 1998) to decrease with increasing Reynolds number.

When considering a strong APG or separation, A singularity occurs when u_τ becomes zero, which can be avoided by introducing the velocity scale,

$$u_p \equiv \left(\nu \frac{1}{\rho} \frac{dP}{dx}\right)^{1/3}. \tag{4}$$

First equation (3) is formulated as

$$\tau^+ = 1 + \left(\frac{u_p}{u_\tau}\right)^3 y^+. \tag{5}$$

The velocity scale u_p has to be used instead of u_τ if the last term in equation (5) becomes very large which happens if $u_\tau \ll u_p$, i.e. the boundary layer is close to separation. This was noted by Stratford (1959), Townsend (1961) and Tennekes & Lumley (1972). By multiplying equation (5) by $(u_p/u_\tau)^2$, the following expression for $\tau^p \equiv \tau/u_p^2$ as a function of $y^p \equiv y u_p/\nu$ is obtained,

$$\tau^p = y^p + \left(\frac{u_\tau}{u_p}\right)^2. \tag{6}$$

Equation (6) has the asymptotic form $\tau^p = y^p$ when separation is approached. Thus, in this rescaled form, the singularity is avoided.

For the ZPG case, the scaling of the total shear stress with u_τ gives a self-similar profile ($\tau^+ = 1$). From equations (5) and (6) it is observed that neither u_τ nor u_p as velocity scale results in a self-similar expression. However, equation (3) can be formulated as

$$\tau^* \equiv \frac{1}{u_*^2}\left(\nu \frac{\partial u}{\partial y} - \langle u'v' \rangle\right) = 1, \tag{7}$$

where u_* is a velocity scale that depends on y and can be expressed in either plus or pressure gradient units,

$$u_*^2 = u_\tau^2 + \frac{u_p^3}{u_\tau} y^+ = u_\tau^2 + u_p^2 y^p. \tag{8}$$

Thus, by scaling the total shear stress with u_*, a self-similar expression is obtained ($\tau^* = 1$). The velocity scale u_* reduces to u_τ if u_p becomes zero, i.e. for a ZPG boundary layer. If instead u_τ becomes zero, i.e. a boundary layer at separation, the velocity scales becomes $u_* = u_p\sqrt{y^p}$.

For the special case with $u_\tau = 0$, the velocity scale u_* is zero at the wall. This is natural since the velocity gradient is zero at the wall. Previous investigators of the mixing length theory have also observed the importance of u_*, see Granville (1989) for references.

From u_* it is possible to define the length scale ν/u_*, and thus a normalized normal coordinate, $y^* \equiv yu_*/\nu$ which can be written,

$$y^* = \sqrt{(y^+)^2 + (y^p)^3}. \tag{9}$$

If a separated flow is considered, the definition of u_τ has to be reconsidered. In the separated region, $\frac{\partial u}{\partial y}$ is negative. Thus, the definition of u_τ in equation (1) involves a square root of a negative number. Instead, the definition will be changed so that the square root will be taken of a positive number.

To proceed with the analysis of the equations, the definition of the friction velocity will have to be changed to

$$u_\tau \equiv \sqrt{-\nu \frac{\partial u}{\partial y}\bigg|_{y=0}}. \tag{10}$$

In the case of a separated flow, the change of sign of the wall shear stress leads to a u_* as,

$$u_*^2 = -u_\tau^2 + \frac{u_p^3}{u_\tau} y^+ \tag{11}$$

The velocity scale u_*^2 is in the case of separation negative for $y^+ < (u_\tau/u_p)^3$, because the shear stress is negative at those values of y^+. Hence, the length scale ν/u_* has to be used with a restriction to positive values of u_*^2. This leads to a y^* of the form,

$$y^* = \sqrt{\max\{0, -(y^+)^2 + (y^p)^3\}}. \tag{12}$$

3. Evaluation of turbulence models

The aim with this part of the work is to investigate how predictions of turbulent boundary layer flow is affected by the complication of a severe APG and separation. In the near-wall part of the flow, turbulence models often utilize damping functions. Their purpose is to damp various physical quantities in the neighborhood of a wall. One important step towards better model predictions in APG flows is the refinement of the damping functions.

The results regarding the near-wall flow reported in Skote & Henningson (1999) and Skote & Henningson (2000) can be utilized in turbulence model predictions directly as, so called, wall-function boundary conditions. Here we are instead interested in resolving the turbulent boundary layer all the way to the wall and thus the wall damping functions become important.

A short description of the DNS and the turbulent boundary layer flows is given in section 3.1. The specific turbulence model used in the present work (EARSM), is described in section 3.2. A priori tests done with DNS data from both simulations are presented in section 3.3, together with the development of damping functions. The relation between two length scales used in the near-wall damping is analyzed in section 3.4. In section 3.5 some examples of the performance of the EARSM model is shown, using the data from DNS.

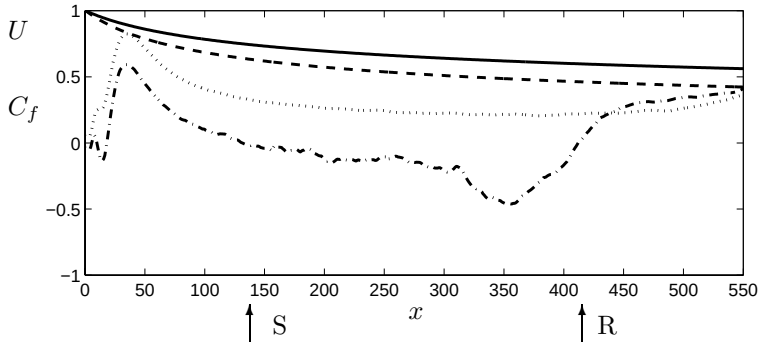

FIGURE 1. APG1: — U; $\cdots$ $C_f \times 100$. SEP: - - U; $-\cdot-$ $C_f \times 100$. S and R denote the points of separation and reattachment respectively for SEP.

	APG1	SEP		
	$x = 150$	$x = 300$	$x = 412$	$x = 450$
U	0.73	0.51	0.46	0.45
u_τ	0.0287	0.0165	0.0024	0.0166
u_p	0.0117	0.0086	0.0074	0.0071

TABLE 1. Some parameters of the turbulent boundary layers at different downstream positions.

3.1. *Description of the test cases*

The data from the two turbulent boundary layers considered in the present work were taken from a DNS performed by Skote & Henningson (2000).

The freestream velocity (U) for the two simulations, APG1 and SEP, are shown in figure 1, together with the skin friction (C_f). As seen from the figure, a small change in the freestream velocity has a great impact on the skin friction. In APG1, the boundary layer is subject to a strong APG, but is everywhere attached. In SEP the boundary layer is separated for a large portion of the computational domain.

The simulations start with a laminar boundary layer at the inflow ($x = 0$) which is triggered to transition by a random volume force near the wall. The flow is fully turbulent at $x = 100$.

The downstream coordinate x is scaled with the displacement thickness (δ^*) at the starting position of the simulation ($x = 0$), where the flow is laminar and $Re_{\delta^*} = 400$.

Table 3.1 serves as a comparison of the two cases at the downstream positions investigated in the present work.

3.2. *The basic models*

In two-dimensional mean flows, the fully self-consistent explicit algebraic Reynolds stress model may be formulated based on any (quasi-)linear pressure-strain model (see Wallin & Johansson (2000) and Girimaji (1997) for details). Neglecting the advection and diffusion of the Reynolds stress anisotropy $a_{ij} \equiv \langle u_i' u_j' \rangle / K - 2\delta_{ij}/3$ results in an implicit and non-linear relation

$$\begin{aligned} 0 = & \left(A_3 + A_4 \frac{\mathcal{P}}{\varepsilon} \right) a_{ij} + A_1 S_{ij} - (a_{ik}\Omega_{kj} - \Omega_{ik}a_{kj}) \\ & + A_2 \left(a_{ik}S_{kj} + S_{ik}a_{kj} - \frac{2}{3} a_{kl}S_{lk}\delta_{ij} \right). \end{aligned} \tag{13}$$

where $S_{ij} \equiv \tau/2(U_{i,j} + U_{j,i})$ and $\Omega_{ij} \equiv \tau/2(U_{i,j} - U_{j,i})$ are the symmetric and antisymmetric parts of the velocity gradient tensor normalized by the turbulent time scale $\tau \equiv K/\varepsilon$.

In a two-dimensional mean flow the solution for the anisotropy becomes

$$\begin{aligned} a_{12} &= \beta_1 S_{12} + 2\beta_4 S_{11}\Omega_{12} \\ a_{11} &= \beta_1 S_{11} + \beta_2 \left(S_{11}^2 + S_{12}^2 - \frac{1}{3} II_S \right) - 2\beta_4 S_{12}\Omega_{12} \\ a_{22} &= -\beta_1 S_{11} + \beta_2 \left(S_{11}^2 + S_{12}^2 - \frac{1}{3} II_S \right) + 2\beta_4 S_{12}\Omega_{12} \\ a_{33} &= \beta_2 \left(-\frac{1}{3} II_S \right) \end{aligned} \tag{14}$$

where the β coefficients are functions of the flow invariants $II_S \equiv S_{ij}S_{ji}$ and $II_\Omega \equiv \Omega_{ij}\Omega_{ji}$ and the model coefficients A_{1-4} in equation (13). Two different EARSMs will be considered; the "W&J" model, Wallin & Johansson (2000), based on a recalibrated LRR (Launder *et al.* 1975) pressure-strain rate model and the "Gir" model, Girimaji (1997), based on the linearized SSG (Speziale *et al.* 1991) pressure-strain rate model. The corresponding A_{1-4} coefficients are given in table 3.2. The "W&J" model results in that the β_2 coefficient is zero and as a consequence $a_{33} = 0$.

In two-dimensional mean flows the β coefficients are given by

$$\beta_1 = -\frac{A_1 N}{Q}, \quad \beta_2 = 2\frac{A_1 A_2}{Q}, \quad \beta_4 = -\frac{A_1}{Q}, \tag{15}$$

where the denominator is

$$Q = N^2 - 2II_\Omega - \frac{2}{3} A_2^2 II_S. \tag{16}$$

	A_1	A_2	A_3	A_4
W&J (Recalibrated LRR)	1.20	0	1.80	2.25
Gir (Linearized SSG)	1.22	0.47	0.88	2.37

TABLE 2. The values of the A-coefficients for different quasi-linear pressure-strain models.

N is given by

$$N = \begin{cases} \frac{A_3}{3} + \left(P_1 + \sqrt{P_2}\right)^{1/3} + \text{sign}\left(P_1 - \sqrt{P_2}\right) \mid P_1 - \sqrt{P_2} \mid^{1/3}, & P_2 \geq 0 \\ \frac{A_3}{3} + 2\left(P_1^2 - P_2\right)^{1/6} \cos\left(\frac{1}{3}\arccos\left(\frac{P_1}{\sqrt{P_1^2 - P_2}}\right)\right), & P_2 < 0 \end{cases} \tag{17}$$

where

$$\begin{aligned} P_1 &= \left(\frac{{A_3}^2}{27} + \left(\frac{A_1 A_4}{6} - \frac{2}{9}{A_2}^2\right) II_S - \frac{2}{3} II_\Omega\right) A_3 \\ P_2 &= P_1^2 - \left(\frac{{A_3}^2}{9} + \left(\frac{A_1 A_4}{3} + \frac{2}{9}{A_2}^2\right) II_S + \frac{2}{3} II_\Omega\right)^3 . \end{aligned} \tag{18}$$

3.3. *Near-wall treatments*

In the model proposed by Wallin & Johansson (2000) the correct near-wall behaviour for zero pressure-gradient boundary layers was obtained by modifying the β coefficients using a damping function of the van Driest type. The original form was based on y^+, but an alternative suggestion of the damping function was based on $y^T = y^T(Re_y)$ in order of avoiding the singularity in separated flows. The function y^T was constructed to be similar to y^+ for $y^+ < 100$ in zero pressure-gradient boundary layers. In this section the different near-wall scalings will be assessed by comparing model predictions using y^+, y^T as well as y^*.

In a two-dimensional mean flow the near-wall corrections for the "W&J" model reads

$$\begin{aligned} \beta_1 &= f_1 \beta_1^* \\ \beta_2 &= f_1^2 \beta_2^* + (1 - f_1^2) \frac{3B_2 - 4}{\max\left(II_S, II_S^{eq}\right)} \\ \beta_4 &= f_1^2 \beta_4^* - (1 - f_1^2) \frac{B_2}{2\max\left(II_S, II_S^{eq}\right)} \end{aligned} \tag{19}$$

where β_1^*, β_2^* and β_4^* are the "high-Re" uncorrected coefficients given by (15) and the damping function

$$f_1 = 1 - \exp(-y^+/A^+) \tag{20}$$

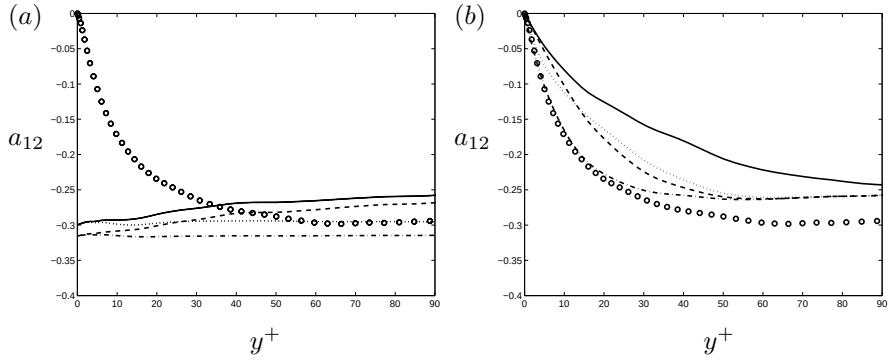

FIGURE 2. APG1 at $x = 150$: (a) ∘ DNS; — non-damped "W&J"; ⋯ non-damped "W&J" with $\beta_4 = 0$; - - non-damped "Gir"; -·- non-damped "Gir" with $\beta_4 = 0$. (b) ∘ DNS. Damped "W&J" with the scaled coordinate in f_1 as — y^+; - - y^*; ⋯ y^T. -·- damped "W&J" with y^+ and $A^+ = 11$.

and the model coefficients

$$\Pi_S^{eq} = 5.74 \qquad B_2 = 1.8 \tag{21}$$

For the damped expressions the turbulent time scale used for normalizing the velocity gradient tensors must be limited by the viscous scale, such as

$$\tau \equiv \max\left(\frac{K}{\varepsilon}, C_\tau\sqrt{\frac{\nu}{\varepsilon}}\right) \tag{22}$$

where $C_\tau = 6.0$ is used.

For the Girimaji (1997) model based on the linearized SSG model no near-wall corrections are present and, thus, only the non-damped "Gir" model will be tested.

3.3.1. *APG1*

In this section different modelling assumptions are tested by using DNS data from the attached APG boundary layer (APG1). The anisotropies are calculated from equation (14) with S_{ij} and Ω_{ij} computed from DNS data. The resulting anisotropies are then compared with those taken directly from the DNS.

The shear anisotropy a_{12} is plotted for one streamwise position ($x = 150$) in figure 2. The behaviour is approximately the same at all streamwise positions for APG1. The anisotropy taken directly from DNS data is shown with circles. The non-damped models "W&J" and "Gir" are shown in figure 2a. Both models overpredict the asymptotic value at large y^+, which is around -0.3 in the DNS data. The failure to correctly predict the asymptotic value is due to that the basic, undamped, models do not correctly respond to the pressure

gradient. The error enters mainly through the non-linear term in equation (14a) and the best result is actually obtained with $\beta_4 = 0$ for the "W&J" model, as shown in figure 2a with the dotted line. Setting $\beta_4 = 0$ should, however, not be considered as an alternative for improving the model behaviour since the β_4 term results from a formal approximation of the basic Reynolds stress transport model. Moreover, the β_4 term gives important contributions for the normal anisotropy components.

Near the wall, damping with f_1 becomes important. The a_{12} profiles from the damped "W&J" model are shown in figure 2b. The standard van Driest damping, equation (20), with the standard value of $A^+ = 26$, does not give the correct near-wall damping (the solid line in figure 2b). Thus, the standard van Driest damping, which gives a good agreement for a ZPG boundary layer, must be improved in order to give reasonable results for an APG flow. The most straight forward correction is to change the value of A^+ in equation (20).

The damped profiles give very different results depending on the value of A^+. The value of $A^+ = 11$ was observed to give the best agreement with the DNS data, (the dash-dotted profile in figure 2b), and by setting $\beta_4 = 0$ almost perfect agreement with DNS was obtained.

There are many relations between A^+ and the ratio u_p/u_τ proposed in the literature. Kays (1971) proposed the relation,

$$A^+ = \frac{26}{1 + 30.18\left(\frac{u_p}{u_\tau}\right)^3}, \tag{23}$$

which gives a value of $A^+ = 8.6$ for APG1. This value is far from the standard value of 26, but does not agree with the best fitted value of 11 for APG1. In the experimental work of Nagano *et al.* (1992) however, the formula (23) gave good predictions. Cebeci (1970) proposed the relation,

$$A^+ = \frac{26}{\sqrt{1 + 11.8\left(\frac{u_p}{u_\tau}\right)^3}}, \tag{24}$$

which gives a value of $A^+ = 19.4$ for APG1. This value is closer to 26, but far from the value of 11. Granville (1989) proposed a relation which is similar to equation (24), with a factor of 12.6 instead of 11.8, which gives very similar values of A^+ as the relation (24).

A list of other relations is included in the work of Granville (1989). However, the above relations were derived from a mixing length hypothesis, which states that the Reynolds shear stress is linked to the velocity gradient through,

$$-\langle u'v'\rangle^+ = (l^+)^2 \left(\frac{du^+}{dy^+}\right)^2, \tag{25}$$

with

$$l^+ = \kappa y^+ f_1 \qquad \text{or} \qquad l^+ = \kappa y^* f_1, \tag{26}$$

and f_1 as in equation (20). The coordinate y^* is given in equation (9). The second form of l^+ above (26b) was, among others, used by Granville (1989). However, he let a factor α reduce the influence of the pressure gradient,

$$y^* = \sqrt{(y^+)^2 + \alpha \left(\frac{u_p}{u_\tau}\right)^3 (y^+)^3} \tag{27}$$

There is some discrepancy regarding the value of α in the literature. Perry *et al.* (1966) proposed a varying α from 0.65 to 0.9, while Granville (1989) specified 0.9 and McDonald (1969) 0.7. When Skåre & Krogstad (1994) investigated the formula (26b), they had to change the value of κ from 0.41 to 0.78 to fit with experimental data through the logarithmic layer. In the present investigation, the influence of α and κ will not be considered important, since the goal is not to create a mixing length theory, but to use the best damping function for the EARSM model.

In the EARSM model, the relation between the Reynolds shear stress and the velocity gradient is more complicated than equation (25), and an analysis is not as straightforward. The damping with f_1 as in equation (20), which was developed from the mixing-length theory, has proved to work well for the EARSM model for channel flow and ZPG boundary layer flow. For the APG boundary layer flow however, the damping of both the mixing-length theory, equation (25), and the EARSM has to be developed. To further investigate this idea for the EARSM model, where no mixing length exists, the viscous scaling of the normal coordinate in f_1 is substituted with the y^*, defined in section 2.

Arguing that u_τ no longer is the relevant velocity scale, the scaled normal coordinate y^+ in equation (20) may be changed to y^*. A different length scale was proposed by Wallin & Johansson (2000), and their scaled normal coordinate y^T, is defined as,

$$y^T = C_{y1}\sqrt{Re_y} + C_{y2}Re_y^2, \tag{28}$$

where $Re_y = \sqrt{K}y/\nu$, $C_{y1} = 2.4$ and $C_{y2} = 0.003$.

Thus, the damping function f_1 can be expressed as,

$$f_1 = 1 - \exp(-y^*/A^+), \tag{29}$$

or

$$f_1 = 1 - \exp(-y^T/A^+). \tag{30}$$

The formulation of f_1 as in equation (29) was actually used for the mixing length damping by Cebeci & Smith (1968).

A third possibility would be to use y^p. However, to change from y^+ to y^p cannot give any improvement since they are linearly dependent of each other. Thus, the same f_1 profile can be obtained by using y^+ or y^p if the constant A^+ is adjusted.

In figure 2b, the "W&J" model damped with f_1 based on the scaled normal coordinates y^* and y^T are shown. They work almost equally well and the original value of $A^+ = 26$ was kept.

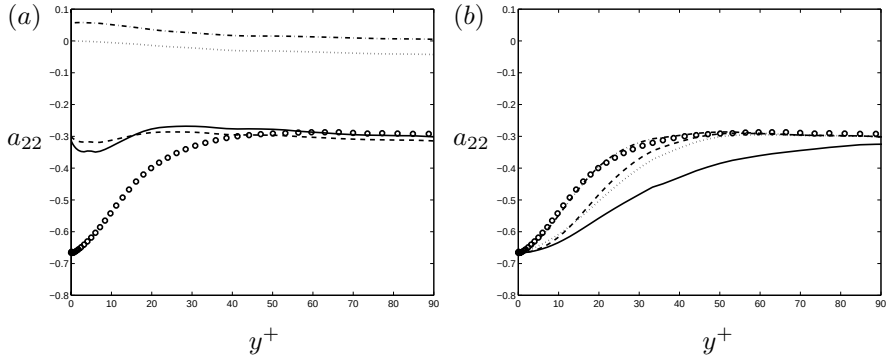

FIGURE 3. APG1 at $x = 150$: (a) ∘ DNS; — non-damped "W&J"; ⋯ non-damped "W&J" with $\beta_4 = 0$; - - non-damped "Gir"; -·- non-damped "Gir" with $\beta_4 = 0$. (b) ∘ DNS. Damped "W&J" with the scaled coordinate in f_1 as — y^+; - - y^*; ⋯ y^T. -·- damped "W&J" with y^+ and $A^+ = 11$.

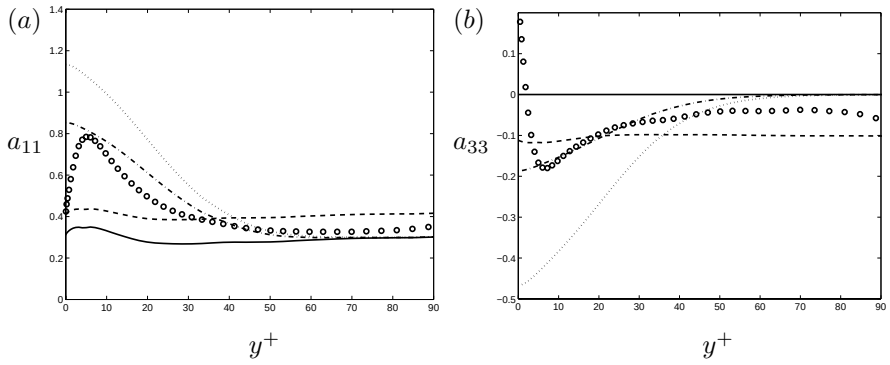

FIGURE 4. APG1 at $x = 150$. (a) a_{11}. (b) a_{33}. ∘ DNS; — non-damped "W&J"; - - non-damped "Gir"; ⋯ damped "W&J" with the scaled coordinate in f_1 as y^T; -·- same as the previous profile but with B_2=1.52.

Since the dependency of A^+ on the pressure gradient and Reynolds number (u_p/u_τ) seems difficult to describe correctly, the rescaled functions (29) and (30) are good alternatives for achieving proper damping in APG flows.

The good results obtained with $\beta_4 = 0$ for a_{12} is not consistent with the results for a_{22}, shown in figure 3. Here, the β_4 coefficient is important to get agreement with DNS data for large values of y^+. Both the "W&J" and "Gir" models predict the asymptotic value of a_{22} well. The profiles from the damped "W&J" model are shown in figure 3b. The alternative length scales y^* and y^T with $A^+ = 26$ are also here very similar and give clear improvements compared

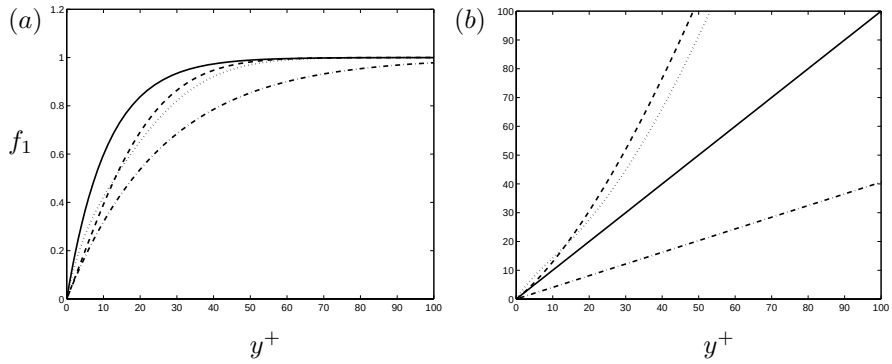

FIGURE 5. APG1 at $x = 150$: (a) f_1 using — y^+ and $A^+ = 11$; - - y^* and $A^+ = 26$; $\cdots$ y^T and $A^+ = 26$; -·- y^+ and $A^+ = 26$. (b) — y^+; - - y^*; $\cdots$ y^T; -·- y^p.

to the y^+ scaling. The best fit is obtained by using y^+ with $A^+ = 11$ also in this case.

The anisotropies a_{11} and a_{33} are shown in figure 4a and b. For a_{11} the "W&J" model gives better agreement with DNS data at large y^+ than the "Gir" model. The damped "W&J" model gives profiles with the same trend as for a_{12} and a_{22}, i.e. the alternative length scales y^* and y^T with $A^+ = 26$ work equally well as y^+ with $A^+ = 11$. Only the y^T damped profile is shown (dotted line) in figure 4a . For a_{33} (figure 4b), the non-damped "W&J" model predicts a value of zero. However, the "Gir" model does not give a better prediction even though it is non-zero. The damped "W&J" model results in a profile (dotted line) that gives a poor agreement with DNS data close to the wall. The wall values of a_{11} and a_{33} are controlled by the B_2 coefficient, and by modifying that to 1.52 almost perfect agreement is obtained (see figure 4). The original value $B_2 = 1.8$ was calibrated from channel flow and the different value obtained for this case indicates that there are a pressure-gradient dependency in B_2.

The damping functions are shown in figure 5a. The function based on y^+ with the optimal value of $A^+ = 11$, and the functions based on y^* and y^T reach unity after approximately $y^+ = 40$. Thus, the damping has no effect for y^+ over approximately 40. The change from the original shape (with y^+ and $A^+ = 26$) is large. In figure 5b the scaled normal coordinates are shown as a function of y^+. From figure 5b it is noted that y^p is proportional to y^+, which is obvious since both u_τ and u_p are independent on y.

In conclusion, the change from y^+ to y^* or y^T, is recommended in favour of keeping the y^+ scaling where the value of A^+ has to be changed for different APG layers. A specific value has to be obtained for each APG and also for each downstream position if the range of Reynolds numbers is large. The value of $A^+ = 11$ is only valid for the APG1 case presented here. For a less severe

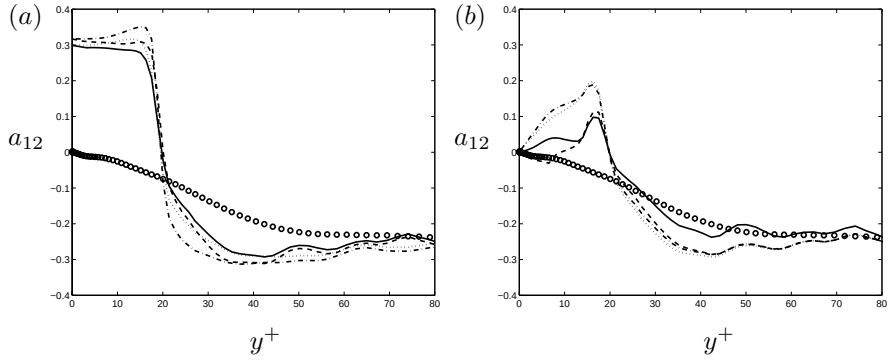

FIGURE 6. SEP at $x = 300$: (a) $\circ$ DNS; — non-damped "W&J" $\cdots$ non-damped "W&J" with $\beta_4 = 0$; - - non-damped "Gir"; -·- non-damped "Gir" with $\beta_4 = 0$. (b) $\circ$ DNS. Damped "W&J" with the scaled coordinate in f_1 as — y^+; - - y^*; $\cdots$ y^T. -·- damped "W&J" with y^+ and $A^+ = 11$.

APG, the value of A^+ has to be increased, whereas the scaling with y^* or y^T can be kept intact. In the extreme case of $u_\tau = 0$, the formulation with y^* or y^T is still valid, whereas the y^+ formulation encounters a singularity, no matter what value of A^+ being used. The extreme case of ZPG is the limit where the value of A^+ is 26 in y^+ formulation and the formulation with y^* is equivalent with the y^+ damping since $y^* = y^+$ for a ZPG boundary layer.

3.3.2. *SEP*

From the case with separation (SEP), three positions will be investigated. The positions are taken from the separated region ($x = 300$), at the reattachment point ($x = 412$), and in the recovery region ($x = 450$). The profiles are presented as functions of y^+ at all positions. Observe that the friction velocity is defined from (1) and (10), so it is everywhere positive.

At $x = 300$ the boundary layer is separated. At this position the non-linear term in the model expression for a_{12} does not give the same strong contribution to the distribution of a_{12} as in the APG1 case (see figure 6a).

The difference between the "W&J" and "Gir" models is supressed at this position where the boundary layer is separated, as seen from figure 6a.

The near-wall behaviour is entirely different from an attached layer. The non-damped profiles reach up to a positive value of 0.3 at the wall, due to that S_{12} is negative in a separated case. S_{12} at $x = 300$ is shown in figure 9a as the solid line. The two other profiles are the S_{12} for $x = 412$ and $x = 450$. Both in the APG1 case and in the SEP case in the attached region ($x = 450$), the non-damped profiles reach a value of -0.3 at the wall, because S_{12} is positive at those positions.

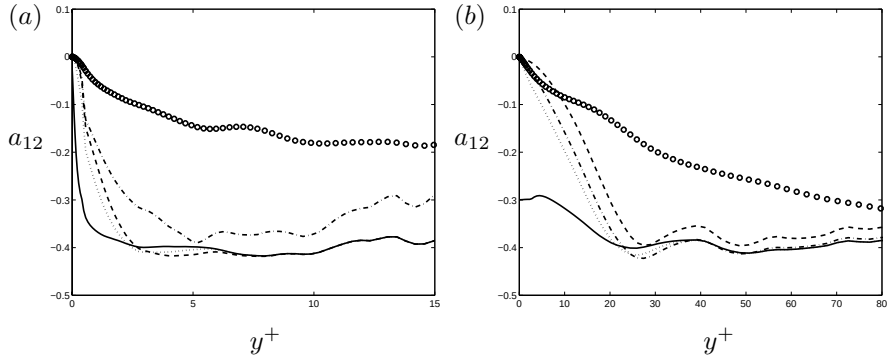

FIGURE 7. SEP at (a) $x = 412$. (b) $x = 450$. ∘ DNS; — non-damped "W&J". Damped "W&J" with the scaled coordinate in f_1 as - - y^*; $\cdots$ y^T; -·- y^+.

The damped "W&J" model at $x = 300$ is shown in figure 6b. Since the pressure gradient is more severe in this case (SEP), we do not expect the same value of A^+ to give the good agreement as for APG1 (remember that A^+ depends strongly on u_p/u_τ). Actually, the value of $A^+ = 26$ (solid line) gives better agreement than $A^+ = 11$ (dash-dotted line) in this case, as seen in figure 6b.

When using y^T in the expression for f_1, no much difference from the case of y^+ together with $A^+ = 11$ can be detected, see figure 6b. The y^* damping (dashed line in figure 6b) gives a better agreement near the wall. This is due to that y^* is zero close to the wall where the back-flow occurs, see equation (12).

At $x = 412$ the boundary layer is at its reattachment point. The DNS data and profiles from the EARSM are shown in figure 7a. At this position the non-damped profile from the "W&J" model stretches up to zero instead of approaching a constant value at the wall. This is due to that S_{12} goes to zero at the wall (zero wall shear stress). S_{12} at $x = 412$ is shown in figure 9a as the dashed line. Note that the boundary layer is much thinner in the viscous scaling at $x = 412$ due to the low value of u_τ at reattachment.

It is interesting to note in the DNS data that a_{12} is negative also in the separation bubble where S_{12} is negative. That means that an effective eddy viscosity is actually negative, which an algebraic model cannot reproduce. This effect is probably due to transport of the anisotropy in the thin near-wall layer.

At $x = 450$ the boundary layer is attached, and the near-wall behaviour is the same for as for APG1. The value of -0.3 is obtained with the non-damped "W&J" model, shown with the solid line in figure 7b. There is not much difference between the three different versions of the damping function, shown in figure 7b. The value $A^+ = 26$ was used for the damped model predictions in figures 7a and b. However, the damping is insensitive to the the value of A^+ at both positions $x = 450$ and $x = 412$. The damping is insufficient for

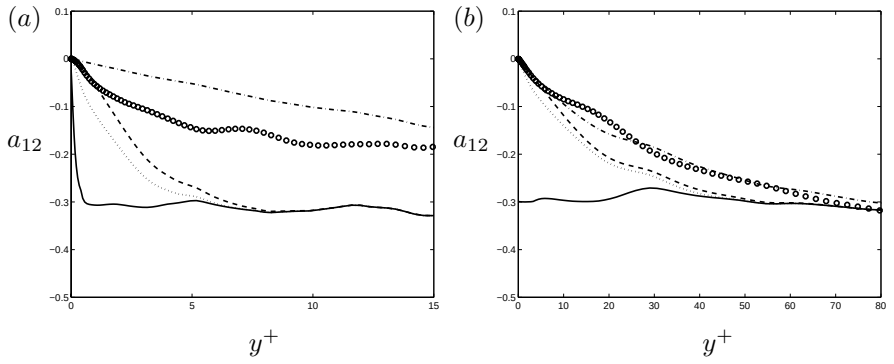

FIGURE 8. $a_{12} = f_1\beta_1 S_{12}$. SEP at (a) $x = 412$. (b) $x = 450$. $\circ$ DNS; — undamped "W&J" ($f_1 = 1$). Damped "W&J" with the scaled coordinate in f_1 as - - y^*; $\cdots$ y^T; -·- y^+.

all versions of f_1, and the reason is that the non-linear terms have influence in this region.

The general near-wall behaviour is the same for both positions $x = 450$ and $x = 412$, except for the important fact that also the non-damped profile at the wall is zero at $x = 412$, due to that the boundary layer is at its reattachment point. Even though the non-damped profiles are 'naturally' damped due to the value of zero at the wall, the damping works just as bad as for the position $x = 450$.

Thus, at both positions $x = 450$ and $x = 412$ (figures 7a and b), it is observed that the damping does not work very well. However, since the equation (14) is dependent on both the linear and non-linear terms, the effect of the damping is complicated. To isolate the effect of the damping of the linear term, only the first part of the expression for a_{12} is shown in figure 8a and b. The damping works very well on the linear part, especially for the position where the boundary layer is attached, figure 8b. The damping based on y^* or y^T gives as good agreement as y^+.

The different versions of the function f_1 (20, 29, 30) are shown at two downstream positions in figure 9b. The formulation with y^+ yields very different shapes at the two positions, whereas y^* and y^T give profiles close to each other. Note that f_1 based on y^* is zero up to $y^+ = 1$ at $x = 412$.

The damping functions at $x = 412$ are shown in figure 10a. The function based on y^+ increases very slowly while the functions based on y^* and y^T reach unity after approximately $y^+ = 8$. In figure 10b, the scaled normal coordinates are shown as a function of y^+. The largest difference between the three coordinates are found at this position where reattachment occurs ($x = 412$).

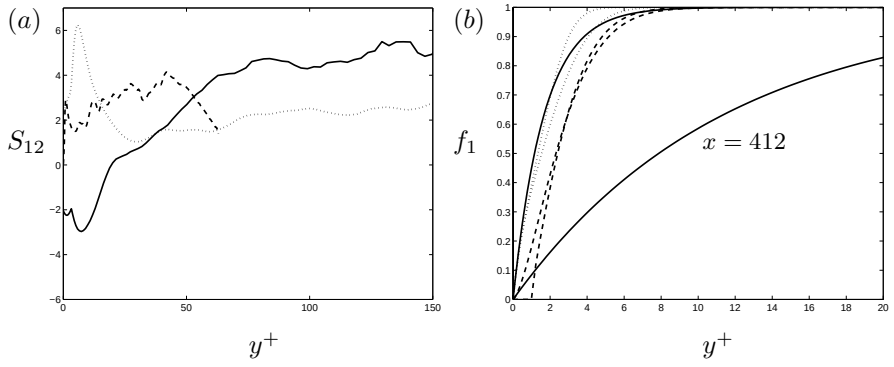

FIGURE 9. SEP: (a) S_{12} at — $x = 300$; - - $x = 412$; $\cdots$ $x = 450$. (b) f_1 at $x = 412$ and $x = 300$, using — y^+; - - y^*; $\cdots$ y^T.

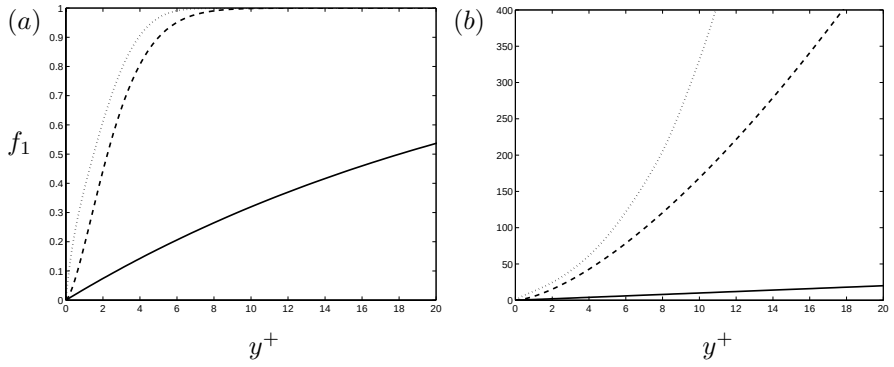

FIGURE 10. SEP at $x = 412$: (a) — y^+; - - y^*; $\cdots$ y^T. (b) f_1 using — y^+; - - y^*; $\cdots$ y^T.

3.4. *Similarities between the y^* and y^T scalings*

Let us try to analyze why the y^* and y^T scalings behave similar. The y^T relation is written in terms of Re_y according to (28). The dominating term, at least for small Re_y, is the $\sqrt{Re_y}$ term so essentially $y^T \sim \sqrt{Re_y}$. The $\sqrt{Re_y}$ term is simply motivated by that $Re_y \sim y^2$ since $K \sim y^2$ and the wanted behaviour is $y^T \sim y$ in the very near-wall region (the viscous sub-layer).

In the log region of the boundary layer there is another relation between Re_y and the y^* scaling that may be derived from the following. Let us first rewrite Re_y by using that $\langle u'v' \rangle = Ka_{12}$ as

$$Re_y \equiv \frac{y\sqrt{K}}{\nu} = y^+\sqrt{K^+} = \frac{1}{\sqrt{-a_{12}}} y^+ \sqrt{-\langle u'v' \rangle^+} \tag{31}$$

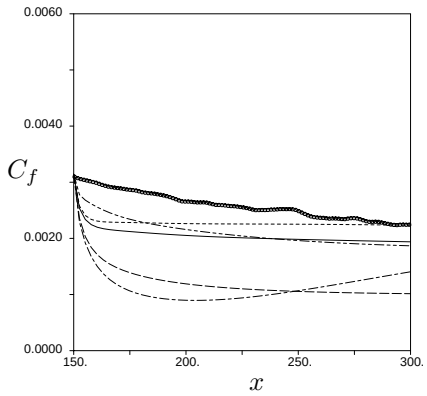

FIGURE 11. Computed skin friction coefficient C_f of the flat plate APG1 boundary layer compared to DNS data: — W&J EARSM with y^T damping; – – W&J EARSM with y^+ damping; - - - Girimaji EARSM with y^T damping; – - – Chien $K-\varepsilon$; – - - – Hanjalić RST.

Away from the viscous sub-layer, the viscosity may be neglected and then $-\langle u'v'\rangle^+ \approx 1 + (u_p/u_\tau)^3 y^+$ (see equation 5). By using the relation (9) the Reynolds number may be related to y^* as

$$Re_y \approx \frac{1}{\sqrt{-a_{12}}}\sqrt{(y^+)^2 + \left(\frac{u_p}{u_\tau}\right)^3 (y^+)^3} = \frac{y^*}{\sqrt{-a_{12}}} \tag{32}$$

Since a_{12} is rather constant (and independent of the pressure gradient) away from the wall there is a linear relation $Re_y \sim y^*$ in the log layer and Re_t and y^* could be expected to respond similarly to pressure gradients.

However, the leading order term in the y^T scaling is proportional to $\sqrt{Re_y}$ and, thus, $y^T \sim \sqrt{y^*}$. The $\sqrt{Re_y}$ dependency is adopted considering the viscous sub-layer where the assumption of neglected viscosity in (32) is basically wrong. This analysis, thus, only gives a qualitative explanation of the relation between y^* and y^T but gives an idea of why the two scalings behave similarly.

3.5. *Performance of the EARSM model*

The APG1 boundary layer was computed with a boundary layer solver using different turbulence models. The DNS data at $x = 150$ were used as inflow condition to the boundary layer computations.

The turbulence models tested are the Wallin & Johansson (2000) EARSM with the wall-damping function based both on y^+ and y^T, the corresponding EARSM based on the linearized SSG model (Girimaji 1997) with the Wallin & Johansson wall-damping function based on y^T, the Chien (1982) eddy-viscosity $K-\varepsilon$ model, and the Hanjalić *et al.* (1995) RST model. All three EARSMs are solved together with the Wilcox (1994) low-Reynolds number $K-\omega$ model.

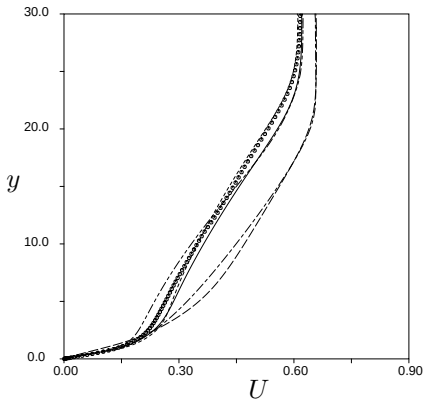

FIGURE 12. Computed mean velocity profiles at $x = 350$ for APG1 compared to DNS data. ∘ DNS data; — W&J EARSM with y^T damping; – – W&J EARSM with y^+ damping; - - - Girimaji EARSM with y^T damping; – - – Chien $K-\varepsilon$; – - - – Hanjalić RST.

Figure 11 shows the computed skin friction coefficient compared with DNS data. After an initial transient the computed skin friction levels out to some asymptotic behaviour. The transient is caused by inconsistency between the inflow data and the turbulence model. In the computations the coefficient $\beta \equiv \frac{\delta^*}{\tau_w}\frac{dP}{dx}$ was kept constant which leads to a reduced effect of the transient. Even though, the extent of the transient is rather large since the Reynolds number is relatively low. Computations with a given pressure gradient resulted in a separated flow for the y^+ based models, which will not be reported here.

There are two models that significantly deviates from the other models. These are the Chien $K-\varepsilon$ and the Wallin & Johansson EARSM with the wall-damping function based on y^+. The wall-damping function in the Chien model is also based on y^+. The other models do not use wall-damping functions based on y^+ and it is a reasonable assumption that the y^+ scaling is the major cause of the deviations. That is clearly seen if one compares the two computations using the Wallin & Johansson EARSM where the only difference between these two is the wall length scaling (y^+ or y^T).

Figure 12 shows the computed velocity profile compared with DNS data. Also here it is observed that the models with y^+ based near-wall damping compares bad with the DNS data while the other models are reasonably accurate. Also here one can notice the difference between the two computations using the Wallin & Johansson EARSM.

4. Conclusion

The viscous sub-layer in the near-wall boundary layer is largely governed by transport and non-equilibrium phenomena, which, in principle, only can be

captured by full Reynolds stress models. Eddy-viscosity models as well as algebraic Reynolds stress models must, thus, be modified by more or less empirical near-wall damping functions in order to have the correct near-wall asymptotic behaviour.

Near-wall damping functions based on y^+ become singular in separation or reattachment points and it was shown that the y^+ scaling also behaves badly in attached boundary layers with adverse pressure gradients. An alternative to y^+ was suggested by Wallin & Johansson (2000) and is basically $y^T \sim \sqrt{Re_y}$ where $Re_y \equiv y u_\tau / \nu$. It was found by use of the DNS data (APG1 and SEP) that the y^T scaling is reasonably similar to the pressure-gradient corrected analytical scaling y^* even close to separation.

In a general three-dimensional CFD method the formulation in terms of y^T is more attractive since that can be derived in every grid point by using local field variables and the wall distance. The use of Y^* involves the skin friction of the nearest wall and also the local pressure gradient. Moreover, in general three-dimensional cases the skin friction, pressure gradient, and external flow are not in general aligned which introduces additional complications.

When damping the a_{12} component of the anisotropy with a van Driest type of wall damping function it was found that the model predictions were much improved by using y^T or y^* compared to y^+ but there was still a significant deviation from the DNS data for the APG1 case. It is obvious that there are other aspects of damping the a_{12} anisotropy in adverse pressure gradients than the wall distance scaling which could not be resolved within this study.

Comparisons between the Wallin & Johansson EARSM based on a LRR-type of pressure-strain model and the Girimaji EARSM which is based on the linearized SSG show no major differences. The only significant difference is that the a_{33} anisotropy component is non-zero for the Girimaji model whereas it is zero for the Wallin & Johansson model away from the viscous sub-layer. However, the deviation from the DNS data is about the same for both models.

References

Cebeci, T. 1970 Behavior of turbulent flow near a porous wall with pressure gradient. *AIAA J.* **8** (12), 2152–2156.

Cebeci, T. & Smith, A. M. O. 1968 A finite-difference solution of the incompressible turbulent boundary-layer equations by an eddy-viscosity concept. 1968 AFOSR-IFP-Stanford Conference. Vol 1.

Chien, K. Y. 1982 Predictions of channel and boundary-layer flows with a low-Reynolds-number turbulence model. *AIAA J.* **20**, 33–38.

Girimaji, S. S. 1997 A Galilean invariant explicit algebraic reynolds stress model for turbulent curved flows. *Phys. Fluids* **9**, 1067–1077, (Also ICASE Report No. 96-38).

Granville, P. S. 1989 A modified van driest formula for the mixing length of turbulent boundary layers in pressure gradients. *J. Fluids Eng.* **111**, 94–97.

Hanjalić, K., Jakirlić, S. & Hadžić, I. 1995 Computation of oscillating turbulent flows at transitional *Re*-numbers. In *Turbulent Shear Flows 9* (eds. F. Durst, N. Kasagi & B. E. Launder), pp. 323–342. Springer-Verlag.

Kays, W. M. 1971 Heat transfer to the transpired boundary layer. ASME Paper No. 71-HT-44.

Launder, B. E., Reece, G. J. & Rodi, W. 1975 Progress in the development of a Reynolds-stress turbulence closure. *J. Fluid Mech.* **68**, 537 – 566.

McDonald, H. 1969 The effect of pressure gradient on the law of the wall in turbulent flow. *J. Fluid Mech.* **35**, 311–336.

Nagano, Y., Tagawa, M. & Tsuji, T. 1992 Effects of adverse pressure gradients on mean flows and turbulence statistics in a boundary layer. In *Turbulent Shear Flows 8* (eds. F. Durst, R. Friedrich, B. E. Launder, F. W. Schmitd, U. Schumann & J. H. Whitelaw), pp. 7–21. Springer-Verlag.

Perry, A. E., Bell, J. B. & Joubert, P. N. 1966 Velocity and temperature profiles in adverse pressure gradient turbulent boundary layers. *J. Fluid Mech.* **25**, 299–320.

Skåre, P. E. & Krogstad, P.-Å. 1994 A turbulent equilibrium boundary layer near separation. *J. Fluid Mech.* **272**, 319–348.

Skote, M., Henkes, R. A. W. M. & Henningson, D. S. 1998 Direct numerical simulation of self-similar turbulent boundary layers in adverse pressure gradients. *Flow, Turbulence and Combustion* **60**, 47–85.

Skote, M. & Henningson, D. 1999 Analysis of the data base from a dns of a separating turbulent boundary layer. Center for Turbulence Research, Annual Research Briefs 1999, 225–237.

Skote, M. & Henningson, D. S. 2000 Direct numerical simulation of a separating turbulent boundary layer. *J. Fluid Mech.* (Submitted).

Speziale, C. G., Sarkar, S. & Gatski, T. B. 1991 Modelling the pressure–strain correlation of turbulence: an invariant dynamical systems approach. *J. Fluid Mech.* **227**, 245–272.

Stratford, B. S. 1959 The prediction of separation of the turbulent boundary layer. *J. Fluid Mech.* **5**, 1–16.

Tennekes, H. & Lumley, J. L. 1972 *A First Course in Turbulence*. The MIT Press.

Townsend, A. A. 1961 Equilibrium layers and wall turbulence. *J. Fluid Mech.* **11**, 97–120.

Wallin, S. & Johansson, A. V. 2000 An explicit algebraic Reynolds stress model for incompressible and compressible turbulent flows. *J. Fluid Mech.* **403**, 89–132.

Wilcox, D. C. 1993 *Turbulence Modeling for CFD*. DCW Industries, Inc.

Wilcox, D. C. 1994 Simulation of transition with a two-equation turbulence model. *AIAA J.* **32**, 247–255.

Paper 6

P6

Reynolds stress budgets in Couette and boundary layer flows

By Jukka Komminaho and Martin Skote

Dept. of Mechanics, KTH, SE-100 44, Stockholm, Sweden

Reynolds stress budgets for both Couette and boundary layer flows are evaluated and presented. Data are taken from direct numerical simulations of rotating and non-rotating plane turbulent Couette flow and turbulent boundary layer with and without adverse pressure gradient. Comparison of the total shear stress for the two flows suggests that the Couette case may be regarded as the high Reynolds number limit for the boundary layer flow close to the wall. The direction of rotation is chosen so that it has a stabilizing effect, whereas the adverse pressure gradient is destabilizing. The pressure strain-rate tensor is in the Couette flow case presented for a split into slow, rapid and Stokes terms.

1. Introduction

The development of cheap, powerful, computers has lead to wide use of CFD codes for the prediction of turbulent flows. These codes almost always use turbulence models to try to capture the characteristics of the turbulent flow, and the prediction is no better than the weakest link in computational chain. Often the weakest link is the turbulence model. But to develop better turbulence models one must have data to compare them against. In the early days of turbulence modelling one had to rely on indirect methods to test the various closure models. Experimental difficulties in measuring pressure and velocity with sufficient resolution did not make direct comparisons possible.

With the development of high-speed supercomputers, and new algorithms, Orszag (1969, 1970); Kreiss & Oliger (1972); Basdevant (1983), it became possible to simulate turbulent flows directly without resorting to large eddy simulations or turbulence models. Now it became possible to evaluate any desirable quantity and use them to test turbulence models. The channel flow simulation by Kim *et al.* (1987) was the first fully resolved simulation of a pressure-driven channel flow, and the database from the simulation has been used extensively to evaluate various turbulence models, Mansour *et al.* (1988).

There are few experimental studies of Couette flow with reports of turbulence statistics. In the study of Couette flow at a Reynolds number of 1300, Bech *et al.* (1995), report both second and higher order statistics from both

experiments and simulations. The agreement between the experiments and the simulation is good for the statistics, but their simulations do not fully capture the very large scale structures of the experiments. This is e.g. seen from the two-point correlations which are lower in the simulation than in the experiment. In Bech & Andersson (1994) they used three different sizes of computational domain and observed large structures in one box, but not in the other two. The reason behind this is unclear.

In Bech (1995) they present Reynolds stress budgets from the simulation in Bech *et al.* (1995), and they look very similar to the ones presented here, despite the higher Reynolds number in their simulation.

In the present paper the budget data for the Reynolds stresses in the Couette flow case are evaluated from the flow fields of the plane Couette flow simulation by Komminaho *et al.* (1996).

Data are also presented from three different turbulent boundary layers. One is a zero pressure gradient (ZPG) boundary layer, and two are boundary layers subject to an adverse pressure gradient (APG). Data from the ZPG boundary layer have not previously been presented. The simulation with a moderate APG (APG1) has been analyzed in Skote *et al.* (1998), while the strong APG case (APG2) has been presented in Skote & Henningson (2000).

The ZPG turbulent boundary layer flow has been studied in a large number of investigations, see e.g. the assessment of data by Fernholz & Finley (1996). Turbulent statistics close to the wall were obtained through DNS by Spalart (1988), and were confirmed later in the experiment of a low Reynolds number ZPG turbulent boundary layer by Ching *et al.* (1995). Various Reynolds stress budgets from DNS of both ZPG and APG boundary layers were presented by Na & Moin (1996). Near-wall limit values of an APG boundary layer were also investigated in the DNS of Spalart & Watmuff (1993) and in the experiment of Nagano *et al.* (1992).

The results from the simulations of Komminaho *et al.* (1996), Skote *et al.* (1998) and Skote & Henningson (2000) are documented here for future use in turbulence model development, in particular for near-wall modelling. The present plane Couette flow data are well suited for this purpose since the condition of a constant total shear is, unlike the situation in the boundary layer, fulfilled for all Reynolds numbers. The boundary layer data can be used for the development of low Reynolds number turbulence models.

2. Data analysis

One can write the Navier–Stokes and continuity equations in a rotating reference frame as,

$$\frac{\partial u_i'}{\partial t} + \frac{\partial}{\partial x_j}(u_i' u_j') = -\frac{1}{\rho}\frac{\partial p'}{\partial x_i} + \nu \frac{\partial^2 u_i'}{\partial x_j \partial x_j} + 2\epsilon_{ijk} u_j' \Omega_k \tag{1a}$$

$$\frac{\partial u_i'}{\partial x_i} = 0. \tag{1b}$$

The effect of the system rotation can be seen as a volume force in the fluid, also known as the Coriolis force and the centrifugal force. The Coriolis force is the last term in the momentum equation, and the centrifugal force has been included in the pressure.

Divide the flow into a mean and a fluctuating part, $u' = U + u$, where the mean part is defined as an ensemble average over N different times, and also an average over the homogeneous directions (x and z in the Couette flow and z in the boundary layer)

$$\overline{u'} \equiv U(y,t) = \frac{1}{NL_xL_z}\sum_{i=1}^{N}\int_0^{L_x}\int_0^{L_z} u'(x,y,z,t)\mathrm{d}x\mathrm{d}z. \tag{2}$$

The Reynolds equation for the mean flow is now obtained as

$$\frac{\partial U_i}{\partial t} + \frac{\partial}{\partial x_j}(U_iU_j) = -\frac{1}{\rho}\frac{\partial P}{\partial x_i} + \nu\frac{\partial^2 U_i}{\partial x_j \partial x_j} - \frac{\partial}{\partial x_j}R_{ij} + \epsilon_{ijk}U_j\Omega_k \tag{3}$$

where $R_{ij} = \overline{u_iu_j}$ is the velocity correlation tensor, and will here be referred to as the 'Reynolds stress tensor'.

2.1. *Couette data*

Plane Couette flow is the flow between two parallel planes, moving in opposite directions with velocity $\pm U_w$ in the x-direction, at a distance $2h$. The wall-normal direction is denoted y. The system rotation Ω applied in the present work is around the z axis.

The various statistical quantities have been evaluated and averaged from 12 different velocity fields, and the average was taken in both x and z direction. The time between the samples was $T = 40$, and they are statistically independent for all but the very largest scales, see Komminaho *et al.* (1996) where the time scale for the integral length scale (Λ_{uux} defined as $\int R_{uu}(\Delta x)\mathrm{d}x$, R_{uu} being the two-point velocity correlation) was found to be more than 50.

2.2. *Boundary layer data*

The statistics have been produced in the same manner as in the Couette case, except for the important difference that the flow is not homogeneous in the streamwise (x) direction. The boundary layer is growing and developing in the $x-$direction due to the increasing Reynolds number. Thus, the statistics are unique for each streamwise position. However, here we are only dealing with the near-wall statistics, which in the viscous scaling should be invariant under the Reynolds number. But in the low Reynolds number flows simulated with DNS, there is a small influence of the increasing Reynolds number. This effect is confined to the part very close to the wall ($y^+ < 3$). In the ZPG simulation e.g., the boundary layer undergoes a doubling of the Reynolds number, but the budgets fall on top of each other for different streamwise positions, except for the small increase of the values at the wall. The statistics are therefore shown for one streamwise position in all three cases.

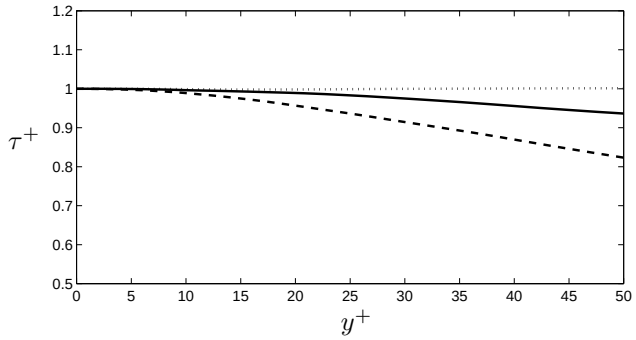

FIGURE 1. Total shear stress. Couette ($\cdots$). Boundary layer: (- -) $Re_{\delta_*} = 539$, (—) $Re_{\delta_*} = 920$.

The simulations APG1 and APG2 were performed with a pressure distribution leading to a self-similar boundary layer at high Reynolds numbers. The pressure gradient parameter β,

$$\beta \equiv \frac{\delta_*}{\tau_w} \frac{\mathrm{d}P}{\mathrm{d}x}, \tag{4}$$

defines the APG in these two simulations.

The Reynolds number at the position where the budgets have been evaluated is shown in table 1, together with the local value of the friction velocity, freestream velocity and pressure gradient parameter.

Case	Re_{δ_*}	Re_Θ	u_τ	U	β
ZPG	920	606	0.048	1.0	0.0
APG1	1064	655	0.036	0.76	0.65
APG2	2573	1309	0.020	0.60	5.0

TABLE 1. Reynolds number, friction velocity, freestream velocity and pressure gradient at the streamwise position where the Reynolds stress budgets have been evaluated.

Another effect of the Reynolds number is the increasing length of the region with constant shear stress (τ^+). This is illustrated in figure 1, which shows the total shear stress at two Reynolds numbers for the ZPG case, as well as for Couette flow. From figure 1 it is clear that the total shear stress for the boundary layer becomes more constant when the Reynolds number is increased. Since τ^+ is constant for the Couette flow, it might be argued that this flow approximates a high Reynolds number boundary layer close to the wall.

2.3. *Reynolds stress budget*

The transport equations for the Reynolds stress tensor are obtained by multiplying (1a) (after subtracting the mean equation 3) with u_j, adding the corresponding equation with switched indices i, j and ensemble averaging. The resulting equations read

$$\frac{\mathrm{D}R_{ij}}{\mathrm{D}t} \equiv \left(\frac{\partial}{\partial t} + U_j \frac{\partial}{\partial x_j}\right) R_{ij} = \mathcal{P}_{ij} - \varepsilon_{ij} + \Pi_{ij} + G_{ij} + D_{ij} + T_{ij} + C_{ij} \quad (5)$$

where

$$\mathcal{P}_{ij} \equiv -\overline{u_i u_k}\frac{\partial U_j}{\partial x_k} - \overline{u_j u_k}\frac{\partial U_i}{\partial x_k}, \quad (6a)$$

$$\varepsilon_{ij} \equiv 2\nu\overline{u_{i,k}u_{j,k}}, \quad (6b)$$

$$D_{ij} \equiv \frac{\partial}{\partial x_k}\left(\nu R_{ij,k}\right), \quad (6c)$$

$$\Pi_{ij} \equiv \frac{1}{\rho}\left(\overline{p\frac{\partial u_i}{\partial x_j} + p\frac{\partial u_j}{\partial x_i}}\right), \quad (6d)$$

$$G_{ij} \equiv -\frac{\partial}{\partial x_k}\left(\frac{1}{\rho}\overline{u_j p}\delta_{ik} + \frac{1}{\rho}\overline{u_i p}\delta_{jk}\right), \quad (6e)$$

$$T_{ij} \equiv -\frac{\partial}{\partial x_k}\overline{u_i u_j u_k}, \quad (6f)$$

$$C_{ij} \equiv -2\Omega_k\left(R_{lj}\epsilon_{ikl} + R_{il}\epsilon_{jkl}\right). \quad (6g)$$

Here $\mathcal{P}_{ij}$ is the production due to mean field gradients, whose trace ($\mathcal{P}_{ii}$) represents twice the production of turbulent energy, the transfer of energy from the mean flow to the turbulent fluctuations.

ε_{ij} is the dissipation rate tensor, and D_{ij} is the diffusion tensor. They both represent viscous effects, but whereas D_{ij} is a molecular diffusion term acting to even out the turbulent stresses by spatial redistribution, ε_{ij} act as a destruction term of turbulent energy (and stresses).

Π_{ij} is the pressure-strain rate correlation tensor, which is traceless and represents inter-component transfer between Reynolds stress terms. G_{ij} is the divergence of the pressure-velocity correlation, and represents transport driven by pressure fluctuations. This split in the above two terms is not unique, there are several different ways in which one may separate the pressure-velocity term when deriving the RST equations, but as the investigation in Groth (1991) shows the above separation seems to make most physical sense.

T_{ij} is the divergence of the triple correlation tensor, acting as a spatial redistribution term.

C_{ij} is the traceless Coriolis tensor, which acts as a redistributive term among the stress components.

The transport equation for the kinetic energy, $K \equiv \frac{1}{2}\mathcal{P}_{ii}$ is

$$\frac{\mathrm{D}K}{\mathrm{D}t} = \mathcal{P} - \varepsilon + \mathcal{D}, \quad (7)$$

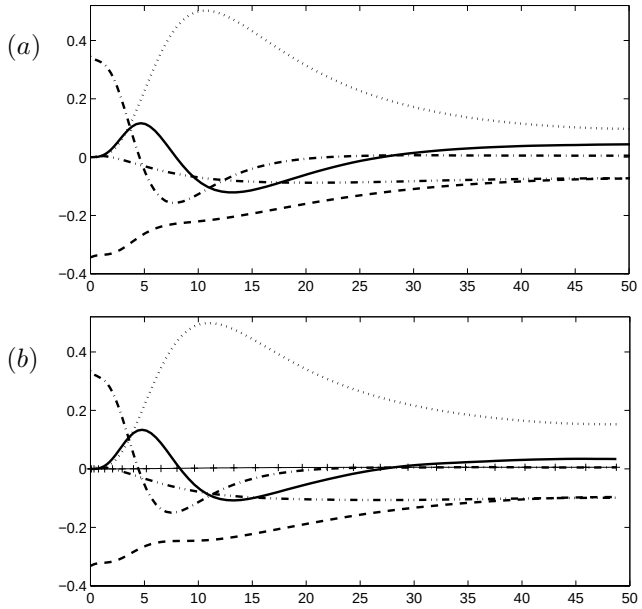

FIGURE 2. Terms in the Couette flow R_{11}-budget for (a) the non-rotating case and (b) the rotating case, $\Omega = -0.005$. The different terms are: ($\cdots$) $\mathcal{P}_{11}$, (- -) $-\varepsilon_{11}$, (- · -) D_{11}, (- · · -) Π_{11}, (—) T_{11}, (+) C_{11}.

where $\mathcal{P} = \frac{1}{2}\mathcal{P}_{ii}$ is the turbulent energy production, $\varepsilon = \frac{1}{2}\varepsilon_{ii}$ is the viscous dissipation, and $\mathcal{D} = \frac{1}{2}\left(T_{ii} + G_{ii} + D_{ii}\right)$ is the sum of the molecular and turbulent diffusion of K. This term acts as a spatial redistribution of K.

In a fully developed plane Couette flow, the flow is homogeneous in the x and z directions, and the relevant non-zero stresses are R_{11}, R_{12}, R_{22} and R_{33}. Figures 2–9 show the terms in the budget of these stresses, as functions of the wall-normal distance $y^+ = yu_\tau/\nu$, where $u_\tau = \sqrt{\tau_w/\rho}$ is the friction velocity. Note that in the non-rotating case the Coriolis term, C_{ij}, is zero. All quantities are shown in $^+$-units, non-dimensionalized with u_τ^4/ν. The simulation flow fields represent a plane Couette flow at a Reynolds number $Re_\tau = u_\tau h/\nu = 52$ ($Re_\tau = 48$ for the rotating case) based on friction velocity u_τ and channel half-height h. This corresponds to a Reynolds number 750 based on wall-velocity and h. Despite this very low Reynolds number it is twice that of the transition Reynolds number of 360, Lundbladh & Johansson (1991); Tillmark & Alfredsson (1992); Komminaho *et al.* (1997). For the rotating case the rotation is as low as $\Omega = -0.005$, corresponding to a Rossby number of 200.

The budgets for the Reynolds stresses in the ZPG case are essentially the same as in Spalart (1988). The moderate APG case, APG1, show very similar profiles in the Reynolds stress budgets as the APG simulation of Na & Moin

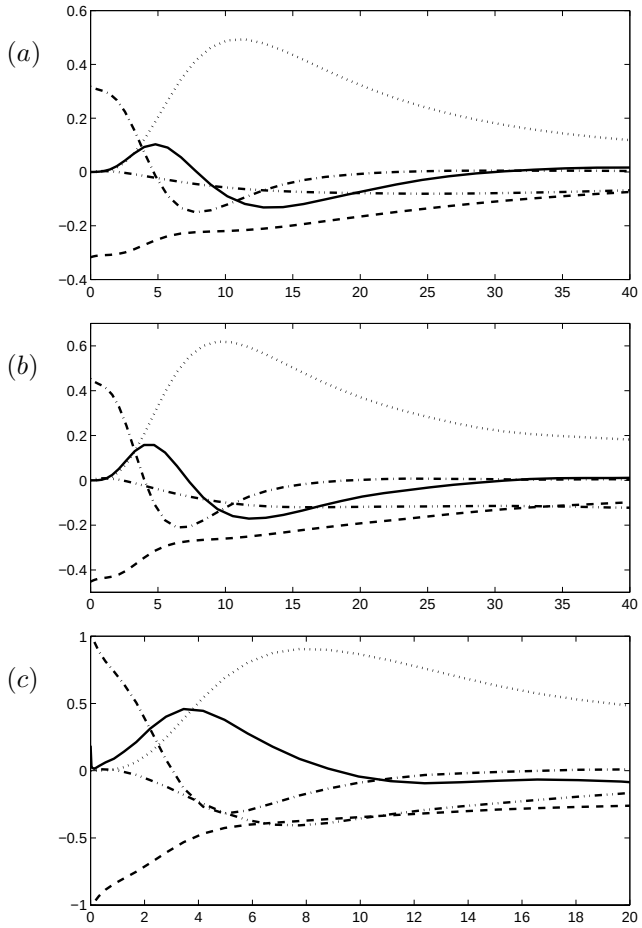

FIGURE 3. Terms in the R_{11}-budget for boundary layer flow (a) ZPG. (b) APG1. (c) APG2. The different terms are: ($\cdots$) $\mathcal{P}_{11}$, (- -) $-\varepsilon_{11}$, (- $\cdot$ -) D_{11}, (- $\cdot\cdot$ -) Π_{11}, (—) T_{11}.

(1996). The effects of the APG will be stronger in the APG2 case, which has a skin friction approximately 60 % of that in APG1. In this work, in contrast to the budgets in Spalart (1988) and Na & Moin (1996), the pressure term is divided into pressure-strain and pressure-velocity diffusion, for comparison with the Couette data.

In figures 2 to 9 the budgets for the Reynolds stresses are shown. The figures include both non-rotating and rotating Couette flow as well as all three boundary layer cases and the profiles from the ZPG case can be compared with the Couette case with zero rotation.

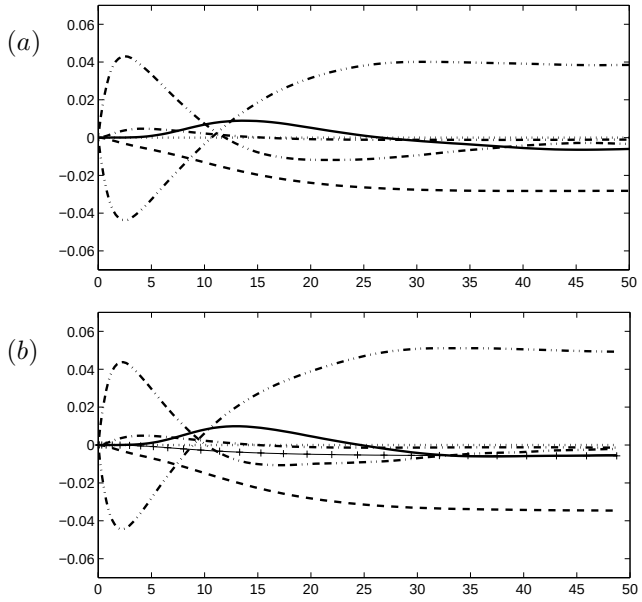

FIGURE 4. Terms in the Couette flow R_{22}-budget for (a) the non-rotating case and (b) the rotating case, $\Omega = -0.005$. The different terms are: (- -) $-\varepsilon_{22}$, (- · -) D_{22}, (- · · -) Π_{22}, (- - · ·) G_{22}, (—) T_{22}, (+) C_{22}.

2.3.1. *Longitudal Reynolds stress*

One may note that the maximum of the production term $\mathcal{P}_{11}$ is 0.5. This is easily obtained by integrating the stream-wise momentum equation once, and multiplying with $\frac{dU^+}{dy^+}$. The advection term is zero in the Couette flow case negligible in the near-wall region for boundary layers. By neglecting the advection term and assuming wall similarity, we obtain the following relation for the turbulence production:

$$\mathcal{P}_{11} \equiv -2\frac{\overline{uv}}{u_\tau^2}\frac{\mathrm{d}U^+}{\mathrm{d}y^+} = 2\frac{\mathrm{d}U^+}{\mathrm{d}y^+}\left(1 - \frac{\mathrm{d}U^+}{\mathrm{d}y^+} + \frac{\nu}{\rho u_\tau^3}\frac{\mathrm{d}P}{\mathrm{d}x}y^+\right), \tag{8}$$

where the pressure gradient term is non-zero only in the adverse pressure gradient (APG) cases. The last term within the parenthesis can be rewritten as $\beta y^+/\delta_*^+$. From the above relation it follows that the maximum of $\mathcal{P}_{11}$ is 0.5 occurring at a position where $\mathrm{d}U^+/\mathrm{d}y^+ = 0.5$ for Couette flow and ZPG boundary layer. This holds irrespective of the value of the Reynolds number and the system rotation and was shown to accurately describe also the low-Reynolds number plane Couette flow simulation of Komminaho *et al.* (1997) where the Reynolds number was as low as 375.

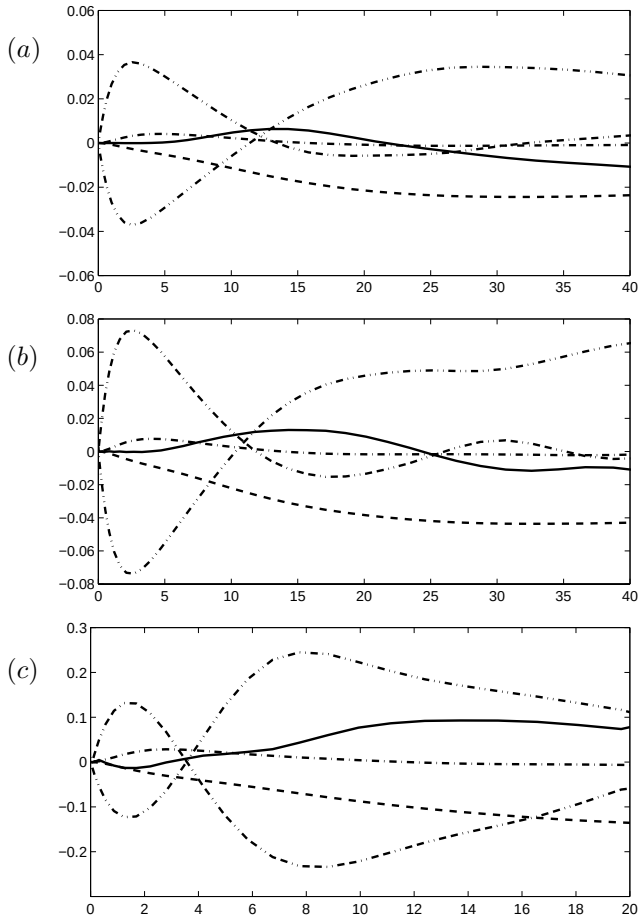

FIGURE 5. Terms in the R_{22}-budget for boundary layer flow (*a*) ZPG. (*b*) APG1. (*c*) APG2. The different terms are: (- -) $-\varepsilon_{22}$, (- · -) D_{22}, (- · · -) Π_{22}, (- - · ·) G_{22}, (—) T_{22}.

The overall character of the different terms in the Reynolds stress budget for R_{ij} is the same as for the channel flow in Mansour *et al.* (1988). Figure 2 shows that the production term $\mathcal{P}_{11}$ is the dominant positive term in the range $y^+ > 5$, and has a maximum of 0.5 in the buffer region, at $y^+ = 11$, falling to 0.10 in the centre of the channel. The location of the peak production can be found to be $y^+ \approx 11$ also in channel and pipe flow, Sahay & Sreenivasan (1999). The non-zero production in the central region is a consequence of the non-zero mean shear in this region.

Π_{11} is negative throughout the channel, thereby transferring energy from R_{11} to R_{22} and R_{33}.

Despite the very low rotation rate for the Couette flow case the effects on some terms in the budgets are significant, away from the wall. The production $\mathcal{P}_{11}$ is about 60% larger in the centre of the channel for the rotating case. The dissipation ε_{11} and the pressure-strain-rate Π_{11} are both 30% larger for the rotating case, whereas the redistributive term T_{11} is about 20% smaller. Near the walls the non-rotating and rotating cases are very similar, as can be expected since the maximum production is 0.5 in both cases.

In figure 3a the budget for the longitudal Reynolds stress is shown for the ZPG case. The maximum of the production term $\mathcal{P}_{11}$ is 0.5 as in the Couette case. The other terms in the budget for R_{11} corresponds very closely to those in the Couette case. The adverse pressure gradient increases the production $\mathcal{P}_{11}$ as seen in figures 3b and c. For APG1 it is 0.6 and APG2 0.9. The increase of the maximum is not explained by the contribution from the streamwise velocity gradient since that part of the production term is negligible close to the wall.

The increased value of $\mathcal{P}_{11}$ is thus explained from the contribution from the pressure gradient in equation (8). For the case APG2 we have a δ_*^+ of 86 so that the last term within the parenthesis in equation (8) $\beta y^+/\delta_*^+$ is about 0.58 at $y^+ = 10$, i.e. near the maximum in production. It can, hence, be seen to be of the order one influence. Since $\beta y^+/\delta_*^+ = \beta y^+ \frac{U_\infty}{u_\tau}/Re_{\delta_*}$ we can see that the effect of the pressure gradient term decreases with increasing Reynolds number.

The position of the maximum is shifted towards the wall, most notably in the APG2 case (figure 3c).

Also the rest of terms show more extreme values in the APG cases, even though the shape of the profiles remain roughly the same. The enhanced values in the near-wall region are partly due to the decrease in the friction velocity (which all the terms in the budget are scaled with). The lower value of u_τ is a consequence of the adverse pressure gradient. One might argue that u_τ is not the correct scaling in an APG flow, since the total shear stress is not constant in this scaling. Alternative scalings, including a velocity scale dependent on the wall normal distance that produce a constant shear stress, are discussed in Skote & Henningson (1999) and Skote & Henningson (2000).

2.3.2. *Normal Reynolds stress*

In figure 4 the budget for R_{22} in the Couette flow case is shown. Π_{22} is negative close to the wall, and positive towards the centre. Thus it transfers energy from the wall-normal components to the horizontal components near the wall. This reversal of the sign was attributed to the splatting effect in the LES study of turbulent channel flow by Moin & Kim (1982) (see also Hunt & Graham 1978). In the turbulence modelling context this effect is normally referred to as the wall-reflection contribution to the pressure strain. The attempts to model this (see Gibson & Launder 1978) typically assumes a variation on a length-scale of the order of the macro-scale. The present results and those of Aronson *et al.* (1997) and Perot & Moin (1995) however show that the effect is confined to a thin region near the wall. In some recent model development (see e.g. Sjögren

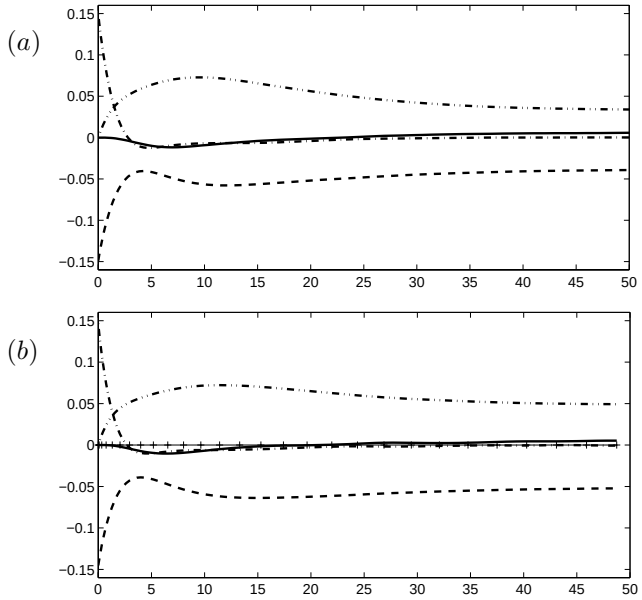

FIGURE 6. Terms in the Couette flow R_{33}-budget for (a) the non-rotating case and (b) the rotating case, $\Omega = -0.005$. The different terms are: (- -) $-\varepsilon_{33}$, (- · -) D_{33}, (- · · -) Π_{33}, (—) T_{33}, (+) C_{33}.

& Johansson 2000) this effect is only indirectly accounted for through realizable models.

The same trend regarding the dissipation and the pressure-strain rate can also be seen in figures 4 and 6 for R_{22} and R_{33} budgets.

In figure 5a the budget for R_{22} in the ZPG case is shown. All the terms show slightly lower values than in the Couette case, while the shapes of the profiles are similar. As the pressure gradient increases, all the terms become larger, as seen from figures 5b and c. A peak in the pressure-strain term has developed in the APG2 case at the position $y^+ = 8$, and exceeds the maximum value of the pressure diffusion. The formation of a peak is not observed in the ZPG and APG1 cases, where a plateau is developed in the pressure-strain, and the value is lower than the pressure-velocity gradient.

2.3.3. *Spanwise Reynolds stress*

In the ZPG budget for the spanwise Reynolds stress, shown in figure 7a, the values of the different terms are, as in the R_{22} budget, lower than in the Couette flow. The shapes of the profiles are similar to those in the Couette case. The pressure gradient enhances the values, but nothing else seems to be affected

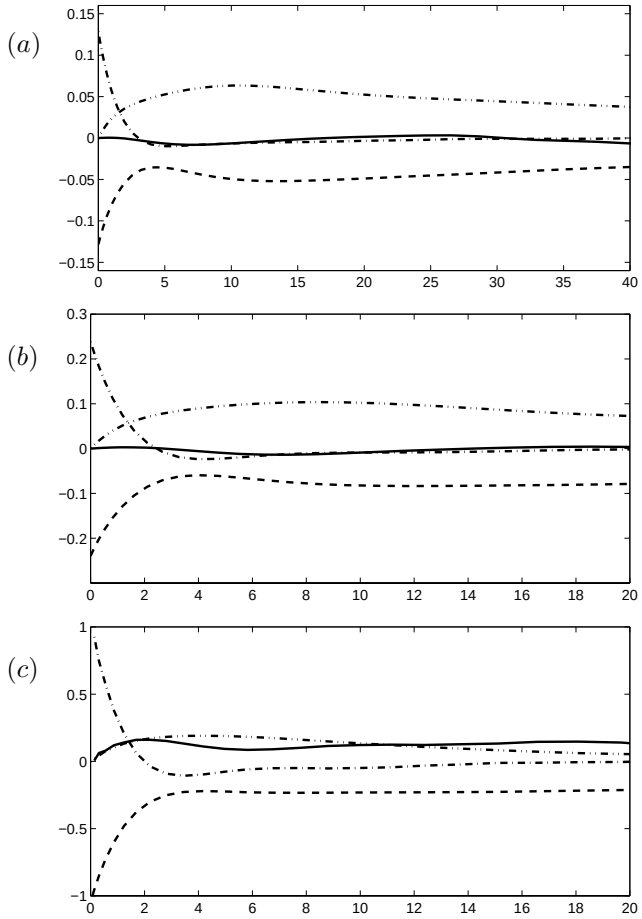

FIGURE 7. Terms in the R_{33}-budget for boundary layer flow (*a*) ZPG. (*b*) APG1. (*c*) APG2. The different terms are: (- -) $-\varepsilon_{33}$, (- · -) D_{33}, (- · · -) Π_{33}, (—) T_{33}.

in the APG1 case. In APG2 however, the turbulent transport is of the same magnitude as the pressure-strain.

2.3.4. *Reynolds shear stress*

The budget for the Reynolds shear stress in Couette flow is presented in figure 8. The pressure strain (Π_{12}) and pressure diffusion (G_{12}) balance each other at the wall. This is also the case in Mansour *et al.* (1988). The value of Π_{12} at the wall in Couette flow is more than twice the value found in the channel flow simulation Mansour *et al.*, and also for ZPG flow it is higher.

The budget for the Reynolds shear stress in boundary layer flow is presented in figure 9. The profiles are approximately the same as in the Couette case,

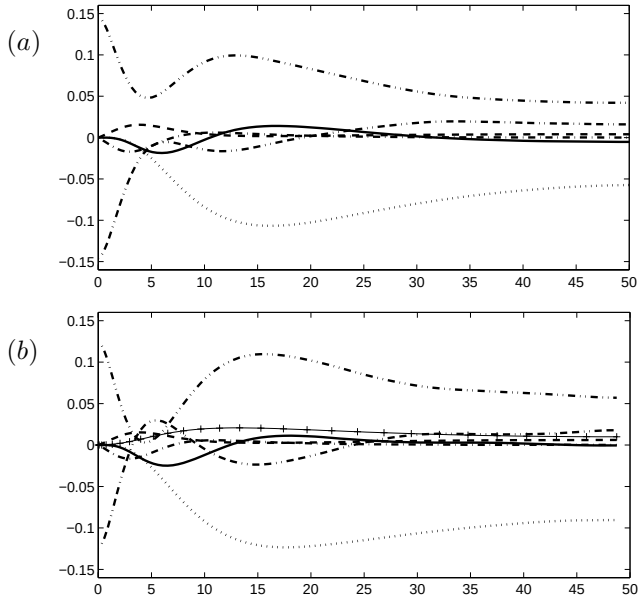

FIGURE 8. Terms in the Couette flow R_{12}-budget for (a) the non-rotating case and (b) the rotating case, $\Omega = -0.005$. The different terms are: ($\cdots$) $\mathcal{P}_{12}$, (- -) $-\varepsilon_{12}$, (- · -) D_{12}, (- · · -) Π_{12}, (- - · ·) G_{12}, (—) T_{12}, (+) C_{12}.

except for the pressure-strain and pressure diffusion at the wall which shows larger values in the Couette case. The outer ($y^+ > 5$) values are however the same in the two flows.

The outer peak (at $y^+ = 6$) of the pressure-strain equals the value at the wall in ZPG and APG2 cases. In the weaker APG boundary layer, APG1, the outer peak has a lower value than at the wall.

2.4. *Near-wall behavior*

There is a balance between dissipation and viscous diffusion on the wall. From the data in figures 2–6 we may also compute the dissipation rate anisotropies, $e_{ij} = \varepsilon_{ij}/\varepsilon - \frac{2}{3}\delta_{ij}$. The limiting values of these (along with the stress anisotropies $a_{ij} = R_{ij}/K - \frac{2}{3}\delta_{ij}$) are given in table 2 and compared with the predictions obtained by the algebraic dissipation rate anisotropy models of Hallbäck *et al.* (1990) and Sjögren & Johansson (2000). The agreement is quite satisfactory for both models in the Couette case, while the Hallbäck *et al.* model is in better agreement with DNS data for the ZPG boundary layer. In the Hallbäck *et al.* model e_{ij} is given by

$$e_{ij} = \left[1 + \alpha(\frac{1}{2}\mathrm{II}_a - \frac{2}{3})\right] a_{ij} - \alpha(a_{ik}a_{kj} - \frac{1}{3}\mathrm{II}_a\delta_{ij}), \quad \alpha = \frac{3}{4}, \tag{9}$$

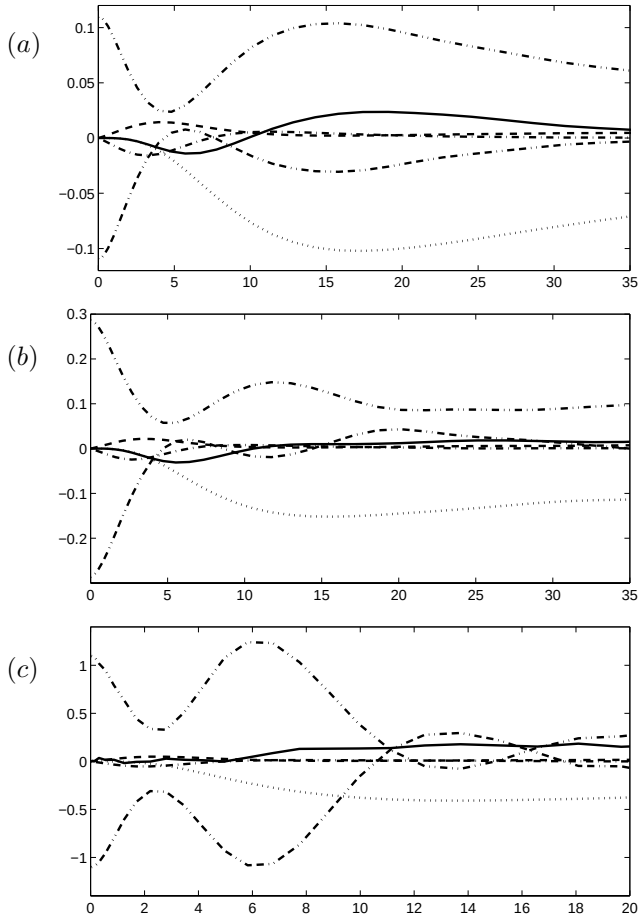

FIGURE 9. Terms in the R_{12}-budget for boundary layer flow (a) ZPG. (b) APG1. (c) APG2. The different terms are: ($\cdots$) $\mathcal{P}_{12}$, (- -) $-\varepsilon_{12}$, (- · -) D_{12}, (- · · -) Π_{12}, (- - · ·) G_{12}, (—) T_{12}.

whereas in the Sjögren & Johansson model we have

$$e_{ij} = (1 - \frac{1}{2}F)a_{ij}, \quad F = 1 - \frac{9}{8}(\mathrm{II}_a - \mathrm{III}_a). \tag{10}$$

In the above expressions we have introduced the two nonzero invariants of the anisotropy tensor,

$$\mathrm{II}_a = a_{ij}a_{ji}, \tag{11}$$

$$\mathrm{III}_a = a_{ij}a_{jk}a_{ki}. \tag{12}$$

The latter model gives $e_{ij} = a_{ij}$ as limiting value in the two-component limit, such as on a solid wall. This describes the situation very accurately in both

component	1,1	2,2	3,3
a_{ij}	0.72	$-\frac{2}{3}$	-0.05
e_{ij}	0.73	$-\frac{2}{3}$	-0.06
$(e_{ij})_{\text{Hallbäck}}$	0.67	$-\frac{2}{3}$	0.00
$(e_{ij})_{\text{Sjögren}}$	0.72	$-\frac{2}{3}$	-0.05

TABLE 2. Couette data: Limiting values for the stress anisotropies a_{ij} and dissipation rate anisotropies e_{ij}, and comparison with models.

component	1,1	2,2	3,3
a_{ij}	0.76	$-\frac{2}{3}$	-0.09
e_{ij}	0.76	$-\frac{2}{3}$	-0.09
$(e_{ij})_{\text{Hallbäck}}$	0.50	$-\frac{2}{3}$	0.17
$(e_{ij})_{\text{Sjögren}}$	0.76	$-\frac{2}{3}$	-0.09

TABLE 3. Boundary layer data: Limiting values for the stress anisotropies a_{ij} and dissipation rate anisotropies e_{ij}, and comparison with models.

Case Re_{δ_*}	u^+_{rms}/y^+	$v^+_{rms}/{y^+}^2$	w^+_{rms}/y^+	$-\langle uv\rangle^+/{y^+}^3$	ε^+
ZPG 539	0.385	0.0112	0.232	0.00099	0.203
ZPG 920	0.398	0.0119	0.252	0.00102	0.223
Couette	0.414	0.0135	0.268	0.00121	0.246

TABLE 4. Limit values for $y^+ \to 0$

cases. One may note that for this extremely low Reynolds number the dissipation rate is highly anisotropic also at the centreline in the Couette case.

Some important limiting values at the wall are given in table 4 and 5. The dependence of the Reynolds number in the boundary layer is strong as seen in table 4. All the values increase for higher Reynolds number, but they do not reach the values of the Couette flow. Hence, one might argue that the Couette data constitute a high Reynolds number limit for the boundary layer.

The effect of the APG on the boundary layer is quite severe as seen from table 5. All limit values are increased when the boundary layer is subject to an APG. The rotation in the Couette case has the opposite effect; all limit values decreases.

Case	u^+_{rms}/y^+	v^+_{rms}/y^{+2}	w^+_{rms}/y^+	$-\langle uv\rangle^+/y^{+3}$	ε^+
APG1 $\beta = 0.65$	0.476	0.0177	0.344	0.00181	0.346
APG2 $\beta = 5.0$	0.728	0.0470	0.764	0.00598	1.35
Couette $\Omega = -0.005$	0.387	0.0124	0.243	0.00093	0.238

TABLE 5. Limit values for $y^+ \to 0$

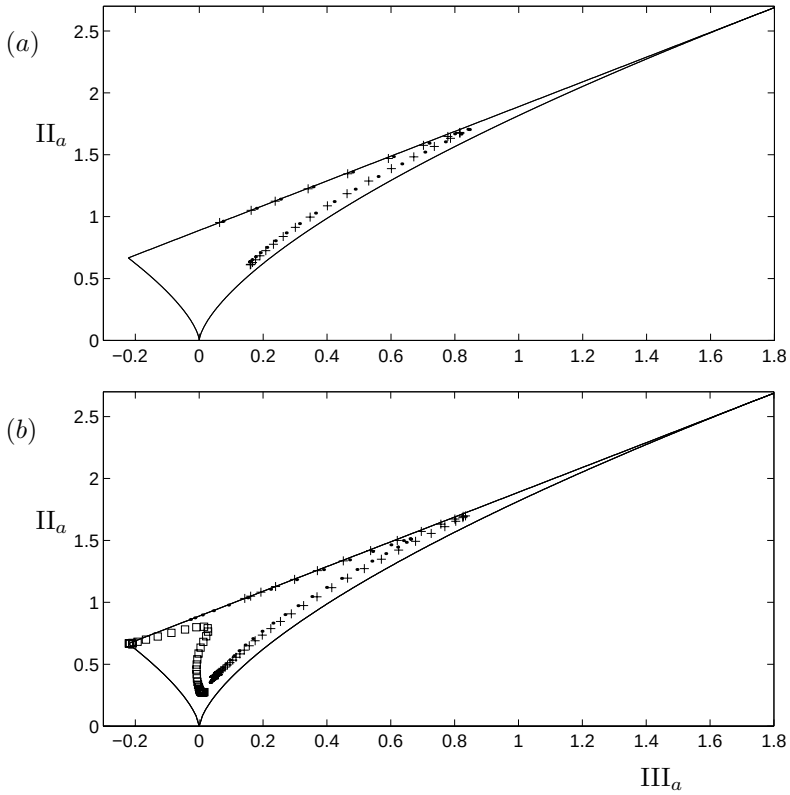

FIGURE 10. The anisotropy invariant map. a) AIM paths for the non-rotating (+) and rotating (·) case. b) AIM paths for ZPG (+) ; APG1 (·); APG2 (□).

2.5. *Anisotropy tensor*

The Reynolds stress anisotropy tensor a_{ij} has, as already mentioned above, two nonzero invariants, II_a and III_a. All anisotropic states can be represented in the anisotropy invariant map (Lumley & Newman 1977) which are bounded by the lines $8/9 + \mathrm{III}_a = \mathrm{II}_a$ and $6\mathrm{III}_a^2 = \mathrm{II}_a^3$. They represent two-component and axisymmetric turbulence, respectively.

In figure 10a the AIM paths for both the non-rotating and rotating Couette cases are shown. Their main characteristics are the same as for the channel flow simulations of Moser *et al.* (1999). Close to the wall the turbulence is very near the two-component limit, approaching the one-component limit near the edge of the viscous sublayer. At $y^+ \approx 8$ the AIM path turns towards the isotropic state. For the present cases the Re_τ is so low that there is nearly no real log-layer in the profiles with corresponding agglomeration of points in the AIM, as observed in the higher-Re channel flow simulations.

The AIM paths for the boundary layer flows are shown in figure 10b. The ZPG case is very similar to the Couette flow. There is some agglomeration of points at the end of the path which is $y^+ \approx 150$ (for ZPG). The path for APG1 starts at a lower value of III_a and represents a lower degree of anisotropy than in the ZPG case. The end of the APG1-path is at $y^+ \approx 100$. The differences between ZPG and APG1 are not so large in comparison with the APG2 case, where the path starts in the lower left corner and represents much lower degrees of anisotropy than in the other cases. This is explained by the less structured turbulence in a strong APG boundary layer. The path for APG3 was terminated at $y^+ \approx 50$, and is similar to the anisotropy states from a backward-facing step, see Le & Moin (1992).

2.6. *Pressure-strain rate split*

The results from a split of the pressure-strain rate is here presented for the Couette flow. The result from taking the divergence of the Navier–Stokes equation is a Poisson equation for the pressure,

$$\frac{\partial^2 p}{\partial x_i \partial x_i} = -\frac{\partial}{\partial x_i}\frac{\partial}{\partial x_j}(u_i' u_j') - 2\epsilon_{ijk}\Omega_j^s \frac{\partial u_k'}{\partial x_i} \tag{13}$$

with the wall boundary condition,

$$\frac{\partial p}{\partial y} = \frac{1}{Re}\frac{\partial^2 v'}{\partial y^2} - 2U\Omega^s. \tag{14}$$

By splitting the source term in the Poisson equation into one part containing the mean velocity gradient and one part containing only gradients of the fluctuating part, we may derive equations for the rapid, slow and Stokes pressure, respectively.

$$\nabla^2 p^{(\mathrm{r})} = -2\left(\frac{\partial U_i}{\partial x_k} + \epsilon_{ijk}\Omega_j^s\right)\frac{\partial u_k}{\partial x_i}, \qquad \frac{\partial p}{\partial y} = 0 \tag{15}$$

$$\nabla^2 p^{(\mathrm{s})} = -\frac{\partial u_i}{\partial x_j}\frac{\partial u_j}{\partial x_i}, \qquad \frac{\partial p}{\partial y} = 0 \tag{16}$$

$$\nabla^2 p^{(\mathrm{St})} = 0, \qquad \frac{\partial p}{\partial y} = \frac{1}{Re}\frac{\partial^2 v}{\partial y^2} - 2U\Omega^s. \tag{17}$$

The Stokes pressure is solely due to the inhomogeneous boundary condition, and may be added to either the rapid or the slow pressure. Note that the last term in the boundary condition for the Stokes pressure is non-zero only for

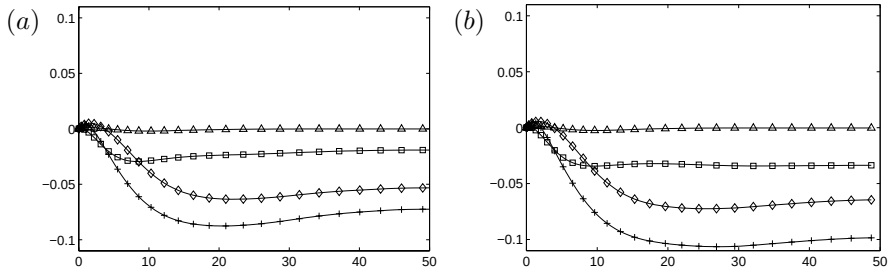

FIGURE 11. The Π_{11}-split for (a) the non-rotating case and (b) the rotating case, $\Omega = -0.005$. The different terms are: $(+)$ $\Pi_{11}^{(\mathrm{tot})}$, $(\diamond)$ $\Pi_{11}^{(\mathrm{s})}$, $(\square)$ $\Pi_{11}^{(\mathrm{r})}$, $(\triangle)$ $\Pi_{11}^{(\mathrm{St})}$.

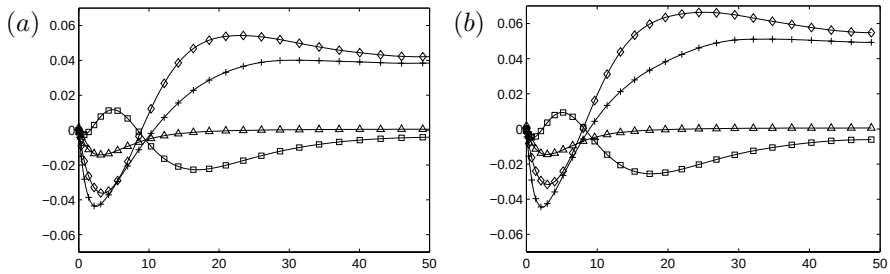

FIGURE 12. The Π_{22}-split for (a) the non-rotating case and (b) the rotating case, $\Omega = -0.005$. The different terms are: $(+)$ $\Pi_{22}^{(\mathrm{tot})}$, $(\diamond)$ $\Pi_{22}^{(\mathrm{s})}$, $(\square)$ $\Pi_{22}^{(\mathrm{r})}$, $(\triangle)$ $\Pi_{22}^{(\mathrm{St})}$.

a moving wall, e.g. Couette flow. Restricting ourself to the present case of a channel with two homogeneous directions the rapid part simplifies further,

$$\nabla^2 p^{(r)} = -2\frac{\mathrm{d}U}{\mathrm{d}y}\frac{\partial v}{\partial x} - 2\Omega^s \omega_3. \tag{18}$$

The split into rapid, slow and Stokes pressure strain-rate can be seen in figure 11–14 for Π_{11}–Π_{12}. The slow part of Π_{11} is larger than the rapid except near the wall, $y^+ < 10$, where the mean velocity gradient is large. The rapid part is more affected by the rotation than the slow part.

Also for the Π_{22}-term the slow part is larger than the rapid part, and contribute most to the pressure strain-rate. Here the slow part is more affected by the rotation.

For the Π_{33}-terms the rapid part contributes most, except for $y^+ < 10$, and is also most affected by the rotation.

The Stokes part for Π_{22}, Π_{33} and Π_{12} is significant only in the region $y^+ < 10$, and for Π_{11} it is negligible throughout the channel.

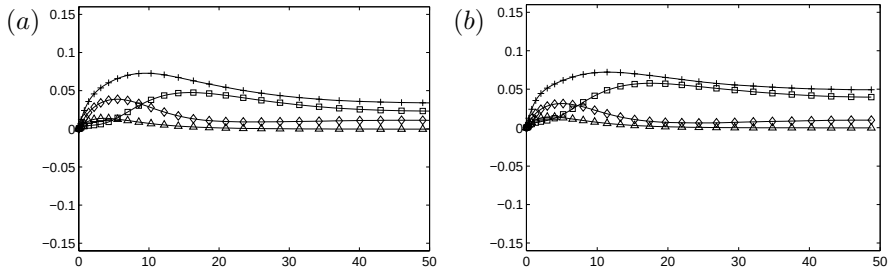

FIGURE 13. The Π_{33}-split for (a) the non-rotating case and (b) the rotating case, $\Omega = -0.005$. The different terms are: (+) $\Pi_{33}^{(\mathrm{tot})}$, ($\diamond$) $\Pi_{33}^{(\mathrm{s})}$, ($\square$) $\Pi_{33}^{(\mathrm{r})}$, ($\triangle$) $\Pi_{33}^{(\mathrm{St})}$.

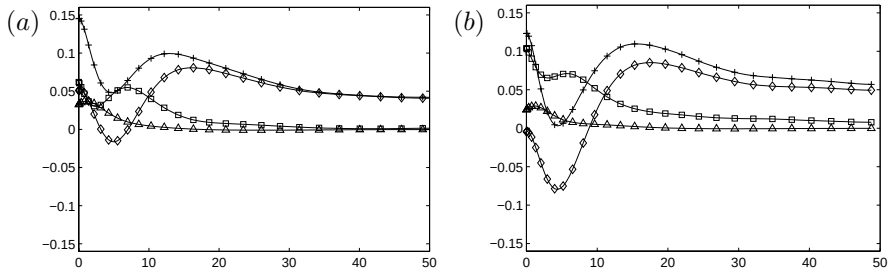

FIGURE 14. The Π_{12}-split for (a) the non-rotating case and (b) the rotating case, $\Omega = -0.005$. The different terms are: (+) $\Pi_{12}^{(\mathrm{tot})}$, ($\diamond$) $\Pi_{12}^{(\mathrm{s})}$, ($\square$) $\Pi_{12}^{(\mathrm{r})}$, ($\triangle$) $\Pi_{12}^{(\mathrm{St})}$.

The general character and amplitude of the various pressure strain rate terms are almost identical even for $Re = 375$, despite the low Reynolds number.

3. Summary

We have used the Couette flow simulation data of Komminaho *et al.* (1996) and the boundary layer data of Skote *et al.* (1998); Skote & Henningson (2000) to compute terms in the transport equation for the Reynolds stresses. For the Couette flow we have also presented data for a split of the pressure strain rate term in rapid, slow and Stokes. Data was presented for both rotating (slow stabilizing rotation) and non-rotating Couette flow. One can see a small effect of the rotation on the limiting values at the wall in the Couette flow, but it is small as could be expected, since it is a very slow rotation. In the centre of the channel the budgets were strongly influenced by the rotation.

Boundary layer data were presented for one zero pressure gradient flow and two adverse pressure gradient flows. Strong influence on the budgets from the adverse pressure gradient were detected. The near-wall limits of turbulence statistics were shown to increase with Reynolds number in the zero pressure

gradient boundary layer, but they did not reach the values obtained from the Couette flow.

Acknowledgements

The authors would like to thank Arne Johansson for many valuable comments on the manuscript.

References

Aronson, D., Johansson, A. V. & Löfdahl, L. 1997 Shear-free turbulence near a wall. *J. Fluid Mech.* **338**, 363–385.

Basdevant, C. 1983 Technical improvement for direct numerical simulation of homogeneous three-dimensional turbulence. *J. Comp. Phys.* **50** (2), 209–214.

Bech, K. H. 1995 Simulation of rotating and non-rotating turbulent plane Couette flow. PhD thesis, Department of Applied Mechanics, Thermodynamics and Fluid dynamics, Norwegian Institute of Technology, Trondheim.

Bech, K. H. & Andersson, H. I. 1994 Very-large-scale structures in DNS. In *Direct and Large-Eddy Simulations I* (eds. P. R. Voke, L. Kleiser & J.-P. Chollet), pp. 13–24. Dordrecht: Kluwer.

Bech, K. H., Tillmark, N., Alfredsson, P. H. & Andersson, H. I. 1995 An investigation of turbulent Couette flow at low Reynolds numbers. *J. Fluid Mech.* **286**, 291–325.

Ching, C. Y., Djenidi, L. & Antonia, R. A. 1995 Low-reynolds-number effects in a turbulent boundary layer. *Exps. Fluids* **19**, 61–68.

Fernholz, H. H. & Finley, P. J. 1996 The incompressible zero-pressure-gradient turbulent boundary layer: An assessment of the data. *Prog. Aerospace Sci.* **32**, 245–311.

Gibson, M. M. & Launder, B. E. 1978 Ground effects on pressure fluctuations in the atmospheric boundary layer. *J. Fluid Mech.* **86**, 491–511.

Groth, J. 1991 Description of the pressure effects in the Reynolds stress transport eqautions. *Phys. Fluids A* **3** (9), 2276–2277.

Hallbäck, M., Groth, J. & Johansson, A. V. 1990 An algebraic model for non-isotropic turbulent dissipation rate term in Reynolds stress closures. *Phys. Fluids A* **2** (10), 1859–1866.

Hunt, J. C. R. & Graham, J. M. R. 1978 Free-stream turbulence near plane boundaries. *J. Fluid Mech.* **84**, 209–235.

Kim, J., Moin, P. & Moser, R. 1987 Turbulence statistics in fully developed channel flow. *J. Fluid Mech.* **177**, 133–166.

Komminaho, J., Lundbladh, A. & Johansson, A. V. 1996 Very large structures in plane turbulent Couette flow. *J. Fluid Mech.* **320**, 259–285.

Komminaho, J., Lundbladh, A. & Johansson, A. V. 1997 Determination of the transition Reynolds number in plane couette flow through study of relaminarization. In *First AFOSR Int. Conf. on DNS/LES* (eds. C. Liu & Z. Liu), pp. 233–240. Louisiana Tech University, Ruston, LA, USA: Grayden Press.

Kreiss, H.-O. & Oliger, J. 1972 Comparison of accurate methods for the integration of hyperbolic equations. *Tellus* **24**, 199–215.

Le, H. & Moin, P. 1992 Direct numerical simulation of turbulent flow over a backward facing step. In *Annual Research Briefs*, pp. 161–173. Stanford Univ. Center for Turbulence Research.

Lumley, J. L. & Newman, G. R. 1977 The return to isotropy of homogenous turbulence. *J. Fluid Mech.* **82**, 161–178.

Lundbladh, A. & Johansson, A. V. 1991 Direct simulation of turbulent spots in plane Couette flow. *J. Fluid Mech.* **229**, 499–516.

Mansour, N. N., Kim, J. & Moin, P. 1988 Reynolds-stress and dissipation-rate budgets in a turbulent channel flow. *J. Fluid Mech.* **194**, 15–44.

Moin, P. & Kim, J. 1982 Numerical investigation of turbulent channel flow. *J. Fluid Mech.* **118**, 341–377.

Moser, R. D., Kim, J. & Mansour, N. N. 1999 Direct numerical simulation of turbulent channel flow up to $\mathrm{Re}_\tau = 590$. *Phys. Fluids* **11** (4), 943–945.

Na, Y. & Moin, P. 1996 Direct numerical simulation of studies of turbulent boundary layers with adverse pressure gradient and separation. *Tech. Rep.* TF-68. Thermosciences Division, Department of Mechanical Engineering, Stanford University.

Nagano, Y., Tagawa, M. & Tsuji, T. 1992 Effects of adverse pressure gradients on mean flows and turbulence statistics in a boundary layer. In *Turbulent Shear Flows 8* (eds. F. Durst, R. Friedrich, B. E. Launder, F. W. Schmitd, U. Schumann & J. H. Whitelaw), pp. 7–21. Springer-Verlag.

Orszag, S. A. 1969 Numerical methods for the Simulation of Turbulence. *Phys. Fluids Suppl. II* **12**, 250–257.

Orszag, S. A. 1970 Transform method for the calulation of vector-coupled sums: Application to the spectral form of the vorticity equation. *J. Athmosph. Sci.* **27**, 890–895.

Perot, J. B. & Moin, P. 1995 Shear-free turbulent boundary layers. part 1. physical insights into near-wall turbulence. *J. Fluid Mech.* **295**, 199–227.

Sahay, A. & Sreenivasan, K. 1999 The wall-normal position in pipe and channel flow at which viscous and turbulent shear stresses are equal. *Phys. Fluids* **11** (10), 3186–3188.

Sjögren, T. & Johansson, A. V. 2000 Development and calibration of algebraic nonlinear models for terms in the Reynolds stress transport equations. *Phys. Fluids* **12** (6), 1554–1572.

Skote, M., Henkes, R. A. W. M. & Henningson, D. S. 1998 Direct numerical simulation of self-similar turbulent boundary layers in adverse pressure gradients. *Flow, Turbulence and Combustion* **60**, 47–85.

Skote, M. & Henningson, D. 1999 Analysis of the data base from a dns of a separating turbulent boundary layer. Center for Turbulence Research, Annual Research Briefs 1999, 225–237.

Skote, M. & Henningson, D. S. 2000 Direct numerical simulation of a separating turbulent boundary layer. *J. Fluid Mech.* (Submitted).

Spalart, P. R. 1988 Direct simulation of a turbulent boundary layer up to $Re_\theta = 1410$. *J. Fluid Mech.* **187**, 61–98.

Spalart, P. R. & Watmuff, J. H. 1993 Experimental and numerical study of a turbulent boundary layer with pressure gradients. *J. Fluid Mech.* **249**, 337–371.

Tillmark, N. & Alfredsson, P. H. 1992 Experiments on transition in plane Couette flow. *J. Fluid Mech.* **235**, 89–102.

Paper 7

P7

Instabilities in turbulent boundary layers

By Martin Skote*, Joseph H. Haritonidis† and Dan S. Henningson*‡

An investigation of a model of turbulence generation in the wall region of a turbulent boundary layer is made through direct numerical simulations. The model is based on the instability of a streak.

First, a laminar boundary layer disturbed by a continuous blowing through a slot is simulated in order to reproduce and further investigate the results reported from the experiments of Acarlar & Smith (1987). An isolated streak with an inflectional profile is generated that becomes unstable, resulting in a train of horseshoe vortices. The frequency of the vortex generation is equal to the experimental results. Comparison of the instability characteristics to those predicted through an Orr-Sommerfeld analysis are in good agreement.

Second, a direct numerical simulation of a turbulent boundary layer is performed to point out the similarities between the horseshoe vortices in a turbulent and a laminar boundary layer. The characteristics of streaks and the vortical structures surrounding them in a turbulent boundary layer compare well with the model streak. The results of the present study suggest that the primary mechanism for the generation of horseshoe vortices in turbulent boundary layers is related to an inflectional instability of the streaks.

1. Introduction

1.1. *Detection of coherent structures*

The occurrence of coherent vortices in wall-bounded turbulent flows has been observed in a large number of investigations by different means. The experimental observations have relied on dye injections or hydrogen bubbles introduced in the flow. Lately, low Reynolds number flows have been investigated numerically through direct numerical simulations (DNS). The flow field variables are all available at the same time and thus more sophisticated detection methods have been developed. Robinson (1991*a*) used the pressure successfully for revealing horseshoe vortices in a data base from a DNS of a turbulent boundary layer. Singer & Joslin (1994) also used the pressure in a numerical simulation

*Department of Mechanics, Royal Institute of Technology (KTH), SE-100 44 Stockholm, Sweden

†Department of Aerospace Engineering and Aviation, Ohio State University, U.S.A.

‡Aeronautical Research Institute of Sweden (FFA), Box 11021, SE-161 11 Bromma, Sweden

for visualizing a horseshoe vortex generated by blowing through a slot. Chong *et al.* (1998) used the discriminant of the deformation rate tensor for identifying flow structures in turbulent boundary layers. They found structures that to a great extent consist of attached vortex loops. Zhou *et al.* (1999) used the imaginary part of the complex eigenvalue of the deformation rate tensor to identify hairpin structures in channel flow. The structures originated from a vortical structure imposed in the flow. By plotting the imaginary part a clear picture of the structure was obtained and the shape was not sensitive to the level chosen for visualization. Jeong & Hussain (1997) and Schoppa & Hussain (1997) used an eigenvalue based on the Hessian of the pressure for identification of vortices in a turbulent channel flow, and used conditional sampling to extract the precise form of the coherent structure.

1.2. *Streamwise versus horseshoe vortex structures*

Jeong & Hussain (1997) did not detect any horseshoe vortices in the channel flow simulation by Kim *et al.* (1987). Instead they extracted a coherent structure consisting of quasi-streamwise vortices by conditional sampling. Jimenez & Moin (1991) and Hamilton *et al.* (1995) observed, by shrinking the computational box, that the self-sustained turbulence is linked to the quasi-streamwise vortices, and does not depend on the outer part of the flow. This scenario is consistent with the model of Waleffe (1997) which states that the vortex is fed by energy from the break up of the streak. Jimenez & Pinelli (1999) used a method of reducing the influence of the outer flow in a numerical simulation to show that the regeneration cycle is independent on the outer flow. Thus, according to these findings, there is little interaction between the inner and outer flow. Consequently, it is possible to model the regeneration of turbulence via a self-sustaining process involving low-speed streak and quasi-streamwise vortex, independent on the outer flow.

On the other hand, horseshoe vortices observed in boundary layer flows reach into the outer flow. The regeneration of horseshoe vortices has been studied numerically by Singer & Joslin (1994) and Zhou *et al.* (1999) and in experiments by Acarlar & Smith (1987). Recently, Adrian *et al.* (2000) have visualized hairpin vortices in a turbulent boundary layer using particle image velocimetry (PIV). They show that hairpin packets (groups of horseshoe vortices) build up the turbulent boundary layer. The number of vortices that constitute a packet is lower in a low Reynolds number flow than in high Reynolds number flows.

The size of the horseshoe vortices seems to vary within the flow and also vary with Reynolds number. A turbulence model for Reynolds average Navier-Stokes (RANS) calculations of turbulent flows has been developed by Perry *et al.* (1994) based on size and strength of the horseshoe structures.

1.3. *Streak instability and turbulence regeneration*

The vortex structures present in turbulent boundary layers seem to be related to streak instabilities. However, the type of instability that occurs in the streaks is not agreed upon. Robinson (1991*b*) proposed that a normal inflectional instability of the instantaneous velocity profile may produce horseshoe vortices. Singer (1992) showed that a normal inflectional instability of the velocity profile may be responsible for the generation of secondary horseshoe vortices. Kim *et al.* (1971) were the first to show that a normal inflectional instability of the instantaneous velocity profile is of importance in the turbulence regeneration cycle. They observed the inflectional velocity profiles in connection with the rapid lift up of the low-speed streaks in the later part of the process of the streak break up.

On the other hand, in the model of Waleffe (1997) the basic state is two-dimensional and consists of the turbulent mean flow with a simple construction of the streak imposed. He found that the dominating instability is sinuous and that it is correlated with the spanwise inflection of the basic state. Kawahara *et al.* (1998) and Schoppa & Hussain (1997) also used such a model and showed that the varicose mode is stable. Schoppa & Hussain argued that this is consistent with the absence of horseshoe vortices in their examination of the DNS data base generated by Kim *et al.* (1987).

Although the references cited above form only a small part of the work that has been put into the detection and analysis of coherent structures, there is surprising disagreement between the studies of what is the important mechanisms in turbulence regeneration. In the last section of this paper we propose a reconciliation of this apparent disagreement, partly based on the results of the present investigation.

1.4. *Present study*

In this work we will pursue the horseshoe vortex dynamics. In the experiments by Acarlar & Smith (1987), hereafter denoted AS, an artificial low-speed streak was generated in a laminar boundary layer by blowing fluid through a slot in the wall. The streak became unstable and horseshoe vortices were formed and were followed downstream. In the present study we reproduce the flow studied by AS through DNS. Moreover, the hypothesis indicated by AS regarding the instability causing the vortices is here further investigated. One of the objectives in the AS experiment was to give insight to the mechanisms and structures in a turbulent boundary layer. In the present work, a stronger link to turbulence is made through comparison with a simulation of a zero pressure gradient turbulent boundary layer.

After a presentation of the numerical method and parameters in section 2, we present the results in section 3. The emphasis is on the results from the laminar simulation, which is compared with the experimental results from AS. Further investigations of the instability mechanism are made. Also comparison

with the turbulent simulation is done, from which strong similarities between the two cases are presented.

2. Numerical methodology

2.1. *Direct numerical simulations*

The code used for the simulation is developed at KTH and FFA (Lundbladh *et al.* 1999). The program uses spectral methods with Fourier discretization in the horizontal directions and Chebyshev discretization in the normal direction. Since the boundary layer is developing in the downstream direction, it is necessary to use non-periodic boundary conditions in the streamwise direction. This is possible while retaining the Fourier discretization if a fringe region is added downstream of the physical domain. In the fringe region the flow is forced from the outflow of the physical domain to the inflow. In this way the physical domain and the fringe region together satisfy periodic boundary conditions. The fringe region is implemented by the addition of a volume force whose form is designed to minimize the upstream influence. Time integration is performed using a third order Runge-Kutta scheme for the advective and forcing terms and Crank-Nicholson for the viscous terms.

All quantities are non-dimensionalized by the freestream velocity (U) and the displacement thickness (δ^*) at the starting position of the simulation ($x = 0$) where the flow is laminar. At that position $Re_{\delta^*} = U\delta^*/\nu = 450$ for all simulations, except for some simulations performed at $Re_{\delta^*} = 290$ for the comparison of frequency characteristics. The length (including the fringe), height and width of the computation box were $260 \times 7 \times 14$ in these units. The number of modes was $432 \times 65 \times 72$. The size and resolution were checked to be sufficient for all cases.

The simulations were performed with an initial objective of reproducing some of the results obtained in the experiments of AS. In their experiments the slot was 63.5 mm in length and 1 mm in width. The simulations were performed with a slot with the same length but twice the width, i.e. 2 mm. This change in geometry results in an enormous decrease in computational cost. The slot in simulation coordinates (δ^*) is approximately 30 long and 1 wide. The flow through the slot is set by a velocity profile resembling a channel flow parabola in the spanwise direction and is increasing from zero to the maximum value during the first 10 % of the slot length at the upstream end, and is likewise terminated at the downstream end. The blowing through the slot was continued without interruption through all of the simulations. To avoid large transients in the beginning of the simulation we ramped up the blowing from zero to the maximum value during an initial time of 10 (δ^*/U). The time step was considerably decreased when the blowing through the wall is applied. The strength of the blowing was varied from 6.5 to 20 % of the freestream velocity.

A low-speed streak is formed immediately above the slot due to the lift-up of low-speed fluid to the flow further out in the boundary layer. A disturbance on this streak was detected and the frequency was observed during a long period

of time, and was then locked by letting a small (1 % of the original blowing) additional time-periodic blowing be superimposed on the blowing forming the streak. The frequency of the initial disturbance on the streak was locked to be able to calculate the growth rate of the disturbance through a Fourier transform in time.

A simulation of a turbulent boundary layer was performed to investigate how the streak instabilities observed in the isolated streak in the laminar boundary layer could be applicable to a turbulent flow. The same code was used, but the laminar boundary layer was disturbed at the beginning of the computational box by a random volume force near the wall. The length (including the fringe), height and width of the computation box were $600 \times 30 \times 34$. The number of modes was $640 \times 201 \times 128$. The simulations were performed at $Re_{\delta^*} = 450$ for the laminar inflow before the tripping, which gives a turbulent $Re_\Theta : 343 - 636$. The resolution in plus units was $\Delta X^+ = 19$, $\Delta Z^+ = 5.5$, and ranging from $\Delta Y^+ = 0.04$ close to the wall to $\Delta Y^+ = 5.6$ at the coarsest part of the grid.

2.2. *The linear stability analysis*

One of the main conclusions of this work will concern the instability mechanism of a low-speed streak leading to horse shoe-shaped vortices. Linear stability theory will be used to describe the early stages of this instability. The disturbance occurring due to the instability of the streak will be denoted secondary disturbance, since the primary disturbance is the streak itself. The velocity profiles close to where the secondary disturbance start to appear, below denoted $U = U(y)$, were analyzed by solving the Orr-Sommerfeld (O-S) equation. The results from the O-S equation are only relevant as long as the disturbance is small enough and variations of the base flow (streak) in the horizontal directions and time is much smaller than the length scale of the instability waves. The O-S equation is the linearized Navier-Stokes equations for the disturbance,

$$\phi'''' - 2\alpha^2\phi'' + \alpha^4\phi = i\alpha R[(U - c)(\phi'' - \alpha^2\phi) - U''\phi]. \tag{1}$$

The two-dimensional disturbance is written as a stream function,

$$\psi = \phi(y)\exp[i\alpha(x - ct)] = \phi(y)\exp[i(\alpha x - \omega t)] \tag{2}$$

Because the secondary disturbance is characterized by its frequency and its growth in space in the simulations, spatial analysis of the O-S equation will be used. In the case of spatial analysis the eigenvalue problem (1) is solved for a given R and ω, which is real. The solution is $\phi(y)$ (eigenfunction) and $\alpha = \alpha_r + i\alpha_i$ (eigenvalue). The value of $-\alpha_i$ is the growth rate, and α_r is the streamwise wavenumber.

The results from the analysis of the O-S equation are compared with the actual behavior of the flow in the DNS. The eigenvalue $-\alpha_i$ is compared with the growth rate of the disturbance. Furthermore, the eigenvalue α_r is compared with the streamwise wavenumber of the disturbance. The analysis of the time

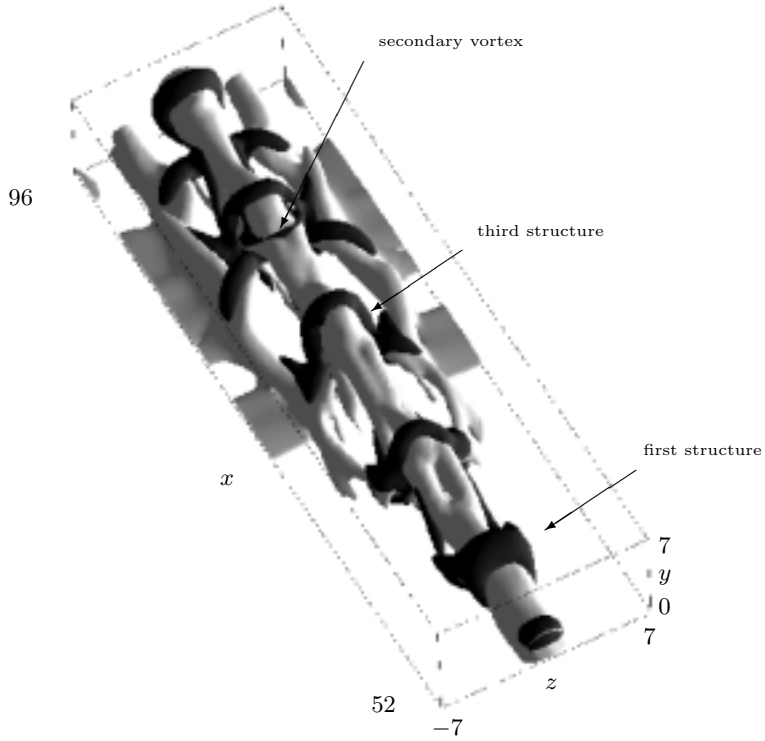

FIGURE 1. The flow field downstream of the slot. The light grey structures represent the low-speed streaks and the darker ones represent regions with low pressure. Contour levels are -0.08 for the streamwise velocity fluctuations and -0.01 for the pressure.

signal from DNS is done through a Fourier transform in time of the velocity fields. For a given frequency, we take the maximum over the spanwise and normal directions. Thus, the results from DNS is contained in a function $\hat{u}(x)$. The growth rate of the disturbance is,

$$\sigma = -Re\left\{\frac{1}{\hat{u}}\frac{d}{dx}\hat{u}\right\}, \tag{3}$$

and the streamwise wavenumber of the disturbance is,

$$\tilde{\alpha} = Im\left\{\frac{1}{\hat{u}}\frac{d}{dx}\hat{u}\right\}. \tag{4}$$

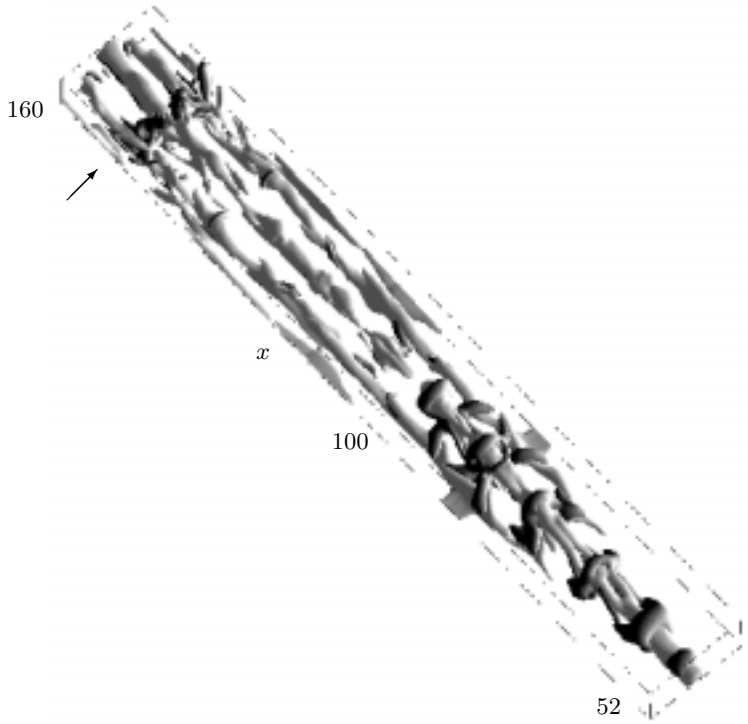

FIGURE 2. The flow field far downstream of the slot. The light grey structures represent the low-speed streaks and the darker ones represent regions with low pressure. Contour levels are -0.11 for the streamwise velocity fluctuations and -0.005 for the pressure.

3. Results

3.1. *Initial observations*

3.1.1. *Comparison with AS experiment*

The development of the streak downstream of the slot is shown in figure 1. Only the part immediately after the slot is shown. The light grey iso-surface represents the low-speed streak, and the dark grey represents the low pressure. The slot ends at $x = 60$ and the first low-pressure structure is observed at that point. The subsequent pressure structures develop downstream and become stronger. Additional streaks on either side are being induced by the pressure structure at $x = 70$. This will be further discussed in section 3.2. Around $x = 94$ the last structure in the train of vortices is observed, and the streak has been lifted upward. The low-pressure structure vanishes, but the streak and the additional, induced streaks persist downstream, as seen from figure 2, where the region downstream of the breakup is also shown. The three streaks

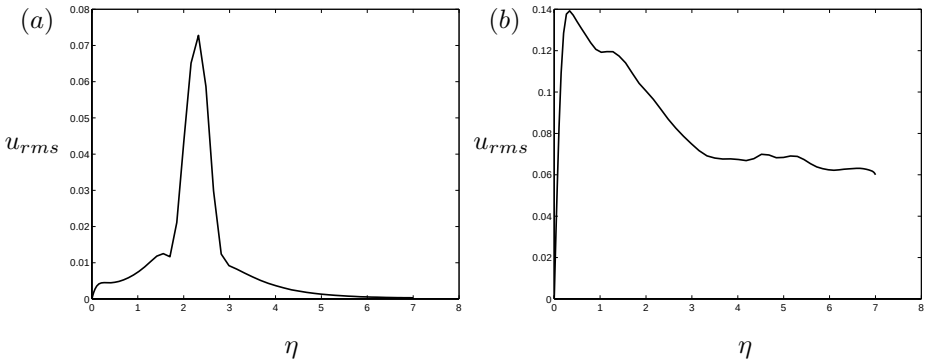

FIGURE 3. u_{rms} at a) $x = 60$ b) $x = 160$.

continues far downstream until more complicated low-pressure structures occur at $x = 145$, marked with an arrow in figure 2. Here the flow has more of a turbulent nature, which is also seen from the $rms-$values shown in figure 3. The u_{rms} profile from a position at the end of the slot is shown in figure 3 (a). This profile has a shape which is a result of an inflectional instability, which will be further discussed in section 3.4. The u_{rms} from a position far downstream ($x = 160$) is shown in figure 3 (b). This profile resembles a profile from a turbulent boundary layer. Thus, the more turbulent like flow at the far downstream region is revealed both in the structures themselves and in the statistical profiles. The streak spacing is actually 100 in viscous units in this region, further indicating attributes of a turbulent boundary layer.

In AS no spreading of the structures were observed and they argue that this is due to the sub-critical laminar boundary layer in their experiment. On the other hand, Singer & Joslin (1994) performed DNS at a larger Reynolds number, and a turbulent spot was developed from a horseshoe vortex. AS do however observe a more turbulent like profile downstream and also three elongated low-speed streaks, originating from secondary streamwise vortices. Our simulation continue further downstream than the experiment by AS, and the persistent low-speed streaks were observed downstream until the more complicated vortices appeared at $x = 145$, see figure 2.

The low-pressure structures seen in figure 1 are vortex loops, consisting of swirling flow. To illustrate that the low-pressure regions consist of rotational flow, the imaginary part of the complex eigenvalue of the deformation rate tensor can be used (Chong *et al.* 1990). Because the vorticity indicates both shear and rotation, showing vorticity can be misleading when seeking parts of the flow where rotating structures are of interest. The imaginary part of the eigenvalue on the other hand, indicates where 'solid-body' rotation, or swirling, occurs.

In figure 4 the low-pressure structures in figure 1 are shown without the low-speed streak to get a clearer picture of the structures themselves. The structures in figure 5 consist of iso-surfaces of the imaginary part of the eigenvalue. The strong correlation indicate that the structures in figure 4 are due to rapid rotation of the flow in the regions of low pressure.

Observe that the Ω-shape of the last structure in figure 5 is reminiscent of the structure observed by Zhou *et al.* (1999). Also, the kink of the legs about one-third of the length from the upstream end are present in the last structure. Note that the background flow in the present simulation is laminar whereas it was turbulent in the study of Zhou *et al.* (1999). The kinked legs and the curled back head of the last structure in figure 5 was also observed by AS at the same downstream position.

A secondary vortex is observed above the primary horseshoe vortex in the two structures before the last one in figure 5. The secondary vortex is also visible in one of the corresponding pressure structures as marked in figure 1. The secondary vortex is visible at approximately the same position as in AS. Zhou *et al.* (1999) found not only secondary horseshoe vortices developing upstream of the primary vortex, but also downstream, which was not observed in the present simulation. Singer & Joslin (1994) observed different kinds of subsidiary vortices (such as necklace or U-shaped vortices) and the initial vortex generated by the blowing finally develops into a turbulent spot. In the experiments of AS, a secondary vortex appears to originate from the position above the legs of primary vortex. It either grows to be an independent vortex, or agglomerates with the upstream or downstream vortex. The same behavior is observed in the present simulations.

Thus, the secondary vortices appearing upstream, above the legs, of the primary one are in common with many of the experimental and numerical investigations, while the generation of downstream secondary vortices depends on the strength and duration of blowing.

3.1.2. *Near-wall turbulence*

The presence of streaky structures in a near-wall turbulent flow has been observed in many experiments and simulations. These structures are low speed regions, where the streamwise velocity is lower than the mean velocity, the mean taken in the spanwise (z) direction for each $x-$ and $y-$position. They are narrow in the spanwise direction and elongated in the streamwise direction with a spanwise spacing of about 100 in wall units. Streaks lying at different positions in z break down at different positions in x. Also, a new streak seems to be born where the old one breaks down. In a number of investigations, events referred to as burst have been observed, and are generally considered to be part of the streak break up.

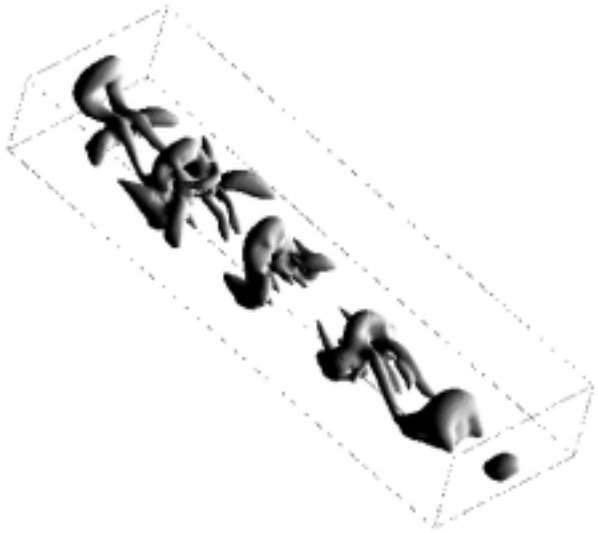

FIGURE 4. Iso-surface of low pressure just downstream of the slot. Same part of the flow field as in figure 1.

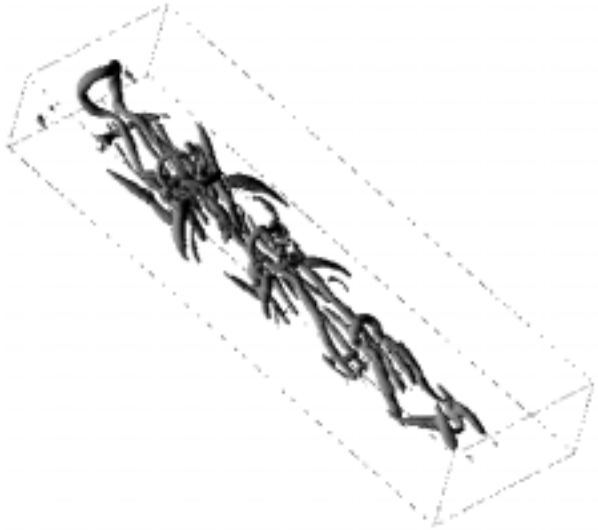

FIGURE 5. Iso-surface of the imaginary part of the eigenvalue of deformation rate tensor. The figure show the eigenvalue calculated from the same velocity field as in figure 4. Contour level at 0.32.

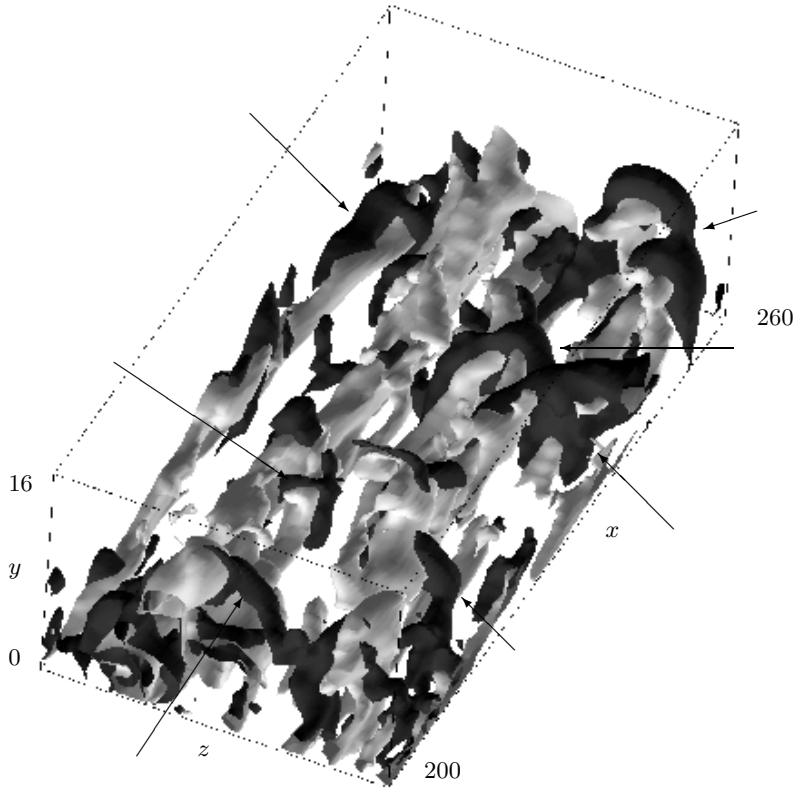

FIGURE 6. Turbulent boundary layer. Only a part of the computational box is shown. The light grey structures represent the low-speed streaks and the darker ones represent regions with low pressure. Contour levels are -0.07 for the streamwise velocity fluctuations and -0.003 for the pressure. The arrows point to some typical horseshoe vortices.

An instantaneous flow field from the simulation of a turbulent boundary layer is shown in figure 6. Only a part of the computational box at approximately $Re_\Theta = 450$ is shown. The spanwise width is about 300 in wall units and the height is 200. The light grey regions represent the low-speed streaks. Also shown in the figure, in the dark grey color, are regions of low pressure. The presence of horseshoe or hairpin vortices is well illustrated by this picture. The most clearly visible ones are marked with arrows in figure 6. It is observed that the vortices are strongly connected to the streaks, since the vortices are positioned with their head above a streak and their leg or legs on either side of the streak. This feature is common to both the laminar and turbulent streaks, c.f. figures 1 and 6.

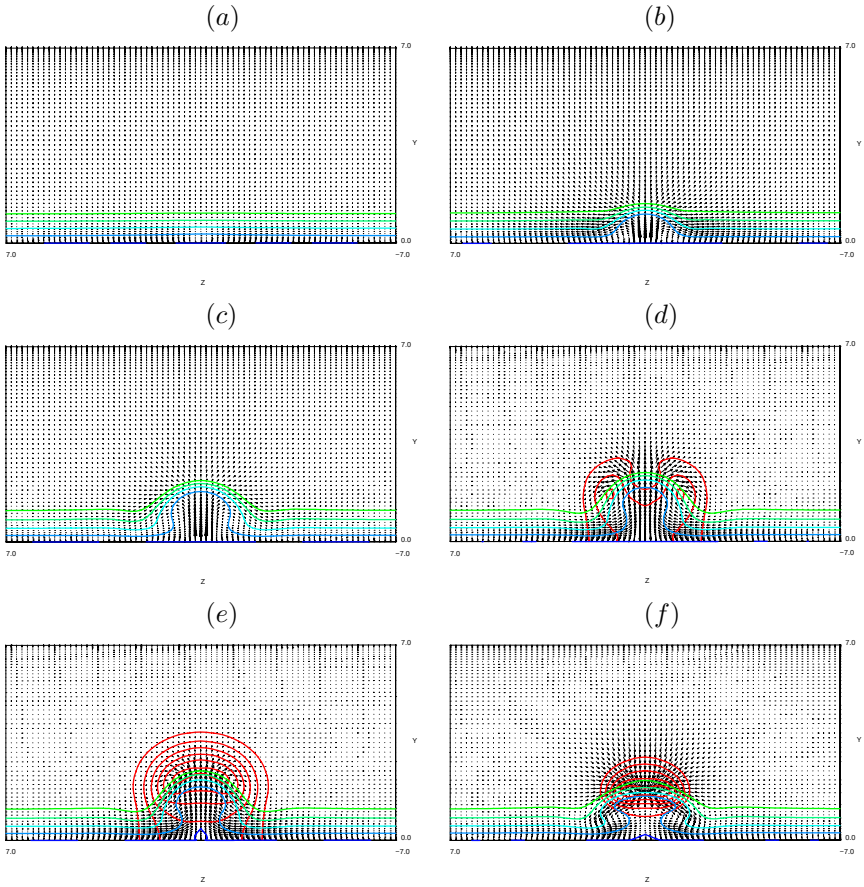

FIGURE 7. Vertical planes in the spanwise (z) and normal (y) directions. Arrows represent the spanwise and normal velocity. Blue through green lines represent constant streamwise velocity from 0 to 0.5. Red lines represent constant pressure. a) $x = 30$ b) $x = 38$ c) $x = 53$ d) $x = 59$ e) $x = 60$ f) $x = 62$

3.2. *Horseshoe vortex formation*

The mechanisms behind the formation of vortices from the streak is here studied in detail in the laminar flow with an artificial streak introduced. The proposed mechanism is that the low-speed streak makes the streamwise velocity profile highly inflectional. The instability is very strong (with a large growth rate). The disturbance grows downstream and higher harmonics occur. The stability analysis is presented in section 3.4.

The results in this section are taken from the simulation at a Reynolds number $Re_{\delta^*} = U\delta^*/\nu = 450$ at $x = 0$, which corresponds to a Reynolds

number $Re_{\delta^*} = 490$ at the beginning of the slot. The normal velocity blowing out of the slot was $V_w = 0.0657$, resulting in a slot Reynolds number of $Re_{V_w} = 28.3$. The blowing was introduced between $x = 30$ and $x = 59$ in the streamwise direction, and between $z = -0.48$ and $z = 0.48$ in the spanwise direction.

3.2.1. *Vortex formation above the slot*

One velocity field is studied, using plots in two dimensions of different planes. In figures 7 (a)—(f) the planes are from different positions in x, showing what happens with the flow above the slot. The lines in the horizontal direction, from blue to green, are the iso-lines of streamwise velocity, while the arrows represents the normal and spanwise velocity components. The first (7a) figure shows the undisturbed laminar boundary layer at the point where the slot starts. The next one (7b) shows a plane further downstream. Here the injection is visible as the strong flow out from the wall. The lines representing constant streamwise velocity are bent outward and thus forming a low-speed streak. The low-speed streak is formed because of the injection velocity that lifts up low-speed fluid from the near-wall region higher up in the laminar boundary layer. In (7c) a swirling flow is observed at either side of the low-speed streak. As the vortical motion becomes stronger it deforms the streak as seen in (7d), where also the vortex is strong enough to be represented with low pressure regions at the center of the vortex. Iso-lines of constant low pressure are shown as red lines. These low pressure regions that evolve from the center of the vortex at either side of the streak are the legs of the first low pressure structure seen in figure 1. The plane in (7d) is located at the end of the slot, thus no more injection velocity can be observed. In (7e) the low pressure region is above the streak and the motion in the region is a flow upward. The plane in (7e) is located a short distance downstream of the plane in (7d). Thus, immediately after the legs have appeared an upward motion is seen in (7e) in the low pressure region now located above the streak, and hence forms the head of the first structure. At the other side (downstream side) of the low pressure region the motion is a downward flow, as seen in figure (7f). This downward velocity at the downstream side of the head indicates that the low pressure structure is a vortex loop. Since the head is observed right after the legs, the structure is very short, which was also observed in figure 1.

3.2.2. *Vortex formation downstream of the slot*

Now that the flow above the slot and around the first structure has been studied, the flow further downstream will be investigated. The same technique is used to get an idea about what happens with the flow around the well developed structure indicated as number three in figure 1. The structure in the laminar simulation is compared with a typical structure found in the turbulent field.

In figure 8 vertical $xy-$planes are shown. In figure 8 (a) the plane is located at the centerline ($z = 0$) in the laminar field. The blue line is an iso-line

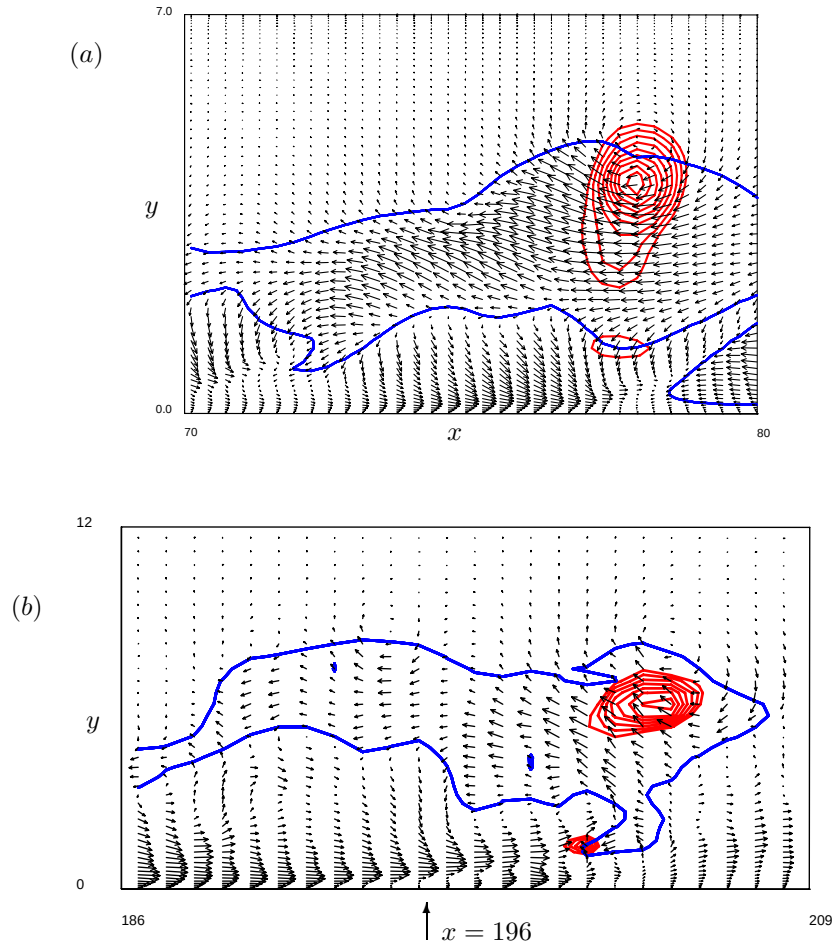

FIGURE 8. Vertical planes in the streamwise (x) and normal (y) directions. Arrows represent the streamwise disturbance velocity and normal velocity components. The blue lines represent constant streamwise disturbance velocity (low-speed streak). The red color represent constant pressure (low pressure). (a) from the laminar simulation. (b) from the turbulent simulation at $z = 1$.

of constant streamwise disturbance velocity and thus represent the low-speed streak, while the red lines are iso-lines of low pressure. The arrows indicate the normal velocity and the streamwise disturbance velocity. The streamwise disturbance velocity is calculated by subtracting the mean velocity (the mean

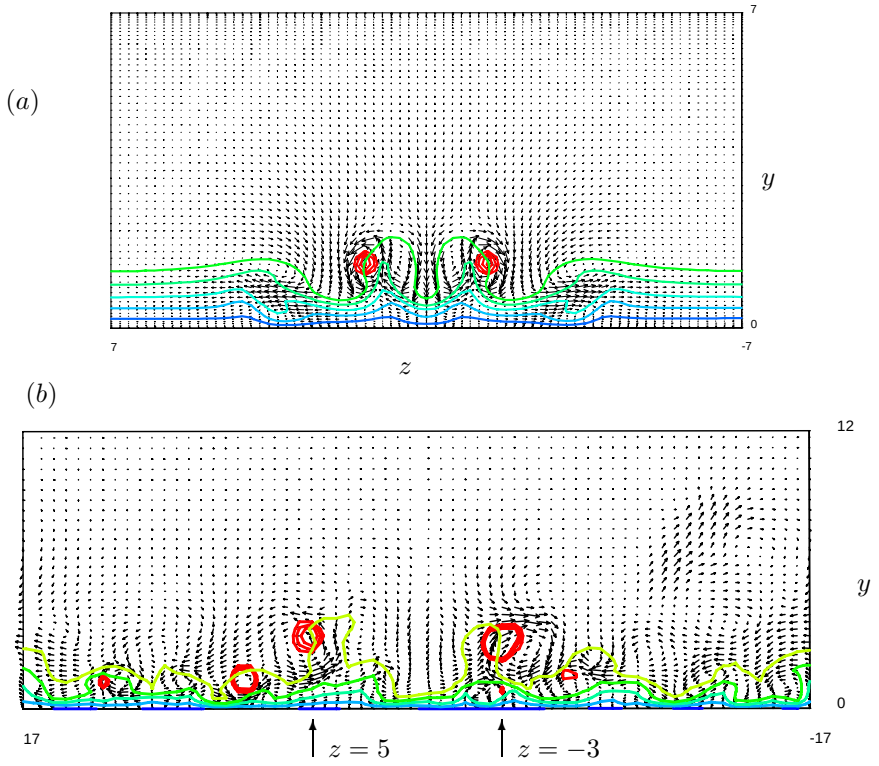

FIGURE 9. Vertical planes in the spanwise (z) and normal (y) directions. Arrows represent the spanwise and normal velocity. Blue through green lines represent constant streamwise velocity. Red lines represent constant pressure. (a) from the laminar simulation. (b) from the turbulent simulation at $x = 196$.

taken in the spanwise direction) at each point. The flow is from left to right and arrows pointing to the left merely indicate low speed compared to the mean. What is seen in figure 8 (a) is thus the head of the pressure structure. The swirling flow around the head is the relative motion when the mean streamwise velocity is subtracted. Contour levels are -0.08 for the streamwise velocity fluctuations and from -0.05 to -0.01 for the pressure.

In figure 8 (b) a structure from the turbulent simulation is shown. The horseshoe vortex was identified with a pressure plot as in figure 6. The structure is representative for a turbulent structure since many can be identified in the same instantaneous pressure field. The specific structure shown in figures 8 (b) and 9 (b) is located approximately in the middle of the computational domain ($x = 200$, $z = 1$), and is similar to the one in the upper right corner in figure 6. Then a horizontal plane is cut through the center (in the spanwise direction)

of the structure and its head is seen as the low pressure region in figure 8 (b). Contour levels are -0.04 for the streamwise velocity fluctuations and from -0.02 to -0.01 for the pressure.

The similarities between figures 8 (a) and (b) are remarkable. In both figures the center of rotation (relative the mean flow) is displaced from the center of low pressure. An additional, but weaker low pressure region is found below the head of both structures. The head of the turbulent structure in figure 8 (b) is located at $y^+ = 135$.

In figure 9, vertical cross-stream ($yz-$) planes are shown. The red contours represent low pressure and blue to yellow lines are the iso-levels of streamwise velocity. The arrows consist of normal and spanwise velocity components. In figure 9 (a) the legs of the structure in the laminar field are clearly visible as the two low pressure regions, and the flow is circling around the low pressure. Also seen are the induced vortices further out from the centerline. These induced vortices were also observed in the experiments by AS. The plane in figure 9 (a) is located at $x = 70$, thus showing the legs belonging to the structure whose head was shown in figure 8 (a). The blue to green contour lines represent streamwise velocity from zero to 0.5.

In figure 9 (b), a cross-stream plane from the turbulent simulation is shown. The plane is located at $x = 196$ (referring to the coordinates in figure 8 (b)), which corresponds to a distance of $x^+ = 184$ (wall units) upstream of the head located at $x = 204$ in figure 8 (b). The legs belonging to the horseshoe vortex whose head was observed in figure 8 (b) are the two low pressure regions located furthest from the wall, located at $z = 5$ and $z = -3$. The normal position of the legs is $y^+ = 70$, and they are separated with a distance $z^+ = 190$. The other low pressure regions close to the wall belong to streamwise vortices. The blue to yellow contour lines represent streamwise velocity from zero to 0.7. In figures 8 (b) and 9 (b) every second point in all directions is omitted for clarity.

The positions of the head and legs of the horseshoe vortex in the laminar simulation are in agreement with the experimental findings in AS. The strength of the transverse and longitudal vortices corresponding to the head and legs were calculated in AS by assuming constant vorticity within the vortex core. However, in the present DNS we find that the vorticity varies through the core. For the vortical structures visualized by low-pressure in figures 8 (a) and 9 (a), the vorticity lines (spanwise and streamwise respectively) formed the same pattern as the corresponding pressure contours. The vorticity ranged from -1 to -0.5 in the transverse vortex and from ± 1.5 to 0 in the longitudal vortices.

3.3. *Frequency characteristics*

In the experiments by AS the frequency of the roll up was measured. Their observations led to the conclusion that the frequency increased when the injection velocity or the freestream velocity was increased. They present the results as a non-dimensionalized frequency ($f\delta^*/U$) as a function of slot Reynolds number ($Re_{V_w} \equiv wV_w/\nu$) and boundary layer Reynolds number (Re_{δ^*}) at the

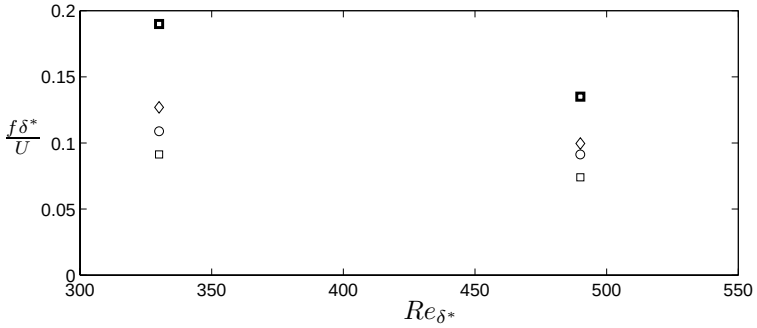

FIGURE 10. Non-dimensional frequency f^* of the disturbance versus Re_{δ^*}. Symbols correspond to different injection velocities. $Re_{V_w} = wV_w/\nu$. $Re_{V_w} = 28.3$ $\Box$; $Re_{V_w} = 33.6$ $\circ$; $Re_{V_w} = 38.7$ $\diamond$. Bold symbols represent experimental data from AS.

beginning of the slot. Here w is the width of the slot. The simulations were performed at two Re_{δ^*}, each with three different Re_{V_w}, for comparison with experimental results from AS. The Re_{δ^*} at the beginning of the computational box were 450 and 290, corresponding to 490 and 330 at the point where the slot starts.

In the present simulations the frequency was calculated using the time-signal of the velocity from various locations in the flow. The frequency of the disturbance was observed over the full extent of the slot at a number of positions in the normal direction. When either of the two Reynolds numbers were changed, the frequency also changed. The frequencies for three different Re_{V_w} at two Re_{δ^*} are plotted in figure 10, together with the results from AS (thick symbols). When the frequency is plotted as a function of the two Reynolds numbers as was done in AS, it is observed that the frequency for $Re_{V_w} = 28.3$ is half of that observed by AS (figure 10). Also, reducing Re_{V_w} further in the simulation caused the vortex generation to cease. In the experiment by AS, $Re_{V_w} = 28.3$ was the largest slot Reynolds number for which an ordered vortex generation was observed, while as low values as $Re_{V_w} = 11.3$ were shown to generate vortices.

Thus, the Re_{V_w} for which vortex generation was observed in the simulations was larger than the corresponding Re_{V_w} in the experiments. For the value of $Re_{V_w} = 28.3$, common to both simulation and experiment, the frequency observed in the simulation was half of that observed in the experiment. These discrepancies might be explained by the value of the blowing velocity, which is half the value in the simulation as compared to the experiment by AS. However, the slot has double width in the simulation, making the slot Reynolds number equal to the experimental value. If the blowing velocity itself, normalized by the freestream velocity, is used as the parameter in the comparison, the frequency

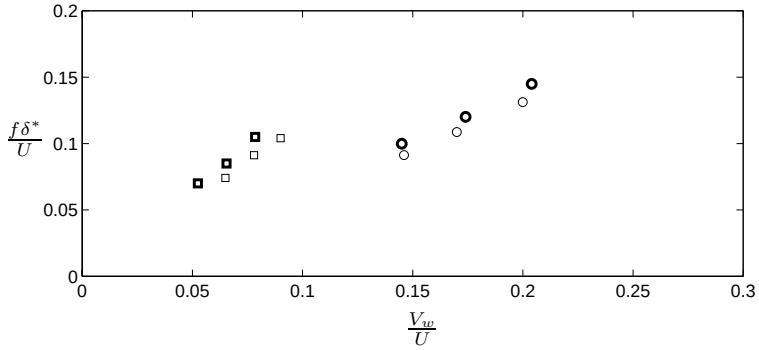

FIGURE 11. Non-dimensional frequency f^* of the disturbance versus V_w/U. Symbols correspond to different Reynolds number. $Re_{\delta^*} = 490$ □; $Re_{\delta^*} = 330$ ∘. Bold symbols represent experimental data from AS.

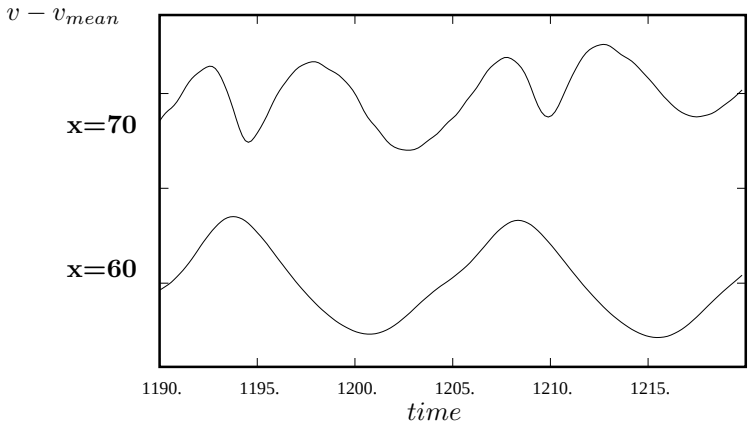

FIGURE 12. Time signal of the normal velocity component at $x = 60$ and $x = 70$.

for various blowing velocities compare well, as seen from figure 11. Thus, the initial guess that the slot Reynolds number in the simulation should be equal to the experimental value to obtain the same frequency is not supported by figure 10. Instead, it is the ratio of blowing velocity to freestream velocity that apparently is the crucial parameter in this respect, as indicated in figure 11. This was also suggested by AS, although they present their frequency data as in figure 10.

From simulation data it was observed that the frequency was doubled when going from a point above the slot to a position further downstream, as shown in figure 12, where the time signal of the normal component (v) of the velocity at the two downstream locations at $y = 0.5$ are shown. As was shown in section

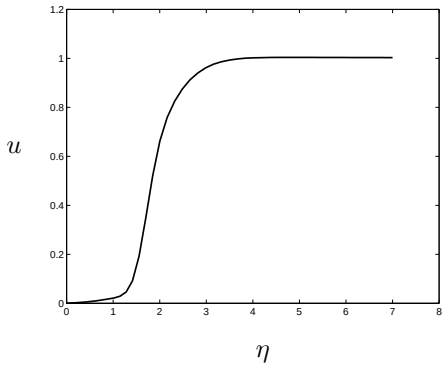

FIGURE 13. Velocity profile at $x = 45$.

3.2, the roll up the structures starts right at the downstream end of the slot ($x = 60$), and the frequency of the primary structures is thus the one measured at $x = 60$ and not the frequency of double value at $x = 70$. The doubling of the frequency is consistent with the growth of a second harmonic of the disturbance further investigated in the next section.

3.4. *Stability analysis*

In this section the laminar and turbulent simulations are treated separately. In both cases the instantaneous velocity profile will be examined. Kim *et al.* (1971) showed that the instantaneous profile in a turbulent boundary layer contained an inflectional instability in the later stages of the low-speed streak lift-up and the instability lead to oscillations. The O-S analysis performed by Kim *et al.* showed good agreement between the growth rates and eigenfunction shape. On the other hand, the mean velocity profile in a turbulent channel flow, deformed by the low-speed streak modeled by a trigonometric function, was shown to be stable to the varicose mode by Schoppa & Hussain (1997) and Kawahara *et al.* (1998).

We believe the instantaneous profile gives more realistic results from the stability analysis in the turbulent case since the growth rate is very strong and the instantaneous profile is far from the mean profile in shape. In the laminar case, the mean and instantaneous profiles are equivalent at the position where the stability calculation is performed.

3.4.1. *The laminar case*

From the observations of their experiment, AS speculate that an inflectional instability causes the oscillations on the low-speed streak leading to vortex roll up. We will here show that this is the most plausible explanation.

As described in section 2.2, the spatial stability analysis is performed with the O-S equation. The input is the Reynolds number, frequency of the disturbance, and the velocity profile. The three inputs are well defined and taken

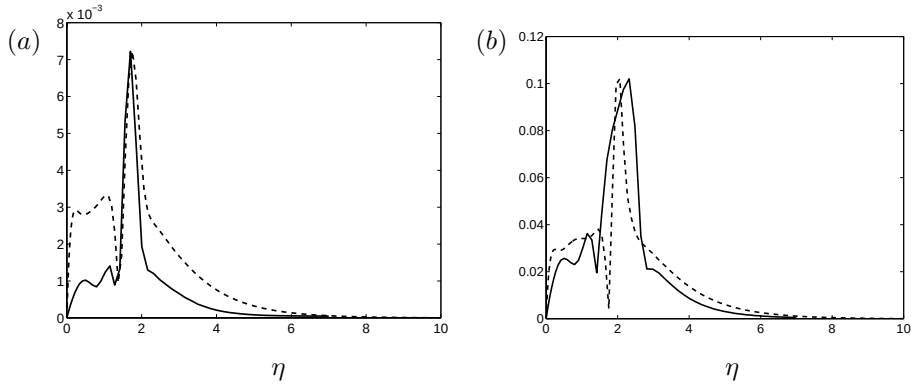

FIGURE 14. Streamwise component. a) $x = 45$. b) $x = 55$. — $rms-$value; - - Eigenfunction.

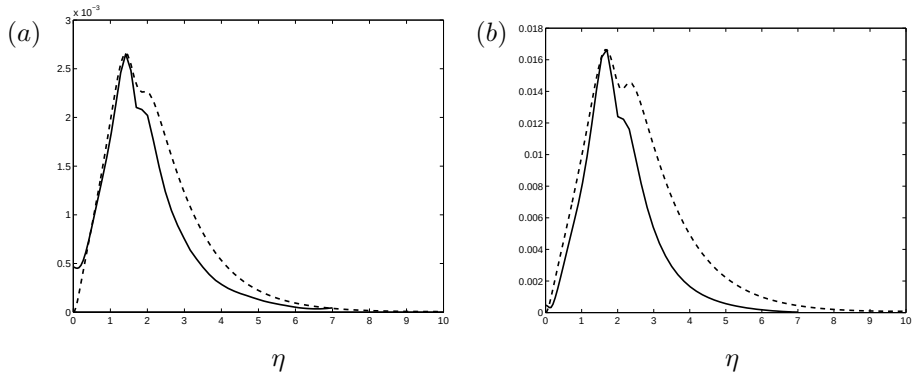

FIGURE 15. Normal component. a) $x = 45$. b) $x = 55$. — $rms-$value; - - Eigenfunction

from the DNS. The output is the eigenfunction, which contains information of the disturbance shape, and the eigenvalue, which gives the growth rate and the streamwise wavenumber.

Throughout this section the laminar simulation with $Re_{\delta^*} = 490$ at the beginning of the slot and a slot Reynolds number of $Re_{V_w} = 28.3$ will be considered. In figure 13 the velocity profile at $x = 45$ and $z = 0$, corresponding to the center of the slot, is shown. The profile is highly inflectional and the O-S analysis will give a large value of the growth rate.

Figures 14 and 15 show the eigenfunction from the O-S together with the $rms-$value of the velocity from DNS at positions $x = 45$ and $x = 55$. The eigenfunctions are calculated using the instantaneous velocity profile at the two $x-$positions as basic states. The $rms-$value from DNS is calculated over

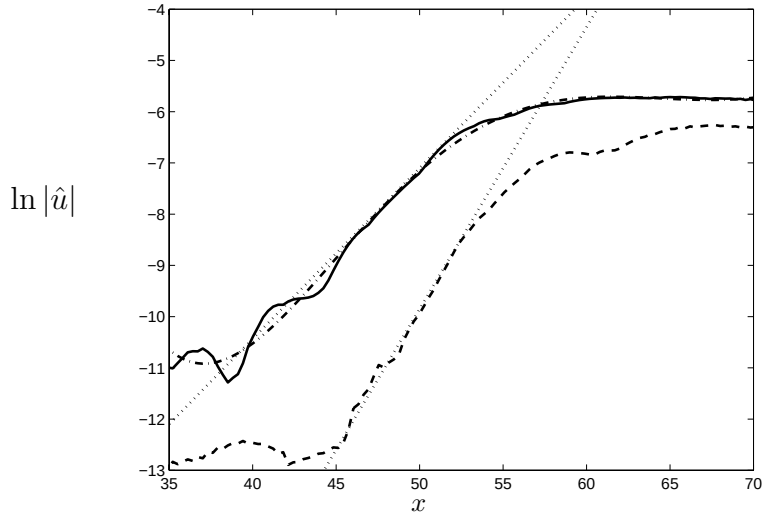

FIGURE 16. Maximum of u. — first harmonic; - - second harmonic; $\cdots$ linear fit; - $\cdot$ - curve fit of first harmonic.

one period of the disturbance, which was $T = 14.8$ (in units of δ^*/U) and the corresponding frequency was $\Omega = 0.425$.

The eigenfunction in the streamwise direction is shown in figures 14 (a) and (b), together with the corresponding u_{rms} from the DNS. The solid line is DNS data and the dashed line is from the O-S analysis. The wall normal coordinate is scaled with the boundary layer thickness. The sharp peak in the profile is due to the shear layer instability. At both x-positions the shape is well predicted. The double inner peak observed in the u_{rms} profile is over predicted by the O-S analysis at $x = 45$ and is lacking at $x = 55$.

The eigenfunction in the normal direction is shown in figures 15 (a) and (b), together with the corresponding v_{rms} from the DNS. The profiles are well predicted by the linear O-S analysis. However, the second, outer peak is over predicted by the linear O-S analysis. Observe that v_{rms} is not zero at the wall due to the injection through the slot.

The results shown in figures 14 and 15 are based on an instantaneous two-dimensional approximation of the basic state. The agreement between the calculated eigenfunctions and the $rms-$profiles found in the fully three-dimensional DNS is remarkable, indicating that the instability mechanism is determined mainly by the local flow conditions.

The growth rate from DNS data is calculated from the Fourier transform in time of velocity fields as a function of x. When comparing the growth rate and streamwise wave number from the O-S analysis with the corresponding values from DNS data, the DNS data has to be smoothed since taking derivatives directly will give spurious oscillations.

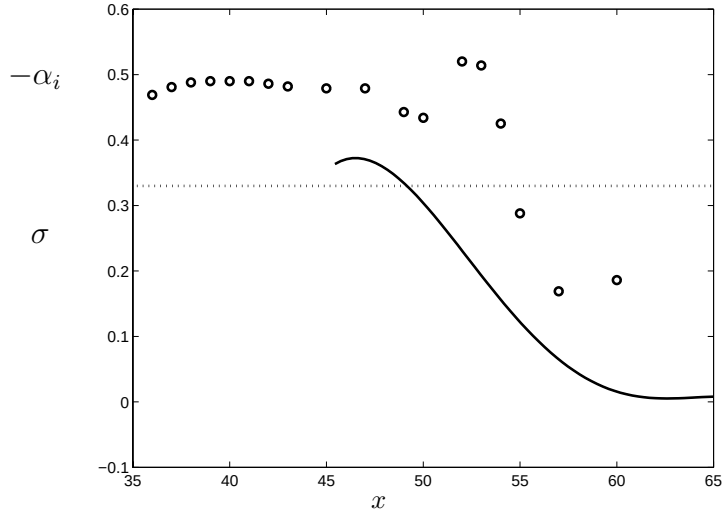

FIGURE 17. ∘ The growth rate from the O-S analysis. — Smoothed DNS data (curve fit). ··· Linear approximation to DNS data.

The growth rate from the DNS data, denoted by σ, is calculated from the development in time of the maximum value of the velocity in the downstream direction. The maximum value is extracted for different frequencies from the Fourier transform in time. The transformed velocity is,

$$\hat{u}(x, y, z, \omega) = \int_{-\infty}^{\infty} u(x, y, z, t) e^{-i\omega t} dt \tag{5}$$

By taking the maximum over y and z and specifying which frequency of interest, only the x-dependency is left, $\hat{u} = \hat{u}(x)$.

In figure 16 the maximum of $\hat{u}$ in the first and second harmonics are shown. The maximum occurs at the centerline. By showing the logarithm of the maximum as in figure 16, a curve fit is possible, shown as the dash-dotted line. Also in figure 16 the linear approximations to both the first and second harmonics are shown as the dotted lines. The slope for the second harmonic is twice the slope for the first.

Now, the growth rate is calculated from equation (3), which can be written as,

$$\sigma = \frac{1}{|\hat{u}|} \frac{d}{dx} |\hat{u}| = \frac{d}{dx} \left(\ln |\hat{u}| \right). \tag{6}$$

The linear approximation to the maximum of $\hat{u}$ in the first harmonic (shown in figure 16) is used for calculating the growth rate, which becomes a constant and is shown as the dotted line in figure 17. By using the curve fit of $\hat{u}$ instead of the linear approximation, the growth rate becomes as the solid line shown in

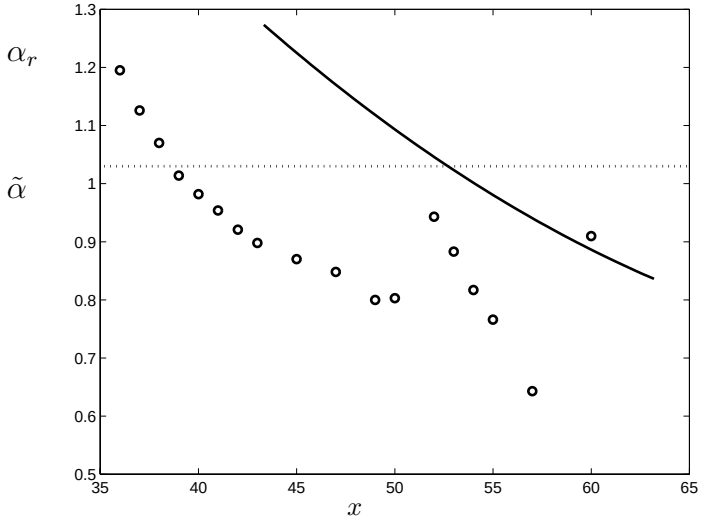

FIGURE 18. ∘ The streamwise wavenumber from O-S the analysis. — Smoothed DNS data (curve fit). ⋯ Linear approximation to DNS data.

figure 17. The circles are the corresponding growth rates calculated from O-S using the instantaneous velocity profiles.

The real part of the eigenvalue (α_r) from the O-S analysis, is shown in figure 18 as circles. To calculate the corresponding α_r from DNS, which is denoted $\tilde{\alpha}$, equation (4) is used. This equation also involves derivatives in the downstream direction which cause spurious oscillations. To equivalently smooth the $\tilde{\alpha}$, equation (4) is rewritten, by noting that $\hat{u} = e^{i\Theta}$, in the form,

$$\tilde{\alpha} = Re\left\{\frac{d\Theta}{dx}\right\}. \tag{7}$$

Thus, it is a matter of smoothing Θ, which is defined by

$$\Theta = -i \ln \hat{u}. \tag{8}$$

The resulting smoothed $\tilde{\alpha}$ is shown in figure 18. The linear approximation becomes a constant and is also shown in the figure.

3.4.2. *The turbulent case*

So far, the the detailed analysis of the low-speed streak in an otherwise laminar boundary layer has confirmed some of the results from the experiment of AS. Furthermore, a thorough analysis of the origin of the instability of the streak was made with linear stability analysis. The simulations also showed the development of more complicated structures further downstream, where the statistics resembled turbulence.

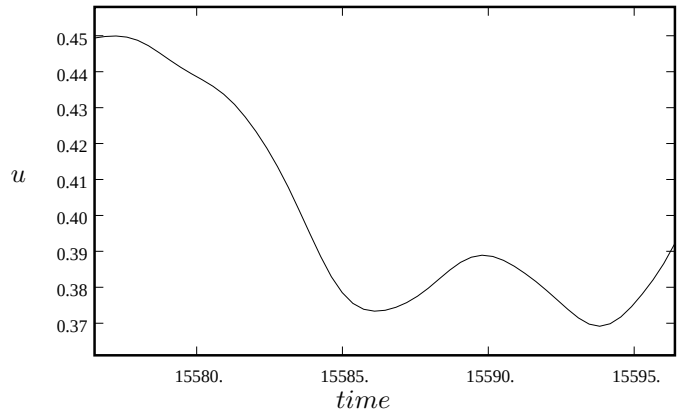

FIGURE 19. Time signal of the streamwise velocity component at $x = 170$, $y = 0.4$, $z = -6.5$.

These results, together with the striking resemblance of the streak development between figures 6 and 1 lead to the hypothesis that, at least to some degree, the break up of streaks in a turbulent field is governed by the same mechanisms as for the isolated streak in the laminar boundary layer.

To qualitatively show that the instabilities of the streaks in a turbulent boundary layer is of the same normal inflectional type as in the laminar case, the O-S analysis was performed with a velocity profile from the turbulent velocity field.

When a horseshoe structure in the turbulent field has been identified, it can be followed backward in time, if velocity fields from earlier times are available. Since the life cycle of a structure is long (over $T = 150\ \delta^*/U$), the requirement for data storage is demanding. As the structure is followed backward in time, it is found further upstream and is weaker. At some point in time and space the structure vanishes. Thus, at this point the birth of the structure can be investigated. By examining the time signal of the velocity from points just upstream of the first appearance of the structure, the frequency of the disturbance leading to the vortex formation can be determined. One example of a time signal of the streamwise velocity is shown in figure 19. The instability wave appears at time 15588.

The point ($x = 170$, $y = 0.4$, $z = -6.5$) where the velocity signal was examined is located just upstream of the first appearance of a structure. The newly born structure is shown in figure 20. The figure shows the low pressure signature of the structure at the time 15596 (referring to figure 19).

The velocity profile was extracted from the turbulent field at a point where the disturbance was small compared to further downstream, i.e. before roll up of the vortex. In this particular case the point was located at ($x = 170$,

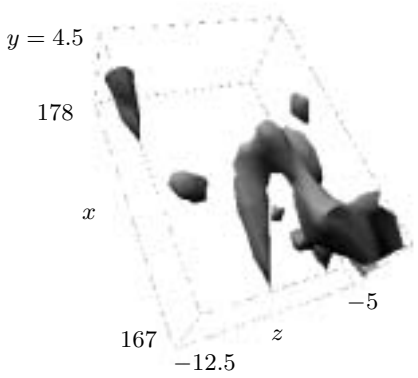

FIGURE 20. Iso-surface of pressure at time 15596. Contour level at -0.004. The height of the box shown is 4.5, corresponding to 80 in wall units.

$z = -6.5$) at the time 15584. This profile was used together with the observed frequency in the O-S equation.

To compare the DNS data with the eigenfunctions from the O-S analysis, the $rms-$profiles were extracted by collecting statistics during a simulation over one period of the disturbance. The $rms-$profiles were taken from the same position as where the frequency of the disturbance was observed for the longest period of time. This position is ($x = 170$, $z = -6.5$) in the example discussed above. The time interval over which the $rms-$profiles were taken was 15584—15596.

This whole procedure was performed for three independent structures, each separated in time over 2000 (δ^*/U). All three of the structures could be traced back to their point of roll up, and the analysis of the velocity profiles gave similar results.

Furthermore, the O-S analysis showed that the resulting eigenfuctions are not sensitive to changes in Re_{δ^*} and frequency (ω). The independence of Reynolds number is explained by the inviscid nature of the inflectional instability. The insensitivity on ω shows that the time-scale of the disturbance is not important for the instability mechanism. This points towards an instability of a Kelvin-Helmholz character.

One example of the velocity profile just before roll up is shown in figure 21. The frequency in this case was $\omega = 0.78$ and the O-S analysis gave a growth rate of $-\alpha_i = 0.024$. The eigenfunctions from the O-S analysis were then compared to $rms-$values taken over one period of the disturbance. The results from this analysis are shown in figures 22 (a) and (b). In the streamwise component (22a), the double peak is predicted by the linear analysis, even though the outer peak is located further out in the u_{rms} profile. In the normal component

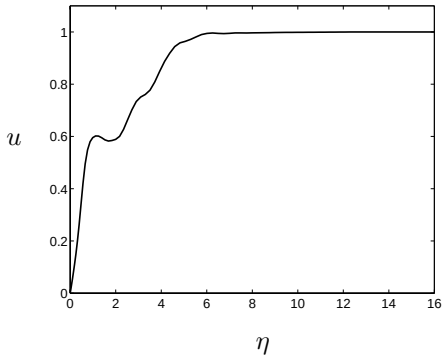

FIGURE 21. Velocity profile from a turbulent boundary layer.

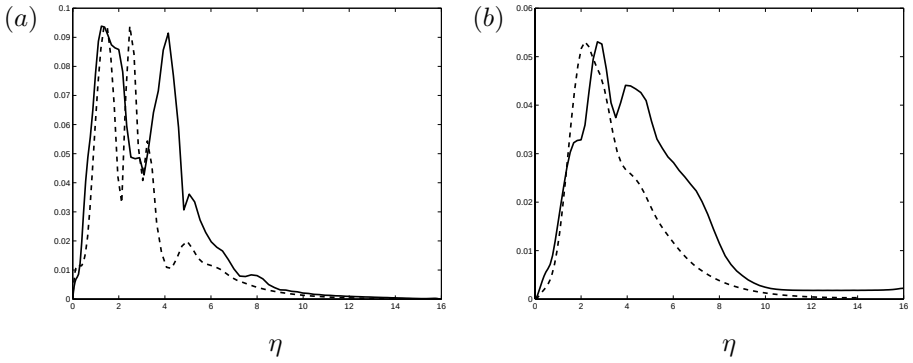

FIGURE 22. (a) Streamwise component. (b) Normal component. — $rms-$value of velocity. - - Eigenfunction from the O-S equation.

(22b), the inner peak is located slightly closer to the wall in the predicted profile. Also a tendency to a second peak is seen, though the v_{rms} profile has a much stronger peak.

Although we have only investigated three randomly picked events, the results are promising and a larger investigation with an objective method for detecting structures, followed by tracing them back in time to their point of origin and the associated inflectional velocity profile, could provide statistical evidence of the horseshoe vortex formation. This is however beyond the scope of the present investigation. The method described here is not suitable since it is too time and storage consuming for any larger statistical evaluation.

4. Discussion and conclusions

A DNS of a laminar boundary layer disturbed by a continuous blowing through a slot in the wall has been performed. The objectives were to reproduce and further investigate the results reported from the experiments of Acarlar &

Smith (1987). The blowing of fluid from the slot creates a low-speed streak which exhibits a disturbance wave growing downstream. This secondary disturbance was shown to originate from a normal inflectional instability in the streamwise velocity profile. An anlasysis using the Orr-Sommerfeld equations gave qualitative agreement in the growth rate and streamwise wavenumber with the corresponding values extracted from the DNS velocity fields. The non-linear effects gave rise to higher harmonics at the end of the slot where the first low-pressure structure was found. The structure consist of a vortex loop that evolves downstream to form a horseshoe vortex. After the horseshoe vortex breaks down the low-speed streak persist together with additional streaks formed by the horseshoe vortex. Further downstream more complicated structures appear and the streak spacing is 100 in wall units.

The frequency of the vortex generation was shown to scale with the ratio between the blowing velocity and freestream velocity. Good agreement with the experimental data was obtained.

Also a DNS of a zero pressure gradient turbulent boundary layer was performed, and horseshoe vortices were observed using low-pressure identification. The similarities between structures in the turbulent field and the ones originating from the low-speed streak in the laminar simulation were presented.

The inflectional instability considered in the present work is of a different type from those investigated in Waleffe (1997), Kawahara *et al.* (1998) and Schoppa & Hussain (1997), who model the turbulent velocity profile as a mean flow with the streaky structure deforming the profile, rather than the instantaneous profile considered here. They showed that it is the sinuous mode which is unstable, whereas the laminar streak investigated here does not show the characteristics of such an instability. Furthermore, it has been shown by Bottaro & Klingmann (1996) for streak instability of Görtler flow, that the growth rate of the sinuous mode scales with the spanwise derivative of the mean flow, just as in the model of Waleffe and in the secondary instability calculations of Andersson *et al.* (2000). Thus it is reasonable to assume that the sinuous instability depends primarily on the appearance of the spanwise inflection. Reddy *et al.* (1998) further showed that the sinuous instability is inhibited by the appearance of normal shear.

We show in this work, as it has been implied in others (e.g. Robinson 1991*b*), that the appearance of an unstable normal velocity profile (in many cases associated with a normal inflection point) is a precursor to the appearance of horseshoe vortices. In terms of a streak instability, Bottaro & Klingmann (1996) among others, have shown that this is related to the varicose mode. Thus the sinuous streak instability is correlated with a basic state with a spanwise inflection and the varicose mode with a basic state with a normal inflection.

It is reasonable to assume that both types of streak instabilities are of importance in a turbulent boundary layer, the sinuous type for the regenaration of near-wall turbulence, as shown by Jimenez & Moin (1991) and Hamilton

et al. (1995), and the varicose type for the production of horseshoe vortices populating the region away from the wall.

References

Acarlar, M. S. & Smith, C. R. 1987 A study of hairpin vortices in a laminar boundary layer. Part 2. Hairpin vortices generated by fluid injection. *J. Fluid Mech.* **175**, 43–48.

Adrian, R. J., Meinhart, C. D. & Tomkins, C. D. 2000 Vortex organization in the outer region of the turbulent boundary layer. *J. Fluid Mech.* **422**, 1–54.

Andersson, P., Brandt, L., Bottaro, A. & Henningson, D. 2000 On the breakdown of boundary layer streaks. *J. Fluid Mech.* (In press).

Bottaro, A. & Klingmann, B. G. B. 1996 On the linear breakdown of Görtler vortices. *Eur. J. Mech., B/Fluids* **15**, 301–330.

Chong, M. S., Perry, A. E. & Cantwell, B. J. 1990 A general classification of three-dimensional flow fields. *Phys. Fluids A* **2**, 765–777.

Chong, M. S., Soria, J., Perry, A. E., Chacin, J., Cantwell, B. J. & Na, Y. 1998 Turbulence structures of wall-bounded shear flows found using dns data. *J. Fluid Mech.* **357**, 225–247.

Hamilton, J. H., Kim, J. & Waleffe, F. 1995 Regeneration of near-wall turbulence structures. *J. Fluid Mech.* **287**, 317–348.

Jeong, J. & Hussain, F. 1997 Coherent structures near the wall in a turbulent channel flow. *J. Fluid Mech.* **332**, 185–214.

Jimenez, J. & Moin, P. 1991 The minimal flow unit in near-wall turbulence. *J. Fluid Mech.* **225**, 213–240.

Jimenez, J. & Pinelli, A. 1999 The autonomous cycle of near-wall turbulence. *J. Fluid Mech.* **389**, 335–359.

Kawahara, G., Jimenez, J., Uhlmann, M. & Pinelli, A. 1998 The instability of streaks in near-wall turbulence. Center for Turbulence Research, Annual Research Briefs 1998, 155–170.

Kim, H. T., Kline, S. J. & Reynolds, W. C. 1971 The production of turbulence near a smooth wall in a turbulent boundary layer. *J. Fluid Mech.* **50**, 133.

Kim, J., Moin, P. & Moser, R. 1987 Turbulence statistics in fully developed channel flow. *J. Fluid Mech.* **177**, 133–166.

Lundbladh, A., Berlin, S., Skote, M., Hildings, C., Choi, J., Kim, J. & Henningson, D. S. 1999 An efficient spectral method for simulation of incompressible flow over a flat plate. *Tech. Rep.* TRITA-MEK 1999:11. Royal Institute of Technology, Stockholm.

Perry, A. E., Marušić, I. & Li, J. D. 1994 Wall turbulence closure based on classical similarity laws and the attached eddy hypothesis. *Phys. Fluids* **6** (2), 1024–1035.

Reddy, S. C., Schmid, P. J., Bagget, P. & Henningson, D. S. 1998 On stability of streamwise streaks and transition thresholds in plane channel flows. *J. Fluid Mech.* **365**, 269–303.

Robinson, S. K. 1991*a* Coherent motions in the turbulent boundary layer. *Ann. Rev. Fluid Mech.* **23**, 601–639.

Robinson, S. K. 1991*b* The kinematics of turbulent boundary layer structure. NASA TM 103859.

Schoppa, W. & Hussain, F. 1997 Genesis and dynamics of coherent structures in near-wall turbulence: A new look. Self-Sustaining Mechanisms of Wall Turbulence (Ed. Panton, R.L), Southampton: Computational Mechanics Pub.

Singer, B. A. 1992 The formation and growth of a hairpin vortex. In *Instability, Transition and Turbulence* (eds. M. Y. Hussaini, A. Kumar & C. L. Street), pp. 367–376. Springer.

Singer, B. A. & Joslin, R. D. 1994 Metamorphosis of a hairpin vortex into a young turbulent spot. *Phys. Fluids* **6**, 3724–3736.

Waleffe, F. 1997 On a self-sustaining process in shear flows. *Phys. Fluids* **9**, 883–900.

Zhou, J., Adrian, R. J., S., B. & Kendall, T. M. 1999 Mechanisms for generating coherent packets of hairpin vortices in channel flow. *J. Fluid Mech.* **387**, 353–396.

Paper 8

P8

The performance of a spectral simulation code for turbulence on parallel computers with distributed memory

By Krister Alvelius and Martin Skote

Department of Mechanics, KTH, SE-100 44 Stockholm, Sweden

The performance of a pseudo spectral turbulence simulation code on various supercomputers, with either shared memory or distributed memory, is presented. The communication with the memory is intense, and careful consideration of the two memory configurations is needed to obtain high performance. The investigations of the performance show that the scaling with the number of processors is excellent for both memory systems. Also, vector processors are compared with super scalar processors, and the performance is generally higher for the vector processor since the code vectorizes well. However, the computers with the scalar processors, and distributed memory, have a much larger number of processors which gives an overall better performance for the total machine. The numerical code, with e.g. $24 \cdot 10^6$ degrees of freedom, was run at 3.5 Gflop/s on 64 processors on an IBM SP2 machine.

1. Introduction

Direct numerical simulation (DNS) of turbulent flows is a major field for the use of super computers world-wide, and has throughout the years been an important factor in driving the process of developing super computers. This is an area which efficiently makes use of all available memory of the computer, and the scaling with the number of processors is excellent. Also the communication between the processors is relatively intense. The performance of DNS codes is hence an important measure of a computers ability to handle real problems of physical interest.

1.1. *Scientific background*

The nature of turbulence is very complex. A turbulent flow consists of both large and small scale motions that fluctuate in time and space. The incompressible flow of e.g. air can be described by the Navier-Stokes (NS) equations together with suitable boundary conditions. They are non-linear equations, which generally need to be discretized in order to yield a solution. In these equations the non-linear term generates turbulent motions and the viscous term dissipates flow fluctuations. The viscous dissipation of turbulence adjusts

itself to the production, which determines the smallest scales in the flow, η, usually referred to as the Kolmogorov micro length scale. The viscous term becomes large in the presence of large velocity gradients associated with small scale motions. It does, however, only scale linearly with the magnitude of the velocity field, while the scaling of the non-linear term is quadratic. Therefore, an increased magnitude in the velocity causes the smallest scales to become even smaller (through the cascading action of the non-linear terms) to yield increased velocity gradients and a larger dissipation which balances the production by the non-linear terms.

The size of the largest scales, l, is usually determined by the geometry of the flow domain. The size of the range of scales in the flow is measured by the Reynolds number ($Re \sim (l/\eta)^{4/3}$) which depends on the type of flow, the magnitude of the flow velocities, the domain size and the kinematic viscosity.

In a DNS of a turbulent flow all scales (l – η) need to be captured by the numerical method. Since turbulent flows are always three-dimensional, even moderate Reynolds numbers give a significant degree of freedom for the resulting discrete dynamic system that needs to be solved. In addition there is a span of timescales that needs to be resolved. The time step is determined by the smallest turbulent timescales and stability requirements of the numerical method. Typically a large number of discrete time integrations needs to be performed in order to include one large time scale in a simulation. In order to obtain statistically converged results it is also necessary to integrate the solution over many large time scales.

DNS have, until recently with the development of modern computers, been an impossible task even for small Reynolds numbers. Therefore, researchers have been led to study the averaged equations instead, which give much smoother solutions and significantly reduces the computational effort. This approach introduces an unknown quantity, the Reynolds stress tensor, which needs to be modelled. Development of such models, with different degrees of complexity, has been an important task for turbulence researchers. Calibrations of models are essential and can be performed in e.g. windtunnel experiments. It shows that the modelled quantities behaves differently in different flow situations. Although it is relatively easy to obtain high Reynolds numbers in the windtunnel experiments, they sometimes fail to give accurate descriptions of complex quantities in the flow. Also, they cannot give a total description of the flow situation since the complete velocity field is not available.

The DNS of turbulent flows gives the time development of the complete velocity field and allows the study of any particular flow phenomenon you choose in detail. This can be used to increase the understanding of the underlying mechanism, resulting in better turbulence models. Also a new method, large eddy simulation (LES), similar to that of DNS, have been developed in recent years where only the smallest scales are modelled in the flow and the large scales are resolved. This method has been found to be successful in computing real engineering flows with complicated geometries, using only simple models

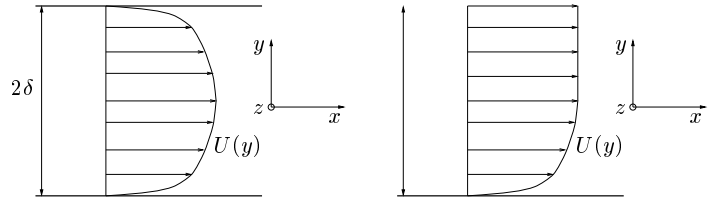

FIGURE 1. The flow configurations of plane channel flow and boundary layer flow.

for the unknown subgrid-scale stresses, since the main effect of the domain geometry on the flow enters through the large scales which are resolved. The numerical implementation of this method is similar to that of DNS. In particular, when developing models for the subgrid-scale quantities, DNS data is essential since the modelled quantities fluctuate in time and space, and the whole velocity field has to be available at a single instant.

Both in DNS and in experimental investigations it is important to know what effects that are important in the flow in order to be able to make correct conclusions. Therefore the flow should be constructed so that effects that you are not interested in are negligible or controllable. One such important test case is the plane channel flow (figure 1) where only effects of plane mean shear and of the solid walls are present. In DNS it is also important to have a simple geometry which simplifies the numerical implementation and improves the accuracy in the numerical discretization. This is true in the plane channel flow which has no curvature and only needs grid stretching in the non-homogeneous wall normal direction. In addition to the shear and wall effects in the plane channel flow, the effect of curvature can be studied by adding system rotation to the governing equations.

The boundary layer flow (figure 1) on a flat plate is another example of a simple flow with a solid wall and plane shear. In this case a free boundary gives a more complicated flow, e.g. the boundary layer grows downstream. The flow can be studied in various aspects. The fully turbulent flow, as well as transitional flow, where a breakdown from laminar to turbulent flow occurs, is of great importance in many industrial applications. There is still no complete picture of the mechanisms behind this breakdown, and further investigations are needed. Both the transitional and turbulent flows can be studied with additional complications such as external pressure gradients or three-dimensional mean flow.

Both the turbulent channel flow and the fully turbulent boundary layers can be studied for gaining data used for calibration and development of turbulence models. But the data are not only used for modeling purposes, the instantaneous turbulent structures can be thoroughly studied since the whole flow field is accessible at each time step.

1.2. *The numerical discretization*

Ideally, the plane channel is considered to be infinitely long and infinitely wide, with the flow driven by a mean pressure gradient in the streamwise direction. In the numerical simulation periodic boundary conditions is imposed in the streamwise and spanwise directions. In the wall normal direction a non-slip condition is applied at the solid walls.

For the boundary layer flow the downstream direction must be treated in a different way. The boundary layer is increasing (getting thicker) downstream, and that direction can thus not be considered periodic. It is possible to create a periodic flow if a so called fringe region is added downstream of the physical domain, figure 2. In the fringe region the flow is forced from the outflow of the physical domain to the inflow. In this way the physical domain and the fringe region together satisfy periodic boundary conditions. The fringe region is implemented by the addition of a volume force which form is designed to minimize the upstream influence.

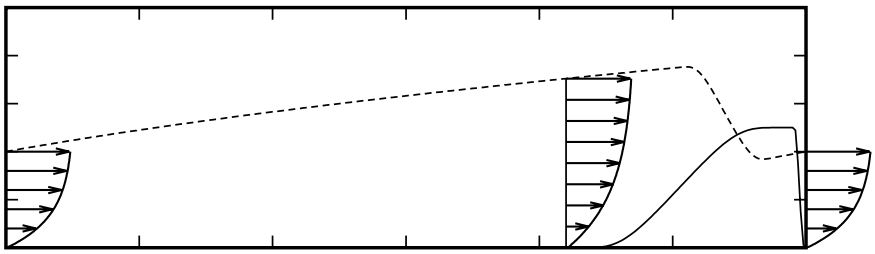

FIGURE 2. Computational box with the fringe region. — the strength of the volume force in the fringe region. - - the boundary layer thickness.

The periodic boundary conditions make it possible to use Fourier representation of the velocity field, which gives an accurate description of the spatial derivatives in the discretization direction. Compared to a finite difference method, which typically gives only a second-order approximation of the spatial derivatives, the numerical accuracy is significantly increased. The wall normal direction is discretized using Chebyshev polynomials. Hence, spectral methods are used in all spatial directions, which gives an overall highly accurate discretization of the governing equations.

The time integration is discretized with a second order Crank-Nicolson scheme for the linear terms and a four stage third-order Runge-Kutta scheme for the non-linear terms. The Crank-Nicolson method is implicit and hence absolutely stable, whereas the Runge-Kutta method is explicit, which imposes a restriction on the time step to yield stable solutions. The time step is determined by the CFL number and adjusts itself automatically to the actual flow situation.

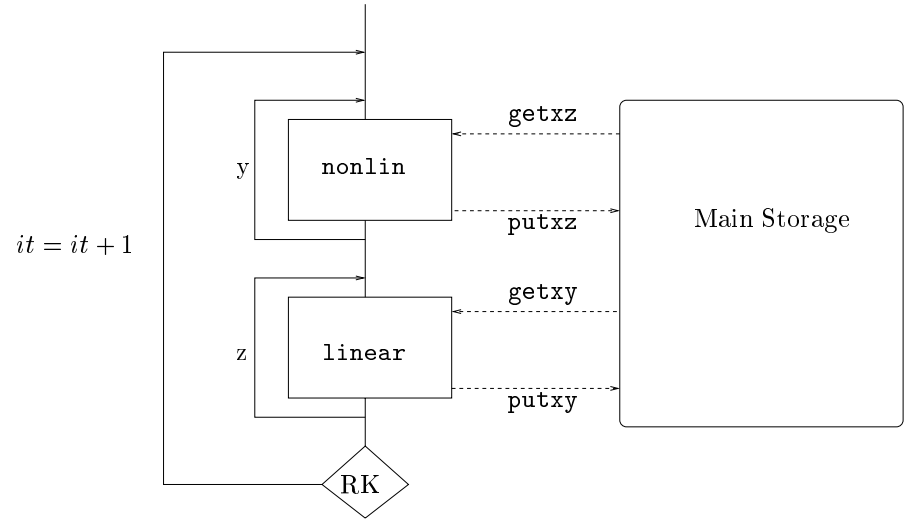

FIGURE 3. The main structure of the program.

Instead of solving for all three velocity components and the pressure, a vorticity-velocity formulation is used, in which the fluctuating pressure is eliminated. In this formulation only two equations need to be solved instead of the original four equations (the NS equations and the continuity equation).

The discretization results in a tri-diagonal equation system in spectral space for each of the two variables, which needs to be solved at each Runge-Kutta step. The non-linear terms in the equations are calculated in physical space, using fast Fourier transforms (FFT) in the transformations between spectral and physical space. The velocity field is represented on a 3/2 times finer mesh in the streamwise and spanwise directions in physical space compared to spectral space. This results in a 3/2-dealiasing method which is energy conserving.

The numerical code is written in FORTRAN and consists of two major parts (figure 3), one linear part (`linear`) where the actual equations are solved in spectral space, and one non-linear part (`nonlin`) where the non-linear terms in the equations are computed in physical space. The actual flow variables are stored at an intermediate level with spectral representation in the streamwise (x) and spanwise (z) directions and physical representation in the wall normal (y) direction. All spatial derivatives are calculated in the spectral formulation. The main computational effort in these two parts is in the FFT.

In the linear part one xy-plane is treated separately for each z variable. The field is transformed in the y direction to spectral space, a solution is obtained and then transformed to physical space in the y direction. This is performed

with an loop over all z values where the subroutine `linear` is called for each z. The xy-planes are transferred from the main storage with the routine `getxy` to the memory where the actual computations are performed. The corresponding storing of data is performed with `putxy`.

In the non-linear part the treatment of the data is similar to that in the linear part. One xz-plane is treated separately for each y variable. The field is transformed in both the x and z directions to physical space where the non-linear terms are computed. Then the field is transformed in the x and z directions to spectral space. This is performed with a loop over all y values where the subroutine `nonlin` is called to at each y. The xz-planes are transferred from the main storage with the routine `getxz` to the memory where the actual computations are performed. The corresponding storing of data is performed with `putxz`.

1.3. *Computer background*

The super computers used for large computations can be divided in two major groups with respect to the memory configuration. The computers can also be divided in two groups when considering the architecture of the processor. Thus there are four different combinations that constitute the type of computer.

The two memory configurations are shared and distributed memory. In the former a common memory is used by all the processors. In the latter case, every processor has its own memory and data must be sent and received if used by another processor. The two types of processors are scalar and vector. The scalar (or super-scalar) processor has registers for data as a scalar quantity and can perform operations on this data fast. There is a small memory set, the cache, in the processor to keep easy access to the data being processed. The data transfer between main memory and the cache is slow, therefore optimized usage of the cache is important. The vector processor has registers for data as a vector quantity and perform operations on the scalar elements of the vector, all at the same time. The processor itself thus operates in parallel. The transfer of data from the main memory is fast if there is no memory contention.

The distributed memory computers typically have many processors (≈ 200) with e.g. 256 Mbyte of memory each, resulting in a larger total memory than a vector computer with typically 4 to 8 Gbyte memory. The forthcoming computers often have a shared memory for a small number of processors but with a (from necessity) overall distributed memory.

The code used for the computations has to be adjusted when ported from one group to another. The four groups are listed in table 1, together with the computers that have been used in the present study. At the time of the present investigation the Cray J90, IBM SP2 and Fujitsu VPP300 have 32, 152 and 3 processors respectively and are located at PDC, KTH in Stockholm. The Cray C90 and T3E have 7 and 232 processors respectively and are located at NSC in Linköping. The Cray T90 has 14 processors and is located at SDSC in

San Diego. The SGI Origin 200 has 4 processors and is the property of Joseph Haritonidis at OSU in Columbus.

	shared memory	distributed memory
scalar processor	SGI Origin 200	Cray T3E, IBM SP2
vector processor	Cray J90, C90, T90	Fujitsu VPP300

TABLE 1. The four categories of super-computers

The optimization and tuning of the code have different features for the different groups. They can be opposed to each other, e.g. tuning for a vector processor will make the code unsuitable for a scalar processor and vice versa.

The code used for the numerical simulation of turbulence was earlier optimized for vector processors and shared memory computers. In resent years distributed memory and scalar processors have become a common architecture for super computers. Therefore a lot of effort has been put into the redesign of the code to perform well on such computers.

Most of the time in the code is spent in the FFT. The vector and scalar optimization is therefore concentrated to this part of the code. There are two different versions of the FFT to be used on the two types of processors.

The parallelization on a shared memory system is fairly straightforward and is very efficient. The MPI (Message-Passing Interface) has been used to parallelize the code on the distributed memory systems. A lot of effort has been put into keeping the memory requirement low as to make it possible to perform large simulations.

1.4. *Examples of simulations*

In order to illustrate the complexity of the flow and give examples of the computational effort two examples are given, one for the turbulent boundary layer flow and one for the rotating channel flow.

1.4.1. *Turbulent boundary layer*

As an example of a flow field from a simulation of a turbulent boundary layer, see figure 4 where contour lines of the downstream velocity component are shown in a plane perpendicular to the wall. The downstream direction is denoted x and the wall normal direction y (observe the different scaling in the two directions in the figure). The simulation starts with a laminar boundary layer and is then tripped to turbulence by a random volume force near the wall. All the quantities are non-dimensionalized by the freestream velocity (U) and the displacement thickness (δ^*) at the starting position of the simulation ($x = 0$) where the flow is laminar and $Re_{\delta^*} \equiv U\delta^*/\nu = 400$. The length (including the fringe), height and width of the computation box were $450 \times 24 \times 24$ in these units. The number of modes was $480 \times 161 \times 96$.

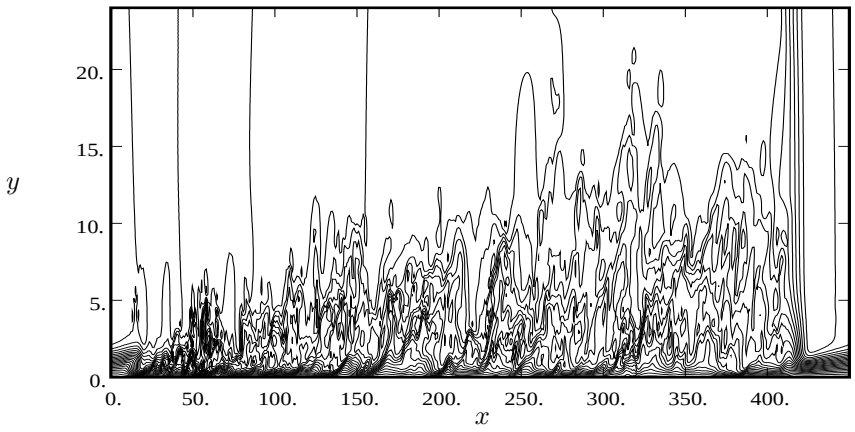

FIGURE 4. Contour lines of the velocity in the downstream direction (x).

To obtain a flow field as the one in figure 4, the simulation need to run for 2500 time units (δ^*/U), starting from a laminar field. The flow traveled through the box approximately 5 times during this period of time, and is sufficient for the turbulence to be adjusted to the imposed boundary conditions such as a pressure gradient. To obtain sufficiently smooth statistical data, the simulation runs for another 2000 time units. Thus the simulation was run for a total of 4500 time units. The time step determined by the CFL number is 0.02, and the CPU-time for one processor on the Cray J90 is 280 seconds, and 66 seconds on the Cray C90. Thus a simulation of this kind needs $63 \cdot 10^6$ CPU seconds on the J90 which is equivalent to 24 CPU-months. If the simulation is run on eight processors on the J90, or two on the C90, the simulation takes three months on either machine. If the time spent in the queuing system is included, at least half a year must be expected before the simulation is completed.

In figure 4 the laminar flow is visible at the beginning of the box, then a rapid transition to turbulence occurs and the turbulence is fully developed at $x = 150$. At $x = 400$ the fringe region starts, the turbulence is suppressed and the flow is forced back to its initial laminar profile. The velocity at the upper boundary, the freestream velocity, is not constant due to an adverse pressure gradient applied through the boundary conditions. The boundary layer is increasing in thickness rapidly in the downstream direction due to the decrease of the freestream velocity. If a strong enough adverse pressure gradient is applied, the boundary layer would separate from the wall. This is what happens on the wing of an aircraft when the stalling angle of attack is approached. Separation also occurs on the rear window of a car and increases the drag. The evaluation of the turbulent statistics from this and similar simulations are presented in Skote *et al.* (1998).

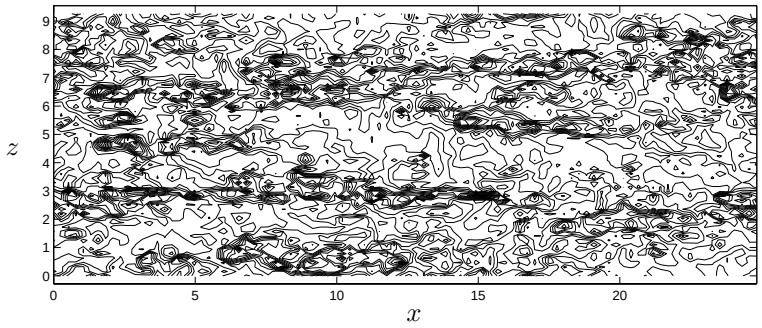

FIGURE 5. Contours of constant streamwise velocity in a rotating channel flow for a plane in the streamwise and spanwise directions at the distance $y = \delta/2$ from unstable wall, where 2δ is the channel width.

1.4.2. *Rotating channel flow*

In rotating channel flow, the extra Coriolis term in the governing equations has a strong effect on the development of the large structures. It has either a stabilizing or a destabilizing effect depending on the sign of the mean velocity gradient. On the unstable side, the Coriolis force makes negative streamwise fluctuating velocities and positive wall-normal fluctuating velocities enforce each other. This effect, which actually is strongest for relatively low rotation rates, produces long structures in the flow (figure 5). The periodic boundary condition requires that the computational domain needs to substantially longer than the largest flow structure if the results is to be unaffected by the domain size. If the domain is too short the numerical artifact of the periodicity condition will, through resonant effects, enforce the long structures and the true behavior of the flow is not captured. Typically, for this case, the computational domain needs to be approximately five times as long compared to the non-rotating flow case, which significantly increases the computational effort.

The present simulation was performed with $384 \times 129 \times 240$ number of modes, which gives a computational effort of the same order as for the boundary layer example above. The length of the largest scales (figure 5) actually suggests that the computational domain should be at least twice as long for this case, which implies that $768 \times 129 \times 240$ grid points have to be used in the simulation.

2. Results

The main aim of optimizing a code is to obtain an overall high performance. This is a complicated matter and different parts of the code might need different treatment. This suggests that the different parts should first be optimized separately. In the present paper the various choices of the compiler options are omitted, and results are only presented for the optimal choice.

The investigations presented here is divided in four sections. In section 2.1 the vectorization is discussed. The FFT is investigated in section 2.2 for the two types of processors through a model problem using the different FFT routines. Section 2.3 is devoted to the parallelization on the two memory configurations. Also here a model problem was created to try out the different techniques for MPI. And finally in section 2.4, the performance of the MPI and the overall performance of the code is presented for the two distributed memory computers IBM SP2 and Cray T3E.

For the shared memory computers with vector processors, the vectorization and parallelization have been tested only for the complete code. The code was already parallelized and optimized for vector processors (Lundbladh *et al.* 1992, 1994), and the results are only included for comparison with the main result concerning the parallelization on distributed memory computers.

Two different sizes of the problem has been tested, table 2. Test case two is too large to be run on the shared memory computers used in this investigation.

case	size	number of points
one	$128 \times 97 \times 128$	$1.6 \cdot 10^6$
two	$512 \times 193 \times 256$	$25.3 \cdot 10^6$

TABLE 2. Numerical mesh for the two test cases

The goal when optimizing a numerical code is to minimize the computational (CPU) time. An usual measure of the performance of a code is the number of floating point operations that is performed per CPU second (flop/s). If two codes do a different number of floating point operations for the same computation it is not really relevant to directly compare the respective performance in flop/s but rather in the computational time. The different versions of the code presented here have a negligible difference in computational work (flop) for the same tasks. The main differences involve moving data in the memory and changing the order of computation which give no contribution to the computational work. Therefore, either the computational speed or the computational time may be compared whichever is found most suitable.

2.1. *Vectorization*

Due to the spectral representation in Fourier series the degree of vectorization is very high. The vectorization is dependent on the size of the problem, a large problem will in a natural way contain long vectors. For small problems the size of the vectors can be increased by arranging the arrays in the code in a proper way. This is done by letting the vectors contain more than one plane. The arrays are collected from the main memory by the routines `getxy` and `getxz` as shown in figure 3. In figure 6 the vectors are shown in the y- or z-direction. In the linear part the xy-planes are treated, thus the length of the vectors is determined by how many z-positions are gathered at the same time by the routine `getxy`. In the non-linear part the length is determined by the number

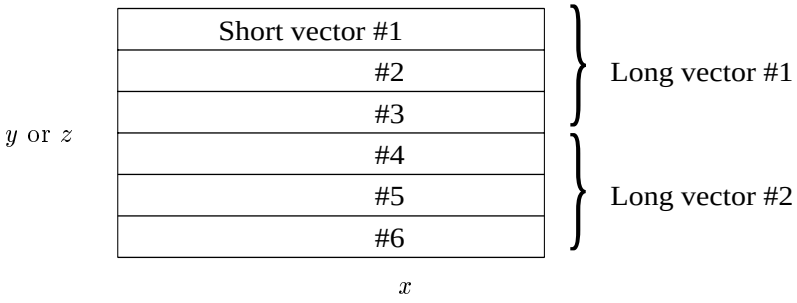

FIGURE 6. The short vectors contain one $xz-$ or xy-plane. The vector length is increased by treating more than one plane at a time. The long vector is constructed by letting the short vectors be stored concurrently in the x-direction. The third direction (z or y) is omitted in the figure.

of y-positions gathered at the same time by `getxz`. The degree of vectorization is crucial for some computers to perform well. The FFT is written in such a way that the vector registers are used to a full extent. The memory used by the code is increased significantly when using longer vector lengths due to the increased size of the two-dimensional working area.

We have tested vector processors from Cray and Fujitsu (table 3). For the specific problem size (case one in table 2) the optimal vector length was obtained when six planes were used at the same time on J90, eight on C90, sixteen on T90 and four on VPP300. When running a smaller problem, the optimal number of planes is higher and when running a larger, it is less. It should be mentioned that the performance is highly dependent on the problem size. The size used here gives a very high efficiency on the C90 (over 50 % of peak performance) while the VPP300 efficiency is only 24 %. However, the code performance was 800 Mflop/s (36 %) on the VPP300 for a different problem size. The J90 is not so dependent on the problem size and performs at 100 Mflop/s for different problem sizes if the tuning parameters are set to obtain the optimal vector length.

	J90	C90	T90	VPP300
peak processor performance	220	952	1700	2200
one plane	93	361	501	303
optimized vector length	100	522	710	525

TABLE 3. The speed on different vector machines for one processor for case one.

2.2. *The FFT*

The FFT package is an extended version of the `FFTPACK` from netlib. The FFT is applied in all three physical directions in the transforms between physical space and spectral space. The transforms are performed on the two-dimensional matrix, where the main difference between the treatment in the three directions is with respect to the memory. The x-transform is performed on the first index, which yields unit stride memory access, while the y- and z-transforms are performed on the second index. The treatment of the y- and z-transforms are hence similar and we shall therefore only investigate the behavior of the x- and z-transforms.

2.2.1. *The original version for vector processors*

The FFT that is used for the transform in the x- and z-directions consists of two one-dimensional FFT:s. In the forward transform they are a real to half-complex in x followed by a half-complex to complex in z. The real data in physical space is stored in two matrices with odd points in x in the first matrix and the even points in x in the second, see figure 7. After transforming in the x-direction, the real and imaginary Fourier components are stored in the two matrices respectively. Then the z-transform is applied to get the full two-dimensional transform. The data is stored all the time with the x-direction column-wise and the z-direction row-wise. The access to data in FORTRAN is row-wise, thus the elements in the x-direction are positioned one after another. However, when performing the z-transform the elements are separated by $nx/2$, i.e. the vector stride is $nx/2$. This means that different memory locations are accessed all the time. For vector processors the access to memory is fast and the most important issue is that no bank-conflicts occur.

2.2.2. *Scalar processor*

As described above, the FFT was originally written for a vector processor. This feature of the FFT is a disadvantage when running on scalar processors. The changes needed in the code for scalar processing was to a great extent already accomplished by the original author, Anders Lundbladh. The alternative FFT was however only fast in the x-direction, where the changes consisted of reducing the amount of data used at the same time. An outer loop in x was introduced as to process data from one row at a time instead of the whole plane (or several planes if the vectorization tuning parameters are used.) To accomplish a faster transform in the z-direction, the z-transform was rewritten to process data for one line at a time, in much the same way as was already done in the x-direction. To perform the transform in this manner, the data need to be transposed before transformed, see figure 8, otherwise the vector stride will prevent the data from lying concurrently.

In the table 4 the original (modified in the x-direction), modified (in the z-direction) and library FFT are compared. Both the x- and z-direction are transformed for a 512×256 grid corresponding to case two in table 2. The

library FFT is faster than the in-house FFT. But the data transfer due to the library FFT usage of complex variables decreases the performance considerably. Also the modified approach with transposing before the transform in the z-direction gives a faster FFT but the transposing itself decreases the performance. The three different transforms performs approximately the same number of operations (flop), thus the difference in performance (Mflop/s) is due to better efficiency. The number of flops correspond to the formula in the book by Canuto *et al.* (1988), flop$\approx$5Nlog$_2$N for one one-dimensional FFT. The decrease of the performance when including the transpose and data transfer respectively, is due to the fact that these redistributions of data do not include any operations (flop). Since the original version do not require any additional rearranging of the data, it is the fastest method for the FFT. Thus, the only difference between the FFT for scalar and vector processors is the treatment in the x-direction.

The routines written by the authors for the transpose are substantially faster than the library routines on the T3E, due to the E-registers which can be used explicitly in the code. Also on the SP2 the library transpose is slower than the ones written in FORTRAN, probably due to the generality of the library routines.

	T3E	SP2
peak processor performance	600	640
original	59	177
modified	64	180
modified incl. transpose	55	100
library	66	209
library incl. transfer	54	82

TABLE 4. The performance of the FFT given in Mflop/s averaged in both the x- and z-directions.

2.3. *Parallelization*

The computation of each xy-plane (in `linear`) and xz-plane (in `nonlin`) is independent of the other planes. Therefore, parallelization of the code is performed by distributing different planes in the loops to the different processors, which then runs in parallel. Since the major part of the computation is spent in the `linear` and `nonlin` subroutines, the code should parallelize efficiently. In the following, n_{proc} denotes the number of processors.

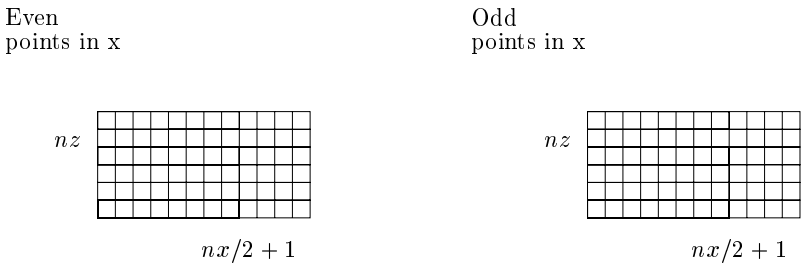

FIGURE 7. The structure of the data in physical space. On this data the transform in the x-direction is performed.

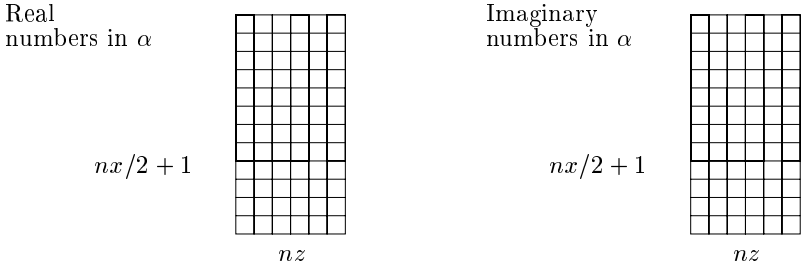

FIGURE 8. The structure of the data in half-complex form after transposing the data. On this data the transform in the z-direction is performed in the modified method.

2.3.1. *The maximum speed up*

The maximum possible speed up of the code when using several processors is determined by the part of the program that do not allow for parallel computing. Ideally, if the the whole program runs in parallel, the maximum speed up equals the number of processors. Some parts of a code are always impossible to divide between the processors. Let a denote the portion of the code that is parallelizable, and b the portion that only can be run on one processor. The maximum possible speed up of the code is then

$$\frac{a+b}{a/n_{proc}+b} = \{\frac{a}{a+b} = q\} = \frac{1}{q/n_{proc}+(1-q)}. \tag{1}$$

This is usually referred to as Amdahls law. As q approaches unity the maximum speed up goes to n_{proc}. It is desirable to have the portion b of the code that only runs on one processor small.

Figure 9 shows that the speed up is far from linear for large values of n_{proc} if q is not very close to unity. In the limit of infinite number of processors the computational time is completely determined by the part of the code that do not run in parallel and the maximum speed up approaches $1/(1-q)$.

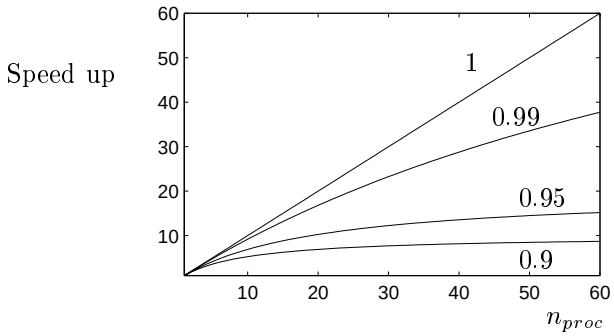

FIGURE 9. The maximum speed up for $q = 1,\ 0.99,\ 0.95,\ 0.9$.

2.3.2. *Shared memory*

The parallelization and optimization of the code for shared memory systems was done in the original version of the code. The two main loops in the code, over the linear and non-linear parts, were splitted as to account for the parallel computing. The parallel processing requires extra two-dimensional local variables, one for each processor in the computation, in order for the different processors not to use the same memory position. A compiler directive must be included in the code because within the loops there are subroutine calls. As can be seen from figure 10 the scaling is excellent on the Cray C90 and J90. When q in Amdahls law (1) is calculated from the measured performance, it gets a value of 0.99. On the Origin 200, with a scalar processor, the measured performance was 53 Mflop/s on one processor and 181 on four, which corresponds to a value of q as low as 0.94.

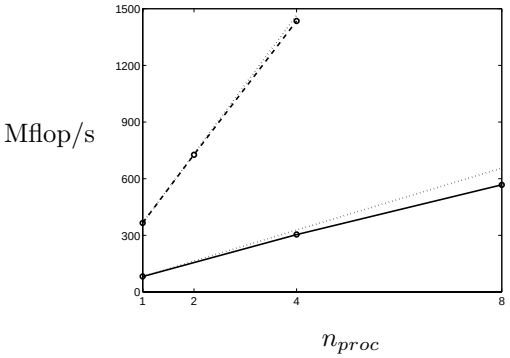

FIGURE 10. Mflop/s rates for different number of processors for case one. — J90; - - C90; $\cdots$ maximum speed up with $q = 1$ in Amdahls law (1).

2.3.3. *Distributed memory*

On distributed memory machines, e.g. IBM SP2 and Cray T3E, the whole field needs to be divided among the different processors. There are three possible spatial directions which can be distributed among the different processors. The x-direction is not suitable to divide since it would give significant communication between the processors in both the linear and nonlinear part of the code. The number of y-discretization points in Chebyshev polynomials is often not even divisible with the number of processors. The discretization in the z-direction by the Fourier series can easily be chosen to obtain a number of discretization modes which is divisible with the number of processors. Also the communication with the main storage is more frequent in the linear part. The whole field is hence divided in the z-direction between the different processors (figure 11a), which yields easy access to the complete field in the linear part since the two dimensional field is available locally on the processor. In the nonlinear part, however, the local two dimensional storage needs to collect data from all the other processors. This is performed with the MPI standard.

The message passing

Two different methods of moving the data with MPI between the processors have been investigated. The first method transposes the whole field at once before the non-linear calculations, so that it becomes divided in the y-direction between the different processors. This makes the two dimensional field available locally at each processor. Before the linear calculation, the data is transposed back to its original position. The transposing of the data requires additional memory, since the whole field is stored twice, and additional moving of data from one field to another. In the second method the main storage is kept at its original position on the different processors. In the non-linear part each processor collects the two dimensional data from the other processors, on which it performs the computations, and then redistributes it back to the main storage. In this way no extra memory is needed. Figure 11b shows an example of the data gathering for one processor. The two methods are described more thoroughly in Appendix A

The amount of communication

The main communication between the processors is in the non-linear part, where five variables are collected from the main memory and three variables are stored to the main memory. Thus a total of eight variables have to be sent. Each processor performs calculations on approximately ny/n_{proc} xz-planes. The amount of data that needs to be collected from the other processors is for each plane $nx(nz - nz/n_{proc})$. This gives that for all variables each processor

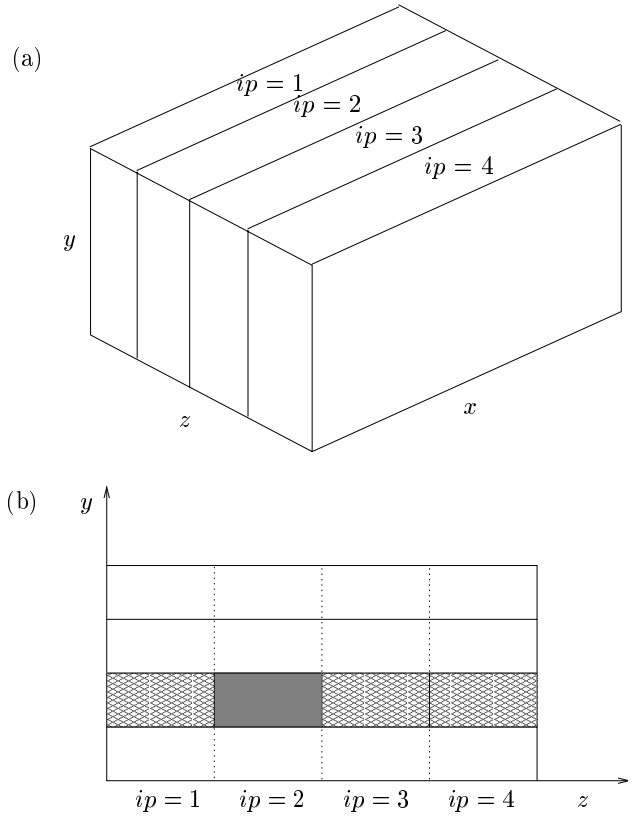

FIGURE 11. a) The distribution of the main storage on four processors $ip = 1, ..., 4$. b) The gathering of data in the nonlinear part (`nonlin`) of the code for processor number two. The completely shaded area is local on the processor and need not to be received from the others, and the half-shaded area is sent to processor number two. The x-direction is omitted for clarity.

needs to collect

$$N_{tot} = \frac{ny\ nx\ nz}{n_{proc}} \left(1 - \frac{1}{n_{proc}}\right) \tag{2}$$

real numbers from the other processors at each Runge-Kutta iteration. The amount of data that each processor needs to send is equally large.

The IBM SP2 communicates with a high performance switch which has a bandwidth of $110 MByte/s$ and a latency of $25 - 30 \mu s$. The MPI on the Cray T3E has a bandwidth of $320 MByte/s$ and a latency of $12.8 \mu s$. In order

to reduce the effect of the latency and use the bandwidth optimally, the data should be arranged in large groups when sent.

2.4. *Performance on the SP2 and T3E*

The main computational work in the code is in the FFT which was treated in the previous chapter. The performance of the two methods of redistributing data described in section 2.3.3 is investigated by using a model problem of the same structure as the code. The performance of the code can then be measured, using the most efficient FFT and message passing method.

The y-direction is not generally even divisible with the number of processors, i.e. ny/n_{proc} is not an integer. Therefore, in the last y-loop count not all processors are active and the loop is not completely parallelizable. If n_{proc} is relatively small compared to ny (as is the case with e.g. the Cray C90 and J90) the effect from this on the performance is small. When n_{proc} is of the same order as ny (as may be the case for e.g. the IBM SP2 and the Cray T3E) this effect may be of importance.

2.4.1. *Performance of the MPI*

The most important feature of the message passing is that it should be fast, i.e. the time spent in moving data between processors should be small so that the speed up of the code is not limited by the message passing. It is also interesting to study how the efficiency of the data transfer depends on the number of processors. The speed up is of course dependent on how much work is performed between the data redistributions. The test problem was set up so that a clear difference could be seen between the two methods.

In figure 12 the two methods are compared for the two cases, table 4. They show that for case two method two is faster than method one for both computers (method one was not possible to run with less than 4 processors due to the large memory requirement). However, for case one method one is faster on the T3E while method two still is faster on the SP2. Hence, method one is better than method two only on the T3E for a small problem (case one) on many processors. However, the size corresponding to case one would not need to run on more than 16 processors in a real application, thus method two is the one to prefer in the code. It is also observed that the SP2 performs better for the small case while the T3E performs better for the larger case.

In the following only results using method two of the data communication will be presented since method one was found not to be useful due to the lower performance, especially on the SP2, and the larger amount of required memory.

If we take into account that the y-loop is not even divisible with the number of processors, the maximum possible speed up of the test problem code is

$$\frac{ny}{\left(\mathrm{Int}\left(\frac{ny}{n_{proc}}\right)+1\right)}. \tag{3}$$

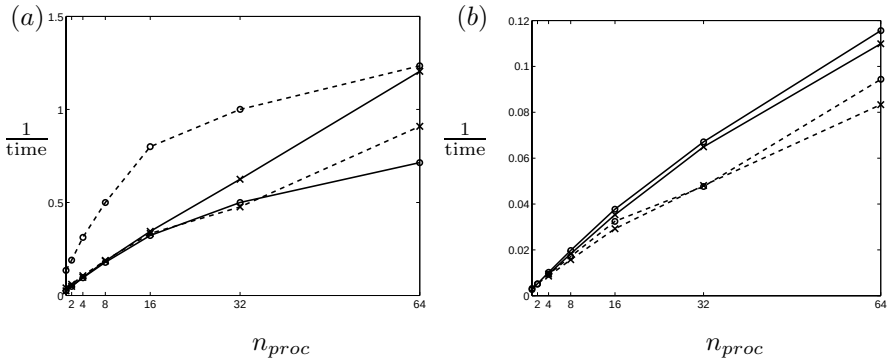

FIGURE 12. Performance on — T3E - - SP2; x Method 1 o Method 2. a) Case one. b) Case two.

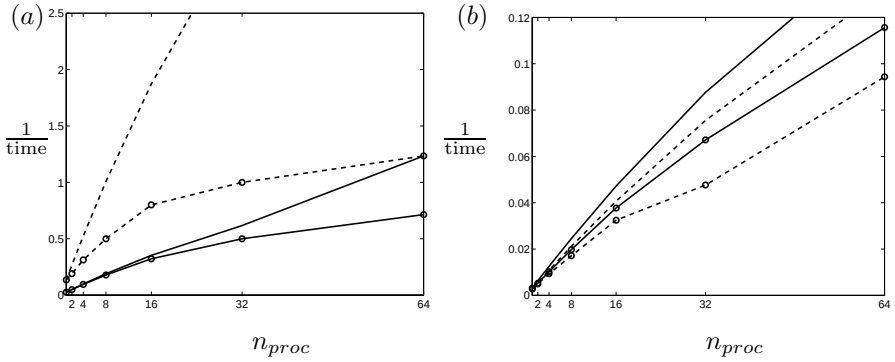

FIGURE 13. Performance on — T3E - - SP2; o Method 2. Curves with no circles are the optimal speed up. a) Case one. b) Case two.

In figure 13 the performance of the test problem is shown together with the optimal speed up from (3). The T3E is slightly closer to the optimal speed up performance than the SP2, indicating that the message passing performs better. We also have a closer adherence to the optimal curves for the larger case (for both T3E and SP2) which is associated with larger data sets which increases the performance of the message passing.

Bandwidth

It is a well known fact that the bandwidth, or the data transfer rate, decreases considerably from the maximum values quoted in section 2.3.3 if the amount of data which is sent decreases below a certain level, e.g. one Mbyte on the T3E.

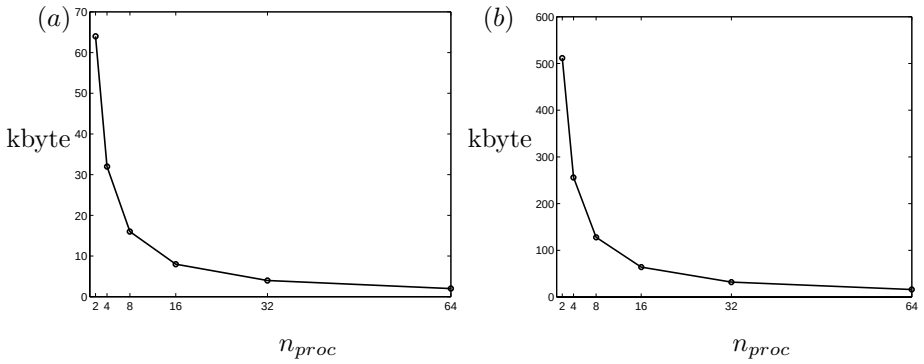

FIGURE 14. Size of data package. a) Case one b) Case two.

The size of the individual data package sent from one processor to another is

$$\text{Size} = \frac{nx\ nz}{n_{proc}}. \tag{4}$$

This quantity is plotted for different number of processors in figure 14. For both cases the size is well below one Mbyte for all values of n_{proc} which would affect the bandwidth. The size decreases with increasing number of processors and consequently the data transfer rate for each individual processor should decrease. Although the performance of each processor decreases, the effective time of the message passing should actually decrease since the amount of data that is sent becomes smaller.

If it is assumed that the parallelization is optimal, i.e. $q = 1$ in Amdahls law (1), the time spent on data transfer, t_{MPI}, is derived as the difference between total time and the total time for one processor divided by the number of processors,

$$t_{\text{MPI}} = t_{n_{proc}} - \frac{t_{n_{proc}=1}}{n_{proc}}, \tag{5}$$

where $t_{n_{proc}}$ is the program CPU time for one processor when a total of n_{proc} processors is used. As already noted in (3) the speed up is not linear in n_{proc} but depends on both n_{proc} and ny. Using this approach a more accurate estimate is obtained,

$$t_{\text{MPI}} = t_{n_{proc}} - \frac{\text{Int}\left(\frac{ny}{n_{proc}}\right) + 1}{ny} t_{n_{proc}=1}. \tag{6}$$

In figure 15 the performance of the test cases is plotted for the two computers together with inverse of the time t_{MPI}. Due to memory limitations on the T3E case two was not possible to run on a single processor and the time t_{MPI} is not available. From figure 15 it is clear that the time of the message passing indeed decreases with increasing values of n_{proc}, except for the small case on the T3E which actually obtains relatively high performance at few processors.

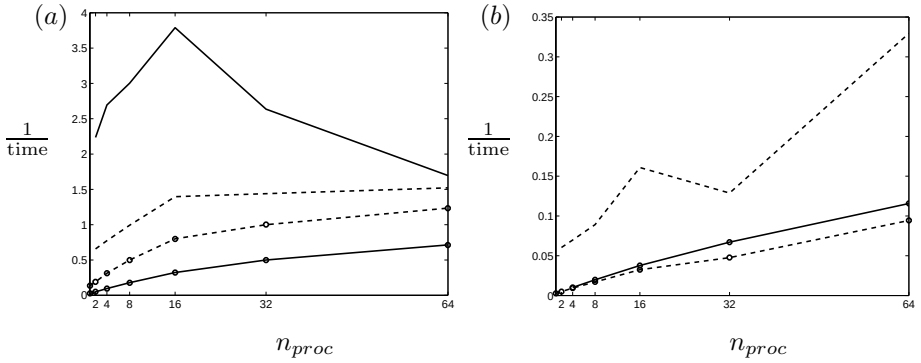

FIGURE 15. Performance on — T3E - - SP2; corresponding curves with no rings show the MPI performance. a) Case one. b) Case two.

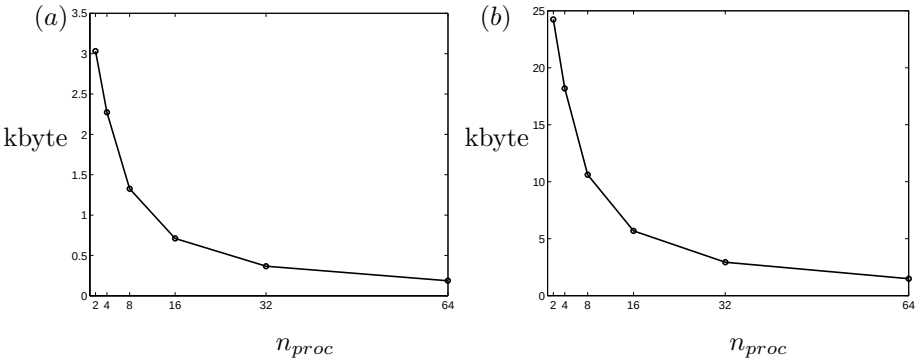

FIGURE 16. Total amount of data sent. a) Case one b) Case two.

For the larger case the message passing takes a smaller amount of time compared to the total time and the increase in performance of the message passing with n_{proc} seems to be stronger.

The amount of data that is being sent by each processor is given by equation (2), and is shown in figure 16. To get the data transfer rate, the amount of data is divided by the time spent on the transfer t_{MPI}. As the communication is very intense between the processors, i.e. each processor needs to both send and receive data from all other, the maximum possible transfer rate of receiving data for each processor is only half of the bandwidth.

The rate is plotted in figure 17 for both cases. For case one the T3E performs better with regards to the bandwidth for a small number of processors. Also, the rate decreases with increasing number of processors, due to the smaller package size observed in figure 14, and the difference between the two computers disappear. In case two the rate is overall higher due to larger data packages and it also shows a slight increase at the highest values of n_{proc}.

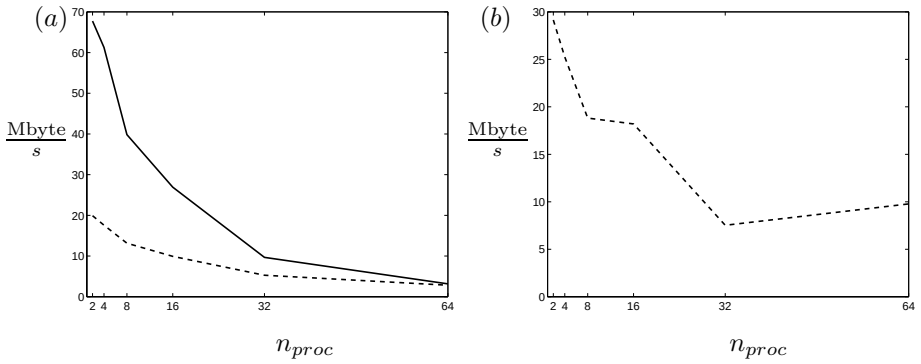

FIGURE 17. Data transfer rate per processor. — T3E - - SP2.
a) Case one. b) Case two.

The theoretical data transfer rate as a function of message buffer size can be found in a Cray manual. The low data transfer rate is surprising since the theoretical values for the T3E are much higher. If case one is considered for two processors, the theoretical value is 230 Mbyte/s. Since this value is for point-to-point communication, the value has to be divided by two to be compared with our case where all the processors are both sending and receiving. The measured rate for our test case one is 70 Mbyte/s on two processors. If the MPI derived data type used in the communication is changed to a standard vector type, and sent to another vector of the same type, the performance increases to 114 Mbyte/s, which is very close to the expected theoretical value. If now the case one on 64 processors is considered the theoretical value is 25 Mbyte/s, whereas the measured value is 3 Mbyte/s. If the same number of bytes is sent between only two processors, the rate increases to 12 Mbyte/s, which again is half of the theoretical value. In this case there is no difference in the performance if a standard vector is used instead of a MPI derived data type. The low bandwidth is thus explained by two different effects. For a small number of processors, when the data packages still are relatively large, the low bandwidth is due to the MPI derived data type which slows down the communication. For a large number of processors, the explanation is the decrease of communication efficiency (network contention) when many processors are being used.

2.4.2. *Performance of the code*

The complete code has been run with the optimal FFT and method two for the message passing for the two cases. Since the non-linear part is not completely parallelizable the factor q in Amdahls law depends on n_{proc} and is difficult to give directly. Most time of the code is spent in the linear and non-linear parts. If it is assumed that they take the same computational time on one processor and that the remaining computational time is negligible the following

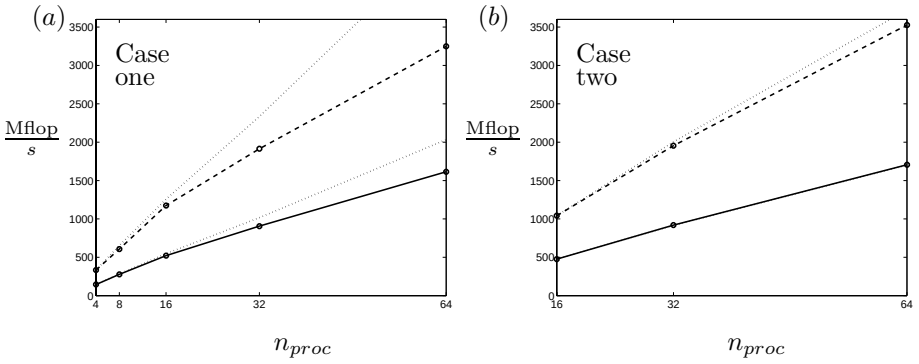

FIGURE 18. Mflop/s rates for different number of processors.
— T3E - - SP2 $\cdots$ maximum speed up.

expression can be derived for the optimal speed up,

$$\frac{2}{\frac{1}{n_{proc}} + \frac{1}{ny}\left(\mathrm{Int}\left(\frac{ny}{n_{proc}}\right) + 1\right)}. \tag{7}$$

This formula, with $n_{proc} = 8$ and $ny = 97$, gives when using Amdahls law (1), a q of value 0.99, corresponding to the measured values in figure 10. In figure 18 the performance of the code is shown as Mflop/s together with the optimal speed up given by (7). The speed up is better for case two than case one. The scaling is better on the T3E for both cases, which was noticed also for the model problem. We actually obtain an optimal performance for the larger case on the T3E. However, the overall performance is better on the SP2, which is approximately twice as fast as the T3E. This was also observed in the model problem for the FFT (see table 4).

Hence, for both the large and small cases, the scaling is better for the T3E associated with the higher performance of the message passing, and the overall performance is better for the SP2, mainly due to the higher performance of the FFT.

For case one it is possible to compare the performance with the vector computers (see figure 10). One processor on the C90 corresponds approximately to four processors on the J90, four processors on the SP2 and eight on the T3E.

3. Conclusions

To be able to implement a code on a parallel computer with distributed memory, a lot of effort must be put into programming the communication between the processors efficiently. The most sensible approach seems to be through a model of the code with the same structure of the variables. By using a test problem, the different options of communication can be tested and evaluated before implementing the communications in the code.

The MPI routines might be working in different ways on different computers, depending on the implementation. The code might be working perfectly on one machine, but this does not imply that the code can be expected to run efficiently, or be working at all, on another. Portability of codes seems to have been lost.

It is concluded that it is possible to achieve high performance on super scalar machines, with computational speeds comparable and higher than those of the traditional vector machines. The code seems to scale efficiently with the number of processors and therefore a high performance might be obtained by using many processors in the simulation. The lower scaling on the smaller case is not critical since it does not need to be run on many processors in a real computation.

Another important issue is the availability of the computer, i.e. how long time the user have to spend queuing before a job begins and how many processors you may use. In some cases the job may be subjected to timesharing with other jobs which reduces the performance.

Acknowledgments

Computer time was provided by the Center for Parallel Computers (PDC) at the Royal Institute of Technology (KTH), the The National Supercomputer Center in Sweden (NSC) at Linköping University, and The San Diego Supercomputer Center (SDSC) at the University of California. In addition we thank Prof. Joseph Haritonidis at the Ohio State University (OSU) for letting us use his Origin 200.

Appendix A.

The first method

The first method was developed by Högberg (1998) and is based on the MPI_ALLTOALLV command. When the problem size and the number of processors have been determined, vectors describing where to send data, and from where to receive data, are set up for each processor individually. When these vectors are available MPI_ALLTOALLV is the only command needed for all communications. Every processor has two data vectors, one for xz-planes and one for xy-planes. The size of these vectors depends on the problem size and the number of processors. Other vectors contain information about how many planes each processor handles, and information about where to take data for sending and where to put received data. These vectors are used with MPI_ALLTOALLV to transpose the whole field that has been distributed among the processors. The main drawback of this method is that data is stored twice, which will increase the memory requirements compared to the second method.

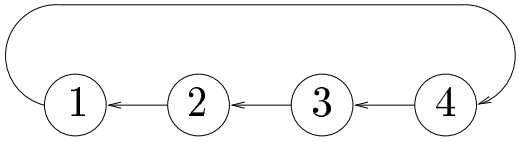

FIGURE 19. The first left neighbor in the four processor case.

The second method

The sending and receiving data is performed with the commands MPI_SEND and MPI_RECV, which are used in the modified `getxz` and `putxz` routines. When parallelized, the original y-loop, which goes from 1 to ny, is changed to a loop that goes from 1 to $\mathrm{Int}[(ny-1)/n_{proc}]+1$. In this modified loop, the number of y-planes treated at the same time is n_{proc}, except for the last loop count where the remaining y-planes are treated. At each loop count each processor sends and receives data to and from all other processors. This is achieved by an inner loop, from 1 to $n_{proc}-1$, in which all processors sends data to another (all different) processor.

Let ip be the number of a processor. Processors ip and $ip-1$ are said to be neighbors (figure 19). In particular processor 1 is a neighbor to processor n_{proc}. At each loop count ii, which goes from 1 to $n_{proc}-1$, each processor sends data to its neighbor number ii to the left, i.e. processor ip sends data to processor $ip-ii$.

At each MPI_SEND command the data that is sent is defined through a special vector in the MPI standard, describing the number of elements in the data set, the length of one element and the distance (stride) between two elements. A corresponding vector is constructed to define where the data is to be stored with the MPI_RECV command. These vectors are determined by the number of discretization modes in each direction and the number of processors.

On the IBM SP2 the MPI_SEND is implemented as a standard send that is not able to complete until the receive has started. Since all processors start with sending and none is receiving a deadlock occurs. In this case a non-blocking standard send, MPI_ISEND, together with a test, MPI_WAIT, are used. If this method is used on the Cray T3E instead of the standard send no change in the performance is detected.

References

CANUTO, C., HUSSAINI, M. Y., QUARTERONI, A. & ZANG, T. A. 1988 *Spectral Methods in Fluids Dynamics*. Springer.

HÖGBERG, M. 1998 Private communication.

Lundbladh, A., Henningson, D. S. & Johansson, A. V. 1992 An efficient spectral integration method for the solution of the Navier-Stokes equations. FFA-TN 1992-28, Aeronautical Research Institute of Sweden, Bromma.

Lundbladh, A., Schmid, P. J., Berlin, S. & Henningson, D. S. 1994 Simulation of bypass transition in spatially evolving flows. Proceedings of the AGARD Symposium on Application of Direct and Large Eddy Simulation to Transition and Turbulence, AGARD-CP-551.

Skote, M., Henkes, R. A. W. M. & Henningson, D. S. 1998 Direct numerical simulation of self-similar turbulent boundary layers in adverse pressure gradients. *Flow, Turbulence and Combustion* **60**, 47–85.

Paper 9

P9

An efficient spectral method for simulation of incompressible flow over a flat plate

By **Anders Lundbladh**[*†], **Stellan Berlin**[†], **Martin Skote**[†], **Casper Hildings**[*†], **Jaisig Choi**[‡], **John Kim**[‡] and **Dan S. Henningson**[*†]

An efficient spectral integration technique for the solution of the Navier-Stokes equations for incompressible flow over a flat plate is described and implemented in a computer code using the FORTRAN language. The algorithm can either be used for temporal or spatial simulation. In the latter case, a fringe region technique is used to allow a streamwise inflow and outflow of the computational domain. At a constant distance from the flat plate an artificial boundary is introduced and a free-stream boundary condition applied. The plate parallel directions are discretized using Fourier series and the normal direction using Chebyshev series. Time integration is performed using third order Runge-Kutta method for the advective and forcing terms and Crank-Nicolson for the viscous terms. The version of the code described in this report can be run on parallel computers with shared memory. A slightly different version also exists which utilizes MPI (Message-Passing Interface) for parallelization on distributed memory computers.

[*]Aeronautical Research Institute of Sweden,Box 11021, SE-161 11 Bromma, Sweden
[†]Department of Mechanics, KTH, SE-100 44 Stockholm, Sweden
[‡]Department of Mechanical and Aero Space, UCLA, 405 Hilgard Ave, LA, CA 90095, USA

Contents

1. Introduction

Solution of the Navier-Stokes equations for the simulation of transition and turbulence requires high numerical accuracy for a large span of length scales. This has prompted a development of accurate spectral methods. Unfortunately even with these methods computations require an immense amount of computer time and memory. In the present report we use spectral methods to derive an accurate algorithm of the flat plate boundary layer flow geometry. The basic numerical method is similar to the Fourier-Chebyshev method used by Kim *et al.* (1987).

The original algorithm (Lundbladh *et al.* 1992*a*) solved the incompressible flow equations in a channel flow geometry. To allow simulations of the flow over a flat plate a free-stream boundary condition is required, and for spatial simulations a fringe region technique similar to that of Bertolotti *et al.* (1992) is described.

For further details about spectral discretizations and additional references see Canuto *et al.* (1988).

The original channel code and the implementation of the present numerical method has been used in a number of investigations.
In channel flow:
Henningson *et al.* (1990), Lu & Henningson (1990), Lundbladh & Johansson (1991), Schmid & Henningson (1992), Lundbladh (1993), Henningson *et al.* (1993), Lundbladh & Henningson (1993), Schmid & Henningson (1993), Elofsson & Lundbladh (1994), Kreiss *et al.* (1994), Lundbladh *et al.* (1994*a*), Schmid *et al.* (1994), Henningson (1995), Reddy *et al.* (1998).
In boundary layer flow:
Lundbladh *et al.* (1992*b*), Berlin *et al.* (1994), Henningson & Lundbladh (1994), Lundbladh *et al.* (1994*b*), Henningson & Lundbladh (1995), Högberg & Henningson (1998), Schmid *et al.* (1996), Nordström *et al.* (1999), Hildings (1997), Berlin & Henningson (1999), Berlin *et al.* (1998*a*), Berlin *et al.* (1999), Berlin *et al.* (1998*b*), Bech *et al.* (1998), Skote *et al.* (1998).

2. The numerical method

2.1. *Derivation of the velocity-vorticity formulation*

The starting point is the non-dimensionalized incompressible Navier-Stokes equations in a rotating reference frame, here written in tensor notation,

$$\frac{\partial u_i}{\partial t} = -\frac{\partial p}{\partial x_i} + \epsilon_{ijk} u_j (\omega_k + 2\Omega_k) - \frac{\partial}{\partial x_i}(\frac{1}{2} u_j u_j) + \frac{1}{R}\nabla^2 u_i + F_i, \qquad (1)$$

$$\frac{\partial u_i}{\partial x_i} = 0, \qquad (2)$$

with boundary conditions at the flat plate and at the free-stream boundary, which are discussed in the next subsections.

The first equation represents conservation of momentum and the second equation incompressibility of the fluid. Here $(x_1, x_2, x_3) = (x, y, z)$ are the streamwise, normal and spanwise coordinates, $(u_1, u_2, u_3) = (u, v, w)$ are the respective velocities, $(\omega_1, \omega_2, \omega_3) = (\chi, \omega, \vartheta)$ are the corresponding vorticities, and p is the pressure. The streamwise and spanwise directions will alternatively be termed horizontal directions. Ω_k is the angular velocity of the coordinate frame around axis k. In practise the most often used case is rotation around the spanwise axis, thus let $\Omega = \Omega_3$ be the rotation number. F_i is a body force which is used for numerical purposes that will be further discussed below. It can also be used to introduce disturbances in the flow. The Reynolds number is defined as $R = U_\infty \delta^* / \nu$, where U_∞ is the undisturbed streamwise free-stream velocity at $x = 0$ and $t = 0$, δ^* is the displacement thickness of the undisturbed streamwise velocity at $x = 0$ and $t = 0$, and ν is the kinematic viscosity. The size of the solution domain in physical space is x_L, y_L and z_L in the streamwise, normal and spanwise directions, respectively.

A Poisson equation for the pressure can be obtained by taking the divergence of the momentum equation,

$$\nabla^2 p = \frac{\partial H_i}{\partial x_i} - \nabla^2(\frac{1}{2} u_j u_j), \qquad (3)$$

where $H_i = \epsilon_{ijk} u_j (\omega_k + 2\Omega_k) + F_i$. Application of the Laplace operator to the momentum equation for the normal velocity yields an equation for that component through the use of equations (3) and (2). One finds

$$\frac{\partial \nabla^2 v}{\partial t} = \left(\frac{\partial^2}{\partial x^2} + \frac{\partial^2}{\partial z^2}\right) H_2 - \frac{\partial}{\partial y}(\frac{\partial H_1}{\partial x} + \frac{\partial H_3}{\partial z}) + \frac{1}{R}\nabla^4 v. \qquad (4)$$

This equation can, for numerical purposes, be written as a system of two second order equations:

$$\begin{aligned} \frac{\partial \phi}{\partial t} &= h_v + \frac{1}{R}\nabla^2 \phi, \\ \nabla^2 v &= \phi, \end{aligned} \tag{5}$$

where

$$h_v = \left(\frac{\partial^2}{\partial x^2} + \frac{\partial^2}{\partial z^2}\right) H_2 - \frac{\partial}{\partial y}\left(\frac{\partial H_1}{\partial x} + \frac{\partial H_3}{\partial z}\right). \tag{6}$$

An equation for the normal vorticity can be found by taking the curl of the momentum equation. The second component of that equation reads,

$$\frac{\partial \omega}{\partial t} = h_\omega + \frac{1}{R}\nabla^2 \omega, \tag{7}$$

where

$$h_\omega = \frac{\partial H_1}{\partial z} - \frac{\partial H_3}{\partial x}. \tag{8}$$

Note that the equations for ϕ, v and ω have similar form, and can thus be solved using the same numerical routine. Once the the normal velocity v and the normal vorticity ω have been calculated the other velocity components can be found form the incompressibility constraint and the definition of the normal vorticity.

2.2. *Boundary condition*

The boundary conditions in the horizontal directions are periodic but we need to specify boundary conditions at the plate and in the free-stream, to solve equations (5) and (7). The natural no-slip boundary conditions read

$$v(y=0) = 0, \ \frac{\partial v(y=0)}{\partial y} = 0, \ \omega(y=0) = 0. \tag{9}$$

For disturbance generation and control by blowing and suction through the plate, an arbitrary time dependent velocity distribution,

$$v(y=0) = v_{BS}(x, z, t), \tag{10}$$

can be used.

The flow is assumed to extend to an infinite distance perpendicularly to the flat plate. However, the discretization discussed below can only handle a finite domain. Therefore, the flow domain is truncated and an artificial boundary condition is applied in the free-stream.

The simplest possible is a Dirichlet condition i.e.,

$$u_i(y = y_L) = \mathcal{U}_i(y = y_L), \tag{11}$$

where $\mathcal{U}_i(x,y)$ is a base flow that is normally chosen as a Falkner-Skan-Cook flow. An arbitrary pressure gradient, to for instance create a separation bubble, can be imposed by choosing $\mathcal{U}_i$ accordingly.

The desired flow solution generally contains a disturbance and that will be forced to zero by the Dirichlet condition. This introduces an error compared to the exact solution for which the boundary condition is applied at an infinite distance from the wall. The error may result in increased damping for disturbances in the boundary layer.

Some improvement can be achieved by using a Neumann condition,

$$\frac{\partial u_i}{\partial y}|_{y=y_L} = \frac{\partial \mathcal{U}_i}{\partial y}|_{y=y_L}. \tag{12}$$

This condition can be shown to be stable if there is outflow at the boundary or the inflow is weaker than $O(1/R)$. This restriction is usually fulfilled if the boundary is placed on a sufficiently large distance from the wall, so that the disturbance velocity is small.

A generalization of the boundary condition used by Malik *et al.* (1985) allows the boundary to be placed closer to the wall. It is an asymptotic condition that decreases the error further and it reads,

$$\left[\frac{\partial \hat{u}_i}{\partial y} + |k|\hat{u}_i\right]_{y=y_L} = \left[\frac{\partial \hat{\mathcal{U}}_i}{\partial y} + |k|\hat{\mathcal{U}}_i\right]_{y=y_L}, \tag{13}$$

where $\hat{}$ denotes the horizontal Fourier transform with respect to the horizontal coordinates, $k^2 = \alpha^2 + \beta^2$ and α and β are the horizontal wavenumbers (see equation 29). Thus this condition is most easily applied in Fourier space. The boundary condition exactly represents a potential flow solution decaying away from the wall. It is essentially equivalent to requiring that the vorticity is zero at the boundary. Thus, it can be applied immediately outside the vortical part of the flow.

2.3. *Forcing for temporal simulation*

A localized disturbance or wave of relatively short wavelength which travels downstream in a slowly growing boundary layer is surrounded by a boundary layer of almost constant thickness which grows slowly in time. This forms the basis of the temporal simulation technique.

Following the ideas of Spalart & Yang (1987) we assume that the boundary layer streamwise velocity is $U(x,y)$ and introduce a reference point $x_r = x_0 + ct$ where c is a reference speed. We now assume that the undisturbed boundary layer in the vicinity of the disturbance has the velocity distribution $U(y,t) = U(x_r,y)$, $V(y,t) = 0$. Since the boundary layer is now parallel (as there is no dependence on x), it is possible to apply periodic boundary conditions in the horizontal directions. However, whereas $U(x,y)$ (with the corresponding

V given by continuity) is a solution to Navier-Stokes or at least the boundary layer equations, this is not true for $\{U(y,t), V(y,t)\}$. Thus to ensure the correct development of the boundary layer profile over extended periods of time it is necessary to add a (weak) forcing to balance the streamwise momentum equation,

$$F_1 = \frac{\partial U(y,t)}{\partial t} - \frac{1}{R}\frac{\partial^2 U(y,t)}{\partial y^2} = c\frac{\partial U(x,y)}{\partial x} - \frac{1}{R}\frac{\partial^2 U(x,y)}{\partial y^2}, \tag{14}$$

where the right hand side should be evaluated at the reference coordinate x_r. The reference speed should be chosen as the group speed of the wave or the propagation speed of the localized disturbance for best agreement with a spatially developing flow. To fully justify the periodic boundary conditions in the case of a wave train, the wave itself should be slowly developing.

2.4. *Forcing for spatial simulation*

The best numerical model of a physical boundary layer, which is usually developing in the downstream direction rather than in time, is a spatial formulation. To retain periodic boundary conditions, which is necessary for the Fourier discretization described below, a fringe region is added downstream of the physical domain, similar to that described by Bertolotti *et al.* (1992). In the fringe region disturbances are damped and the flow returned to the desired inflow condition. This is accomplished by the addition of a volume force which only increases the execution time of the algorithm by a few percent.

The form of the forcing is :

$$F_i = \lambda(x)(\mathcal{U}_i - u_i), \tag{15}$$

where $\lambda(x)$ is a non-negative fringe function which is significantly non-zero only within the fringe region. $\mathcal{U}_i$ is the same flow field used for the boundary conditions, which also contains the desired flow solution in the fringe. The streamwise velocity component is calculated as,

$$\mathcal{U}_x(x,y) = U(x,y) + [U(x+x_L,y) - U(x,y)]\, S\left(\frac{x - x_{mix}}{\Delta_{mix}}\right), \tag{16}$$

where $U(x,y)$ is normally a solution to the boundary layer equations. Here x_{mix} and Δ_{mix} are chosen so that the prescribed flow, within the fringe region, smoothly changes from the outflow velocity of the physical domain to the desired inflow velocity. S is given below. The wall normal component $\mathcal{U}_y$ is then calculated from the equation of continuity, and the spanwise velocity $\mathcal{U}_z$ is set to zero for simulations where the mean flow is two dimensional. For three dimensional boundary layers $\mathcal{U}_z$ is computed from a boundary layer solution in fashion analogous to that for $\mathcal{U}_x$. This choice of $\mathcal{U}$ ensures that for the undisturbed laminar boundary layer the decrease in thickness is completely confined

to the fringe region, thus minimizing the upstream influence. A forced disturbance to the laminar flow can be given as inflow condition if that disturbance is included in $\mathcal{U}_i$.

A convenient form of the fringe function λ is as follows,

$$\lambda(x) = \lambda_{max}[S\left(\frac{x - x_{start}}{\Delta_{rise}}\right) - S\left(\frac{x - x_{end}}{\Delta_{fall}} + 1\right)]. \tag{17}$$

Here λ_{max} is the maximum strength of the damping, x_{start} to x_{end} the spatial extent of the region where the damping function is non-zero and Δ_{rise} and Δ_{fall} the rise and fall distance of the damping function. $S(x)$ is a smooth step function rising from zero for negative x to one for $x \geq 1$. We have used the following form for S, which has the advantage of having continuous derivatives of all orders.

$$S(x) \quad = \quad \begin{cases} 0 & x \leq 0 \\ 1/[1 + \exp(\frac{1}{x-1} + \frac{1}{x})] & 0 < x < 1 \\ 1 & x \geq 1 \end{cases} . \tag{18}$$

To achieve maximum damping both the total length of the fringe and λ_{max} have to be tuned. The actual shape of $\lambda(x)$ is less important for the damping but it should have its maximum closer to x_{end} than to x_{start}. The damping is also strongly effected by the resolution of the disturbance that should be damped. An investigation of how the fringe parameters effect the disturbance in the fringe can be found in Appendix C.

For maximum computational efficiency the simulated flow has to be considered when the fringe parameters are tuned. Assuming that the achieved damping is sufficient, a short fringe reduces the box length and therefore the required CPU time per iteration. However, if the flow gradients introduced in the fringe region are larger than those in the physical domain that may decrease the time step and consequently increase the necessary number of iterations. Note that the boundary layer growth causes outflow through the free-stream boundary. The streamwise periodicity requires that all that fluid enters in the fringe region.

Analysis of Navier-Stokes equations with a fringe forcing term yields that there is an additional part of the disturbance associated with the pressure whose decay is not dependent on λ. For a boundary layer, this solution decays appreciably over a downstream distance equal to the boundary layer thickness, and thus the fringe region must be some factor (say 10 to 30) times this thickness to get a large decay factor, see Nordström *et al.* (1999).

2.5. *Temporal discretization*

The time advancement is carried out by one of two semi-implicit schemes. We illustrate them on the equation

$$\frac{\partial \psi}{\partial t} = G + L\psi, \tag{19}$$

	$a_n/\Delta t^n$	$b_n/\Delta t^n$	$c_n/\Delta t^n$
RK3	8/15	0	0
3-stage	5/12	-17/60	8/15
	3/4	-5/12	2/3
RK3	8/17	0	0
4-stage	17/60	-15/68	8/17
	5/12	-17/60	8/15
	3/4	-5/12	2/3

TABLE 1. Time stepping coefficients.

which is on the same form as equation (5) and (7). ψ represents ϕ or ω, G contains the (non-linear) advective, rotation and forcing terms and depends on all velocity and vorticity components, L is the (linear) diffusion operator. L is discretized implicitly using the second order accurate Crank-Nicolson (CN) scheme and G explicitly by a low storage third order three or four stage Runge-Kutta (RK3) scheme. These time discretizations may be written in the following manner : (G and L are assumed to have no explicit dependence on time)

$$\psi^{n+1} = \psi^n + a_n G^n + b_n G^{n-1} + (a_n + b_n)\left(\frac{L\psi^{n+1} + L\psi^n}{2}\right), \qquad (20)$$

where the constants a_n and b_n are chosen according to the explicit scheme used. The two possibilities for the RK3 schemes are shown in the table 1. Note that the RK3 schemes have three or four stages which imply that a full physical time step is only achieved every three or four iterations. The time used for the intermediate stages are given by $t = t + c_n$, where c_n is given in table 1.

To obtain some insight into the properties of these discretizations they will be applied to the two dimensional linearized Burgers' equation with a system rotation. The eigenvalue analysis yields a necessary condition for stability which must be augmented by an experimental verification. Putting the equation into the form of equation (19) yields :

$$\begin{aligned}
\psi &= \begin{bmatrix} u \\ w \end{bmatrix}, \\
G &= \begin{bmatrix} u_0\partial/\partial x + w_0\partial/\partial z & 2\Omega \\ -2\Omega & u_0\partial/\partial x + w_0\partial/\partial z \end{bmatrix} \begin{bmatrix} u \\ w \end{bmatrix}, \\
L &= \frac{1}{R}\begin{bmatrix} \partial^2/\partial x^2 + \partial^2/\partial z^2 & 0 \\ 0 & \partial^2/\partial x^2 + \partial^2/\partial z^2 \end{bmatrix}. \qquad (21)
\end{aligned}$$

It can be seen as an approximation to equation (1). The dependence of ψ on both the streamwise and spanwise coordinate directions have been included in

order to indicate how multiple dimensions enter into the stability considerations.

We will for simplicity use Fourier discretization in the spatial directions. The Chebyshev method acts locally as a transformed Fourier method and thus the stability properties derived here can be applied with the local space step. An exception to this occurs at the endpoints where the transformation is singular. It can be shown that the Chebyshev method is more stable there. A numerical study of a 1-dimensional advection equation using the Chebyshev discretization yields that the upper limit of its spectrum along the imaginary axis is about 16 times lower than the simple application of the results from the Fourier method. This allows a corresponding increase of the time step when the stability is limited by the wall normal velocity at the free-stream boundary.

Fourier transforming in x and z yields:

$$\hat{\psi}_t = \begin{bmatrix} i\alpha u_0 + i\beta w_0 & 2\Omega \\ -2\Omega & i\alpha u_0 + i\beta w_0 \end{bmatrix} \hat{\psi} - \frac{\alpha^2+\beta^2}{R}\hat{\psi}, \tag{22}$$

where α and β are the wavenumbers in the x- and z-directions, respectively. This equation can be diagonalized to yield the equation,

$$\hat{u}_t = i(\alpha u_0 + \beta w_0 \pm 2\Omega)\hat{u} + \frac{\alpha^2+\beta^2}{R}\hat{u}. \tag{23}$$

We assume that the absolute stability limit will first be reached for the largest wavenumbers of the discretization α_{max} and β_{max}, which corresponds to a wavelength of $2\cdot\Delta x$ and $2\cdot\Delta z$, respectively. Δx and Δz are the discretization step lengths in physical space. The following parameters are useful for our analysis,

$$\begin{aligned} \mu &= \Delta t[2|\Omega_k| + (\alpha_{max}|u_0| + \beta_{max}|w_0|)] \\ &= \Delta t\left[2|\Omega_k| + \pi\left(\frac{|u_0|}{\Delta x} + \frac{|w_0|}{\Delta z}\right)\right], \end{aligned} \tag{24}$$

$$\begin{aligned} \lambda &= \frac{1}{R}\Delta t(\alpha_{max}^2 + \beta_{max}^2) \\ &= \frac{1}{R}\pi^2\Delta t\left(\frac{1}{\Delta x^2} + \frac{1}{\Delta z^2}\right). \end{aligned} \tag{25}$$

The parameter μ is usually called the spectral CFL number, in analogy with the stability theory for finite difference equations. Henceforth it will be termed simply the CFL number. Using the RK3-CN time discretization we have the

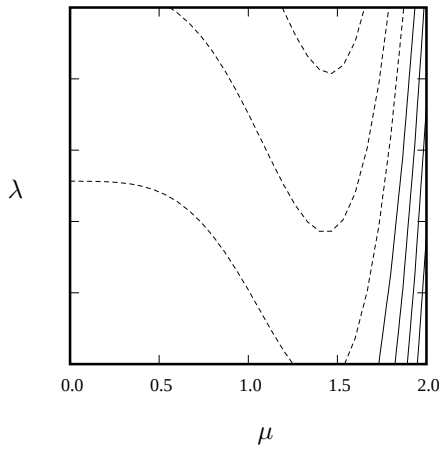

FIGURE 1. Contours of constant amplification factor for the RK3-CN method. Contour spacing is 0.05 with dashed lines indicating that the amplification factor is below unity.

following three stages in each time step for the model equation (23),

$$\begin{aligned}
\hat{u}^{n+1} &= \hat{u}^n + i\mu a_1 \hat{u}^n - \frac{\lambda}{2} a_1 (\hat{u}^{n+1} + \hat{u}^n), \\
\hat{u}^{n+2} &= \hat{u}^{n+1} + i\mu (a_2 \hat{u}^{n+1} + b_2 \hat{u}^n) - \frac{\lambda}{2}(a_2 + b_2)(\hat{u}^{n+2} + \hat{u}^{n+1}), \qquad (26) \\
\hat{u}^{n+3} &= \hat{u}^{n+2} + i\mu (a_3 \hat{u}^{n+2} + b_3 \hat{u}^{n+1}) - \frac{\lambda}{2}(a_3 + b_3)(\hat{u}^{n+3} + \hat{u}^{n+2}).
\end{aligned}$$

The absolute stability regions, i.e. the regions where all solutions to the above difference equations are bounded in the μ – λ plane, can now be found by calculating the roots of the associated characteristic polynomials. Contours of constant absolute values of the roots are given in figure 1. Figure 1 shows the curves for the RK3-CN method. Note that higher values of λ (lower Reynolds number) stabilizes the method, i.e. increases the CFL number (μ) that is allowed for an absolutely stable solution. In the limit of infinite Reynolds number the RK3-CN method approaches the limit $\sqrt{3}$, a result which also can be arrived at through the standard analysis of the RK3 scheme alone. The analysis for the four stage method is analogous and the stability limit is $\sqrt{8}$.

If the time advancement scheme (20) is applied to equations (5) and (7) we find (for the moment disregarding the boundary conditions),

$$\begin{aligned}
(1 - \frac{a_n + b_n}{2R}\nabla^2)\phi^{n+1} &= (1 + \frac{a_n + b_n}{2R}\nabla^2)\phi^n + a_n h_v^n + b_n h_v^{n-1}, \\
\nabla^2 v^{n+1} &= \phi^{n+1}, \qquad (27)
\end{aligned}$$

and

$$(1 - \frac{a_n + b_n}{2R}\nabla^2)\omega^{n+1} = (1 + \frac{a_n + b_n}{2R}\nabla^2)\omega^n + a_n h_\omega^n + b_n h_\omega^{n-1}. \quad (28)$$

2.6. *Horizontal discretization – Fourier expansions*

The discretization in the horizontal directions uses a Fourier series expansions which assumes that the solution is periodic.

The streamwise and spanwise dependence of each variable can then be written

$$u(x,z) = \sum_{l=-(\frac{N_x}{2}-1)}^{\frac{N_x}{2}-1} \sum_{m=-(\frac{N_z}{2}-1)}^{\frac{N_z}{2}-1} \hat{u}(\alpha,\beta)\exp[i(\alpha_l x + \beta_m z)], \quad (29)$$

where $\alpha_l = 2\pi l/x_L$ and $\beta_m = 2\pi m/z_L$, and N_x and N_z are the number of Fourier modes included in the respective directions. Note that the indices on the discrete wavenumbers α and β are sometimes left out for notational convenience and that $k^2 = \alpha^2 + \beta^2$.

2.6.1. *Normal velocity and normal vorticity equations*

Expanding the dependent variables of equation (27) in Fourier series gives

$$\begin{aligned}\left(1 - \frac{a_n + b_n}{2R}(D^2 - k^2)\right)\hat{\phi}^{n+1} &= \left(1 + \frac{a_n + b_n}{2R}(D^2 - k^2)\right)\hat{\phi}^n \\ &+ a_n\hat{h}_v^n + b_n\hat{h}_v^{n-1}, \\ (D^2 - k^2)\hat{v}^{n+1} &= \hat{\phi}^{n+1}, \end{aligned} \quad (30)$$

where D signifies a derivative in the normal direction. Note that the above equations are two linear constant coefficient second order ordinary differential equations in y. A similar equation can also be derived from equation (28). These three equations can be written as follows,

$$(D^2 - \lambda^2)\hat{\phi}^{n+1} = \hat{f}_v^n, \quad (31)$$

$$(D^2 - k^2)\hat{v}^{n+1} = \hat{\phi}^{n+1}, \quad (32)$$

$$(D^2 - \lambda^2)\hat{\omega}^{n+1} = \hat{f}_\omega^n, \quad (33)$$

where

$$\lambda^2 = k^2 + 2R/(a_n + b_n), \quad (34)$$

$$\hat{f}_v^n = \hat{p}_v^n - \frac{2Ra_n}{a_n + b_n}\hat{h}_v^n, \quad (35)$$

$$\hat{f}_\omega^n = \hat{p}_\omega^n - \frac{2Ra_n}{a_n + b_n}\hat{h}_\omega^n, \quad (36)$$

and

$$\begin{aligned}\hat{p}_v^n &= -\left[D^2-\lambda^2+\frac{4R}{a_n+b_n}\right]\hat{\phi}^n-\frac{2Rb_n}{a_n+b_n}\hat{h}_v^{n-1}\\ &= -\hat{f}_v^{n-1}-\left[\frac{2R}{a_{n-1}+b_{n-1}}+\frac{2R}{a_n+b_n}\right]\hat{\phi}^n-\frac{2Rb_n}{a_n+b_n}\hat{h}_v^{n-1}, \qquad (37)\\ \hat{p}_\omega^n &= -\left[D^2-\lambda^2+\frac{4R}{a_n+b_n}\right]\hat{\omega}^n-\frac{2Rb_n}{a_n+b_n}\hat{h}_\omega^{n-1}\\ &= -\hat{f}_\omega^{n-1}-\left[\frac{2R}{a_{n-1}+b_{n-1}}+\frac{2R}{a_n+b_n}\right]\hat{\omega}^n-\frac{2Rb_n}{a_n+b_n}\hat{h}_\omega^{n-1}. \qquad (38)\end{aligned}$$

We will denote the quantities $\hat{p}_\omega^n$ and $\hat{p}_v^n$ the partial right hand sides of the equations.

2.6.2. *Horizontal velocities and wavenumber zero*

Having obtained $\hat{v}$ and $\hat{\omega}$ we can find $\hat{u}$ and $\hat{w}$ using equation (2) and the definition of the normal vorticity component, both transformed to Fourier space. We find

$$\hat{u} = \frac{i}{k^2}(\alpha D\hat{v}-\beta\hat{\omega}), \qquad (39)$$

$$\hat{w} = \frac{i}{k^2}(\alpha\hat{\omega}+\beta D\hat{v}). \qquad (40)$$

Similarly, we can find the streamwise and spanwise component of vorticity in terms of $\hat{\omega}$ and $\hat{\phi}$,

$$\hat{\chi} = \frac{i}{k^2}(\alpha D\hat{\omega}+\beta\hat{\phi}), \qquad (41)$$

$$\hat{\vartheta} = \frac{-i}{k^2}(\alpha\hat{\phi}+\beta D\hat{\omega}). \qquad (42)$$

These relations give the streamwise and spanwise components of velocity and vorticity for all wavenumber combinations, except when both α and β are equal to zero. In that case we have to use some other method to find $\hat{u}_0$, $\hat{w}_0$, $\hat{\chi}_0$ and $\hat{\vartheta}_0$ (the zero subscript indicates that $k=0$). The appropriate equations are found by taking the horizontal average of the first and the third component of equation (1). Due to the periodic BC all horizontal space derivatives cancel out, i.e.,

$$\frac{\partial u_0}{\partial t} = H_1+\frac{1}{R}\frac{\partial^2 u_0}{\partial y^2}, \qquad (43)$$

$$\frac{\partial w_0}{\partial t} = H_3+\frac{1}{R}\frac{\partial^2 w_0}{\partial y^2}. \qquad (44)$$

After a time discretization we find,

$$(D^2 - \lambda^2)\hat{u}_0^{n+1} = \hat{f}_{01}^n, \tag{45}$$

$$(D^2 - \lambda^2)\hat{w}_0^{n+1} = \hat{f}_{03}^n, \tag{46}$$

where

$$\hat{f}_{0i}^n = \hat{p}_{0i}^n - \frac{2Ra_n}{a_n + b_n}\hat{H}_{0i}^n, \tag{47}$$

and

$$\begin{aligned}\hat{p}_{0i}^n &= -\left(D^2 - \lambda^2 + \frac{4R}{a_n + b_n}\right)\hat{u}_{0i}^n - \frac{2Rb_n}{a_n + b_n}\hat{H}_{0i}^{n-1} \\ &= -\hat{f}_{0i}^{n-1}(\psi_0) - \left(\frac{2R}{a_{n-1} + b_{n-1}} + \frac{2R}{a_n + b_n}\right)\hat{u}_{0i}^n - \frac{2Rb_n}{a_n + b_n}\hat{H}_{0i}^{n-1}.\end{aligned} \tag{48}$$

Here the 0 index in $\hat{H}_{0i}$ refers to the zero wavenumber in both horizontal directions. Note that the above system contains the same type of equations as the system (32), and can thus be solved using the same numerical algorithm. Once $\hat{u}_0$ and $\hat{w}_0$ are calculated, the streamwise and spanwise components of vorticity for $k = 0$ can be found as follows,

$$\hat{\chi}_0 = D\hat{w}_0, \qquad \hat{\vartheta}_0 = -D\hat{u}_0. \tag{49}$$

2.6.3. *Solution procedure with boundary conditions*

A problem with the above equations is that the boundary conditions do not apply to the quantities for which we have differential equations. To remedy this, each of the equations can be solved for a particular solution with homogeneous boundary conditions. Then a number of homogeneous solutions with non-homogeneous boundary conditions are found for the same equations. Finally the boundary conditions are fulfilled by a suitable linear combination of particular and homogeneous solutions. Explicitly we proceed as follows:

For all $k = \sqrt{\alpha^2 + \beta^2} \neq 0$ and each of the two symmetries (symmetric and antisymmetric with respect to reflections around $y = y_L/2$) we solve :

$$(D^2 - \lambda^2)\hat{\phi}_p^{n+1} = \hat{f}_v^{n+1} \qquad \hat{\phi}_p^{n+1}(y_L) = 0 \tag{50}$$

$$(D^2 - k^2)\hat{v}_p^{n+1} = \hat{\phi}_p^{n+1} \qquad \hat{v}_p^{n+1}(y_L) = \begin{cases} \frac{\hat{v}_{BS}}{2} & \text{symmetric} \\ -\frac{\hat{v}_{BS}}{2} & \text{antisymmetric} \end{cases} \tag{51}$$

$$(D^2 - \lambda^2)\hat{\phi}_h^{n+1} = 0 \qquad \hat{\phi}_h^{n+1}(y_L) = 1 \tag{52}$$

$$(D^2 - k^2)\hat{v}_{ha}^{n+1} = \hat{\phi}_h^{n+1} \qquad \hat{v}_{ha}^{n+1}(y_L) = 0 \tag{53}$$

$$(D^2 - k^2)\hat{v}_{hb}^{n+1} = 0 \qquad \hat{v}_{hb}^{n+1}(y_L) = 1 \tag{54}$$

$$(D^2 - \lambda^2)\hat{\omega}_p^{n+1} = \hat{f}_\omega^{n+1} \qquad \hat{\omega}_p^{n+1}(y_L) = 0 \tag{55}$$

$$(D^2 - \lambda^2)\hat{\omega}_h^{n+1} = 0 \qquad \hat{\omega}_h^{n+1}(y_L) = 1, \tag{56}$$

where the subscripts p, h, ha and hb indicate the particular and the homogeneous parts. $\hat{v}_{BS}$ is only non-zero for cases with blowing and suction through the plate. Note that only one boundary condition is needed for each second order equation since the assumption of symmetry (or antisymmetry) takes care of the other. $\hat{v}_p^{n+1}(y_L) = 0$ when the symmetric and antisymmetric solutions are added and all the other solutions are zero at $y = 0$. Equations (52) and (56) have zero right hand sides and the same boundary conditions. The solution coefficients are therefore identical and so are also their symmetric and antisymmetric coefficients. Thus, four calls of the the equation solver can be reduced to one.

To fulfill the the remaining boundary conditions we first construct $\hat{v}_{p1}$, $\hat{v}_{h1}$ and $\hat{v}_{h2}$,

$$\hat{v}_{p1}^{n+1} = \hat{v}_p^{n+1} + C_{p1}\hat{v}_{ha}^{n+1} \quad \hat{v}_{p1}^{n+1}(y_L) = 0 \quad \hat{v}_{p1}^{n+1}(0) = v_{BS}/2 \tag{57}$$

$$\hat{v}_{h1}^{n+1} = \hat{v}_{ha}^{n+1} / \frac{\partial \hat{v}_{ha}}{\partial y}(y = y_L) \quad \hat{v}_{h1}^{n+1}(y_L) = 0 \quad \hat{v}_{h1}^{n+1}(0) = 0 \tag{58}$$

$$\hat{v}_{h2}^{n+1} = \hat{v}_{hb}^{n+1} + C_{h2}\hat{v}_{ha}^{n+1} \quad \hat{v}_{h2}^{n+1}(y_L) = 1 \quad \hat{v}_{h2}^{n+1}(0) = 0, \tag{59}$$

where C_{p1} and C_{h2} are chosen to fulfills the boundary condition $\partial v/\partial y = 0$ at the lower wall for each of the two symmetries of $\hat{v}_{p1}$ and $\hat{v}_{h2}$. As the symmetric and antisymmetric parts of $\partial \hat{v}_{h1}/\partial y$ cancel at the lower wall their sum v_{h1} fulfills $\partial v_{h1}/\partial y = 0$.

Now the solutions (v_{p1}, ω_p), $(v_{h1}, \omega = 0)$, $(v_{h2}, \omega = 0)$ and $(v = 0, \omega_h)$ fulfill all the physical boundary conditions at the lower wall. The total normal velocity and vorticity is then given by

$$\hat{v}^{n+1} = \hat{v}_{p1}^{n+1} + C_{v1}\hat{v}_{h1}^{n+1} + C_{v2}\hat{v}_{h2}^{n+1}, \tag{60}$$

$$\hat{\omega}^{n+1} = \hat{\omega}_p^{n+1} + C_\omega \hat{\omega}_h^{n+1}, \tag{61}$$

where C_{v1},C_{v2} and C_ω are chosen such that the boundary conditions at the upper boundary are fulfilled. The u and w velocities are found from the definition of the normal vorticity and the incompressibility constraint.

In general we have to find u and w first to evaluate the boundary conditions. Thus with the C's unknown we find :

$$\hat{u}^{n+1} = \hat{u}_{p1}^{n+1} + C_{v1}\hat{u}_{h1}^{n+1} + C_{v2}\hat{u}_{h2}^{n+1} + C_\omega \hat{u}_h^{n+1}, \tag{62}$$

$$\hat{w}^{n+1} = \hat{w}_{p1}^{n+1} + C_{v1}\hat{w}_{h1}^{n+1} + C_{v2}\hat{w}_{h2}^{n+1} + C_\omega \hat{w}_h^{n+1}, \tag{63}$$

where (u_{p1}, w_{p1}), (u_{h1}, w_{h1}), (u_{h2}, w_{h2}) and (u_h, w_h) are found from (v_{p1}, ω_p), $(v_{h1}, \omega = 0)$, $(v_{h2}, \omega = 0)$ and $(v = 0, \omega_h)$ using equation (39) and (40).

Assuming the boundary conditions are linear we can write them as :

$$L_i(\hat{u}, \hat{v}, \hat{w}) = \hat{D}_i; \qquad i = 1, 2, 3. \tag{64}$$

Here L_i is the linear operator for the ith boundary condition. This can include derivatives in the wall normal direction. The operator may also depend on the wave number (for example when the boundary condition contains horizontal derivatives). Note that the expression for evaluation L_i may include $\hat{\omega}$ as this is equivalent to horizontal derivatives. $\hat{D}_i$ is the data for the boundary condition, the most common form of which is is either zero (homogeneous boundary conditions) or the operator L_i applied to a base flow.

Finally inserting the expressions (60), (62) and (63) into equation (64) and moving all terms containing the particular solution to the right hand side, we get a three by three linear system of equations which is easily solved to find the C's.

For $k = 0$ we solve

$$(D^2 - \lambda^2)\hat{u}_{p0}^{n+1} = \hat{f}_{01}^n \qquad \hat{u}_{p0}^{n+1}(0) = u_{low};\ \hat{u}_{p0}^{n+1}(y_L) = u_{upp} \tag{65}$$

$$(D^2 - \lambda^2)\hat{w}_{p0}^{n+1} = \hat{f}_{03}^n \qquad \hat{w}_{p0}^{n+1}(0) = w_{low};\ \hat{w}_{p0}^{n+1}(y_L) = w_{upp} \tag{66}$$

$$(D^2 - \lambda^2)\hat{u}_{h0}^{n+1} = 0 \qquad \hat{u}_{h0}^{n+1}(0) = 0;\ \hat{u}_{h0}^{n+1}(y_L) = 2 \tag{67}$$

$$(D^2 - \lambda^2)\hat{w}_{h0}^{n+1} = 0 \qquad \hat{w}_{h0}^{n+1}(0) = 0;\ \hat{w}_{h0}^{n+1}(y_L) = 2, \tag{68}$$

where u_{low}, u_{upp}, w_{low} and w_{upp} denote the lower and upper wall velocities. Computations in a moving reference frame can increase the time step. If the boundary condition at the upper wall is in the form of Dirichlet type (specified velocity) then

$$\hat{u}_0 = \hat{u}_{p0}, \tag{69}$$

$$\hat{w}_0 = \hat{w}_{p0}. \tag{70}$$

For other types of upper wall boundary conditions we find the complete solution from :

$$\hat{u}_0 = \hat{u}_{p0} + C_u \hat{u}_{h0}, \tag{71}$$

$$\hat{w}_0 = \hat{w}_{p0} + C_w \hat{w}_{h0}, \tag{72}$$

where C_u and C_w are chosen so that $\hat{u}_0$ and $\hat{w}_0$ fulfill the boundary conditions.

The above equations are all in Fourier space, where the non-linear terms h_v, h_ω, H_1 and H_3 become convolution sums. These sums can be efficiently calculated by transforming the velocities and vorticities using FFTs to physical space, where they are evaluated using pointwise products.

2.7. *Normal discretization – Chebyshev expansion*

The typical equation derived above is a second order constant coefficient ODE of the form

$$(D^2 - \kappa)\hat{\psi} = \hat{f} \qquad \hat{\psi}(0) = \gamma_{-1}, \quad \hat{\psi}(y_L) = \gamma_1. \tag{73}$$

First map the interval $[0, y_l]$ to $[-1, 1]$ by setting $y' = 2y/y_L - 1$. Then

$$(D'^2 - \nu)\hat{\psi} = \hat{f} \qquad \hat{\psi}(-1) = \gamma_{-1}, \quad \hat{\psi}(1) = \gamma_1, \tag{74}$$

where $\nu = \kappa y_L^2/4$. In the following we have for simplicity dropped the prime.

This equation can be solved accurately if the dependent variable $\hat{\psi}$, its second derivatives, the right hand side $\hat{f}$ and the boundary conditions are expanded in Chebyshev series, i.e.,

$$\hat{\psi}(y) = \sum_{j=0}^{N_y} \tilde{\psi}_j T_j(y), \tag{75}$$

$$D^2\hat{\psi}(y) = \sum_{j=0}^{N_y} \tilde{\psi}_j^{(2)} T_j(y), \tag{76}$$

$$\hat{f}(y) = \sum_{j=0}^{N_y} \tilde{f}_j T_j(y), \tag{77}$$

$$\hat{\psi}(1) = \sum_{j=0}^{N_y} \tilde{\psi}_j = \gamma_1, \tag{78}$$

$$\hat{\psi}(-1) = \sum_{j=0}^{N_y} \tilde{\psi}_j (-1)^j = \gamma_{-1}, \tag{79}$$

where T_j are the Chebyshev polynomial of order j and N_y the highest order of polynomial included in the expansion. If the Chebyshev expansions are used

in equation (74), together with the orthogonality properties of the Chebyshev polynomials, we find the following relation between the coefficients

$$\tilde{\psi}_j^{(2)} - \nu\tilde{\psi}_j = \tilde{f}_j \qquad\qquad j = 0, ...N_y. \tag{80}$$

By writing the Chebyshev functions as cosines and using well known trigonometric identities, one finds relations between the Chebyshev coefficients of $\hat{\psi}$ and those of its derivative that can be used for differentiation and integration (see Canuto *et al.* (1988))

$$\tilde{\psi}_j^{(p)} = \sum_{\substack{m=j+1 \\ m+j\ odd}}^{N_y} m\tilde{\psi}_m^{(p-1)} \qquad\qquad j = 1, ...N_y, \tag{81}$$

$$\tilde{\psi}_j^{(p-1)} = \frac{1}{2j}(c_{j-1}\tilde{\psi}_{j-1}^{(p)} - \tilde{\psi}_{j+1}^{(p)}) \qquad\qquad j = 1, ...N_y, \tag{82}$$

where the superscript p indicates the order of the derivative and $c_j = 2$ for $j = 0$ and $c_j = 1$ for $j > 0$. In the first differentiation relation one observes that an error in the highest order coefficients of $\tilde{\psi}^{(p-1)}$ influences all coefficients of its derivative $\tilde{\psi}^{(p)}$. This problem is what is supposed to be avoided by the Chebyshev integration method discussed below. In the second relation we assume that $\tilde{\psi}_j^{(p)} = 0$ for $j > N_y$ and note that $\tilde{\psi}_0^{(p-1)}$ is an integration constant needed when the function $\hat{\psi}^{(p-1)}$ is found by integrating $\hat{\psi}^{(p)}$. Note also that the integration procedure introduces a truncation error, since an integration of a Chebyshev polynomial would result in a polynomial of one degree higher. The coefficient $\tilde{\psi}_{N_y+1}^{(p-1)}$ which would have multiplied T_{N_y+1} is in the present truncation set to zero.

If the relations (82) are used together with relation (80) a system of equations can be derived for either coefficients $\tilde{\psi}_j$ or $\tilde{\psi}_j^{(2)}$. The second approach, called the Chebyshev integration method (CIM), was proposed by Greengard (1991) to avoid the ill conditioned process of numerical differentiation in Chebyshev space. It was implemented in the original channel code by Lundbladh *et al.* (1992*a*) and is also included in the present implementation. However, we have found that using this method, subtle numerical instabilities occur in some cases and we therefore recommend to solve for the coefficients of the function itself, $\tilde{\psi}_j$. Such a Chebyshev tau method (CTM), almost identical to that used by Kim, Moin & Moser, is also implemented and is so far found to be stable. We first present the CTM, then the CIM and finally we discuss the instabilities observed in computations with the CIM. Note that the instabilities have occurred only a few times and that the results otherwise are the same for the two methods.

2.7.1. *Chebyshev tau method-CTM*

If the recursion relation (82) is used to express equations (80) in the coefficients $\tilde{\psi}_j$, one arrives at the system of equations (83 below). A more detailed derivation can be found in Canuto *et al.* (1988), but observe the sign errors therein. We have

$$-\frac{c_{j-2}\nu}{4j(j-1)}\tilde{\psi}_{j-2}+\left(1+\frac{\nu\beta_j}{2(j^2-1)}\right)\tilde{\psi}_j-\frac{\nu}{4j(j+1)}\tilde{\psi}_{j+2}$$
$$=\frac{c_{j-2}}{4j(j-1)}\tilde{f}_{j-2}-\frac{\beta_j}{2(j^2-1)}\tilde{f}_j+\frac{\beta_{j+2}}{4j(j+1)}\tilde{f}_{j+2},\quad j=2,\ldots,N_y \tag{83}$$

where

$$\beta_j=\begin{cases}1 & 0\le j\le N_y-2\\ 0 & j>N_y-2\end{cases}. \tag{84}$$

Note that the even and odd coefficients are uncoupled. Since a Chebyshev polynomial with an odd index is an odd function, and vice versa, the decoupling of the systems of equations is just a result of the odd and even decoupling of equation (74) itself. The same can be achieved for the boundary conditions (78) and (79) if they are added and subtracted,

$$\sum_{\substack{j=0\\ j\ even}}^{N_y}\tilde{\psi}_j=\frac{\gamma+\gamma_-}{2},\qquad \sum_{\substack{j=1\\ j\ odd}}^{N_y}\tilde{\psi}_j=\frac{\gamma-\gamma_-}{2}. \tag{85}$$

These boundary conditions together with the equations (83) constitute a linear system of N_y+1 equations that can be solved for the coefficients $\tilde{\psi}_j$ ($j=0,\ldots,N_y$). The structure of the equations involving the even coefficients forms a tridiagonal system and so does the equation for the odd coefficients. The boundary conditions fill the top row of both systems and make the systems only quasi-tridiagonal, but it only takes $16N_y$ operations to solve both systems.

The system (83) has in fact been truncated to only contains N_y-1 equations and two equations have been replaced by boundary conditions. That truncation introduces what is usually called the tau error. In solution algorithms that solve for the three velocity components of the Navier-Stokes equations and the pressure, the coupling between the equations for the velocities and that for the pressure requires corrections of the tau error (Kleiser & Schumann 1980). We have chosen to eliminate the pressure in the Navier-Stokes equations and solve for the normal velocity and the normal vorticity. As those equations do not couple in the same way, we do not have to correct the tau error.

2.7.2. *Chebyshev integration method-CIM*

Instead of solving for the coefficients $\tilde{\psi}_j$, the CIM solves for the coefficients of the Chebyshev series for the second derivative, $\tilde{\psi}_j^{(2)}$. The major advantage is

supposed to come in the calculation of derivatives of the solution $\hat{\psi}$. Derivatives are needed in the calculation of the remaining velocities and vorticities using equations (39)-(42). In the CIM the second derivative is already calculated and the first derivative and the function itself can be found by the numerically well conditioned process of integration.

If the relations (82) are used to write (80) in terms of $\tilde{\psi}_j^{(2)}$ the result is the following system of equations,

$$\begin{aligned}
j=0: &\quad \tilde{\psi}_0^{(2)} - \nu\tilde{\psi}_0 &&= \tilde{f}_0 \\
j=1: &\quad \tilde{\psi}_1^{(2)} - \nu(\tilde{\psi}_0^{(1)} - \tfrac{1}{8}\tilde{\psi}_1^{(2)} + \tfrac{1}{8}\tilde{\psi}_3^{(2)} &&= \tilde{f}_1 \\
2\le j\le N_y-2: &\quad \tilde{\psi}_j^{(2)} - \nu\tfrac{1}{4j}\left[\tfrac{c_{j-2}\tilde{\psi}_{j-2}^{(2)}}{j-1} - \tilde{\psi}_j^{(2)}\left(\tfrac{1}{j-1}+\tfrac{1}{j+1}\right) + \tfrac{\tilde{\psi}_{j+2}^{(2)}}{j+1}\right] &&= \tilde{f}_j \quad (86) \\
j=N_y-1: &\quad \tilde{\psi}_{N_y-1}^{(2)} - \nu\tfrac{1}{4(N_y-1)}\left[\tfrac{\tilde{\psi}_{N_y-3}^{(2)}}{N_y-2} - \tilde{\psi}_{N_y-1}^{(2)}\left(\tfrac{1}{N_y-2}+\tfrac{1}{N_y}\right)\right] &&= \tilde{f}_{N_y-1} \\
j=N_y: &\quad \tilde{\psi}_{N_y}^{(2)} - \nu\tfrac{1}{4N_y(N_y-1)}(\tilde{\psi}_{N_y-2}^{(2)} - \tilde{\psi}_{N_y}^{(2)}) &&= \tilde{f}_{N_y}.
\end{aligned}$$

The equations for odd and even coefficients decouple and so do the boundary conditions on the form (85). However, we now need to rewrite them with the aid of (80) to contain the coefficients of $\tilde{\psi}^{(2)}$ that we are now solving for. We find that the first sum in (85) takes the form,

$$\begin{aligned}
\tilde{\psi}_0 + \tilde{\psi}_0^{(1)} \quad &+\tfrac{1}{4}\tilde{\psi}_0^{(2)} - \tfrac{1}{12}\tilde{\psi}_1^{(2)} - \tfrac{7}{48}\tilde{\psi}_2^{(2)} + \textstyle\sum_{j=3}^{N_y-2}\frac{3\tilde{\psi}_j^{(2)}}{(j-2)(j-1)(j+1)(j+2)} \\
&-\tfrac{(N_y-6)\tilde{\psi}_{N_y-1}^{(2)}}{4(N_y-3)(N_y-2)N_y} - \tfrac{\tilde{\psi}_{N_y}^{(2)}}{2(N_y-2)(N_y-1)N_y} = \gamma_1. \qquad (87)
\end{aligned}$$

Thus, the solution of equation (74) is found by solving the system of equations for the second derivative of $\tilde{\psi}$ (87) together with the boundary conditions (87) and the corresponding one at $y=-1$. We now have two more equations than for the tau method and the solution to the full system is a set of N_y+1 coefficients of the second derivative and the two integration constants $\tilde{\psi}_0^{(1)}$ and $\tilde{\psi}_0^{(2)}$ representing the zeroth order Chebyshev coefficient of $D\hat{\psi}$ and $\hat{\psi}$ itself, respectively. The function $\hat{\psi}$ is then found by two integrations, which in Chebyshev space can easily be constructed using the relations (82). The same quasi-tridiagonal form of the equation systems for the odd and even coefficients appears as for the CTM and the same solution routine can be used.

2.7.3. *Integration correction*

When the solution for $\hat{\psi}^{(2)}$ is found by the CIM and integrated to obtain $\hat{\psi}^{(1)}$ and $\hat{\psi}$ the same truncation is used for both the derivatives and $\hat{\psi}$ itself. They are all represented with N_y+1 non-zero Chebyshev coefficients. This means

that the truncations are not compatible, since the derivative of a function represented as a finite Chebyshev series should have one coefficient less than the function itself. For example, if the coefficients $\tilde{\psi}_j$ are used to construct those for the derivative, using the recurrence relation (81), the result will not be the same as the coefficients $\tilde{\psi}_j^{(1)}$. There will be a slight difference in half of the coefficients for the derivative, the size depending on the magnitude of the coefficient $\tilde{\psi}_{N_y}$. The expression for the difference can be derived as follows. We write $\hat{\psi}$ explicitly using the coefficients $\tilde{\psi}_j^{(1)}$ and the relation (82),

$$\hat{\psi} = \tilde{\psi}_0 T_0 + \sum_{j=1}^{N_y-1} \frac{1}{2j}(c_{j-1}\tilde{\psi}_{j-1}^{(1)} - \tilde{\psi}_{j+1}^{(1)})T_j + \frac{1}{2N_y}\tilde{\psi}_{N_y-1}^{(1)} T_{N_y}. \tag{88}$$

Now (81) is applied to the Chebyshev coefficients in (88) to calculate the derivative $D\hat{\psi}$. Let $\tilde{\psi}_j^D$ be its new coefficients. We find that these new coefficients will not equal $\tilde{\psi}_j^{(1)}$ and the following relation is found between them,

$$\begin{aligned} \tilde{\psi}_j^D &= \tfrac{2}{c_j} \textstyle\sum_{\substack{q=j+1 \\ q+j\ odd}}^{N_y} (c_{q-1}\tilde{\psi}_{q-1}^{(1)} - \tilde{\psi}_{q+1}^{(1)}) + \quad \frac{1}{c_j}\tilde{\psi}_{N_y-1}^{(1)} \\ &= \tilde{\psi}_j^{(1)} \qquad\qquad q + N_y\ odd, \end{aligned} \tag{89}$$

$$\begin{aligned} \tilde{\psi}_j^D &= \tfrac{2}{c_j} \textstyle\sum_{\substack{q=j+1 \\ q+j\ odd}}^{N_y} (c_{q-1}\tilde{\psi}_{q-1}^{(1)} - \tilde{\psi}_{q+1}^{(1)}) \\ &= \tilde{\psi}_j^{(1)} - \tfrac{1}{c_j}\tilde{\psi}_{N_y}^{(1)} \qquad\qquad q + N_y\ even. \end{aligned} \tag{90}$$

Thus, we have a method of correcting the coefficients $\tilde{\psi}_j^{(1)}$ so that they represent $D\hat{\psi}$ with the same truncation as $\tilde{\psi}_j$ represent $\hat{\psi}$. A similar correction can be derived for the coefficients $\tilde{\psi}_j^{(2)}$ of the second derivative. After some algebra we find,

$$\tilde{\psi}_j^{D^2} = \tilde{\psi}_j^{(2)} - \frac{1}{c_j}\left(1 + \frac{(N_y-1)^2 - j^2}{4N_y}\right)\tilde{\psi}_{N_y-1}^{(2)} \qquad j + N_y\ odd, \tag{91}$$

$$\tilde{\psi}_j^{D^2} = \tilde{\psi}_j^{(2)} - \frac{1}{c_j}\tilde{\psi}_{N_y}^{(2)} \qquad j + N_y\ even, \tag{92}$$

where $\tilde{\psi}_j^{D^2}$ are the corrected Chebyshev coefficients for $D^2\hat{\psi}$.

When the horizontal components of velocity and vorticity are found using the relations (39) to (42), we need $\hat{\phi}$, $D\hat{v}$ and $D\hat{\omega}$. The above corrections are therefore needed in order for the velocity and vorticity fields to exactly satisfy the incompressibility constraint (2). Note that an error in the highest Chebyshev coefficients will by the above correction scheme affect all other coefficients of the first and second derivative. Exactly what was supposed to be avoided by the integration method.

The CTM and CIM methods are equally efficient and give the same results with the exception of a few very rare cases. We have found that numerical instabilities may occur when the wall normal resolution is very low and the velocity and vorticity fields are not divergence free. We have also found that it in those cases is enough to make the vorticity divergence free to stabilize the calculations. With integration correction or the CTM method, both velocity and vorticity are completely divergence free. However, for one channel flow case so far, and more frequently in the boundary layer, a numerical instability occurs with the integration correction but not without.

Fortunately the instability causes the calculation to blow up in a few time steps and before that the results are the same as for a stable version of the code. With sufficient wall normal resolution (which is required anyhow) and without the integration correction the boundary layer code has been found completely reliable. The CTM method is, however, to prefer.

2.8. *Pressure*

By expressing the Navier-Stokes equations in the form of equations (4) and (7), the pressure need not to be taken into account. However, it might be of interest to solve for this quantity as well as the velocity components. The pressure can, for example, be used for detecting regions of rapid motion in a turbulent boundary layer.

The Poisson equation for the pressure derived above, equation (3), is written as

$$\nabla^2(p+E) = \frac{\partial H_i}{\partial x_i}, \tag{93}$$

where $E = \frac{1}{2}u_i u_i$ and $H_i = h_i + F_i = \epsilon_{ijk}u_j(\omega_k + 2\Omega_k) + F_i$. Note that the term F_i does not contain the disturbances in the fringe region for the spatial simulations and is zero for the temporal boundary layer. This equation has a similar form as the equations for ϕ, v and ω and can thus be solved using the same numerical routine.

The boundary conditions at the wall ($y = 0$) and at the upper boundary ($y = y_L$) are derived from the normal component of the Navier-Stokes equations. The boundary condition with non-zero wall velocities becomes

$$\left.\frac{\partial}{\partial y}(p+E)\right|_{y=0} = \left.\left[\frac{1}{R}\nabla^2 v + h_2 - \frac{\partial v}{\partial t}\right]\right|_{y=0}. \tag{94}$$

The term $\frac{\partial v}{\partial t}$ is included for the case of flow control like blowing/suction from the wall. For a wall with zero velocities the boundary condition becomes

$$\left.\frac{\partial}{\partial y}(p+E)\right|_{y=0} = \left.\frac{1}{R}\frac{\partial^2 v}{\partial y^2}\right|_{y=0}. \tag{95}$$

At $y = y_L$ the boundary condition becomes

$$\frac{\partial}{\partial y}(p+E)\bigg|_{y=y_L} = \left[\frac{1}{R}\nabla^2 v + h_2 + \lambda(x)(\mathcal{U}_y - v) - \frac{\partial v}{\partial t}\right]\bigg|_{y=y_L}, \qquad (96)$$

where $\lambda(x)$ is the fringe function described in section 2.4.

For wavenumber zero the boundary condition (96) is automatically fulfilled if boundary condition (94) is fulfilled. It is required by the compatibility condition

$$\int_0^{y_L} \frac{dH_2}{dy} dy = \frac{\partial}{\partial y}(p+E)|_{y=y_L} - \frac{\partial}{\partial y}(p+E)|_{y=0}, \qquad (97)$$

which comes from the integration of equation (93). A second boundary condition for p itself is needed at $y = 0$ and this is chosen to be $p = 0$. The mean pressure at the wall cannot be determined and $p = 0$ at the wall is a reference pressure. It is not possible to choose $p = 0$ at $y = y_L$ because the location of the free-stream is arbitrary chosen for numerical purposes.

It might seem to be a better approach to rewrite equation (3) as

$$\nabla^2 p = -\frac{\partial u_i}{\partial x_j}\frac{\partial u_j}{\partial x_i} + \frac{\partial}{\partial x_i}(2\epsilon_{ijk}u_j\Omega_k) + \frac{\partial F_i}{\partial x_i}, \qquad (98)$$

and solve for the pressure directly. The solution to equation (98) turns out to be sensitive to the values of the velocities at the upper boundary. When using different boundary conditions for the velocities, the solutions are slightly different, hence the pressure will be different. The sensitivity comes from the fact that derivation in the normal direction in Chebyshev space is dependent on the coefficients in all the collocation points. These coefficients change when transforming back and forth to physical space. Thus the derivations must be, for consistency, performed at the same time, with no transformations between them. These problems are avoided by solving for the pressure plus energy as in equation (93).

The pressure can be calculated from a specific velocity field with the post processing program **pre**. The pressure needs thus not be calculated in the simulation itself. If turbulent statistics involving pressure are being calculated during a simulation, the pressure is calculated in those time steps where the sampling occurs.

3. Implementation

In implementing the algorithm presented above a significant effort has been put into portability, flexibility and computational efficiency. The language is standard FORTRAN 77 with the extension of the INCLUDE statements, eight character names and lower case characters. Especially the demands on the data structure have forced an encapsulation of the access to the main storage which requires some attention. Also the vectorization and the need to process suitably large chunks of data at a time adds complexity in exchange for execution speed.

3.1. *Program structure of* **bla**

The program **bla** has been divided into subroutines each with one specific task. The main program steps the time and calculates the adaptive time step. The subroutines **nonlinbl** and **linearbl** carry out the main part of the algorithm aided by smaller subroutines for integration, equation solving etc. The FFTs are taken from **VECFFT** which was developed specifically for the simulation codes but is an independent package of vectorizable Fourier and Chebyshev transforms.

3.1.1. *Coarse program structure, step 1 - 4*

Since some computers cannot hold all of the three dimensional data in the main memory simultaneously, and in any case the number of three dimensional arrays should be minimized to save space, the three dimensional computation is carried out by slicing the data into two dimensional planes.

In the main time stepping loop the data needs to be stepped through twice. First slicing in x-z-planes to calculate the FFTs and the pointwise product for non-linear terms, step 2, and second in x-y-planes to calculate the normal Chebyshev transforms and solve the equation systems for the new velocities and vorticities, step 3. Step 1 reads input files, initializes the FFTs and calculates the partial right hand sides needed to start the time stepping loop and computes the base flow. Step 4 stores the final velocity field.

3.1.2. *Step 1, initialization*

Subroutine **ppar** prints the contents of the parameter file to standard output as a check of which size of problem the image is compiled for.

Subroutine **rparambl** reads the file **bla.i** which contains control information for the program, especially the input and output filenames and the final time to which the simulation is to be done, cf. section 5.2.

Subroutine **rdiscbl** reads the resolution, the computational box size and a few parameters defining the flow from the file **namnin**. The velocities are then read from the file and put into the main storage positions 1-3. If the resolution of the image and the file do not correspond, this is printed on standard output and the program stops execution. The check can be disabled by the `varsiz` flag in the **bla.i** file in which case the field is extended by zero-padding or truncated to fit the image resolution.

Subroutine **rescale** rescales all data read from **bla.i** from boundary layer scaling to the channel flow scaling used internally, see Appendix B.

Subroutine **fskch** computes the base flow boundary layer profile.

Subroutine **preprbl** calculates wavenumbers and collocation points, and initializes the FFTs.

Subroutine **fshift** computes a Galilei transformation which can be used to increase the maximum stable time step.

Subroutine **rwavebl** reads the profile of forcing waves to be introduced in the fringe region.

Subroutine **getdt** calculates the initial time step to set get a CFL number equal to the `cflmax` value. The subroutine is only used if the time stepping is adaptive.

Subroutine **prhs** calculates the initial partial right hand sides $\hat{p}_\phi$ $\hat{p}_\omega$, $\hat{p}_{01}$, $\hat{p}_{03}$ and places the first two in positions 6 and 7 of the main storage. The streamwise and spanwise vorticities are also calculated and put into positions 4 and 5 of the storage.

Subroutine **bflow** generates a base flow used for spatial simulations.

Subroutine **cbflow** reads or writes the base flow boundary layer profile in **basic.i** for spatial simulations.

Subroutine **blfou** computes the streamwise Fourier transform of the base flow.

Some initial parameter values for the time stepping mechanism are prepared in the main program and output files are opened.

3.1.3. *Step 2, computations in physical space*

The subroutine **wplbl** writes data to 2-d plane files.

The subroutine **blshift** shifts the base flow and boundary conditions to be aligned with the computational domain when a Galilean transform is used, i.e. if the lower wall is "moving".

The subroutine **gtrip** generates a random force flow trip.

The subroutine **boxxys** computes the spanwise and time averaged statistics for one xz-box.

The subroutine **nonlinbl** calculates H_i as pointwise products in physical space and stores them in position 1 to 3 of the main storage. It also computes the volume forcing and adds it to H_i. As the main storage is in Fourier-physical space, cf. section 3.2.2 below, the velocities and vorticities must be transformed back to physical space before the product can be formed. Likewise the products H_i must be transformed to Fourier space before storing them. The velocity rms amplitudes are computed in Fourier-physical space. The maximum CFL number and the extrema of the velocities are calculated from the velocities in physical space.

The xy-statistics, CFL number, and rms-amplitude and extremum statistics are written to the respective files.

3.1.4. *Step 3, computations in Fourier-Chebyshev space*

The time step is recalculated to regulate the CFL number close to `cflmax` if adaptive time stepping is enabled. The time stepping parameters are calculated for the next time step.

Subroutine **linearbl** transforms the non-linear products into Chebyshev space and constructs the complete right hand sides for the evolution equations. The Chebyshev-tau or Chebyshev-integration method is used to solve for the evolution variables from a set of tridiagonal equations. The chosen boundary conditions are applied. All velocities and vorticities are constructed and partial right hand sides are computed for the next time step. Finally the velocities and vorticities are transformed back to physical space in the y-direction. The velocities are stored into positions 1 to 3, the streamwise and spanwise vorticity into 4 and 5 and the partial right hand sides into 6 and 7 of the main storage.

For selected times the 3-dimensional velocity data is written to file.

Time is incremented and execution is continued with the next time step from step 2 if the the final time `tmax` is not reached.

If `pressure` is set to one in the file **par.f**, the following two subroutines are entered if statistics are sampled in this step. In **nonlinp** the terms $H_{1,1} + H_{3,3}$ and H_2 are calculated and stored in position 4 and 5. The energy E is calculated and stored in position 8. In **linearp** the linear and non-linear parts of the boundary conditions and the sum $H_{1,1} + H_{2,2} + H_{3,3}$ are calculated. The equation for the pressure is solved and the streamwise and spanwise vorticity need to be recalculated. Pressure is stored in position 8.

3.1.5. *Step 4, output*

The subroutine **wdiscbl** handles the output of a velocity field to an external file. The final values of xy-statistics are written to file by **wxys**. The pressure is written to an external file by **wdiscp** if `pressure` is set to one. The amplitude files are written by **wamp**, and planes are written by **wplbl**. All opened files are closed.

3.2. *Data structure*

As the size of a problem is explicitly compiled into the program, the memory allocation is for the most part static. Some effort was put into minimizing not only the three dimensional storage but also the two dimensional arrays

since this is the only part residing in main memory when the three dimensional storage is located on an external device.

3.2.1. *Complex numbers and FFTs*

Most of the algorithm above works with quantities in Fourier space. These are in general complex which requires storage of both real and imaginary parts. Though FORTRAN has the capability of automatically handling complex numbers most compilers produce inefficient code for this, especially for mixed real and complex expressions. Moreover FORTRAN stores complex numbers with alternating real and imaginary parts, which causes a severe performance loss for vector fetches on certain computers as the stride will be even. To circumvent this, it was decided to store all complex quantities in double arrays, one for real and one for imaginary parts. As the algorithm neither includes general complex-complex multiplications nor divisions this did not add very much code.

The FFTs in **VECFFT** are built for separate storage of the real and imaginary parts, but can optionally be used with standard FORTRAN storage.

3.2.2. *Main storage, boxes, drawers, and planes*

As mentioned above, to save on space the algorithm traverses the three dimensional volume twice to complete a time step. The three dimensional storage is in some cases too large to fit in the main memory in which case it may be put on an external device such as an SSD or a disk. In order to efficiently access this external device the records need to be long, preferably much longer than the typical vector length needed to get good CPU performance. If the three dimensional storage is divided into x-z- and x-y-planes the largest common element between these is a single vector in the x-direction, a *pencil* containing `nx` words. In order to increase this number, planes are combined into a *box* consisting of an integer number of adjacent planes e.g., an x-y-box holds `mbz` x-y-planes and an x-z-box holds `mby` x-z-planes. The intersection between an x-y- and an x-z-box then holds `mby*mbz` pencils, which is called a *drawer*. Most subroutines are made to handle a box rather than a plane at a time, with the additional advantage that the vector length increases by a factor of `mbz` or `mby`.

The variables in the main storage are in Fourier-physical format, i.e., the axes are α, physical y and β, except for the partial right hand sides $\hat{p}_v$ and $\hat{p}_\omega$, which are stored in Fourier-Chebyshev space.

The structure of the file used for the three dimensional storage is as follows: File format : unformatted, direct access, scratch, record length `nx*mby*mbz*npreal` bytes, name **ur**. `npreal` is the number of bytes used to store a real number (usually 4 or 8 bytes). Storage sequence: the drawers are stored in increasing `y, z` and `i` order, with `y` varying the fastest and `i` slowest. Within each drawer

the coefficients are stored in increasing `x, y, z` order with `x` varying the fastest and `z` slowest. All the real data is stored in the first half of the drawer and imaginary data in the second. The number of records is `nby*nbz*7`.

The main storage is accessed box-wise by the routines **getxy, putxy, getxz** and **putxz**. The routines select between core storage and file storage depending on the value of the integer `nfc` (1/0); for the latter case the routines **getdr, putdr** move one drawer from or to the file.

3.2.3. *Naming conventions*

The variable names in the algorithm description above have been followed as closely as possible. One important exception is that N_y in the algorithm corresponds to `ny-1`. Greek letters have been replaced by abbreviations. In the case a variable is complex it has been replaced by two with the last letters 'r' and 'i', for the real and imaginary parts. An example of this is `pomyr` which is the real part of the array $\hat{p}^n_\omega$. Note that the superscripts 'n' etc. and the hat symbol are generally left out, when needed for distinction they are replaced by suffices , e.g. a^{n+1} becomes `anp1`. The component indices '1,2,3' in, e.g., H_1 are usually found as the last index of the array. Instead numbers in the array names are used to distinguish between the same variable when represented by two different arrays in step 2 and step 3. Normal derivatives are denoted by prefixes `d` and `d2`. Sometimes a 'b' is used for 'box', cf. above, e.g., `bbeta` is the wavenumber beta vector expanded to correspond to other box sized arrays.

All variables are declared a specific type and the program has been compiled with an `implicit none` statement, which was changed to `implicit logical (a-z)` as the former is non-standard. Thus the type rules are not into effect and have not been adhered to; note especially that `x`, `y`, `z` are integer indices in do loops.

4. Operation

The program **bla** reads a velocity field from an external device, steps the field to a selected final time while producing some log information on the standard output device and writes the final velocities back to a file. During the simulation it may also output a file of the velocity and vorticity rms amplitudes, a file of the amplitude of specific wavenumbers, a file of extremum amplitudes, a file of statistics averaged over the spanwise direction, files with velocities in two dimensional planes at regular intervals in time and files containing complete 3-d velocity fields at selected times. The simulation can be run with the pressure solver to get the pressure at the same time steps as the velocities.

The program **bls** may be used to produce the initial velocity field.

The program **rit** performs post processing of 3-d velocity fields into Tektronix, Postscript or ppm (portable pixel map) compatible graphics. Linear combinations (for example difference) of one or more 3-d velocity fields can be computed with **cmp**, which also can calculate rms and maxnorm amplitudes of the result. This is useful for, for example, convergence checks.

The program **pre** calculates the pressure for a 3-d velocity field and produces a 3-d pressure field which is post processed with **ritpre**.

Postprocessing of two dimensional planes is done by the program **rps** in a way similar to **rit**. Plots of amplitude files are generated by the programs **pamp1** and **pamp2**, which handle one and multiple amplitude files respectively. Wave amplitude files are plotted by the program **pampw** and **pampw2** and extremum amplitude files by **pext1**.

To reduce the storage requirements of 3-d velocity files, they can be compressed by **dfc** and similarly for two dimensional plane files by **dpc**. Note that regular compression programs such as gzip or compress give a negligible reduction in size of these binary data files. An additional advantage with using the compression routines is that they produce a binary data format which is portable between machines with different file formats and floating point representations.

These programs along with the Fourier transform library **VECFFT**, the compression library **dclib** and the plot library **plot1** forms a completely self contained and portable system written in FORTRAN 77.

4.1. *Compiling*

Most of the programs need to be recompiled for each size of problem to be run. Under UNIX this is most easily handled with a makefile. As stated above the compiler must handle INCLUDE statements and lower case characters. For compilation most of the programs require Fourier transforms from the package **VECFFT**. These are also written in standard FORTRAN 77 and can be compiled along with the code. The number of grid points and some other parameters must be set prior to compilation in the file **par.f**. The same **par.f** file should be used for the compilation of all programs to work on a specific simulation. Which routines that need to be recompiled after changing the parameter file is determined by the makefiles.

The number of spectral modes in each direction is set by the parameters `nx`, `ny`, `nz`. The following restrictions apply : `nx` and `ny-1` must be even and factorable by 2, 3 and 5, `nz` must be factorable by 2, 3, 5 and at least 2. Note that `ny` is the number of Chebyshev polynomials and thus is equal to $N_y + 1$ used in section 2 above.

Dealiazing, i.e. padding to remove aliazing errors, can be switched on (=1) or off (=0) independently for each direction by the flags `nfxd`, `nfyd` and `nfzd`. If

dealiazing in the respective direction is used `nx`, `ny-1` must be divisible by 4, and `nz` must be divisible by 2. Z-symmetry can be used to reduce computation time and storage by setting `nfzsym`=1. If this is done `nz` must be divisible by 4, and if used simultaneously with dealiazing in the z-direction `nz` must be divisible by 8.

There is an option to run 2 1/2 dimensional simulations, i.e., simulations of flow in a two dimensional geometry with all three velocity components non-zero, which is sometimes called the infinite swept flow. (Two dimensional flow is a special case of this.) In this case set `nz`=1 `nfzsym`=0 and `nfzd`=0. (In this case the limitations on `nz` given above do not apply.)

Normally (`nfc`=1) all the storage resides in primary memory but it is possible to put the main three dimensional arrays in the external file `ur` by setting `nfc`=0. To achieve maximum performance, especially for external main storage, the parameters `mby` and `mbz` can be changed from the default value =1, see section 4.4 below. Note that `nz` must be divisible by `mbz`. The program can be coarse grain parallelized, in which case the parameter `nproc` should be changed from the default value one to the number of available processors. This is also discussed in section 4.4. To allow for simultaneous calculation of velocities and pressure, the parameter `pressure` should be set to 1. All other parameters in the **par.f** file are computed and should not be changed manually. Note that most subroutines except those in the libraries **dclib**, **VECFFT** and **plot1** must be recompiled after changing **par.f**.

The codes are written in single precision, i.e. with REAL and COMPLEX declaration. However, in most cases there is a need to run the code in double precision, i.e., with at least 10-12 digit precision. For this purpose the supplied makefile convert the programs to double precision. Note that for the programs to work with the libraries and together with binary files all routines must be compiled with the same precision. The makefile automatically compile the libraries with the same precision as the program. For the double precision, you can also use the compiler option by specifying the default size of variables as DOUBLE PRECISION like "-r8". This option varies from one machine to another. In case of work stations, the compiler option for the double precision is used. See the Makefile for more informations.

However, to change precision (i.e., compiling the programs as double precision where they have previously been compiled as single or vice versa) it is necessary to delete all object files before recompiling. This is not handled automatically by the makefiles.

The same makefile named "Makefile" can be used in most machines including Crays, IBM, SGI, SUN, DEC and HP. You must have "cpp" in path and may need to change preprocessor option because it varies from machine to machine. The C language preprocessor, cpp performs the preprocessing directives in some

programs like ctim.f. It is useful to handle system dependent functions in one file.

4.2. *Generation of initial velocity fields with* **bls**

An initial velocity field consists of a header and an array with the three components of velocity in Fourier space fulfilling the equation of continuity. The format of the file is described in section 5.3. The routine **bls** may be used to generate an initial velocity field, consisting of a basic laminar flow, a localized disturbance, waves and a random noise. The different disturbances can be switched off to allow zero to three disturbances to be inserted.

The initial velocity field file has the same format as files generated by subsequent execution of the **bla** program so that it is possible to feed the initial velocity field to the postprocessing directly for examination.

To compute a velocity field a velocity profile file must first be generated. The subroutine **fskch** finds velocity profiles from the Blasius/Falkner-Skan/Falkner-Skan-Cooke family. These are similarity boundary layer profiles derived from the laminar boundary layer flow equations for flow over a flat plate, wedge and infinite swept wedge. **bls** is generating a temporal/spatial or parallel/non-parallel velocity field depending on flow type parameter **fltype**.

bls is intended for batch execution and has no interactive input. The input comes from the file **bls.i**. The format of this file is given in section 5.1. All input is non-dimensionalized with the displacement thickness and free-stream velocity at the inflow boundary ($x = 0$) at $t = 0$.

4.3. *Generation of non-similarity base flows*

In case the streamwise free-stream velocity is not a power of the downstream distance, the boundary layer equations do not have a self similar solution. To generate a base flow for this situation we can first use **bls** to generate a similarity flow field (without disturbances) which is a good approximation to the sought flow around the inflow boundary. I.e., a flow such that boundary layer thickness and acceleration are correct around the inflow boundary. Then this flow field can be advanced in time with **bla** to find a steady state using a streamwise free-stream velocity given in tabular form as a function of the downstream distance (see section 5.2 and 5.10). The generated steady flow field can be input to **bls** and disturbances superimposed. The same flow field can be used to specify the baseflow to **bla** for subsequent simulations.

4.4. *Execution of* **bla**

The program is intended to be used in batch mode and so has no interactive input. The main configuration is done at compile time through changes to the

file **par.f** (see section 4.1) and at runtime by **bla.i** (see section 5.2). An initial velocity field, which can be produced by the program **bls**, see above, is needed to start execution.

4.4.1. *Storage requirements*

The core size depends on the compiled size of the code, the resolution of the simulation, and whether dealiazing in the y-direction is used, the tuning parameters `mby`, `mbz` and `nproc` and if the three dimensional storage is in the core.

The two dimensional storage for step 2 is `7*nx*nz*mby*nproc` words; multiply by a factor 1.5 each for dealiazing in the x and z-directions, by 0.5 for z-symmetry and by 8/7 if the pressure solver is activated. For step 3 storage is `19.5*nx*ny*mbz*nproc` words; multiply by 1.5 for dealiazing in the y-direction and 8/7 for pressure solver. The storage for step 2 and step 3 overlaps so that the total two-dimensional storage is equal to the maximum of the requirement for step 2 and step 3.

The three dimensional storage is `7*nx*ny*nz` words, multiply by a factor of 1.5 for dealiazing in the y-direction, by 0.5 for z-symmetry. This storage can be kept out of the core by setting `nfc`=0.

4.4.2. *Tuning*

The code itself has been written for maximum speed on a vectorizing computer using a highly optimizing compiler. To achieve highest possible performance the main storage should preferably be kept in the core. If this is is not possible the performance in terms of wall time will degrade due to waiting for I/O, but the CPU time will only increase in the order of 10%.

For tuning of the program to a given installation two parameters `mby` and `mbz` can be set in **par.f**. This has the greatest impact on performance if the storage of the main data is out of core. For large in-core simulations `mby`=`mbz`=1 will generally give good performance. Note that `nz` must be divisible by `mbz`.

If the three dimensional storage is in the core the value of `mby` and `mbz` affects only the vector lengths. The basic vector length is `nxp/2*(mby-1)+nx/2` in most of step 2 (where `nxp` is equal to `nx` without x-dealiazing and `nx*3/2` with x-dealiazing, and `nz*mby` in the x-transform, multiply the latter by 1.5 for z-dealiazing and multiply by 0.5 and add 1 for z-symmetry. The vector length in step 3 is `nx/2*mbz`. If these values are lower than what is needed to get a good performance, `mby` and `mbz` can be increased.

If the three dimensional storage is out of core it is important to keep the record length, `nx*mby*mbz*npreal` bytes (where `npreal` is the number of bytes used to store a real number, in communication with the main storage file as large as

possible. Since increasing `mby` and `mbz` increases the amount of internal storage, this is preferably done by balancing the amount of storage needed for step 2 and step 3, cf. above. A suggestion is to put `mby`=`mbz`=2 and see if this gives an acceptable performance in terms of wall time/CPU time. If not, they can be increased to see if this improves the situation. Note finally that nothing can be done to the finite bandwidth of the transfer between disk and processor, the program will do about 4 flops for every byte transferred between disk and processor (8 when using 4-byte reals), so it is quite likely that the program will spend a large portion of the time waiting for the disk.

The program is prepared to be coarse-grain parallelized. Step 2 and step 3 can each be divided on as many processors as there are boxes to process; typically this is no limitation. There are directives for several compilers inserted before the loops 2 and 3, these may have to be replaced for compilers not previously used. To achieve parallelization `nproc` in **par.f** should be set to the number of processors to be used. Then all subroutines have to be compiled as recursive, i.e. with dynamic local storage. In addition a parallelizing option has to be added to the compile statement for the main program. The code has been run in parallel mode on the Alliant FX-80 and FX-2800, the SGI Powerstation, Challenge and Power Challenge, the CRAY-2, J90 and C90. The typical speed-up is 3.5-3.8 for four processors.

A slightly different version of the code has been implemented on various computers with distributed memory, such as IBM SP2 and CRAY T3E. The communications between the processors are handled with the Message-Passing Interface (MPI). The efficiency has been tested and is reported in Alvelius & Skote (2000).

4.5. *Post processing*

4.5.1. *Post processing velocity files with* **pre** *and* **ritpre**

The program **pre** generates a pressure field from a velocity field. The pressure can be examined with the program **ritpre** in the same way a velocity field is post processed with **rit**.

4.5.2. *Post processing velocity files with* **rit**

The program **rit** generates various graphs from a velocity field file. The graphs can be generated in either Tektronix 4014 format or Postscript. There is also a possibility to produce black and white portable pixel maps (ppm). When executed, **rit** prompts for an input file name. The file is read and the program offers a choice of various types of graphs. It is mainly intended for interactive execution and should be self explanatory.

It is possible to use **rit** in a batch environment by compiling it into a input program. This is run interactively to produce a file **ritin**, which is subsequently read by the batch code to produce the desired plots. Note that if plots in batch mode are produced 'to the screen' the resulting Tektronix graphic characters will be written to the log file. To compile a batch program, set `imode` to 2 in the **rit.f** file and compile a second time with `imode`=3 to get an input program. To get an interactive program `imode` should be left at 1.

4.5.3. *Post processing velocity files with* **cmp**

The program **cmp** is used for subtracting and adding different velocity fields. This is useful when comparing velocity fields.

4.5.4. *Post processing plane files with* **rps**

Planes saved during a simulation can be examined with the program **rps**.

4.5.5. *Post processing velocity files with* **fou**

When a number of velocity fields has been saved during a simulation, the program **fou** can be used to make Fourier transforms in both time and space.

4.5.6. *Postprocessing amplitude files with* **pamp1**, **pamp2**, **pampw**, **pampw**, **pampw2** *and* **pext1**

The programs **pamp1** and **pamp2** can be used to produce plots of the time history of various amplitudes from the amplitude files by written **bla**. **pamp1** works on one file and **pamp2** can plot one quantity from multiple files. **pext1** makes plots of time histories of extremum values (i.e. min and max values) of velocities and vorticities and the location of extrema. **pampw** and **pampw2** similarly plot amplitudes of wave components (streamwise-spanwise Fourier mode) from one or multiple wave-amplitude files. The programs are intended to be self explanatory and prompt for input file names. Since the amplitude files are formatted and normally relatively small, no batch versions of these programs are available. The files contain no headers so that files from sequential runs of one flow case can be concatenated and then plotted to show the complete evolution of the amplitudes.

4.5.7. *Postprocessing xy-statistics files with* **pxyst**

To get good statistics of space developing flows with one homogeneous direction (spanwise), the data needs to be averaged in time. The plotting of time and spanwise averaged data saved to file is performed by **pxyst**. Note that these files have headers, and thus cannot be concatenated together. The statistics in

different files can be added together by the program **addxyst**. The format of the statistics files is given in section 5.9 below.

pxyst generates plots both of the raw statistical data and of a number of derived quantities. It is also possible to generate various special plots of the mean flow, such as boundary layer thicknesses and skin friction.

There is an initial option to filter data, which applies to the raw data, before computing other quantities. There is also an option to filter data prior to producing plots, the filter is then applied to the derived quantity. The results of the two filtering processes may differ. In both cases the filter is applied in the streamwise direction.

5. File formats

These are the input/output files used by the programs. For the format of the external main storage file see section 3.2.2 above.

5.1. **bls.i** *file*

bls.i is formatted and sequential. Comments can be put after data on lines not containing character input. All input is non-dimensionalized with the displacement thickness at $x = 0$, $t = 0$ and the free-stream velocity at $x = 0$, $t = 0$. For more explanations see section 4.2. Contents line by line :

1. `namnin` Optional input velocity field file name; character*32.

As an option the base flow can instead be given in the form of an input velocity field file.

2. `namnut` Output velocity file name; character*32.

3. `re` The Reynolds number (based on the units above); real.

4. `xlb` The length of the computational box; real.

5. `h2` The height of the computational box; real.

6. `zlb` The width of the computational box; real.

The dimension of the simulation box in all three dimensions must be given. The streamwise extent of the box must for spatially developing flows include the length of the fringe region, which is typically set to 30-100 displacement thicknesses. The vertical extent of the box must include the whole boundary layer. Depending on the choice of free-stream boundary condition, the box may include only the boundary layer or a few times more. The sufficiency of the box height may be investigated through numerical experiments.

7. `fltype` Type of flow (-2 temporal Falkner-Skan-Cooke, -1 temporal Falkner-Skan, 3 temporal Blasius BL, 6 spatial Blasius BL, 7 spatial Falkner-Skan, 8 spatial Falkner-Skan-Cooke, 9 spatial parallel Blasius/Falkner-Skan/Falkner-Skan-Cooke; integer.

8. If `fltype` = -1 or $\geq$ 7: `rlam` The acceleration exponent of the velocity in the free-stream; real.

9. If `fltype` = -2 or $\geq$ 8: `spanv` The spanwise free-stream velocity; real.

10. If `fltype` $\geq$ 6: `bstart` The x-value of the start of the blending of the base flow; real.

11. If `fltype` $\geq$ 6: `bslope` The length of base flow blending region; real.

The base flow can either be parallel or space developing. The parallel base flow is for the present version only of Blasius type and is selected by setting `fltype`=3. The space developing base flow can be either Blasius (`fltype`=6), Falkner-Skan (`fltype`=7), or Falkner-Skan-Cooke (`fltype`=8). For the two latter the acceleration exponent `rlam` for the streamwise free-stream velocity must be given (i.e. m in $U = Cx^m$). For Falkner-Skan-Cooke (swept wedge) flow the spanwise velocity in the free-stream must be specified. Note that the spanwise direction is parallel to the leading edge of the wedge for this case, and that the spanwise free-stream velocity is constant. For spatially developing flows the base flow from the upstream and the downstream end are blended in the fringe region. The start and blending length must be specified. Typically the start is given as a negative number i.e., the distance upstream of the inflow boundary where the blend starts is given. (see section 2.4)

12. `ushift` The Galilei shift velocity, =0 for no shift; real.

13. `locdi` Flag to generate a localized disturbance; logical.

13.a If `locdi` is true: `ditype` The type of disturbance , only useful values 1 to 3; integer.

13.b If `locdi` is true: `amp` The amplitude of a localized disturbance; real.

13.c If `locdi` is true: `theta` The rotation angle of the localized disturbance in radians; real.

13.d If `locdi` is true: `xscale` The streamwise scale of the disturbance; real.

13.e If `locdi` is true: `xloc0` Origin of the disturbance in x-direction; real.

13.f If `locdi` is true: `yscale` The wall normal scale of the disturbance; real.

13.g If `locdi` is true: `zscale` The spanwise scale of the disturbance; real.

13.h If `locdi` is true: `ipoly` The wall normal distribution of the disturbance, only useful values 1 to 4; integer.

The `ditype` determines the type of disturbance. See **bls.i** for more information. The example below is for `ditype` set to 1.

The localized disturbance is governed by the amplitude, the rotation angle, the length and spanwise scale. The rotation angle is the angle by which the spanwise symmetric disturbance is rotated about the y-axis. The x-scale and the z-scale of the disturbance are given to be applied to the disturbance before rotation. The form of the disturbance is in a coordinate system aligned with disturbance:

$$\begin{aligned} u' &= 0 \\ v &= -\frac{\partial \psi}{\partial z} \\ w' &= -\frac{\partial \psi}{\partial y} \\ \psi &= amp \frac{x'}{x_{scale}} \frac{z'}{z_{scale}} p(\frac{y}{y_{scale}}) e^{-(\frac{x'}{x_{scale}})^2 - (\frac{z'}{z_{scale}})^2} \end{aligned} \tag{99}$$

where $p(s)$ is determined by `ipoly`, see **bls.i**. The relation between the disturbance aligned velocities and coordinates (with $'$) and the computational box aligned ones is :

$$x = x' \cos(theta) + z' \sin(theta) \tag{100}$$

$$z = -x' \sin(theta) + z' \cos(theta) \tag{101}$$

$$u = w' \sin(theta) \tag{102}$$

$$w = w' \cos(theta) \tag{103}$$

14. `waves` Flag to generate a pair of oblique waves; logical.

14.a If `waves` is true: `energy` Energy density of the waves; real.

14.b If `waves` is true: `ystart` The lowest y-value of non-zero wave amplitude; real.

14.c If `waves` is true: `yend` The largest y-value of non-zero wave amplitude; real.

14.d If `waves` is true: `yrise` The switch distance from zero to max wave amplitude; real.

14.e If `waves` is true: `yfall` The highest y-value of non-zero wave amplitude; real.

14.f If `waves` is true: `walfa` Streamwise wave number of the waves; real.

14.g If `waves` is true: `wbeta` Spanwise wave number of the waves; real.

15. `os` eigen modes flag, `.true.` for use of tabulated eigen modes; logical.

16. `noise` noise flag, `.true.` for noise; logical.

16.a If `noise` is true: `ed` The mean energy density of the noise; real.

16.b If `noise` is true: `nxn` The maximum streamwise wavenumber of the noise, should be $\leq$ `nx`/2; integer.

16.c If `noise` is true: `nyn` The number of vertical Stokes modes in the noise, should be even, $<$ `ny*2/3`; integer.

16.d If `noise` is true: `nzn` The maximum spanwise wavenumber of the noise, should be odd, $<$ `nz`; integer.

16.e If `noise` is true: `seed` A random number seed in the range -700000 to -1; integer.

The noise is in the form of Stokes modes, i.e., eigenmodes of the flow operator without the convective term. These fulfill the equation of continuity and the boundary condition of vanishing velocity at the lower and upper boundaries. Although the actual boundary condition may allow a non-zero amplitude at the free-stream boundary the restriction of zero amplitude for the noise doesn't have a large impact in practise.

The noise can be switched on by a flag in the input file. If noise is used the mean energy density must be given along with the number of wave numbers to be randomized for each direction. In the wall normal direction the number of Stokes modes to be randomized is given. The same noise will be generated for the same setting of this seed, if the physical size of the simulation box is unchanged. In particular the resolution can be changed without affecting the noise, as long as the number of grid points is sufficient to resolve the noise modes. This is useful for convergence studies.

5.2. **bla.i** *file*

bla.i is formatted and sequential. Comments can be put after data on lines not containing character input. For more explanations see section 4.4. Contents line by line :

1. `namnin` Input velocity file name; character*32.

2. `namnut` Output velocity file name; character*32.

3. If `pressure` in **par.f** is 1: `namnutp` Output pressure file name; character*32.

4. `tmax` The final time to which to simulate; real.

5. `maxit` The maximum number of iterations to simulate; integer.

6. `cpumax` The maximum CPU time in seconds; real.

The input and output file names and the final time `tmax` determine the scope of the simulation, in addition setting the maximum number of iterations puts a limit on the number of iterations to be taken through the main time step loop. The latter parameter is useful with variable time stepping in a batch environment to ensure that the execution terminates before running out of execution time. If the maximum number of iterations is used before the final time is reached the execution will terminate normally by saving the present velocity field to the output velocity file. Note that for RK3 a time step consists of three or four iterations. The execution will only stop after completing an integer number of physical time steps. If adaptive time stepping is used the program will adjust the final four time steps so that it reaches exactly the final time. You can also control maximum execution time in CRAY systems by giving the maximum CPU time for batch job so that it terminates by `cpumax`. You just give a very big number if you do not need to control maximum execution time.

7. `dt` The time step length; real.

`dt` is the length of the time step, if it is set ≤ 0 the adaptive time stepping is used. The time step is regulated to keep the CFL number close to `cflmax`, which is set to $0.9\sqrt{3}$ for the three stage Runge-Kutta and $0.9\sqrt{8}$ for the four stage Runge-Kutta. When using a fringe region the time step is also limited by the numerical stability for the damping term, this is $1.75/$`fmax` for the three stage RK and $1.96/$`fmax` for the four stage RK (`fmax` is the max strength of the fringe region, see below). If `dt` is set < 0 then $-$`dt` is used as an additional limit on the variable time step.

8. `nst` The number of stages in the time discretization; integer (3 three stage Runge-Kutta, 4 four stage Runge-Kutta).

`nst` selects between the different formulas for the explicit time discretization. The 4 stage Runge-Kutta method is about 20% more efficient than the 3 stage version.

9. `xl` The new box length. If lower than the old length, the old value will be used; real.

10. `varsiz` Flag to allow read of a file of different size than the code is compiled for; logical.

If `varsiz` is set true the program may start from an input field of a different resolution than the program is compiled for. The spectral coefficients are

ibc	BC at free-stream boundary
0	$u = v = w = 0$
1	$Du = Dv = Dw = 0$
2	$D^2u = D^2v = D^2w = 0$
3	$D^3u = D^3v = D^3w = 0$
10	$Du + ku = Dv + kv = Dw + kw = 0$
11	$D^2u + kDu = D^2v + kDv = D^2w + kDw = 0$
12	$D^3u + kD^2u = D^3v + kDv = D^3w + kD^2w = 0$
20	$Dv + kv = D^2v + kDv = \omega = 0$
100	$u = U, v = V, w = W$
101	$Du = DU, Dv = DV, Dw = DW$
110	$Du + ku = DU + kU, Dv + kv = DV + kV, Dw + kw = DW + kW$
120	$Dv + kv = DV + kV, D^2v + kDv = D^2V + kDV, \omega = 0$
130	$u = U, Du = DU, w = W$
140	$u = U, v = dDV, w = W$
150	$u = U, Du - vx = 0, Dw = 0$

TABLE 2. Free-stream boundary conditions. u, v, w are the solution velocities. U, V, W are the base flow velocities. D is the velocity derivative normal to the boundary, k is the modulus of the horizontal wavenumber ($k^2 = \alpha^2 + \beta^2$).

padded with zeroes or truncated to achieve a spectrally accurate interpolation. However, the resolution cannot be reduced in the normal direction as the truncated field in general will not fulfill the equation of continuity and the boundary conditions.

11. `rot` The rotation rate, 0. for no rotation ; real.

`rot` is the angular velocity of the coordinate frame around the z-axis. For non-rotating flows it should be set to zero.

12. `ibc` The boundary condition number; integer.

`ibc` is the number of the free-stream boundary condition. The implemented boundary conditions are given in table 2. See also section 2.2 above. A number of these boundary conditions makes the numerical scheme unstable. Among the stable boundary conditions , the most used are number 101 and 110.

13. `cim` Flag to use chebyshev integration method. If false the tau method is used; logical.

14. If `cim` is true: `icorr` Flag to use integration correction; logical.

`icorr` is a flag to use integration correction. The combination of using integration correction and boundary conditions other than of Dirichlet type may lead to numerical instability. The flag is normally set false.

15. `gall` Flag to compute and use a Galilei transformation to increase max stable time step; logical.

16. `spat` Flag to perform spatial simulation; logical.

`spat` turns on spatial simulations, if it is set false the program performs a temporal simulation. For spatial simulations a number of parameters specifying the fringe region must be given, see section 2.4 above.

17. If `spat` is true: `tabfre` Flag to use a tabulated free-stream velocity; logical.

To use a tabulated free-stream velocity the flag `tabfre` is set true. The format of the free-stream velocity file is given in section 5.10 below.

18. If `spat` and `tabfre` are true: `namfre` Name of file containing free-stream velocity table; character*32.

19. If `spat` is true: `rbfl` Flag to use a 3-d flow field as a base flow; logical.

To use a 3-d flow file to define the base flow the flag `rbfl` is set true. The format of the 3-d flow file is given in section 5.3 below.

20. If `spat` and `rbfl` are true: `nambfl` Name of file containing a 3-d base flow; character*32.

21. If `spat` is true : `fmax` Maximum strength of the fringe region; real.

22. If `spat` is true : `fstart` x-position of the start of the fringe region; real.

23. If `spat` is false : `fend` x-position of the end of the fringe region; real.

24. If `spat` is true : `frise` The distance from the start of the fringe region to the first point of maximum damping; real.

25. If `spat` is true : `ffall` The distance from the last point of maximum damping to the end of the fringe region; real.

26. If `spat` is true : `ampob` The amplitude of oblique waves forced in the fringe; real.

A pair of oblique waves can be generated in the fringe region by setting `ampfw` non-zero. The format of the waveform file **wave.d** is given in section 5.11.

27. If `spat` is true : `amp2d` The amplitude of two dimensional T-S wave forced in the fringe; real.

28. If `spat` is false : `cdev` The reference speed for the parallel boundary layer growth; real.

For temporal simulations `cdev` must be set to the reference speed of the boundary layer growth, see section 2.3 above.

29. `loctyp` to generate a localized volume force disturbance; integer.

`loctyp` can take values from 1 to 5. Various disturbances can be created. See **locf** for more information. The different values of `loctyp` each require a distinct number of parameters in the file **bla.i**, see **rparambl** for more information. As an example, a localized volume force disturbance to generate wave packets is created by setting `loctyp` to 1. The following parameters (28.a-i) are required if `loctyp` is 1. Different parameters are needed when `loctyp` is 2, 3, 4 or 5. This is explained in **rparambl** and **locf**.

29.a If `loctyp` is 1 : `ampx` Max amplitude of the localized volume force disturbance in x-direction; real.

29.b If `loctyp` is 1 : `ampy` Max amplitude of the localized volume force disturbance in y-direction; real.

29.c If `loctyp` is 1 : `ampz` Max amplitude of the localized volume force disturbance in z-direction; real.

29.d If `loctyp` is 1 : `xscale` Length scale of the localized volume force disturbance in x-direction; real.

29.e If `loctyp` is 1 : `xloc0` Origin of the localized volume force disturbance in x-direction; real.

29.f If `loctyp` is 1 : `yscale` Length scale of the localized volume force disturbance in y-direction; real.

29.g If `loctyp` is 1 : `zscale` Length scale of the localized volume force disturbance in z-direction; real.

29.h If `loctyp` is 1 and `zscale` < 0 : `lskew` The obliqueness of waves of the localized volume force disturbance; real.

29.i If `loctyp` is 1 : `tscale` Time scale of the localized volume force disturbance; real.

If `loctyp` is 1, the form of the localized disturbance is:

$$\begin{bmatrix} F_1 \\ F_2 \\ F_3 \end{bmatrix} = \begin{pmatrix} amp_x \\ amp_y \\ amp_z \end{pmatrix} e^{-(y/y_{scale})^2} g(x,z) f(t), \tag{104}$$

where

$$\begin{aligned} z_{scale} > 0 \quad g(x,z) &= e^{-[(x-x_{loc0})/x_{scale}]^2 - (z/z_{scale})^2} \qquad (105) \\ z_{scale} < 0 \quad g(x,z) &= \cos(2\pi(z - x_{lskew})/z_{scale}) e^{-}[(x - x_{loc0})/x_{scale}]^2, \end{aligned}$$

and

$$\begin{aligned} t_{scale} > 0 \quad f(t) &= e^{-(t/t_{scale})^2} \\ t_{scale} < 0 \quad f(t) &= S(-t/t_{scale})) \\ t_{scale} = 0 \quad f(t) &= 1, \end{aligned} \tag{106}$$

and

$$S(x) = \begin{cases} 0 & x \le 0 \\ 1/[1+\exp(\frac{1}{x-1}+\frac{1}{x})] & 0 < x < 1 \\ 1 & x \ge 1 \end{cases} . \tag{107}$$

30. `tripf` Flag to generate a random "sandpaper" volume force trip strip; logical.

30.a If `tripf` is true : `tamps` Max stationary amplitude of the trip; real.

30.b If `tripf` is true : `tampt` Max time varying amplitude of the trip; real.

30.c If `tripf` is true : `txsc` x length scale of the trip; real.

30.d If `tripf` is true : `tx0` x origin of the trip; real.

30.e If `tripf` is true : `tysc` y length scale of the trip; real.

30.f If `tripf` is true : `nzt` Number of z Fourier modes in the trip; integer.

30.g If `tripf` is true : `tdt` Time interval between change of the time dependent part of the trip; real.

30.h If `tripf` is true : `seed` Negative number in the range -700000 to -1 to initialize the random number generator for the trip ; integer.

`tripf` is a flag to enable forcing of a volume force trip strip at the wall running in the spanwise direction. The trip can be used to generate turbulence or at lower amplitude levels to test the stability of a boundary layer or flow structure. The trip has a steady amplitude `tamps`, and a time dependent amplitude `tampt` which allow both steady and time varying trips to be generated. The volume force has one continuous time derivative and is independent of the time discretization. The random numbers are generated such that if the random number `seed` and other trip parameters are unchanged, the same trip forces are generated. This is true even if the simulation is split into two or more runs. For every run beyond the first the random number generator is run forward to the correct state. The form of the volume force, which is directed normal to the wall, is as follows :

$$F_2 = \exp[((x - t_{x0})/t_{xsc})^2 - (y/t_{ysc})^2]f(z,t), \tag{108}$$

where

$$f(z,t) = t_{amps}g(z) + t_{ampt}[(1 - b(t))h^i(z) + b(t)h^{i+1}(z)], \tag{109}$$

and

$$\begin{aligned} i &= \mathrm{int}(t/t_{dt}), \\ b(t) &= 3p^2 - 2p^3, \\ p &= t/t_{dt} - i. \end{aligned} \tag{110}$$

$g(z)$ and $h_i(z)$ are Fourier series of unity amplitude with `nzt` random coefficients.

31. `wbci` Boundary conditions at wall; integer.

`wbci` can be set to 0, 1, 2 or 3. If `wbci` is not equal to zero, additional parameters must be provided. See **rparambl** and **cwallbc**. The example below is for `wbci` set to 1.

31.a If `cwallbc` is 1 : `amp` Max amplitude of the localized blowing/suction; real.

31.b If `cwallbc` is 1 : `damp` Damp amplitude. No effect if less than one; real.

31.c If `cwallbc` is 1 : `xstart` Start position of disturbance; real.

31.d If `cwallbc` is 1 : `xend` End position of disturbance; real.

31.e If `cwallbc` is 1 : `xrise` Rise length of disturbance; real.

31.f If `cwallbc` is 1 : `xfall` Fall length of disturbance; real.

31.g If `cwallbc` is 1 : `zbet` Spanwise variation; real.

31.h If `cwallbc` is 1 : `tomeg` Time variation; real.

The blowing and suction at the wall is implemented in **cwallbc**. The form of the boundary condition below is for `wbci` set to 1.

$$v|_{y=0} = amp \cdot f(x) \cdot cos(zbet \cdot z) \cdot sin(tomeg \cdot t), \tag{111}$$

where

$$f(x) = S\left(\frac{x - x_{start}}{x_{rise}}\right) - S\left(\frac{x - x_{end}}{x_{fall} + 1}\right), \tag{112}$$

and $S(x)$ is given by equation (107).

32. `icfl` Number of time iterations between calculation of the CFL number; integer.

`icfl` is the calculation interval for the CFL number. If the CFL number is computed each iteration this adds a few percent to the execution time, but since it is used to regulate the time step it should not be computed too sparsely, preferably every complete time step, i.e. `icfl` = `nst`.

33. `iamp` Number of time iterations between calculation of rms amplitudes; integer.

33.a If `iamp` > 0 : `namamp` Output file for rms amplitudes; character*32.

`iamp` is the interval for evaluation of the amplitude. As for the CFL number continuous calculation of the amplitude costs a number of percent in execution speed. If `iamp`=0 no amplitudes will be calculated and no amplitude file will be written. To get the correct time accuracy `iamp` should be an integer multiple of `nst`.

34. `longli` Flag to generate amplitude for each horizontal plane (y-value). Applies both to rms amplitudes (items 46-47) and wave component amplitudes (items 58-60).

`longli` is set true the program will produce y-dependent statistics and write these to the amplitude files, both for the global statistics and statistics by wavenumber. The statistics files can become quite long if the flag is set true.

35. `iext` Number of time iterations between calculation of extremum amplitudes; integer.

`iext` is the interval for evaluation of the extremum values and their coordinates. This evaluation is somewhat more time consuming than that for the amplitudes. If `iext`=0 no extremum amplitudes will be calculated. To get the correct time accuracy `iext` should be an integer multiple of `nst`.

35.a If `iext` > 0 : `namext` Output file for extremum amplitudes; character*32.

36. `ixys` Number of time iterations between calculation of xy-statistics; integer.

`ixys` is the interval for evaluation of xy-statistics, used by **pxyst**. The statistics generated and the output file format are described in section 5.9. The file is written to every `ixyss` iterations, overwriting older data. To get the correct time accuracy `ixys` should be an integer multiple of `nst`.

36.a If `ixys` > 0 : `namxys` Output file for xy-statistics; character*32.

36.b If `ixys` > 0 : `ixyss` Number of time iterations between saving of xy-statistics data to file; integer.

36.c If `ixys` > 0 : `txys` Time to start accumulation of xy-statistics; real.

37. `msave` The number of complete intermediate velocity fields to be saved. If non-zero, items a and b are repeated for each file; integer.

37.a If `msave`> 0 : `tsave` The time for which to save an intermediate field; real.

37.b If `msave`> 0 :`nmsave` The name of the intermediate velocity file; character*32.

`msave` is the number of intermediate velocity fields to be saved, maximum 20. If higher than zero the times and names of the files to be saved must be given. If the time stepping is adaptive the program automatically adjusts the time step to reach exactly the desired times. For fixed time step the save is done at the nearest time.

38. `mwave` The number of wavenumbers to save amplitudes for. If non-zero, item b is repeated for each wavenumber; integer.

38.a If `mwave`> 0: The name of the wave amplitude file; character*32.

38.b If `mwave`> 0: `kx`,`kz` The streamwise wavenumber as multiples of the fundamental $2\pi/x_L$, the spanwise wavenumber as multiple of the fundamental $2\pi/z_L$; both integers.

`mwave` sets the number of specific wavenumbers to calculate amplitudes for. For each wave, the x and z wavenumbers must be specified as integers to be multiplied by $2\pi/x_L$ and $2\pi/z_L$ respectively. The wavenumbers are counted in the physical way for positive and negative `kz` and `kx` zero and up, not in the way of the internal storage. The wave amplitudes are calculated for each of the six velocities and vorticities at intervals set by the `iamp` value.

39. `npl` The number of planes to be continuously saved during the simulation. If non-zero, items b through e are repeated for each plane; integer.

39.a If `npl` > 0: `ipl` The saving interval for planes in number of iteration; integer.

39.b If `npl` > 0: `tpl(i,1)` The type of plane to be saved. 1 for xy,2 for xz; integer.

39.c If `npl` > 0: `tpl(i,2)` The variable to be saved, i.e. 1 for u, 2 for v, 3 for w; integer.

39.d If `npl` > 0: `cpl` The coordinate for which to save the plane; real.

39.e If `npl` > 0: `nampl` The name of the file in which to save the planes; character*32.

`npl` is the number of 2d planes to be saved every `ipl` iterations during the simulation. To get the correct time accuracy `ipl` should be an integer multiple of `nst`. It is these files which are used by **rps** for plotting, the format is described in section 5.8 below.

5.3. *Velocity file*

Format of a 3-d uncompressed velocity file. The format is used for any 3-d input or output from **bls** and **bla**. The file is unformatted, sequential.

Record 1: Reynolds number; real, `.false.` (this is to be backward compatible with channel flow files); logical, x_L; real, z_L; real, the time for this field; real, the length by which the box has been shifted to the right since time zero; real.

Record 2: Number of spectral modes in the x-direction; integer, the number of points in the physical y-direction; integer, the number of spectral modes in the z-direction reduced for symmetry; integer, 0/1 no z-symmetry/z-symmetry; integer.

Record 3: Flow type `fltype`; integer, displacement thickness expressed in half box heights `dstar`; real.

Record 4: If `fltype` ≥ 4 : start of blending region `bstart`, end of blending region `bslope`, if `fltype` ≥ 7: acceleration exponent of streamwise free-stream velocity `rlam`, spanwise free-stream velocity `spanv`. For other values of `fltype` this record is omitted.

Record 5: The u, v, w-velocities in Fourier x, z and physical y space. One record contains `nx`/2 complex coefficients in normal Fortran format. The records are stored in `y`, `z`, `i` order with `y` varying the fastest and `i` the slowest. The number of points in the y-direction is `nyp` and the number in the z-direction `nzc`. Total number of records `nyp*nzc*3`.

5.4. *Pressure file*

Format of a 3-d uncompressed pressure file. The format is the same as for the velocity file, except the last record which contains only the pressure.

5.5. *Amplitude file*

Formatted, sequential. The rms-levels are an average over the physical box. For each time three records are saved:

1. Time; real, u_{rms}; real, v_{rms}; real, w_{rms}; real.

2. χ_{rms}; real, ω_{rms}; real, ϑ_{rms}; real,ω^2/k^2; real.

3. $DUuv$; real, energy for wavenumber zero; real, h^+, i.e. the box half-height in wall units; real.

if `longli` is `.true.` then for each time the above is followed by statistics by y-plane in descending y-coordinate order as follows :

4. mean squared streamwise velocity without Blasius base flow; real, mean squared normal velocity ; real, mean squared spanwise velocity ; real, mean squared streamwise vorticity ; real, mean squared normal vorticity ; real, mean squared spanwise vorticity without Blasius base flow ; real, mean squared vorticity squared over wavenumber square average, no (0,0); real, Reynolds stress

average; real, mean streamwise disturbance velocity squared; real, mean spanwise disturbance velocity squared; real.

5.6. *Wave amplitude file*

Formatted, sequential. The data in this file is in internal scaling. For each time are saved:

1. Time; real, number of waves saved; integer, number of points in the y-direction; integer, Reynolds number; real, fundamental wavenumber in the x-direction; real, fundamental wavenumber in the z-direction; real, flag `longli`.

2. The wavenumber α as multiples of the fundamental $2\pi/x_L$; integer, the wavenumber β as multiple of the fundamental $2\pi/z_L$; integer, u_{rms}; real, v_{rms}; real, w_{rms}; real, ω_{rms}; real.

Item 2 is repeated for each wave.

if `longli` is `.true.` then for each time the above is followed by statistics by y-plane in descending y-coordinate order as follows :

3. if the wavenumber is zero : $\hat{u}$ for each y-plane (with the imaginary part zero), otherwise $\hat{v}$ for each y-plane; complex.

4. if the wavenumber is zero : $\hat{w}$ for each y-plane (with the imaginary part zero), otherwise $\hat{\omega}$ for each y-plane; complex.

Item 3 and 4 are repeated for each wave.

5.7. *Extremum file*

Formatted, sequential. For each time are saved:

1. Time; real.

2. Min $u - U_{laminar}$; real, x-coordinate for this minimum; real.

3. y-coordinate; real, z-coordinate; real.

4. and 5. same for min v

6. and 7. same for min w

8. and 9. same for min χ

10. and 11. same for min ω

12. and 13. same for min ϑ

14. and 15. same for min $\vartheta - \vartheta_{laminar}$

16. through 29. same as 2. through 15. but for maximum

5.8. *Plane velocity file*

Unformatted, sequential.

Record 1: Reynolds number; real, `.false.` (this is to be backward compatible with channel flow files); logical, x_L; real, z_L; real, the time for this field; real, the length by which the boxed has been shifted to the right since time zero; real.

Record 2: Number of spectral modes in the x-direction; integer, the number of points in the physical y-direction; integer, the number of spectral modes in the z-direction reduced for symmetry; integer, 0/1 no z-symmetry/z-symmetry; integer.

Record 3: The type of plane, 1 for xy,2 for xz; integer, the variable number, i.e., 1 for u, 2 for v, 3 for w; integer, the coordinate of the plane; real, flow type `fltype`; integer, displacement thickness expressed in half box heights; real.

Record 4: Time; real, the length by which the boxed has been shifted to the right since time zero; real.

Record 5: The velocity array in physical space; x-y-planes are `nx`×`nyp` with `x` varying the fastest; x-z-planes are `nx`×`nz` for the non-symmetric case and `nx`×`(nz/2+1)` for the symmetric case with `x` varying the fastest.

Record 4-5 are repeated for each time when the plane is saved.

5.9. *xy-statistics file*

Unformatted, sequential.

Record 1: Reynolds number; real, `.false.` (this is to be backward compatible with channel flow files); logical, x_L; real, z_L; real, the time for this field; real, the length by which the boxed has been shifted to the right since time zero; real.

Record 2: Number of spectral modes in the x-direction; integer, the number of points in the physical y-direction; integer, the number of spectral modes in the z-direction reduced for symmetry; integer, 0/1 no z-symmetry/z-symmetry; integer.

Record 3: Flow type `fltype`; integer, displacement thickness expressed in half box heights; real.

Record 4: If `fltype` ≥ 4 : start of blending region `bstart`; real , end of blending region `bslope`; real , if `fltype` ≥ 7 acceleration exponent of streamwise free-stream velocity `rlam`; real, spanwise free-stream velocity `spanv`; real. For other values of `fltype` this record is omitted.

Record 5. Sum of the length of the time steps at which statistics have been sampled `sumw`; real, number of statistics calculated `nxys`; integer.

Record 6-5+`nxys`. Each record contains a `nx` $\times$ `nyp` plane of statistics with the x-index varying the fastest. The statistics are averaged over time and the z-direction.

Record 6-11 u, v, w, u^2, v^2, w^2.

Record 12-17 $\omega_1, \omega_2, \omega_3, \omega_1^2, \omega_2^2, \omega_3^2$

Record 18-20 uv, uw, vw

Record 21-23 $u(x)u(x+1), v(x)v(x+1), w(x)w(x+1)$ (i.e. one point separation auto correlations, x counted cyclically).

Record 24-26 $u(y)u(y+1), v(y)v(y+1), w(y)w(y+1)$

Record 27-29 $u(z)u(z+1), v(z)v(z+1), w(z)w(z+1)$ (z counted cyclically)

Record 30 $R\epsilon_{11} = u_x^2 + u_y^2 + u_z^2$, ϵ_{ij} is the dissipation tensor

Record 31 $R\epsilon_{22} = v_x^2 + v_y^2 + v_z^2$

Record 32 $R\epsilon_{33} = w_x^2 + w_y^2 + w_z^2$

Record 33 $R\epsilon_{12} = u_x v_x + u_y v_y + u_z v_z$

Record 34 $R\epsilon_{13} = u_x w_x + u_y w_y + u_z w_z$

Record 35 $R\epsilon_{23} = v_x w_x + v_y w_y + v_z w_z$

Record 36-47 $p, p^2, pu, pv, pw, pux, pvy, pwz, puy, pvx, upx, wpz$

5.10. *Free-stream velocity table file*

formatted, sequential

Record 1: `n` number of table entries

Record 2 - `n`+1: `xtab` streamwise coordinate; real, `utab` free-stream velocity; real.

5.11. **wave.d** *forced wave file*

formatted, sequential

Record 1: `rew` Reynolds number of wave (not used by **bla**); real.

Record 2: `alfaw` the streamwise, `betaw` the spanwise wavenumber of the wave; both real.

Record 3: `eig` the eigenvalue of the wave, the real part of which is used as the angular frequency of the wave; complex.

Record 4-`n`+3: `n` chebyshev coefficients of the mode shape of the normal velocity, of which the first `nyp` are used. If there are not enough coefficients they are padded by zeroes; complex.

5.12. **basic.i** *Base flow profile file*

basic.i is unformatted and sequential. **basic.i** is an output file from **cbflow**. **basic.i** saves the basic flow profile only for non-parallel spatial simulations if the file does not exist, or reads the basic flow profile for the same simulation parameters.

Record 1: Reynolds number; real, x_L; real, the length by which the boxed has been shifted to the right since time zero; real, displacement thickness expressed in half box heights `dstar`; real, start of blending region `bstart`, end of blending region `bslope`, acceleration exponent of streamwise free-stream velocity `rlam`, spanwise free-stream velocity `spanv`, the number of points in the physical x-direction; integer, the number of points in the physical y-direction; integer.

Record 2: The basic u, v, w-velocities in the physical x, y space.

Acknowledgments

The authors thank The Aeronautical Research Institute of Sweden (FFA) for generous financial support during the code development.

References

Alvelius, K. & Skote, M. 2000 The performance of a spectral simulation code for turbulence on parallel computers with distributed memory. *Tech. Rep.* TRITA-MEK 2000:17. Royal Institute of Technology, Stockholm.

Bech, K. H., Henningson, D. S. & Henkes, R. A. W. M. 1998 Linear and non-linear development of localized disturbances in zero and adverse pressure gradient boundary layers. *Phys. Fluids* **10**, 1405–1418.

Berlin, S., Hanifi, A. & Henningson, D. S. 1998*a* The neutral stability curve for non-parallel boundary layer flow. In Berlin, S. 1998, Oblique waves in boundary layer transition, Ph.D. Thesis, Department of Mechanics, KTH, Stockhom, TRITA-MEK 1998:7.

Berlin, S. & Henningson, D. S. 1999 A nonlinear mechanism for receptivity of free-stream disturbances. *Phys. Fluids* **11**, 3749–3760.

Berlin, S., Kim, J. & Henningson, D. S. 1998*b* Control of oblique transition by flow oscillations. *Tech. Rep.* TRITA-MEK 1998:6. Royal Institute of Technology, Stockholm.

Berlin, S., Lundbladh, A. & Henningson, D. S. 1994 Spatial simulations of oblique transition. *Phys. Fluids* **6**, 1949–1951.

Berlin, S., Wiegel, M. & Henningson, D. S. 1999 Numerical and experimental investigation of oblique boundary layer transition. *J. Fluid Mech.* **393**, 23–57.

Bertolotti, F. P., Herbert, T. & Spalart, P. R. 1992 Linear and nonlinear stability of the Blasius boundary layer. *J. Fluid Mech.* **242**, 441–474.

Canuto, C., Hussaini, M. Y., Quarteroni, A. & Zang, T. A. 1988 *Spectral Methods in Fluids Dynamics*. Springer.

Elofsson, P. A. & Lundbladh, A. 1994 Ribbon induced oblique transition in plane poiseulle flow. In *Bypass transition - proceedings from a mini-workshop* (ed. D. S. Henningson), pp. 29–41. TRITA-MEK Technical Report 1994:14, Royal Institute of Technology, Stockholm, Sweden.

Greengard, L. 1991 Spectral integration and two-point boundary value problems. *SIAM J. Numer. Anal.* **28**, 1071–1080.

Henningson, D. S. 1995 Bypass transition and linear growth mechanisms. In *Advances in turbulence V* (ed. R. Benzi), pp. 190–204. Kluwer Academic Publishers.

Henningson, D. S., Johansson, A. V. & Lundbladh, A. 1990 On the evolution of localized disturbances in laminar shear flows. In *Laminar-Turbulent Transition* (eds. D. Arnal & R. Michel), pp. 279–284. Springer-Verlag.

Henningson, D. S. & Lundbladh, A. 1994 Transition in Falkner-Skan-Cooke flow. *Bull. Am. Phys. Soc.* **39**, 1930.

Henningson, D. S. & Lundbladh, A. 1995 Evaluation of turbulence models from direct numerical simulations of turbulent boundary layers. FFA-TN 1995-09, Aeronautical Research Institute of Sweden, Bromma.

Henningson, D. S., Lundbladh, A. & Johansson, A. V. 1993 A mechanism for bypass transition from localized disturbances in wall bounded shear flows. *J. Fluid Mech.* **250**, 169–207.

Hildings, C. 1997 Simulations of laminar and transitional separation bubbles. *Tech. Rep.*. Department of Mechanics, The Royal Institute of Technology, Stockholm, Sweden.

Högberg, M. & Henningson, D. S. 1998 Secondary instability of cross-flow vortices in Falkner-Skan-Cooke boundary layers. *J. Fluid Mech.* **368**, 339–357.

Kim, J., Moin, P. & Moser, R. 1987 Turbulence statistics in fully developed channel flow. *J. Fluid Mech.* **177**, 133–166.

Kleiser, L. & Schumann, U. 1980 Treatment of incompressibility and boundary conditions in 3-D numerical spectral simulations of plane channel flows. In *Proc. 3rd GAMM Conf. Numerical Methods in Fluid Mechanics* (ed. E. H. Hirschel), pp. 165–173. Vieweg. Braunschweig.

Kreiss, G., Lundbladh, A. & Henningson, D. S. 1994 Bounds for threshold amplitudes in subcritical shear flows. *J. Fluid Mech.* **270**, 175–198.

Lu, Q. & Henningson, D. S. 1990 Subcritical transition in plane Poiseuille flow. *Bull. Am. Phys. Soc.* **35**, 2288.

Lundbladh, A. 1993 Growth of a localized disturbance in inviscidly stable shear flow. TRITA-MEK 93-04, Royal Institute of Technology, Stockholm, Sweden.

Lundbladh, A. & Henningson, D. S. 1993 Numerical simulation of spatial disturbance development in rotating channel flow. FFA-TN 1993-30, Aeronautical Research Institute of Sweden, Bromma.

Lundbladh, A., Henningson, D. S. & Johansson, A. V. 1992*a* An efficient spectral integration method for the solution of the Navier-Stokes equations. FFA-TN 1992-28, Aeronautical Research Institute of Sweden, Bromma.

Lundbladh, A., Henningson, D. S. & Reddy, S. C. 1994*a* Threshold amplitudes for transition in channel flows. In *Transition, Turbulence and Combustion, Volume I* (eds. M. Y. Hussaini, T. B. Gatski & T. L. Jackson), pp. 309–318. Dordrecht: Kluwer.

Lundbladh, A. & Johansson, A. V. 1991 Direct simulation of turbulent spots in plane Couette flow. *J. Fluid Mech.* **229**, 499–516.

Lundbladh, A., Johansson, A. V. & Henningson, D. S. 1992*b* Simulation of the breakdown of localized disturbances in boundary layers. Proceedings of the 4th European Turbulence Conference, Delft, The Netherlands.

Lundbladh, A., Schmid, P. J., Berlin, S. & Henningson, D. S. 1994*b* Simulation of bypass transition in spatially evolving flows. Proceedings of the AGARD Symposium on Application of Direct and Large Eddy Simulation to Transition and Turbulence, AGARD-CP-551.

Malik, M. R., Zang, T. A. & Hussaini, M. Y. 1985 A spectral collocation method for the Navier-Stokes equations. *J. Comp. Phys.* **61**, 64–88.

Nordström, J., Nordin, N. & Henningson, D. S. 1999 The fringe region technique and the fourier method used in the direct numerical simulation of spatially evolving viscous flows. *SIAM J. Sci. Comp.* **20** (4), 1365–1393.

Reddy, S. C., Schmid, P. J., Bagget, P. & Henningson, D. S. 1998 On stability of streamwise streaks and transition thresholds in plane channel flows. *J. Fluid Mech.* **365**, 269–303.

Schmid, P. J. & Henningson, D. S. 1992 A new mechanism for rapid transition involving a pair of oblique waves. *Phys. Fluids A* **4**, 1986–1989.

Schmid, P. J. & Henningson, D. S. 1993 Nonlinear energy density transfer during oblique transition in plane Poiseuille flow. *Tech. Rep.* TRITA-MEK 1993:5. Royal Institute of Technology, Stockholm.

Schmid, P. J., Lundbladh, A. & Henningson, D. S. 1994 Spatial evolution of disturbances in plane Poiseuille flow. In *Transition, Turbulence and Combustion, Volume I* (eds. M. Y. Hussaini, T. B. Gatski & T. L. Jackson), pp. 287–297. Dordrecht: Kluwer.

Schmid, P. J., Reddy, S. C. & Henningson, D. S. 1996 Transition thresholds in boundary layer and channel flow. In *Advances in Turbulence VI* (eds. S. Gavrilakis, L. Machiels & P. A. Monkewitz), pp. 381–384. Kluwer Academic Publishers.

Skote, M., Henkes, R. A. W. M. & Henningson, D. S. 1998 Direct numerical simulation of self-similar turbulent boundary layers in adverse pressure gradients. *Flow, Turbulence and Combustion* **60**, 47–85.

Spalart, P. R. & Yang, K. 1987 Numerical study of ribbon induced transition in blasius flow. *J. Fluid Mech.* **178**, 345–365.

Appendix A. Release notes

This manual refers to the following programs and packages :

bla v3.3

bls v1.8

rit v1.9

pre v1.0

ritpre v1.0

rps v1.13

cmp v1.9

fou v1.4

pxyst v1.5

pamp1 v1.1

pamp2 v1.3

pampw v1.1

pext1 v1.1

dfc v1.1

dpc v1.1

plot1 v1.7

VECFFT v1.1

dclib v1.4

fsdf v1.2

This is software which is distributed free on a limited basis; it comes with no guarantees whatsoever. Problems can be reported to henning@mech.kth.se or hnd@ffa.se, but no action is promised. If results obtained by using these programs are published the authors would like an acknowledgment.

Distribution of the code is done by email using a `uuencode`ed, `compress`ed `tar` file. A complete directory structure including all of the material above can be obtained by executing the following commands on the saved mail file, preferably called `prog`

```
uudecode   prog
uncompress prog.tar.Z
tar -xf    prog.tar
```

Makefiles appropriate for compiling the codes are also included for those using the UNIX operating system.

A version of **bla** (**blap** v1.0) exists that runs on computers with distributed memory. This version is slightly different from the one described in this report, and its efficiency has been thoroughly tested by Alvelius & Skote (2000).

Appendix B. Scaling of variables

We have chosen a scaling for all parameters based on the displacement boundary layer thickness and free-stream velocity at $t = 0$, $x = 0$ for the reference or base flow. However, internally in the simulation code **bla** the implementation uses a scaling based on the half box height. (The external and internal velocity scale is the same.) This means that all external data must be rescaled when read into the program, and the reverse scaling applied on output. If we let `dstar` be the displacement thickness expressed in half box heights, then the following scaling relationships hold:

time(internal)=time(external)*dstar

length(internal)=length(external)*dstar

velocity(internal)=velocity(external)

vorticity(internal)=vorticity(external)/dstar

force(internal)=force(external)/dstar

All formatted input and output files except the wave amplitude file use external scaling, whereas the unformatted files and the wave amplitude file use internal scaling.

Appendix C. Investigation of the fringe method

In some flow cases with large growth rates, e.g. flows with adverse pressure gradients and separation bubbles, a badly chosen fringe might not offer sufficient damping. The present study aims to give guidelines to choose an optimum fringe. Three types of flow have been studied, channel flow, boundary-layer flow with zero pressure gradient and boundary-layer flow with an adverse pressure gradient.

Although this report does not contain a description of the channel flow code, we include this flow case in the fringe investigation. This is done since it makes it possible to exemplify the properties of the fringe only related to the damping of disturbances, excluding the large forcing needed to return the mean or basic flow to its required inflow state.

The main parameters deciding the damping properties of the fringe are

- Length of Fringe (L)
- Strength of Fringe (λ)
- Shape of Fringe
- Resolution
- Influence of Blending (For Boundary-Layer)

Variations in all of these parameters have been made, with the main focus on the length and strength of the fringe. The shape of the fringe, i.e. how λ is varied in the fringe region, is of some importance. To simplify the investigation and reduce the number of variables it was decided to use a fringe where the strength is gradually increased until a maximum is reached and then immediately decreased to zero. This way only two variables describe the shape of the fringe, see figure 2. Generally the rise has been three fourths of the total length and the decrease of fringe strength one fourth of the length. The maximum strength is what will be denoted with λ hereafter. The gradual change of strength of the fringe is done with a smooth step function that has continuous derivatives of all orders, equation (114). Throughout this investigation the damping has been measured as the difference in amplitude of the disturbance when going into the fringe compared with the value going out of the fringe. All calculations were continued until the disturbance had been convected through the computational domain more than once, thus ensuring that a steady state was reached.

C.1. *Channel flow*

In the channel flow calculations, a fixed physical box of length 80 $h/2$ was used and thus the length of the computational box was varied when the length of

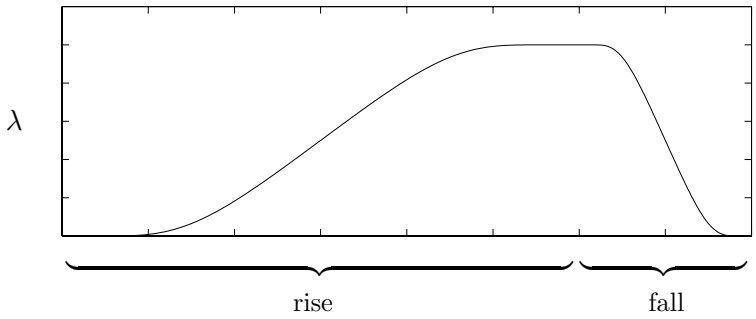

FIGURE 2. Schematic picture of the fringe used in the investigations. For this fringe the sum of the rise and fall is the same as the total length.

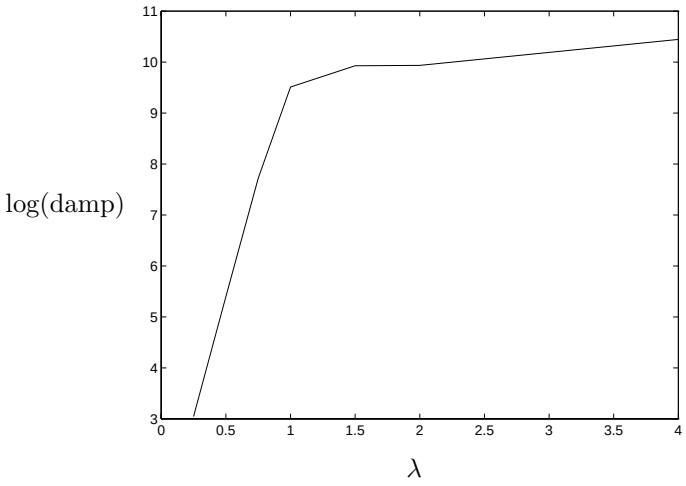

FIGURE 3. Damping as function of λ for channel flow.

the fringe changed. The Reynolds number based on the channel half height and centerline velocity was 3000 for all computations. To obtain the results shown in figures 3 and 4 a periodic volume force located at $x = 30$ with $\omega = 0.3$ has been used to introduce a disturbance that then evolved downstream. Figure 3 shows the damping as function of λ for a fixed length of the fringe. Note that the damping increases very rapidly with λ until it reaches a certain level from where further increase in damping is very modest. It is obvious that the strength integrated over the length of the fringe plays a major role of the damping. In figure 4 this is shown in a different way. Contours of the damping are plotted as function of the length and strength of the fringe region. For a given integral of the fringe region it is however advantageous to have a longer fringe with a lower λ.

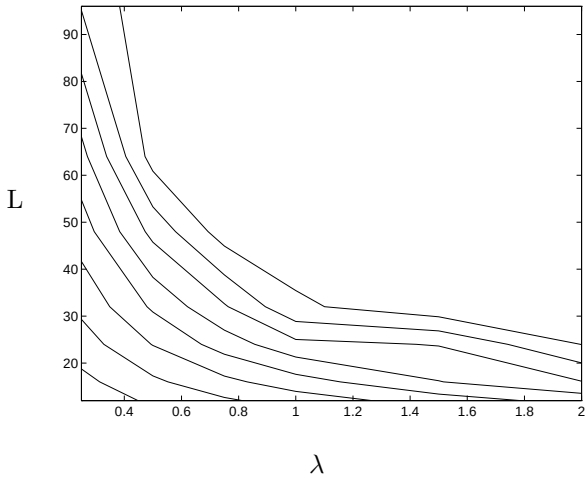

FIGURE 4. Contours of damping as function of the length of the fringe and λ. Each contour represents a magnitude of amplitude, from 2 to 9. Picture for channel flow.

In figure 5 the damping is shown as function of $\alpha = 2\pi/\sigma$, where σ is the wavelength, for three different frequencies. In all the cases the same fringe parameters have been used. The curves are obviously very close. This implies that without sufficient resolution the fringe cannot damp disturbances efficiently regardless of how well the fringe parameters are chosen. There is however an upper limit of the fringe damping regardless of the resolution. It is desirable to be close or at least know where this limit is. Based on this investigation one should strive for αdx to be approximately 0.5, i.e. $\sigma/dx = 2\pi/0.5 \approx 12.5$. This is a very high value for optimum performance of the fringe, it is however not likely that the highest frequencies are particularly amplified in other parts of the computational box and thus need the best damping. It is also possible that other parts of the flow require better resolution than the fringe, in which case the above requirement would not determine the necessary resolution.

C.2. *Boundary-Layer Flow*

In boundary-layer geometry the forcing is gradually varied from the corresponding outflow boundary-layer to the desired inflow. This variation in the forcing function is accomplished by the blending. The blending is achieved by varying the streamwise component of the velocity toward which the solution is forced according to

$$u_1^*(x,y) = U(x,y) + \Big[U(x + x_{period}, y) - U(x,y)\Big] S\left(\frac{x - x_{start}}{x_{rise}}\right), \qquad (113)$$

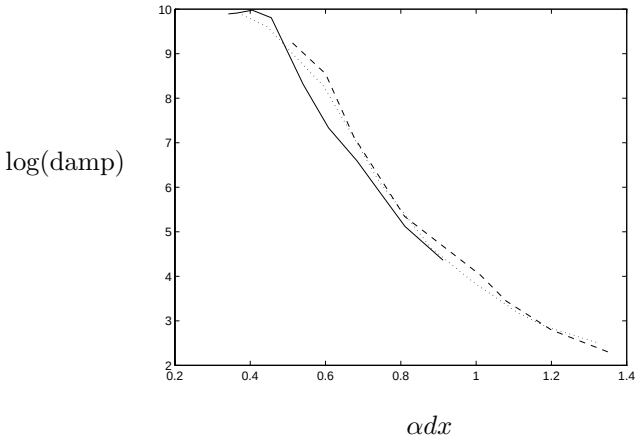

FIGURE 5. Damping as function of resolution for three different angular frequencies, $\omega = 1$ solid line, $\omega = 1.65$ dotted line and $\omega = 3$ dashed line, where $\alpha = 2\pi/\sigma$. Result for channel flow.

where $U(x, y)$ typically is a solution to the boundary-layer equations, x_{period} the streamwise length of the simulation box and

$$S(x) = \begin{cases} 0 & x \leq 0 \\ 1/[1 + \exp(\frac{1}{x-1} + \frac{1}{x})] & 0 < x < 1 \\ 1 & x \geq 1 \end{cases} . \tag{114}$$

The wall normal component of the velocity toward which the solution is forced is calculated from continuity.

Tests showed that the blending is of little importance for the damping. The blending should therefore be determined for maximum computational efficiency. If the flow is laminar or almost laminar the longest possible blending should be used, as the greatest gradients of the flow are likely to appear due to the blending, and thus regulate the finest resolution. If on the other hand the flow is turbulent, the largest gradients are usually in other parts of the domain and the resolution requirements due to the flow in the fringe are of less importance, allowing both shorter fringe and blending. It is worth noting that the profiles which the flow is forced towards are generally not solutions of the Navier-Stokes equations, rather these are usually similarity solutions of the boundary-layer equations.

For the calculations of the zero pressure-gradient boundary-layer flow a physical box of length 400 δ_0^* ($\delta_0^* = \delta^*$ at inflow) and height 10 δ_0^* was used. The Reynolds number was 1000 and the disturbance was introduced at $x = 200$ δ_0^* with $\omega = 0.1$

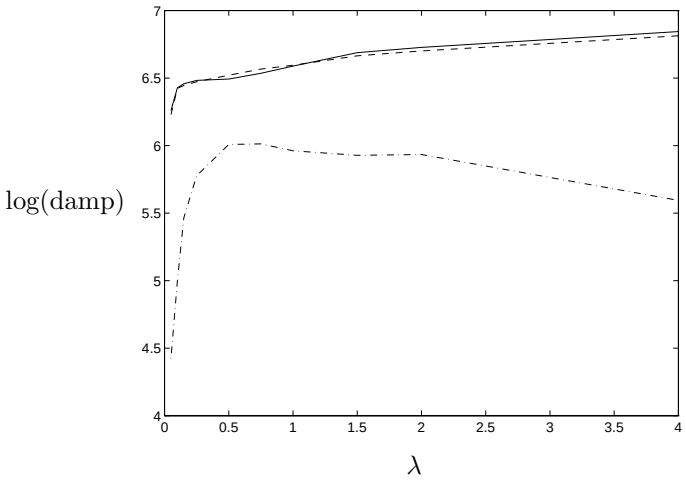

FIGURE 6. Damping as function of λ for three different boundary conditions. Solid line for bc prescribing the normal derivatives, dashed line for bc prescribing the streamwise velocity and dash-dotted line for the asymptotic condition. Length of fringe 400, with 75 % used for rise and 25 % for fall of the fringe function. Note that the damping is less than for channel flow.

For boundary-layer flow, there are differences in the fringe damping depending on the boundary condition used. Three different boundary conditions have been used in this investigation, the condition prescribing the normal derivatives, 101 in table 2, the asymptotic condition, 110 in table 2, and finally the boundary condition prescribing the streamwise velocity, 150 in table 2. In figure 6 the damping is plotted as function of λ for the different boundary conditions. The damping using the asymptotic boundary condition is somewhat less than the other two, and all three are smaller than in the channel flow calculations.

In figure 7 contours of damping are shown as function of strength and length of the fringe. The basic characteristics are the same as in the channel case. Figure 8 shows the effect of the shape of the fringe. The differences between the different cases are not large. This implies that there is only a small dependence on where the maximum strength of the fringe is reached, although the case with a very early maximum strength is the worst and should be avoided.

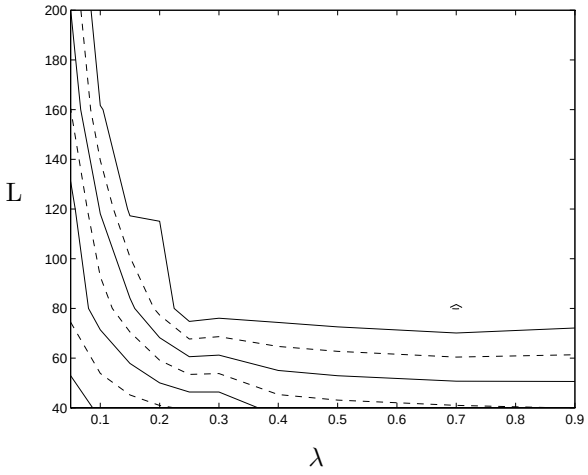

FIGURE 7. Damping as function of length of fringe and λ. Solid lines denote magnitudes of damping, from 2 to 5. The boundary condition prescribing the streamwise velocity has been used.

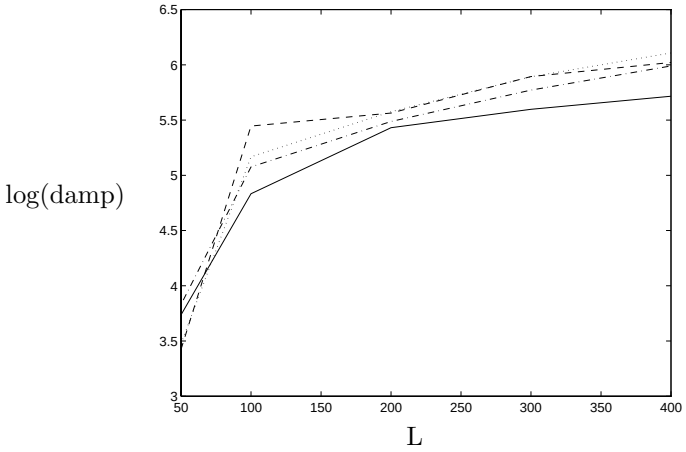

FIGURE 8. Damping as function of shape of fringe. Solid line corresponds to 25 % rise and 75 % fall. Dashed 50/50, dotted 75/25 and dash-dotted 100 % rise and zero distance for fall. The integral was held constant for the different lengths. The boundary condition prescribing the streamwise free-stream velocity, 150 in table 2, has been used.

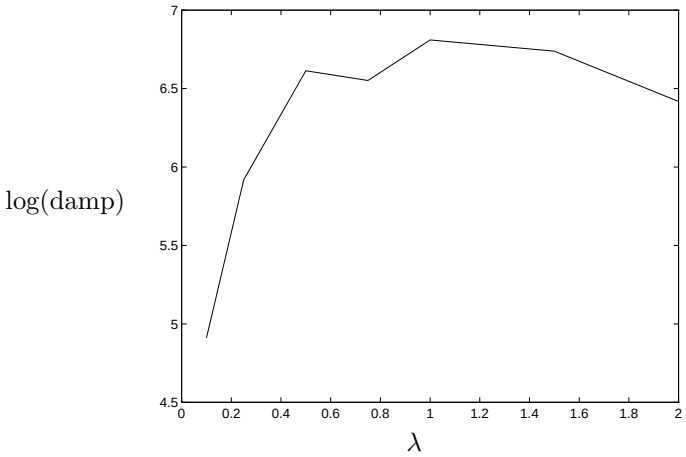

FIGURE 9. Damping as function of λ for boundary-layer flow with an adverse pressure gradient. Length of fringe was 200 δ_0^*. The boundary condition prescribing the streamwise velocity has been used.

C.3. *Boundary-Layer with Pressure Gradient*

C.3.1. *Qualities of the fringe*

For these calculations $Re_{\delta_0^*} = 1000$ and Hartree-Parameter $\beta = -0.18$ were chosen. Length of the physical part of the box was set to 200 δ_0^* and the height to 12. The blending started at the end of the physical box and used a rise distance of 100. A volume force with $\omega = 0.13$ was applied at $x = 100\ \delta_0^*$.

The main characteristics from the investigation with boundary layer flow are unchanged. However, there is now a much stronger natural amplification of disturbances. The same behavior of the damping as a function of λ as was observed for the investigation without pressure gradient is observed in figure 9. The total damping in the fringe is somewhat better than in the case without pressure gradient. In figure 10 contours of the damping are shown as function of the strength and length of the fringe. Quite surprisingly the damping deteriorates in some cases when the strength increases. The best damping is obtained with rather low values of λ.

C.3.2. *Spatial evolution of a disturbance*

The purpose of the remaining figures is mainly to show the evolution of a disturbance when it is convected through the computational box. Two different cases are studied, one without any forced disturbance and one with an introduced Tollmien-Schlichting wave. In figure 11 the frequency spectra at several

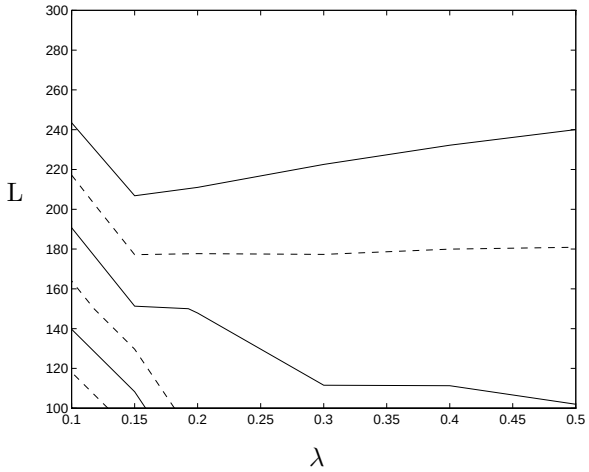

FIGURE 10. Contours of damping. Solid lines denote magnitudes of amplitude. The boundary condition prescribing the streamwise velocity has been used.

downstream positions are shown for the undisturbed case. Each curve shows the general disturbance level at the corresponding streamwise position. It is apparent that frequencies with $\omega = 0.1$ to 0.2 are the most amplified. The smallest disturbances are found at $x = 350$ and are mainly due to truncation errors. As the strength of the fringe decreases they start to grow. They reach their maximum intensity at $x = 200$, where they enter the fringe and are quickly damped. In figure 12 this evolution as well as that for the forced disturbance are shown, but only for the frequency that the TS-wave is forced with. Note that after the forcing the growth of the forced disturbance is greater than that of the unforced. It is also possible to see the upstream influence of the forcing. Of great importance is that the curve of the forced disturbance is above the curve of the undisturbed one. Figure 13 shows the evolution of the forced disturbance in the same manner as figure 12, i.e. the evolution for different frequencies at several streamwise positions. The greatest difference with the unforced case is the well defined peak at the frequency of the forcing. It is also possible to see that other frequencies than the forced one are the ones which grow at the end of the fringe.

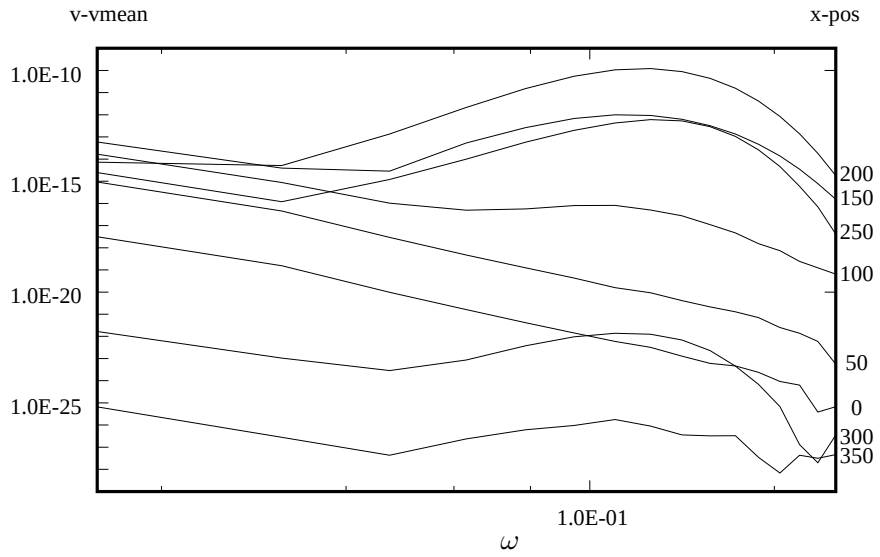

FIGURE 11. Frequency spectrum for different x-positions. For each line the x-position is given to the right. The fringe starts at $x = 200$ and total the length of the computational box is 400. No forcing is applied to create a disturbance, instead truncation errors grow in the physical part of the box.

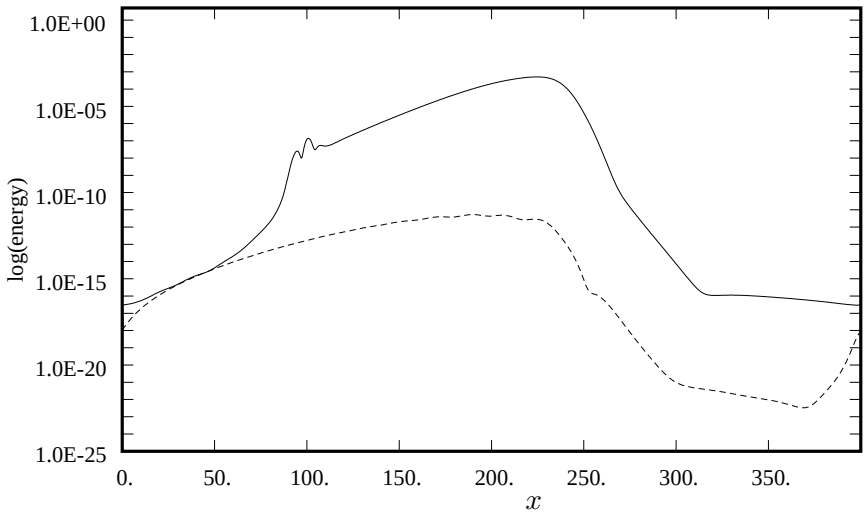

FIGURE 12. Energy of the forced wave as function of x. The solid line denotes a case where a volume force was introduced at $x = 100$. The dashed line represents the case of no forcing.

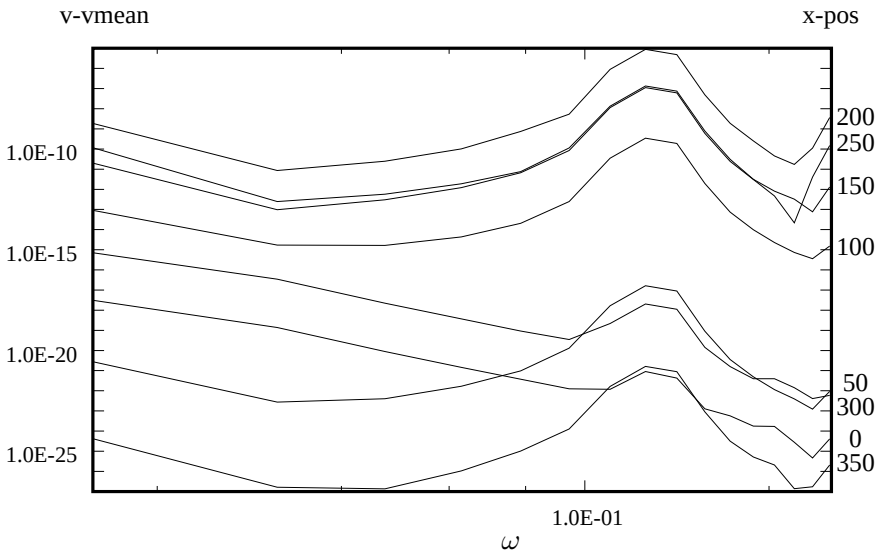

FIGURE 13. Frequency spectrum for different x-positions. For each line the x-position is given to the right. The fringe starts at $x = 200$ and total length of the computational box is 400. A volume force is applied at $x = 100$ with the frequency $\omega = 0.13$.

Appendix D. Examples, user created files

D.1. *Example* **par.f**, **bls.i**, **bla.i** *file for a simple simulation*

Below is an example of the adjustable part of a **par.f** include file. It is set up for a $32 \times 33 \times 32$ spectral mode simulation without spanwise symmetry, dealiazing in the x and z-direction, and in-core storage. The parameters `mby` and `mbz` are set for minimum storage.

```
c par.f contains size of problem
.
.
.
c adjustable parameters
c number of spectral modes
      parameter (nx=32,ny=33,nz=32)
c     dealiazing flags
      parameter (nfxd=1,nfyd=0,nfzd=1)
c symmetry flag
      parameter (nfzsym=0)
c core storage flag
      parameter (nfc=1)
c boxsize
      parameter(mby=1,mbz=1)
c number of processors
      parameter(nproc=1)
c bla with pressure solver (1)
c bls,rit,pre,cmp and bla without pressure (0)
      parameter(pressure=0)
c statistics
      parameter (nxys=42)
c computed parameters
.
.
.
```

Below is an example of a simple **bls.i** file to generate a localized disturbance in a file named **bl0.u**. Note that comments are allowed on lines with non-character data.

```
bl0.u
950.    re
100.    xl
10.     yl
50.     zl
3       fltype
0.      no Galilei shift velocity
.true.  generation of localized disturbance
1       type of disturbance
0.0002  amplitude
```

```
0.      rotation angle
2.      scale in x-direction
0.      origin in x-direction
2.      scale in y-direction
2.      scale in z-direction
1       type of distribution in the wall normal direction
.false. no waves
.false. no noise
```

Below is an example of a simple **bla.i** file to run initial data in file **bl0.u** to time 10 and output the result to file **bl10.u**. An amplitude list is written to bl10amp.d

```
bl0.u
bl10.u
10.             time for simulation
100             max iterations
7200.           max CPU time to stop(give a big value if not needed)
0.0             time step, =0 for automatic variation
4               number of time integration stages (1/3/4)
100.            keep old box length
.false.         no variable size
.0              rotation rate; no rotation
110             boundary condition at the free-stream
.false.         no chebyshev integration method; tau method
.false.         no Galilei transformation
.false.         no spatial simulation; temporal simulation
0.5             the boundary layer development speed
0               no localized volume force
.false.         no trip force
0               the boundary condition at the wall; no blowing/suction
4               cfl calc interval
4               amp calc interval
bl10amp.d
.false.         no y-dependent statistics
0               extremum calc interval; no extremum calc
0               xy-statistics calculation interval; no xy-stat calc
0               number of saved 3-d fields
0               number of saved wavenumbers
0               number of save planes
```

D.2. *Example* **par.f**, **bla.i** *file for a simulation of a turbulent boundary layer under an adverse pressure gradient.*

When running this example the turbulent statistics are stored in the file **endxys.u**. The simulation has to be run for a long time for the statistics to be sufficiently smooth. On a super computer the job can be restarted again after accomplishing a run. The different files for the statistics are then added together by the **addxys** program. The statistics are evaluated with the program **pxyst**. The velocity field **bl3400.u** and free-stream table **freestream.d015** are required when running this example.

```
c par.f contains size of problem
.
.
.
c adjustable parameters
c number of spectral modes
      parameter (nx=480,ny=161,nz=96)
c     dealiazing flags
      parameter (nfxd=1,nfyd=0,nfzd=1)
c symmetry flag
      parameter (nfzsym=0)
c core storage flag
      parameter (nfc=1)
c boxsize
      parameter(mby=2,mbz=2)
c number of processors
      parameter(nproc=6)
c bla with pressure solver (1)
c bls,rit,pre,cmp and bla without pressure (0)
      parameter(pressure=1)
c statistics
      parameter (nxys=42)
c computed parameters
.
.
.
```

Below is the **bla.i** file.

```
bl3400.u
bl3416.u
p3416.u
3416.            total simulation time
4000000          number of iterations
3600000.         cpu time
0.0              time step
4                1/3/4 number of stages
450.             keep old box length
.false.          variable size
.0               rotation rate
101              boundary condition number
.false.          no cim; use tau method
.false.          no Galilean transform
.true.           spatial simulation
.true.           read tabulated free-stream
freestream.d015
.false.          read in base flow; no base flow
1.25             strength of fringe region
-50.             start of fringe region
```

```
.0              end of fringe region
40.             rise distance of fringe
10.             fall distance of fringe
0.0             no oblique waves forced in the fringe
0.0             no two dimensional T-S wave
0               no localized volume force
.true.          trip forcing
0.0             steady forcing amplitude
0.2             time dependent forcing amplitude
4.0             x-length scale of trip
10.             x-origin of trip
1.0             y-length scale of trip
10              number of z-modes in trip
4.0             time-scale of trip
-1              random number seed for trip
0               the boundary condition at the wall; no blowing/suction
4               cfl calc interval
0               amp calc interval; no amplitude calculation
.false.         no y-dependent statistics
0               extremum calc interval; no extremum calculation
20              xy statistics calculation interval
endxys.u
50000           iterations between saves; do not save until finished
0.              time to start accumulation of statistics
3               number of saved 3-d fields
3404.
bl3404.u
3408.
bl3408.u
3412.
bl3412.u
0               number of saved wavenumbers
0               number of save planes
```

Royal Institute of Technology
Department of Mechanics
SE-100 44 Stockholm, Sweden
http://www.mech.kth.se